

DISSERTATION

SYNTHESIS AND CHARACTERIZATION OF FLUORINE-CONTAINING C₆₀
DERIVATIVES AND THEIR CHARGE CARRIER PHOTOPHYSICS IN ORGANIC
PHOTOVOLTAICS

Submitted by

Bryon W. Larson

Department of Chemistry

In partial fulfillment of the requirements

For the Degree of Doctor of Philosophy

Colorado State University

Fort Collins, Colorado

Fall 2013

Doctoral Committee:

Advisor: Steven H. Strauss
Co-Advisor: Garry Rumbles

Anthony Rappé
Randy Bartels
Eugene Chen
Raymond S. Robinson

ABSTRACT

SYNTHESIS AND CHARACTERIZATION OF FLUORINE-CONTAINING C₆₀ DERIVATIVES AND THEIR CHARGE CARRIER PHOTOPHYSICS IN ORGANIC PHOTOVOLTAICS

Transformative advances in the science of new materials and technological solutions for energy conversion and storage require focused efforts from scientists across different disciplines. One of the major frontiers for modern chemistry is the molecular design of advanced materials from earth-abundant elements with finely tuned chemical, photophysical, and electronic properties. In this work, several highly efficient and, in some cases, highly regioselective synthetic methodologies have been developed for the first time that resulted in a wide array of versatile fullerene-based organic electron acceptors with highly tunable electronic properties. The classes of these newly synthesized and characterized materials include mono-perfluorocarbocyclic C₆₀ derivatives, highly functionalizable ω-X-perfluoroalkylfullerenes (X = SF₅, Br, I, COOEt), twenty one new isomers of deca-trifluoromethyl[60]fullerenes, and several new isomers of octa- and hexa-trifluoromethyl[60]fullerenes. Improved synthetic and separation techniques yielding up to multi-gram amounts of difluoromethylene[60]fulleroid and several other classes of technologically important perfluoroalkylfullerenes have also been developed, which enabled several organic photovoltaic-relevant studies using state-of-the-art facilities at the National Renewable Energy Laboratory. This included the first experimental determination of an optimal driving force for the relative yield of free carrier generation in a family of polyfluorene polymers by using a series of trifluoromethylfullerene acceptors with a large range of electron

affinities synthesized by the author. In another study, a judiciously selected series of acceptors was applied for a time-resolved microwave conductivity (TRMC) study that provided the first compelling experimental evidence that the yield for uncorrelated free charge generation in organic photovoltaic (OPV) device-relevant blends of donor:acceptor active layers is a function of carrier mobility. Finally, a new fullerene acceptor rivaling one of the champion fullerene derivatives, phenyl-C₆₁-butyric acid methyl ester (PCBM), in OPV performance was studied by TRMC and in OPV devices.

ACKNOWLEDGEMENTS

First and foremost, I respectfully offer my greatest appreciation to my advisors Prof. Steve Strauss and Prof. Olga Boltalina, for without their guidance, support, and enthusiasm during the past five years I would not be the person I am today. They are truly caring and wonderful people, and I am lucky and proud to have had them as my research mentors and to call them friends. I also want to acknowledge and thank the past and present members of the Strauss-Boltalina research group for their helpful research discussions, enjoyable company, and steadfast support. It has been such a pleasure working with each and every one of you. I'd also like to extend thanks to my committee members Prof. Eugene Chen, Prof. Tony Rappe, Prof. Randy Bartels, and Prof. Ray Robinson for their support and advice. Additionally, I'd like to thank Prof. Mike Elliott and Prof. Amy Prieto for their useful discussions and advice.

My appreciation and respect also goes out to my co-advisor Dr. Garry Rumbles, for his support and advice during the time I spent at the National Renewable Energy Laboratory. I also want to specifically thank Dr. Nikos Kopidakis for teaching me almost everything I know about solar cell photophysics, and for being such a great mentor and friend. I would also like to thank Dr. Andrew Ferguson, Dr. David Coffey, and Dr. Obadiah Reid for their tremendously helpful discussions, suggestions, and assistance.

Finally, I want to thank my greatest fan base, the rock solid foundation of my life, who have always encouraged me to follow my dreams and believed in me with endless support, my parents. I love you both very much. Also, to the rest of family and friends, thank you for always being there to bring me joy.

TABLE OF CONTENTS

Abstract.....	ii
Acknowledgements.....	iv
Chapter 1: Synthesis, Purification, and Characterization of Perfluorocarbocycle Derivatives of	
C_{60}	1
1.1. Introduction.....	1
1.2. $C_{60}(CF_2)$	2
1.3. $C_{60}(C_2F_4)$	9
1.4. $C_{60}(C_4F_8)$	16
1.5. References.....	20
Chapter 2: Synthesis, Purification, and Characterization of Functionalizable R_F Derivatives of	
C_{60} : ω -X-PFAFs.....	22
2.1. Introduction.....	22
2.2. $C_{60}(CF_2CO_2Et)_2$ and $C_{60}(CF_2CO_2Et)H$	23
2.3. $C_{60}(C_4F_8X)_2$, X = Br, I, SF_5	40
2.4. References.....	46
Chapter 3: Synthesis, Purification, and Characterization of Trifluoromethyl[60]fullerenes.....	47
3.1. Isomers of $C_{60}(CF_3)_{10}$	47
3.1.1. Background.....	47
3.1.2. General Comments on New Isomers of $C_{60}(CF_3)_{10}$	57
3.1.3. Synthesis and Isolation of New $C_{60}(CF_3)_{10}$ Compounds.....	58
3.1.4. X-ray Structures of Six New 60-10's.....	82

3.1.5. Characterization of New 60-10's by ^{19}F NMR Spectroscopy and Correlations between $\delta(^{19}\text{F})$ and J_{FF} Values and Addition Patterns	96
3.1.6. Electrochemical Study of New 60-10's	113
3.1.7. Links Between Additions Patters, $E_{1/2}$ Values, Electron Affinities, and DFT-Predicted LUMOs and LUMO Energies.....	121
3.2. Synthesis and Improved Isolation of Lower C_{60} -Trifluoromethylfullerenes	128
3.2.1. Introduction.....	128
3.2.2. Large-scale Synthesis and Improved Isolation Methods	129
3.3. Experimental	142
3.4. References.....	145
Chapter 4: Phenyl- C_{61} -Butyric Acid Methyl Ester (PCBM).....	149
4.1. General Remarks.....	149
4.2. Electronic Properties of PCBM	150
4.2.1. Introduction.....	150
4.2.2. Experimental	151
4.2.3. Results and Discussion	153
4.2.3.1. Gas-phase Electron Affinity	153
4.2.3.2. DFT Study.....	153
4.2.3.3. Cyclic Voltammetry and $E(\text{LUMO})$ Approximations	156
4.2.4. Summary and Conclusions	163
4.3. Thermal Instability.....	164
4.3.1. Introduction.....	164
4.3.2. Experimental Section	166

4.3.3. Results and Discussion	167
4.3.3.1. Thermal Behavior of PCBM	170
4.3.3.2. Formation, Isolation, and Characterization of a New Isomer of PCBM	172
4.3.3.3. Sublimation Study of PCBM	180
4.3.4. Summary and Conclusions	190
4.4. References.....	191
Chapter 5: Charge Generation and Decay Dynamics in Polymer:PFAF Organic Photovoltaic	
Active Layers	197
5.1. General Introduction to Organic Photovoltaics	197
5.2. Charge Generation in Organic Photovoltaics	200
5.3. Spectroscopic Techniques.....	206
5.3.1. Time-resolved Photoluminescence, TRPL	207
5.3.2. Time-resolved Microwave Conductivity, TRMC.....	211
5.4. Fundamental and Applied Studies of PFAFs in OPVs	215
5.4.1. Exciton Quenching in P3HT:PFAF Films	215
5.4.2. TRMC Studies of Energetic Driving Force and Free Carrier Yield in OPV Active Layers Containing TMFs	221
5.4.3. TRMC Study of Electron Mobility in P3HT:TMF Active Layers	232
5.4.4. OPV Devices Containing PFAF Acceptors	249
5.5. Summary and Conclusions	266
5.6. References.....	267

Chapter 1: Synthesis, Purification, and Characterization of Perfluorocarbocycle Derivatives of C₆₀.

1.1. Introduction.

Most common fullerene C₆₀ and its derivatives are useful molecules for a number of applied and fundamental studies. The work described in this dissertation concerns in large part the chemistry and purification methods for the largest class of well-characterized C₆₀ derivatives known, perfluoroalkylfullerenes (PFAFs). These types of derivatives are recognized for their superior chemical and thermal stabilities, long-lived radical anion lifetimes in solution, and wide range of accessible electron accepting properties based on the number, nature, and specific location of each perfluoroalkyl (R_F) addition to the fullerene cage. Due to the vast number of practically accessible R_F groups that can be attached to C₆₀, and the innumerable addition patterns possible for those R_F substituents (which gives rise to a large span of molecular properties), the field remains rich with new possibilities and exciting discoveries. In Chapters 1–3, the synthesis and characterization of several families of new PFAF and PFAF-like compounds is presented. First, an original synthetic method for C₆₀ derivatives carrying perfluorocarbocycles, in a variety of sizes, is discussed. A new PFAF-like group of compounds, which retain the properties of a PFAF, but have a functional group for further chemical elaboration, known as ω-X-PFAFs are also described. Finally, large-scale and tunable trifluoromethylation reactions employing a gas-solid gradient-temperature reactor are described, which produced 21 new isomers of C₆₀(CF₃)₁₀, in addition to the six that were previously known, that were studied by electrochemical, spectroscopic, structural, and theoretical methods. Additionally, syntheses were scaled to multi-gram of C₆₀, yielding a number of TMFs in high

purity and large quantity that enabled their extensive studies as electron acceptors in organic photovoltaic active layers, as shown in Chapter 5.

1.2. $C_{60}(CF_2)$.

This is a unique and interesting molecule for a number of reasons. From a fundamental perspective, this was shown to be the only example, in 2007 by Pimenova *et al.*,¹ of an opened [6,6]-bond fulleroid, and currently remains so, not just for C_{60} but for any fullerene cage! Typically, when a carbene is added across a [6,6]-double bond, it does not insert into the cage, but rather a cyclopropyl ring is formed exohedrally, which has been documented in the literature for every other carbene addition ($R = CR', H, Cl, Br, I$).^{2,3} This observation has not only been limited to methyleno- (or methano-) additions, but also holds true for epoxides formed across hex-hex junctions.⁴⁻⁶ Here, it is noted that this “difluoromethylene-homo[60]fullerene” has actually been inaccurately termed as a fullerene in the literature; fullerenes consist of *only* pentagons and hexagons by definition. Closed convex polyhedra consisting of faces larger than hexagons are termed fulleroids, and therefore $C_{60}(CF_2)$, which contains two heptagons as a result of CF_2 *insertion* across a hex-hex junction, is more accurately named here as a difluoromethylene[60]fulleroid.

As a result of insertion rather than addition, $C_{60}(CF_2)$ is purple-red when dissolved in aromatic solvents and almost indistinguishable from C_{60} , which is not surprising since the pi system is minimally perturbed. However, the presence of the CF_2 group improves solubility and increases the electron affinity, thus introducing why this molecule is also interesting from an applied point of view. In 2009, a theoretical study of $C_{60}(CF_2)_n$ ($n=1,2$) compounds as electron transport materials concluded that overall the electron transport properties in these compounds

are slightly diminished compared with C_{60} (this is expected for any covalent addition to C_{60}), but reorganization energies for the various isomers (ca. 150 meV) are not impacted greatly, and therefore transport in films should be good.⁷ Also, the increase in electron affinity (ca. 0.1 – 0.5 eV for various isomers)⁸ should improve charge injection compared to C_{60} . Finally, film quality of difluoromethylene[60]fulleroids was postulated to be enhanced due to ordering of the molecules in the solid state based on the introduced dipole of the CF_2 addition(s). While other computational studies have followed these reports, currently none of these hypotheses have been experimentally evaluated.

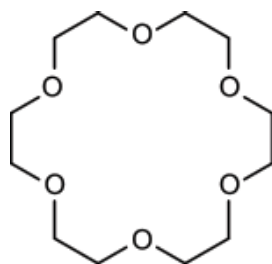
The preparation of difluoromethylene[60]fulleroids is fairly straightforward; the synthesis by Pimenova *et al.* involved generation of CF_2 radicals via thermal decomposition of sodium chlorodifluoroacetate in a refluxing *ortho*-dichlorobenzene solution of C_{60} facilitated by use of the phase transfer catalyst (PTC) 18-crown-6 ether.¹ A follow-up report on the optimization of this synthetic procedure examined the effects of reaction time, PTC choice, and relative molar ratios of reagents on the yield of $C_{60}(CF_2)$.⁸ Concerning the part of that study on the PTC choice, however, the authors only investigated 18-crown-6, *n*-tetrabutylammonium bromide, or running reaction without a PTC; in that study, 18-crown-6 ether was found to give optimal yield of $C_{60}(CF_2)$ (70% yield from 45% conversion of C_{60} based on HPLC chromatogram integration).

In this work, a further improvement of the synthesis of $C_{60}(CF_2)$ was achieved giving an 80% yield from 70% converted C_{60} , also based on HPLC chromatogram integration. The key differences between the synthesis developed in this work and that of Pimenova *et al.* is that the reaction is performed under Schlenk conditions (i.e., in air-free conditions) and a more appropriate choice of PTC is applied.

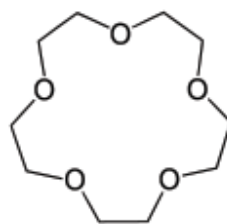
The cavity diameter of some crown ethers as well as their suitably sized alkali metal counterions are shown in Figure 1.1. Considering the ionic radius of the sodium cation in the difluoromethylene source for this reaction ($\text{CF}_2\text{ClCO}_2\text{Na}$) is ca. 1.94 Å, the use of 18-crown-6 ether, which has a cavity diameter of 2.6 – 3.2 Å, is not the optimal choice for efficiently complexing Na^+ . Instead, the cavity in 15-crown-5 is better suited for a sodium ion, and indeed its use as a PTC in this work led to a nearly twice higher yields of $\text{C}_{60}(\text{CF}_2)$. Figure 1.2. shows the comparison of three HPLC chromatograms representing the following syntheses: (i) 18-crown-6 PTC under benchtop conditions (literature) (ii) 18-crown-6 PTC under inert atmosphere, and (iii) 15-crown-5 PTC under inert atmosphere. Otherwise, the reactions were performed using identical conditions. Comparison of the black and blue chromatograms clearly shows the advantage of performing the synthesis under an inert atmosphere compared to benchtop conditions. The intensities of the C_{60} peak in the HPLC chromatograms of the 18-crown-6 and 15-crown-5 reactions have been normalized to highlight the increased conversion of C_{60} due to use of 15-crown-5. It is likely that higher C_{60} conversion in the latter case is a consequence of the higher concentration of the reactive species in solution. Slight differences in retention times between the HPLC chromatograms from this study and the literature chromatogram¹ are due to variations in flow rate, eluent, and column size.

The UV-vis spectrum of $\text{C}_{60}(\text{CF}_2)$ is very similar to that of C_{60} , and does not have the characteristic feature between 426 and 434 nm indicative of [6,6]-closed additions,

Crown Ether	"Cavity" Diameter	Cation (Ionic Radius)
12-crown-4	1.2 – 4.5 Å	Li ⁺ (1.39 Å)
15-crown-5	1.7 – 2.2 Å	Na ⁺ (1.94 Å)
18-crown-6	2.6 – 3.2 Å	K ⁺ (2.66 Å)



18-crown-6



15-crown-5

Figure 1.1. Top: The cavity diameters of three crown ethers are shown, along with complimentary ionic radii of selected cations. The structures of 18-crown-6 and 15-crown-5 ethers are shown below.

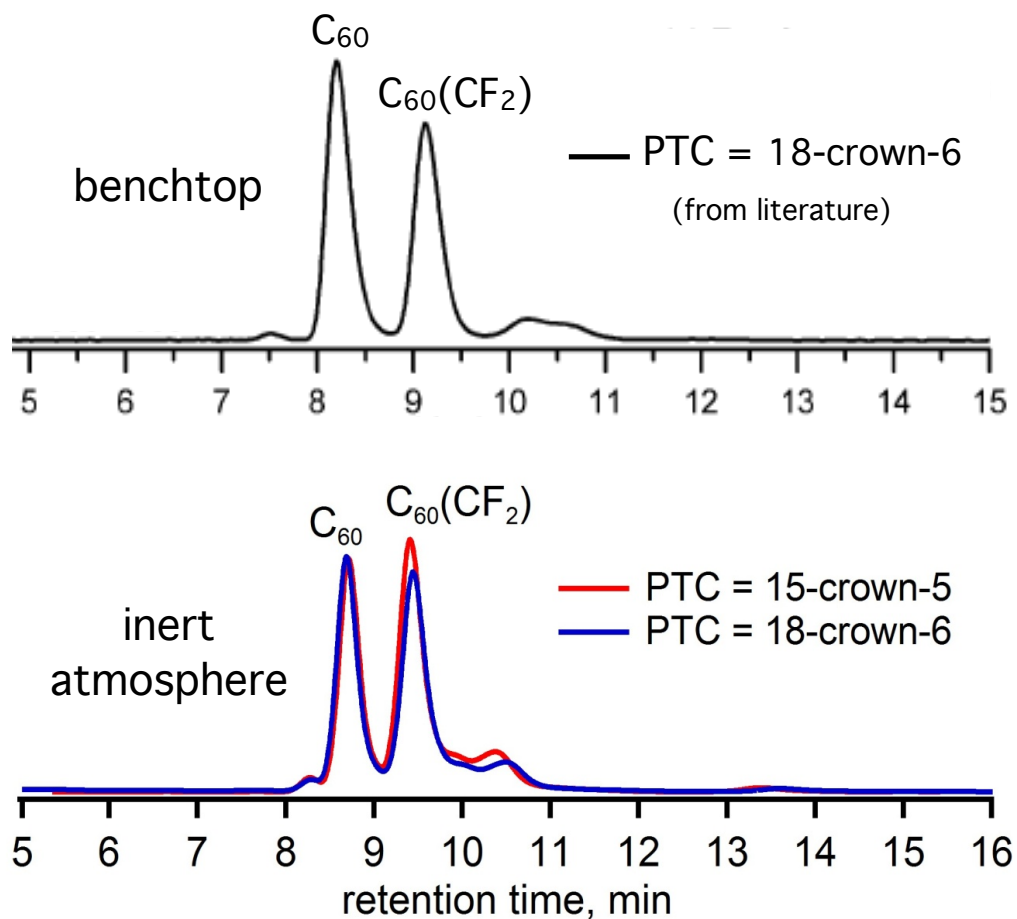


Figure 1.2. The HPLC chromatograms are shown for syntheses of $C_{60}(CF_2)$ as optimized in the literature (top – adapted from ref.¹) and two improved methods reported here (bottom).

shown in a toluene dilution series in Figure 1.3, and is consistent with the literature spectrum. The ^{19}F NMR spectrum for $\text{C}_{60}(\text{CF}_2)$ was first discussed in 2007 by Pimenova *et al.*;¹ the two fluorine atoms in the [6,6] isomer are equivalent by symmetry and therefore display a singlet ($\delta -118.4$ in a benzene- d_6 /ODCB mixture with C_6F_6 standard) while the asymmetric [5,6] isomer shows expected AB splitting of the two fluorine atoms ($\delta -120.6$). In the literature report, the exact mixture of NMR solvent was not provided, so the two isomers are reported here in 100% CDCl_3 (C_6F_6 standard, 376.5 MHz). The chemical shift of the [6,6] isomer appears at -122.0 ppm and the [5,5] isomer AB system is at -124.2 ppm, as shown in Figure 1.3.

Experimental. All operations were performed using Schlenk technique conditions. A nitrogen-flushed 250 mL three-neck flask was charged with 50 mg C_{60} (99%; MTR, Ltd.), 3 equivalents or 32 mg of $\text{CF}_2\text{ClCO}_2\text{Na}$ (98%; Aldrich), 100 mL *o*-dichlorobenzene (previously bubbled with N_2), and several boiling beads. A reflux condenser was equipped to the 3-neck flask and, under N_2 flush, 0.3 equivalents or 4.1 μL of the phase transfer catalyst 15-crown-5 ether was added via syringe. The solution was refluxed vigorously for one hour under N_2 at which point the heating mantle was turned off and the solution was allowed to cool naturally still under N_2 . The ODCB was pumped off via dynamic vacuum and the product was redissolved in ~ 10 mL toluene, filtered, and analyzed by HPLC using 100% toluene eluent. Approximate conversion of C_{60} (by HPLC chromatogram integration) was 70% with 85% selectivity for $\text{C}_{60}(\text{CF}_2)$.

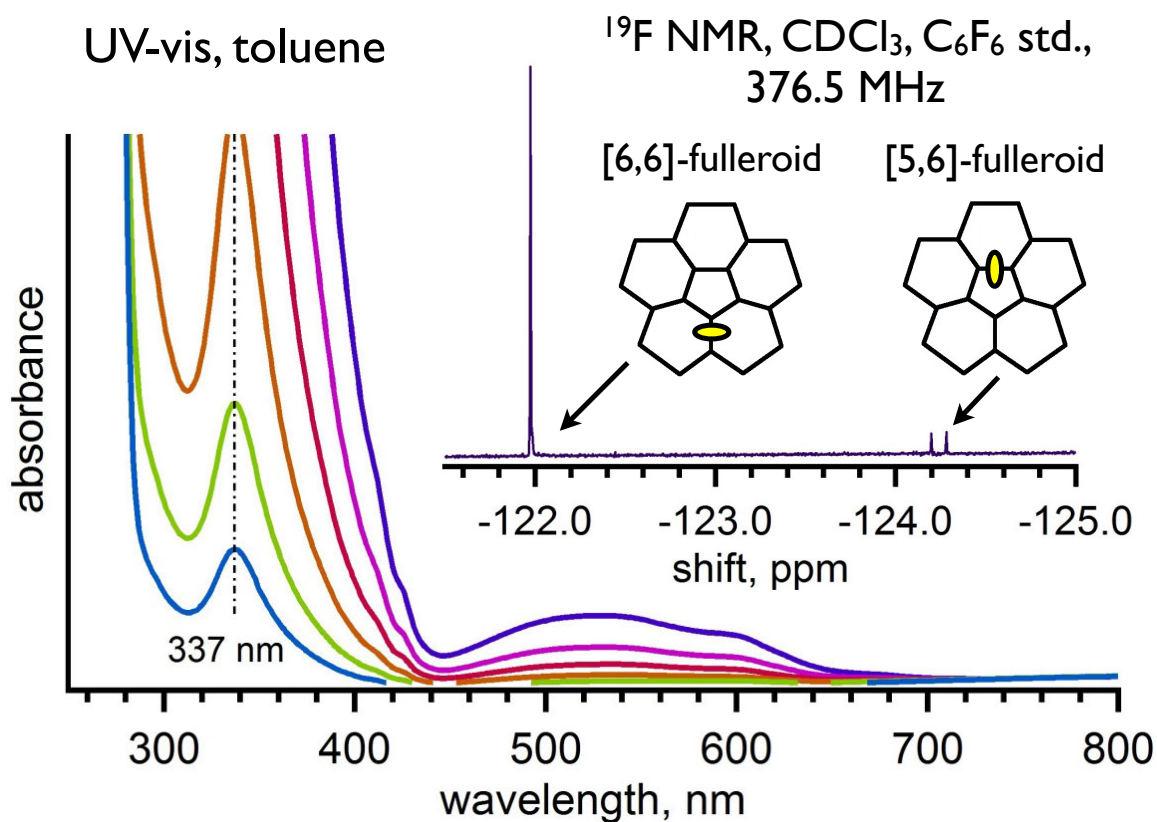


Figure 1.3. The UV-vis absorption spectra of a dilution series of $\text{C}_{60}(\text{CF}_2)$ in toluene. The inset shows the ^{19}F NMR spectrum of a sample comprised of primarily the [6,6]-fulleroid with a small amount of the [5,6]-fulleroid. The CF_2 locations are also shown on a relevant portion of the cage, depicting the symmetry of the [6,6] isomer and asymmetry of the [5,6] isomer.

1.3. $C_{60}(C_2F_4)_n$.

Only one report,⁹ which was preceded by a communication,¹⁰ on the biradical [2+2] addition of C_2F_4 groups to C_{60} exists in the literature. In this case, the synthesis was carried out by heating solid C_{60} and excess 1,2-diiidotetrafluoroethane, IC_2F_4I , in an evacuated and sealed ampoule for 4–24 hours at 400–450 °C, resulting in a complex mixture of 4 to 16 additions. However, HPLC separation of such complex crude product mixtures did not produce any pure isomers of $C_{60}(C_2F_4)_n$. Instead, crystals suitable for synchrotron single crystal x-ray diffractometry experiments obtained from compositionally pure fractions (by MALDI-MS analysis only) revealed two isomers of $C_{60}(C_4F_8)_2$ and one isomer of $C_{60}(C_4F_8)_6$. The authors postulated that telomerization of IC_2F_4I under the high-temperature reaction conditions during synthesis was likely the cause of the observed [4+2] products ($C_{60}(C_4F_8)_n$ compounds were synthesized using an alternative method here and more discussion of these compounds can be found in the following section). MALDI-MS was used as is the primary means of crude product characterization in that report, but it is impossible to distinguish m/z peaks corresponding to molecular ions due to *two* C_2F_4 additions versus *one* C_4F_8 addition from another. The authors did not attempt HPLC separation of the obtained crude product mixture in their first publication,¹⁰ since it was prohibitively complex; it contained a broad distribution of compounds, many isomers, and a mixed composition of products including C_2F_4 , C_4F_8 , and possibly other telomerized substituents. In the later work, however, several $C_{60}(C_4F_8)_n$ isomers were isolated from such mixtures, and structurally characterized.⁹

The main problem with the literature synthesis⁹ is that it is a heterogeneous reaction, which necessarily means that a high temperature must be used in order to ensure products sublime away and fresh reactive C_{60} is exposed. However, using a high reaction temperature

inevitably leads to the telomerization, oligomerization, or polymerization of $\text{IC}_2\text{F}_4\text{I}$ starting material,¹¹ which is what was observed by Pimenova *et al.*¹⁰ Simply lowering the reaction temperature in that synthesis would drastically decrease the rate of refreshing of the pristine C_{60} surface material in the solid, since fewer molecules, once derivatized, will sublime into the gas phase. This drastically reduces the conversion of C_{60} , and leads to unproductive use of $\text{IC}_2\text{F}_4\text{I}$ via side reactions, e.g., formation of fluorocarbons $\text{C}_n\text{F}_{2n+2}$.

Both of these challenges were overcome in this work, by applying the low-temperature sealed ampoule homogeneous solution technique, which was co-developed by the author and other members of the Strauss group. Using this low-temperature approach, a selective preparation of $\text{C}_{60}(\text{C}_2\text{F}_4)$ was achieved for the first time, as well as its characterization. In this synthesis, C_{60} and $\text{IC}_2\text{F}_4\text{I}$ are stirred vigorously in refluxing *o*-DCB in the presence of Cu powder (which serves as a scavenger of iodine and radical promoter).¹² The temperature of the reaction was found to be the most important parameter in optimizing the yield of $\text{C}_{60}(\text{C}_2\text{F}_4)$. At 190 °C no $\text{C}_{60}(\text{C}_2\text{F}_4)$ is formed after 72 hours of heating. At 205 °C, with just 4 eq. $\text{IC}_2\text{F}_4\text{I}$ the 48- hour reaction proceeds with high selectivity albeit with low yield of $\text{C}_{60}(\text{C}_2\text{F}_4)$. At 215 °C with 24 eq. $\text{IC}_2\text{F}_4\text{I}$, the reaction is complete in 5 hours, producing $\text{C}_{60}(\text{C}_2\text{F}_4)$ in high yield and selectivity, as shown in the HPLC chromatogram in Figure 1.4. These results indicate that the rate of $\bullet\text{C}_2\text{F}_4\text{I}$ addition to C_{60} drastically increases as reactions temperatures exceed 200 °C.

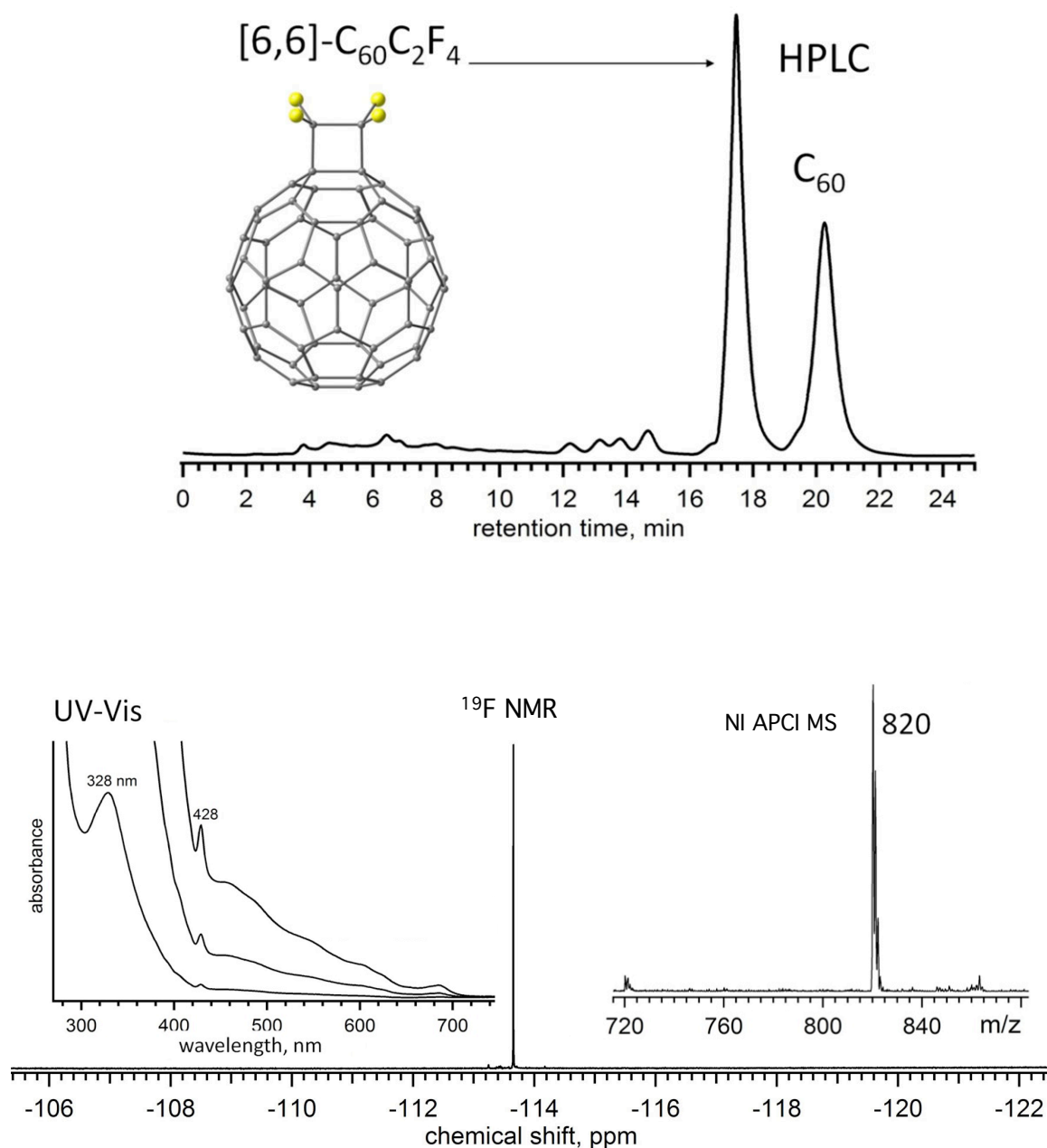


Figure 1.4. The HPLC chromatogram is shown for the selective synthesis of $C_{60}(C_2F_4)$, depicted in the inset. Analysis was performed using a Cosmosil Buckyprep column with v/v 70/30 toluene/acetonitrile eluent at 16 mL/min flow rate (300 nm detection). The UV-vis, ^{19}F NMR, and negative ion APCI mass spectra are shown for $C_{60}(C_2F_4)$, from left to right, respectively.

Characterization of the crude product mixtures of reactions with up to 30 eq. $\text{IC}_2\text{F}_4\text{I}$ by APCI-MS did not reveal any fullerene products with iodine-containing substituents. Therefore, it appears that after attachment of one $\bullet\text{C}_2\text{F}_4\text{I}$ to C_{60} , the reaction pathway towards intra-cyclization to form $\text{C}_{60}(\text{C}_2\text{F}_4)$ is more favorable than the attachment of a second $\bullet\text{C}_2\text{F}_4\text{I}$ to form $\text{C}_{60}(\text{C}_2\text{F}_4\text{I})_2$, even at higher $\text{IC}_2\text{F}_4\text{I}$ concentrations. It is not unexpected considering the close proximity of the weak terminal carbon-iodine bond to the reactive carbon atom on the C_{60} cage in ortho position to the first addition at the junction of two cage hexagons. Additionally, this addition pattern is verified by both the ^{19}F NMR and UV-vis absorption spectra. Of the two possible isomers of $\text{C}_{60}(\text{C}_2\text{F}_4)$, only in the case of [2+2] addition to [6,6] junction would one expect a singlet in the ^{19}F NMR spectrum for all four fluorine atoms due to symmetry, which is observed, shown in Figure 1.4. This also suggests that the two fluorine atoms on either carbon of the addition are totally eclipsed from a side projection, since no second order through-space coupling is observed.

Additional support of the proposed structure of $\text{C}_{60}(\text{C}_2\text{F}_4)$ was obtained from the study of the in situ vis-NIR spectra of the mono- and dianions of $\text{C}_{60}(\text{R}_\text{F})_2$ adducts carried out by collaborator Dr. A. Popov using the compound prepared by the author. Kadish and coworkers reported that absorption spectra of anions are more sensitive to the isomeric structures of C_{60}R_2 bis-adducts than the spectra of the neutral forms. In particular, they have shown that anions of *o*- $\text{C}_{60}(\text{CH}_2\text{C}_6\text{H}_5)_2$ exhibited a single absorption peak in the near-IR range, while two peaks were found in the absorption spectra of the anions of the *p*- $\text{C}_{60}(\text{CH}_2\text{C}_6\text{H}_5)_2$.^{13,14} Earlier we have found that mono- and dianions of *para*- $\text{C}_{60}(\text{CF}_3)_2$ indeed exhibited two NIR bands, whose assignment was accomplished with the help of TD-DFT computations.¹⁵ NIR bands of the anions of C_{60} derivatives correspond to the well-known NIR absorption bands of the underivatized C_{60}^- and

C_{60}^{2-} .¹⁶ However, in bare C_{60} anions this transition is two-fold degenerate, while lower symmetry of the fullerene derivative anions results in the splitting of these excitations into two components. In the *ortho*-adducts a higher-energy component has low intensity and can hardly be seen, whereas in the spectra of *para*-adducts both components have comparable intensities.¹⁵

Figure 1.5 shows Vis-NIR absorption spectra of *o*- $C_{60}(C_2F_4)$ cycloadduct from this work, two $C_{60}(CF_2C_6F_5)_2$ isomers and *p*- $C_{60}(CF_3)_2$ compared to the spectra of and measured *in situ* during electrochemical reduction at the first and second reduction steps. The spectra of the anions provide a compelling evidence of the proposed isomeric structures of the $C_{60}(CF_2C_6F_5)_2$ isomers. The spectra of the *p*- $C_{60}(CF_2C_6F_5)_2$ exhibit main NIR bands at 1540/955 nm (monoanion) and 1340/890 nm (dianion) and are very similar to the spectra of *p*- $C_{60}(CF_3)_2$ in the corresponding charged states. At the same time, the spectra of *o*- $C_{60}(CF_2C_6F_5)_2$ are almost identical to those of *o*- $C_{60}(C_2F_4)$. Monoanions of the *ortho*-adducts indeed exhibit only one band at ca. 1020 nm, whereas in the spectra of dianions a weak feature at 1360 nm can be found, in addition to the strong band at 880 nm. Thus, our study shows that absorption spectra of anions are more sensitive to the addition pattern than the spectra of neutral molecules and can help in the structure elucidation even when the spectra of neutral compounds are almost identical.

Electrochemical properties were determined for the title compound using CV and squarewave voltammetry (Table 1.1). DFT was used to calculate gas-phase *EA* and *E(LUMO)* values listed Table 1.2, shown along with the available literature data on other bis-adducts $C_{60}(R_F)_2$.

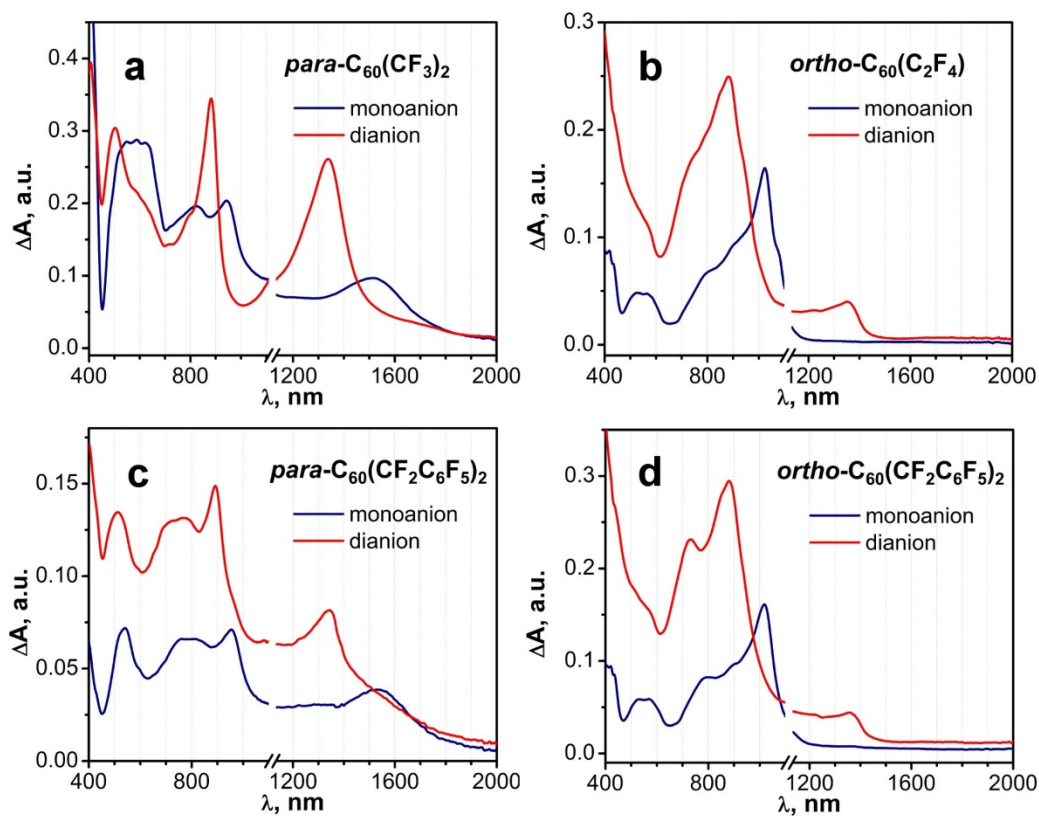


Figure 1.5. *In situ* vis-NIR spectra of the mono- and dianions of $C_{60}(R_F)_2$ adducts: (a) *para*- $C_{60}(CF_3)_2$; (b) *ortho*- $C_{60}(C_2F_4)$; (c) *para*- $C_{60}(CF_2C_6F_5)_2$; (d) *ortho*- $C_{60}(CF_2C_6F_5)_2$. The spectra were measured during cyclic voltammetry at the first (blue) and second (red) reduction steps.

Table 1.1. Experimental $E_{1/2}$ values for [6,6]- $C_{60}C_2F_4$ and $C_{60}(R_F)_2$.¹⁷ All experiments were carried out in *o*-DCB solution at 100 mV/sec with TBABF₄ supporting electrolyte. The values in parentheses were obtained from square wave voltammetry. All values are given versus the first reduction of C_{60} .

Compound	Relative $E_{1/2}$ [V] vs $C_{60}^{0/-}$ in <i>o</i> DCB			
	0/-	-2-	2-/3-	3-/4-
C_{60}	0.00	-0.39	-0.85	-1.31
[6,6]-$C_{60}C_2F_4$	0.03	-0.36	-0.86	-1.31
<i>p</i> - $C_{60}(CF_3)_2$	0.13	-0.28	-0.81	-1.26
<i>p</i> - $C_{60}(C_2F_5)_2$	0.13	-0.30	-0.82	-1.29
<i>p</i> - $C_{60}(1-C_3F_7)_2$	0.13	-0.29	-0.82	(-1.29)
<i>p</i> - $C_{60}(2-C_3F_7)_2$	0.13	-0.31	-0.83	(-1.31)
<i>p</i> - $C_{60}(1-C_4F_9)_2$	0.13	-0.30	-0.83	-1.30
<i>p</i> - $C_{60}(2-C_4F_9)_2$	0.11	-0.32	(-0.85)	(-1.33)
<i>p</i> - $C_{60}(1-C_8F_{17})_2$	0.12	-0.30	-0.82	-1.28
<i>p</i> - $C_{60}(CF_2C_6F_5)_2$	0.10	-0.33	(-0.85)	(-1.36)
<i>o</i> - $C_{60}(CF_2C_6F_5)_2$	0.00	-0.39	-0.90	(-1.34)

Table 1.2. Experimental and DFT-computed EA , $E_{1/2}(0/-)$, and ΔE_{solv} values. ^a an anion of *o*- $C_{60}(CF_2C_6F_5)_2$ fragmented under the ESI conditions, yielding the anionic fragments: $(C_{60}CF_2C_6F_5^-F)^-$, $EA = 2.790 \pm 0.008$ eV; and $(C_{60}CF_2C_6F_5)^-$, $EA = 3.720 \pm 0.015$ eV.

	$EA(\pm)$, eV		$E_{1/2}(0/-)$, V		ΔE_{solv} , eV
	exp	calc	exp	calc	calc
C_{60}	2.685(8)	2.642	0.00	0.000	-1.083
<i>p</i> - $C_{60}(CF_3)_2$	2.920(8)	2.767	0.13	0.067	-1.026
<i>p</i> - $C_{60}(C_2F_5)_2$	2.950(8)	2.793	0.13	0.071	-1.004
<i>p</i> - $C_{60}(2-C_3F_7)_2$	2.950(8)	2.803	0.13	0.066	-0.989
<i>p</i> - $C_{60}(1-C_3F_7)_2$	2.970(10)	2.808	0.13	0.068	-0.986
<i>p</i> - $C_{60}(2-C_4F_9)_2$	2.960(10)	2.823	0.11	0.062	-0.964
<i>p</i> - $C_{60}(1-C_4F_9)_2$	2.985(8)	2.826	0.13	0.072	-0.971
<i>p</i> - $C_{60}(1-C_8F_{17})_2$	3.010(8)	2.842	0.12	0.069	-0.952
<i>p</i> - $C_{60}(CF_2C_6F_5)_2$	3.005(10)	2.822	0.10	0.047	-0.951
<i>o</i> - $C_{60}(CF_2C_6F_5)_2$ ^a	n/a	2.718	0.00	-0.057	-0.950
<i>o</i>-$C_{60}(C_2F_4)$	n/a	2.633	0.03	-0.057	-1.035

Experimental. All materials and solvents were used as received. A 20 mL Schlenk tube was charged with 25 mg C₆₀ (MTR, ltd.), 400 mg copper power (Fisher Scientific), 10 mL 1,2-dichlorobenzene (Acros, ACS grade), and 151 μ L (24 eq.) IC₂F₄I (Synquest Labs). A stirbar was added and the purple solution was freeze-pump-thawed three times. Upon warming to room temperature under static vacuum, the reaction tube was submerged just above the solution level into a 215 °C oil bath with stirring, within moments, the solution was rigorously refluxing inside the tube. After five hours, the solution was brown with white CuI visible, at which point the tube was removed from the oil bath and allowed to cool to room temperature. The crude solution was then filtered, the ODCB was removed under dynamic vacuum, the brown product mixture was redissolved in HPLC grade toluene (Fisher Labs), and analyzed by HPLC in 70/30 v/v toluene/acetonitrile at 16 mL/min flow rate through a 25 x 250 mm Cosmosil BuckyPrep column.

1.4. C₆₀(C₄F₈).

The extension of the class of perfluorocarbocycle derivatives of C₆₀ reported here includes the first synthesis and characterization of C₆₀(C₄F₈) by radical [4+2] addition in solution under similar conditions to those used to prepare C₆₀(C₂F₄). As mentioned in the previous section, C₆₀ carrying multiple additions of C₄F₈ cycles were reported by Pimenova *et al.*¹⁰ that formed during the attempted synthesis of C₆₀(C₂F₄). X-ray structures were obtained for two isomers of C₆₀(C₄F₈)₂ and one isomer of C₆₀(C₄F₈)₆. Later, the synthesis of C₇₀(C₄F₈)_n, n = 1-9, was reported; solid C₇₀ was heated for 40-45 minutes in a sealed glass ampoule in the presence of excess 1,4-C₄F₈I₂ at 450–500 °C. In that report, MALDI-MS analysis of the crude product mixtures revealed poor selectivity for lower additions in the reaction, and instead a broad product distribution

centered at an m/z corresponding to 5 additions was observed. The authors used multi-stage HPLC separation to isolate $C_{70}(C_4F_8)$, which eluted from a Cosmosil Buckyprep column at 46-49 minutes with a 1:1 toluene:hexane mixture as mobile phase. However, synthesis of C_{60} bearing a mono-adduct of C_4F_8 has not been successful until now. After all, C_{60} is more readily formed in current commercial fullerene production methods, and therefore is a less expensive candidate if these compounds are to be considered for materials applications.

Using low-temperature homogeneous conditions in a sealed reaction vessel, the synthesis of $C_{60}(C_4F_8)$ was achieved for the first time by heating a solution of C_{60} and 4-10 eq. 1,4- $C_4F_8I_2$ in the presence of copper powder for 3-5 hrs at 230 °C, and characterized here by ^{19}F NMR spectroscopy as shown in Figure 1.6.

The most important reaction parameter on conversion of C_{60} to the mono cycloaddition of C_4F_8 was found to be the number of equivalents of 1,4- $C_4F_8I_2$ in the reaction. When more than 10 molar equivalents of 1,4- $C_4F_8I_2$ were added, the main product formed was the bis-adduct $C_{60}(C_4F_8I)_2$, which is discussed in detail in Section 1.3. Therefore, the concentration of 1,4- $C_4F_8I_2$ had to be minimized to tilt the balance in favor of cycle formation of the first C_4F_8I addition over the rate of a second addition of C_4F_8I , at the expense of lower yield and conversion, though.

Hence, regarding the cycle-forming tendency of 1,4- $C_4F_8I_2$ versus 1,2- $C_2F_4I_2$, it was found that cycles are exclusively formed in the case of 1,2- $C_2F_4I_2$, but formation of bis-adducts of $C_{60}(C_4F_8I)_2$ is favored over cycle formation in the case of 1,4- $C_4F_8I_2$. Clearly, this indicates the chain length of the α,ω -diiodoperfluoroalkane has a significant impact on formation of cycles versus multiple additions of iodo-terminated R_F chains, as evidenced by increasing the R_F chain length by only two carbon atoms. Probably this is due to a combination of the terminal carbon (that would complete the cycle) being further away from the cage as the R_FI chain length

increases and overall decreased chain flexibility that hinders the bend back for cycle formation; it is known that R_F chains are more rigid than corresponding R_H chains. Based on this analysis, it is hypothesized that $R_F [n+2]$, where $n > 4$, cycloadditions will be increasingly more sensitive to stoichiometric considerations for synthesis of mono-cycloadducts under these conditions. That is, the concentration of α,ω -diiodoperfluoroalkane would need to be low enough when n is high to not outcompete the associated slower rate of cycle formation with the rate of bis-adduct formation, which is proportional to α,ω -diiodoperfluoroalkane concentration.

Experimental. A 20 mL Schlenk tube containing a stirbar was charged with 25 mg C_{60} (99%; MTR, Ltd.), 405 mg Cu powder (Fisher Labs), and 10 mL *o*-DCB (ACS grade; Aldrich). To the purple solution was added 10 equivalents (63 μ L) IC_4F_8I (Synquest Labs) via syringe before three cycles of freeze-pump-thaw. The solution was heated with stirring at 230°C for 3 hours, at which point its color turned red-brown with wispy white CuI visible. After filtration, the *o*-DCB was pumped off and the crude product mixture was redissolved fully in toluene and analyzed and separated by HPLC (equipped with a Cosmosil Buckyprep column) using 100% toluene mobile phase at 16 mL/min flow rate.

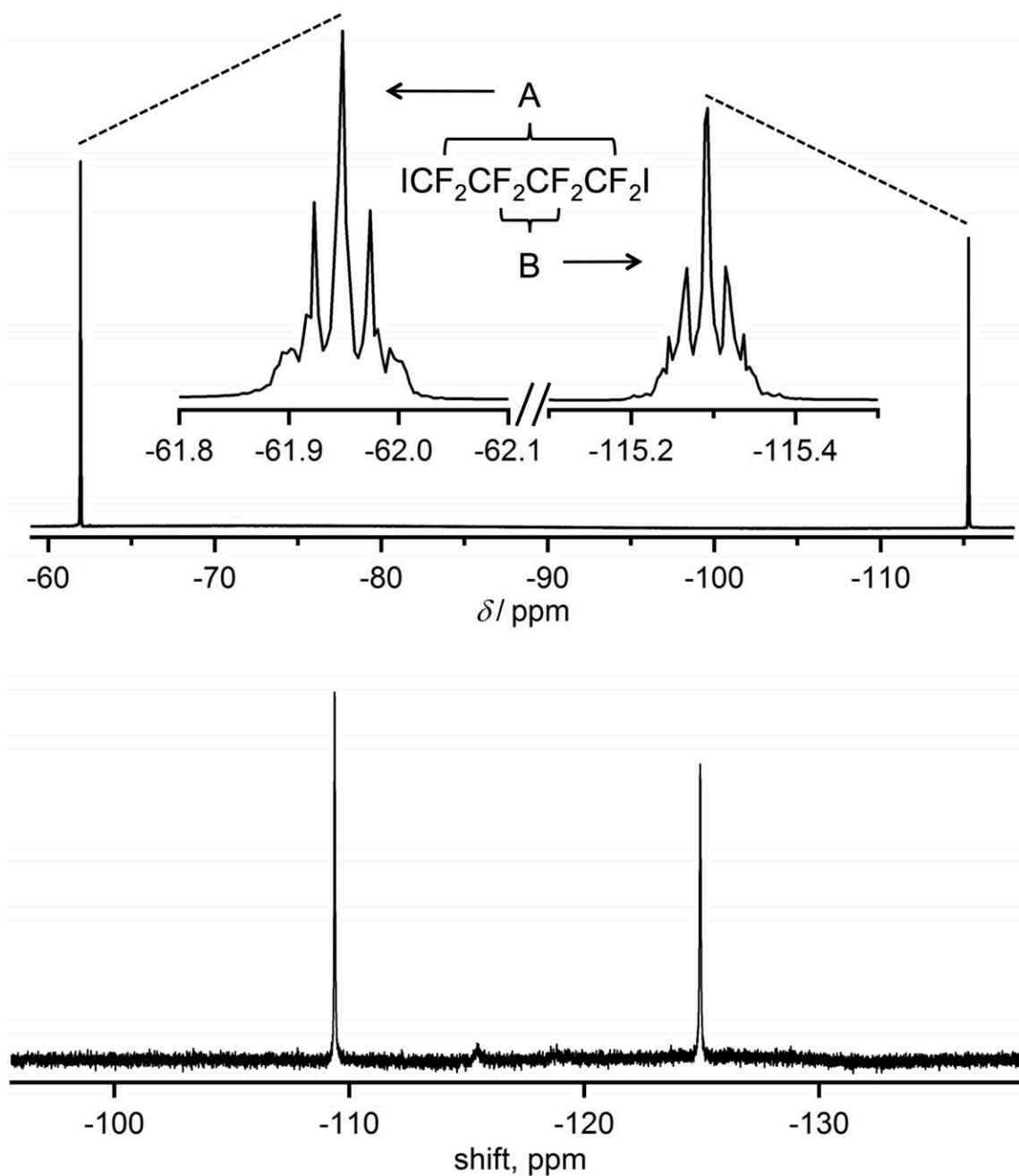


Figure 1.6. Fluorine-19 NMR spectra recorded at 376.48 MHz are shown for 1,4-diiodoheptafluorobutane (top) and $\text{C}_{60}(\text{C}_4\text{F}_8)$ (bottom) in chloroform-d solvent, referenced to C_6F_6 internal standard (-164.9 ppm).

1.5. References.

- (1) Pimenova, A. S.; Kozlov, A. A.; Goryunkov, A. A.; Markov, V. Y.; Khavrel, P. A.; Avdoshenko, S. M.; Vorobiev, V. A.; Ioffe, I. N.; Sakharov, S. G.; Troyanov, S. I.; Sidorov, L. N.: Preparation and structures of 6,6 -open difluoromethylene 60 fullerenes: C-60(CF₂) and C-60(CF₂). *Dalton T* **2007**, 5322-5328.
- (2) Tsuda, M.; Ishida, T.; Nogami, T.; Kurono, S.; Ohashi, M.: Synthesis and Characterization of Dichlorocarbene Adducts of C₆₀. *Tetrahedron Lett.* **1993**, 34, 6911.
- (3) Osterodt, J.; Vögtle, F.: C₆₁Br₂: a new synthesis of dibromomethanofullerene and mass spectrometric evidence of the carbon allotropes C₁₂₁ and C₁₂₂. *Chem. Commun.* **1996**, 547-548.
- (4) Huang, S.; Yang, X.; Zhang, X.; Hu, X.; Gan, L.; Zhang, S.: Preparation of Covalent-Bound Iodofullerene through Selective Opening of Fullerene Epoxide To Form Halohydrin Fullerene Derivatives. *Synlett.* **2006**, 8, 1266-1268.
- (5) Creegan, K. M.; Robbins, J. L.; Robbins, W. K.; Millar, J. M.; Sherwood, R. D.; Tindall, P. J.; Cox, D. M.; Smith III, A. B.; McCauley Jr., J. P.; Jones, D. R.; Gallagher, R. T.: Synthesis and Characterization of C₆₀O, the First Fullerene Epoxide. *J. Am. Chem. Soc.* **1992**, 114, 1103-1105.
- (6) Al-Matar, H.; Hitchcock, P. B.; Avent, A. G.; Taylor, R.: Isolation and characterisation of Cs-symmetry C₆₀Me₅O₂OH, the first methylated fulleranol; a bis-epoxide with two oxygens in a pentagonal rings. *Chem. Commun.* **2000**, 1071-1072.
- (7) Tokunaga, K.; Ohmori, S.; H. Kawabata, H.: Theoretical study on possible usage of difluoromethylene fullerenes as electron-transport materials. *Thin Solid Films* **2009**, 518, 477-480.
- (8) Goryunkov, A. A.; Kornienko, E. S.; Magdesieva, T. V.; Kozlov, A. A.; Vorobiev, V. A.; Avdoshenko, S. M.; Ioffe, I. N.; Nikitin, O. M.; Markov, V. Y.; Khavrel, P. A.; Vorobiev, A. K.; Sidorov, L. N.: Electrochemical, ESR and theoretical studies of [6,6]-opened C₆₀(CF₂), cis-2-C₆₀(CF₂)₂ and their anions. *Dalton Trans.* **2008**, 6886-6893
- (9) Gruzinskaya, N. I.; Pimenova, A. S.; Khavrel', P. A.; Sidorov, L. N.; Kemnitz, E.; Troyanov, S. I.: Octafluorocyclohexa derivatives of [60]fullerene: C₆₀(C₄F₈)_n (n = 2, 3, 4, and 6). *Russian Chemical Bulletin* **2009**, 58, 2276-2282.
- (10) Pimenova, A. S.; Sidorov, L. N.; Kemnitz, E.; Troyanov, S., I.: Fluorocycloalkylated Fullerenes in the Systems C_{60/70}-C₂F₄I₂. *Eur. J. Org. Chem.* **2007**, 4999-5002.
- (11) David, G.; Boyer, C.; Tonnar, J.; Ameduri, B.; Lacroix-Desmazes, P.; Boutevin, B.: Use of iodocompounds in radical polymerization. *Chemical Reviews* **2006**, 106, 3936-3962.
- (12) Kuvychko, I. V.; Strauss, S. H.; Boltalina, O. V.: Solution-phase perfluoroalkylation of C-60 leads to efficient and selective synthesis of bis-perfluoroalkylated fullerenes. *J. Fluorine Chem.* **2012**, 143, 103-108.
- (13) Kadish, K. M.; Gao, X.; Caemelbecke, E. V.; Suenobu, T.; Fukuzumi, S.: *J. Phys. Chem. A* **2000**, 104, 3878-3883.
- (14) Zheng, M.; Li, F.; Shi, Z.; Gao, X.; Kadish, K.: Electrosynthesis and Characterization of 1,2-Dibenzyl C₆₀: A Revisit. *J. Org. Chem.* **2007**, 72, 2538-2542.
- (15) Popov, A. A.; Kareev, I. E.; Shustova, N. B.; Strauss, S. H.; Boltalina, O. V.; Dunsch, L.: *J. Am. Chem. Soc.* **2010**, 132, 11709-11721.
- (16) Reed, C. A.; Bolskar, R. D.: *Chem. Rev.* **2000**, 100, 1075-1120.

(17) Kuvychko, I. V.; Whitaker, J. B.; Larson, B. W.; Folsom, T. C.; Shustova, N. B.; Avdoshenko, S. M.; Chen, Y. S.; Wen, H.; Wang, X. B.; Dunsch, L.; Popov, A. A.; Boltalina, O. V.; Strauss, S. H.: Substituent effects in a series of 1,7-C-60(R-F)(2) compounds (R-F = CF₃, C₂F₅, n-C₃F₇, i-C₃F₇, n-C₄F₉, s-C₄F₉, n-C₈F₁₇): electron affinities, reduction potentials and E(LUMO) values are not always correlated. *Chem. Sci.* **2012**, *3*, 1399-1407.

Chapter 2: Synthesis, Purification, and Characterization of Functionalizable R_F Derivatives of C_{60} : ω -X-PFAFs.

2.1. Introduction.

Perfluoroalkyl fullerenes have shorter, stronger adduct—cage bonds compared to their alkylated analogues, making them both chemically, photochemically, and thermally more robust, which may make them suitable candidates for numerous applications where such properties are required. However, even though PFAFs are the largest and most diverse class of well-characterized fullerene derivatives, the breadth of possible applications that requires more specifically tailored physical and chemical properties cannot be fully satisfied by the existing PFAF compounds. Therefore, PFAF building blocks that can be further modified may offer a more practical and versatile approach. Due to the high chemical and thermal stability of PFAFs, the task of selectively modifying an R_F substituent already on the fullerene cage is difficult (i.e. – breaking a C–F bond) without numerous side reactions or also other unwanted additions to the cage. Some examples exist in the organofluorine literature that allow for reductive defluorination of R_F groups, and many require highly reactive reagents and/or harsh conditions.^{1,2} Another approach is the addition of a particular functional group directly to the cage of a PFAF, however, unless the PFAF is carrying a large number of substituents, there will be many open reactive sites on the remainder of the cage, thus introducing a problem of selective functionalization. One example of such an approach relied on taking advantage of a highly reactive cage bond between carbon cage atoms 33 and 34 in the compound $C_{70}(CF_3)_{10}$ -1.^{3,4} The authors were able to selectively attach an organic moiety via either Diels-Alder or Bingel-Hirsch reactions. Although the method was successful, the drawback in this approach is that addition of new substituents to

the cage changes the π system on the fullerene core, and thus the properties of the starting PFAF substrate. An alternative idea has been proposed and experimentally tested in this work. A PFAF-like fullerene synthetic building block was conceived with the formula $C_{60}(R_F X)_n$, where X is a functional group and n is the number of adducts, such molecule is dubbed ω -X-PFAF here. This functionalizable ω -X-PFAF building block offers two key benefits: (i) the X group introduces a site for chemical elaboration of the compound that does not rely on cage reactivity, (ii) the cage— CF_2X linkage ensures the adduct's chemical and thermal stability is retained, allowing for a myriad of possibilities for further elaboration of the molecule, specific to an application, even under harsh conditions (that would otherwise result in adduct detachment), and (iii) the CF_2 fluorine atoms provide a useful handle for spectroscopic characterization by ^{19}F NMR to monitor further elaboration steps. In January 2011 an invention disclosure form was submitted by the author to CSU Ventures office titled, "Preparation of fullerene-(perfluorinated linkage)-(complex functional substituent) systems via a novel two-step procedure", also co-authored by Dr. Igor Kuvychko, and Professors Olga Boltalina, and Steven Strauss. The following section details the synthesis, optimization, and characterization of $C_{60}(R_F X)_n$ and related compounds.

2.2. $C_{60}(CF_2COOEt)_2$ and $C_{60}H(CF_2COOEt)$.

These two compounds offer the versatility of having either one or two functional units (in this case the ethyl acetate moiety can be modified by a number well-known organic chemistry reactions), as well as different electronic and structural properties since the addition motif is 1,4- for the bis- $R_F X$ adduct and 1,2- for the mono-hydride compound. A 1,4-addition refers to two substituents in *para* position to one another on a single hexagon of the C_{60} cage, and a 1,2-

addition corresponds to two substituents in *ortho* position to one another at the junction of two hexagons (two substituents *ortho* to one another on a hexagon at the junction of a cage pentagon and hexagon is not considered here). Concerning the electronic properties of the synthon, two additions to the fullerene cage minimally disrupt the conjugated pi-system, and thus have a minimal impact on the associated desirable properties of the parent molecule. Concerning sterics, the $C_{60}H(R_F X)$ compound may be useful in organic electronics applications where minimal adduct “shielding” of the cage is required for efficient electron transport in the material. It was shown recently that charge collection in OPV devices containing a tris-adduct of indene- C_{60} was less efficient compared to devices containing mono- and bis-adducts as acceptors.⁵ Therefore, minimizing exohedral cage “clutter” by having only one bulky functional unit on the cage can be beneficial.

The new compound $C_{60}(CF_2COOEt)_2$ was initially prepared by heating an ODCB solution of C_{60} and ICF_2CO_2Et in the presence of vigorously stirring copper powder using a sealed glass ampoule similar to a method published recently for perfluoroalkylation of C_{60} (using liquid $R_F I$ precursors) under heterogenous conditions. However, it was found that the reactivity of ICF_2CO_2Et was not the same as found for $R_F I$ compounds. Therefore, an apparatus was designed and built (glassblowing by Dr. Igor Kuvychko) (shown in Figure 2.1.) that would allow sampling of the reaction mixture without having to end the reaction and break open the ampoule, thus enabling the reaction progress to be monitored and optimized in an efficient manner. By having two Teflon valves attached to the ampoule, small aliquots could be taken from the reaction mixture to follow the reaction progress by HPLC analysis without exposing the reaction mixture to air since the ‘antechamber’ of the glass ampoule could be evacuated on a Schlenk line in between sampling aliquots. Figure 2.2 shows an example of a reaction optimization HPLC study

carried out in this work for the reaction between C_{60} and ICF_2CO_2Et . The glass apparatus also features a built-in Teflon stirbar large enough to vortex even full capacity syntheses (50 mL), since the copper powder needs to be evenly dispersed to efficiently abstract iodine and generate CF_2CO_2Et radicals.

When a large excess of ICF_2CO_2Et reagent was used, in attempt to exhaustively add ethyl difluoroacetate groups to C_{60} , up to 8 CF_2CO_2Et additions were observed by APCI-MS in the crude product. This relatively small number of added R_F (cf. up to 23 CF_3 groups or 10 C_2F_5 groups observed for C_{60} previously)⁶ indicates that the addition of more than two ethyl difluoroacetate moieties will most likely favor formation of an ‘isolated pair’ motif addition pattern, as opposed to continuous ribbon additions, which are observed for less bulky groups such as CF_3 and C_2F_5 .⁷⁻⁹ Compounds such as $C_{60}(CF_2CO_2Et)_{n>2}$ can be converted into water soluble derivatives useful for biomedical applications. For such applications, having an isolated pair addition pattern is beneficial since the functional groups are more uniformly dispersed around the hydrophobic cage. The optimal conditions for selective synthesis of compound $C_{60}(CF_2CO_2Et)_2$ were selected based on the dynamic HPLC study data (Figure 2.2). Depending on the reaction scale, $C_{60}(CF_2CO_2Et)_2$ can be prepared in 4-8 hours, the largest scale used so far is 200 mg of starting C_{60} (details in experimental section).

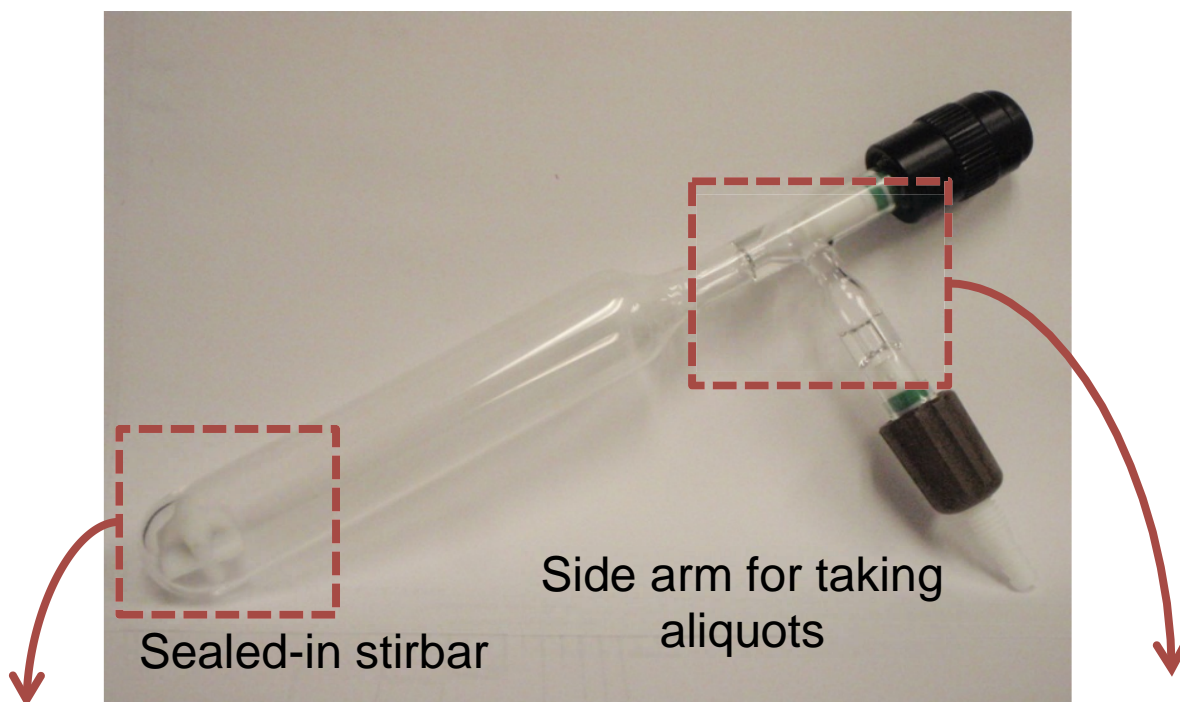


Figure 2.1. Glass reactor used for homogeneous reactions with C_{60} with capability to monitor reaction progress via sampling through side arm.

A single-stage HPLC separation (Figure 2.3) was used to isolate $C_{60}(CF_2CO_2Et)_2$. The structure of this new derivative was elucidated using a combination of 1H and ^{19}F NMR spectroscopy, UV-vis spectroscopy, and mass spectrometry. There are two signals in the 1H NMR spectrum of the sample isolated from the main peak shown in the HPLC chromatogram at 5.5 minutes, a triplet at 1.44 ppm and a quartet at 4.56 ppm in a 3:2 ratio, respectively (Figure 2.4). This indicates the ethyl (CH_2CH_3) terminus of the substituent is intact. The four fluorine atoms in $C_{60}(CF_2CO_2Et)_2$ exhibit AA'BB' splitting, shown in the ^{19}F NMR spectrum of the sample in Figure 2.5, with F—F through-space coupling being $J_{AA'} \approx J_{BB'} \approx J_{AB'} \approx 40$ Hz and F—F through-bond coupling being $J_{AB} \approx 270$ Hz. These coupling constants and splitting pattern were shown for a similar compound, whose structure was confirmed by single crystal x-ray diffraction, $C_{69}(CF_2CF_3)_2$, which has the two perfluoroethyl substituents in *para* position to one another on a cage hexagon. Furthermore, the UV-vis spectrum of the compound (Figure 2.6) exhibits identical absorption features as other C_{60} -bisadducts whose structures were solved by single crystal XRD where the two substituents are in *para* position to one another on a cage hexagon. The UV-vis spectrum of a bis-adduct of C_{60} where the two substituents are in *ortho* position to one another at the junction of two cage hexagons has a characteristic feature not observed here, which rules out that as an addition pattern of the two CF_2CO_2Et groups on the cage (an example will be shown later in this section for the 1,2-bisadduct). Mass spectrometric analysis using APCI in the negative ion mode showed a molecular ion with $m/z = 966.27$ (Figure 2.2.11); the calculated molecular weight of $C_{60}(CF_2CO_2Et)_2$ is 966.80 g/mol. These data combined provide convincing evidence for the assigned structure of 1,4- $C_{60}(CF_2CO_2Et)_2$.

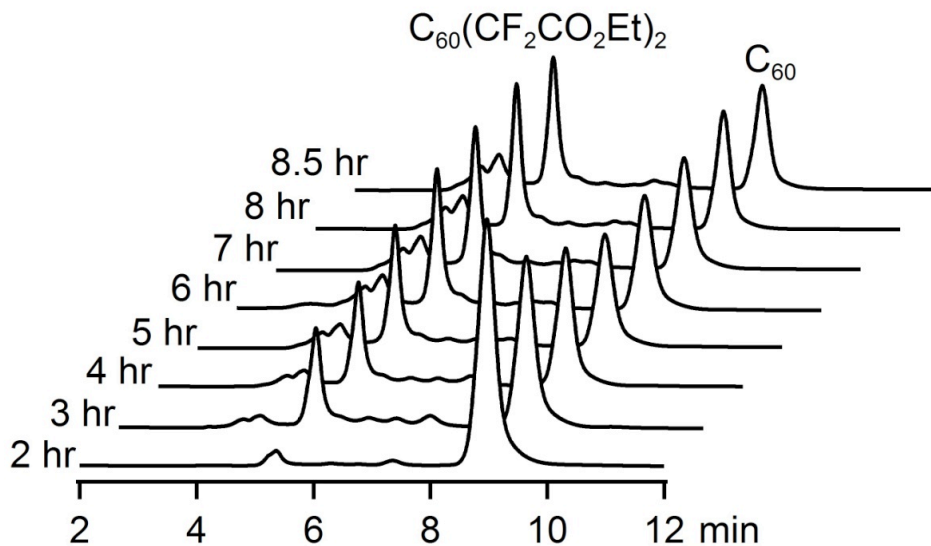


Figure 2.2. 3-D waterfall view of HPLC traces of crude reaction products between C_{60} and ICF_2CO_2Et . Each HPLC chromatogram represents an aliquot sampled during the course of the reaction (100% toluene eluent, 25×250 mm I.D. Cosmosil Buckyprep column, 16 mL/min flow rate, 300 nm detection).

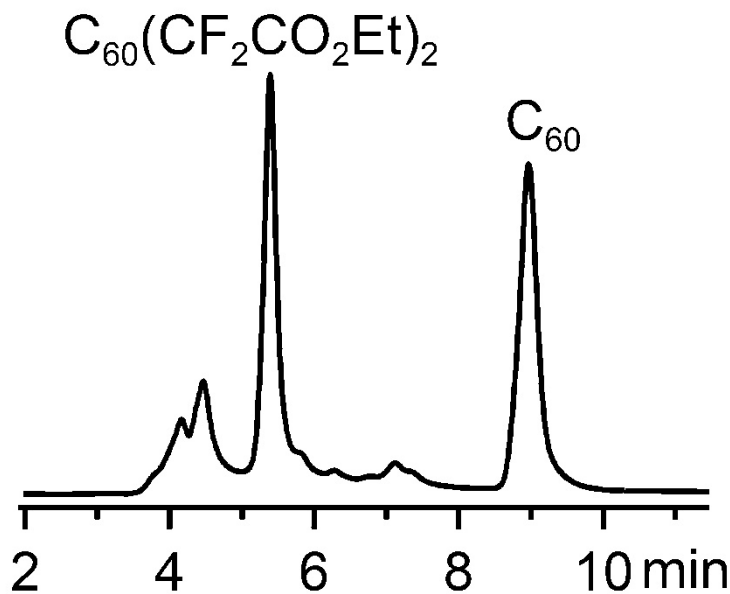


Figure 2.3. HPLC trace of the product mixture for the optimized synthesis of $C_{60}(CF_2CO_2Et)_2$ (100% toluene eluent, 25×250 mm I.D. Cosmosil Buckyprep column, 16 mL/min flow rate, 300 nm detection).

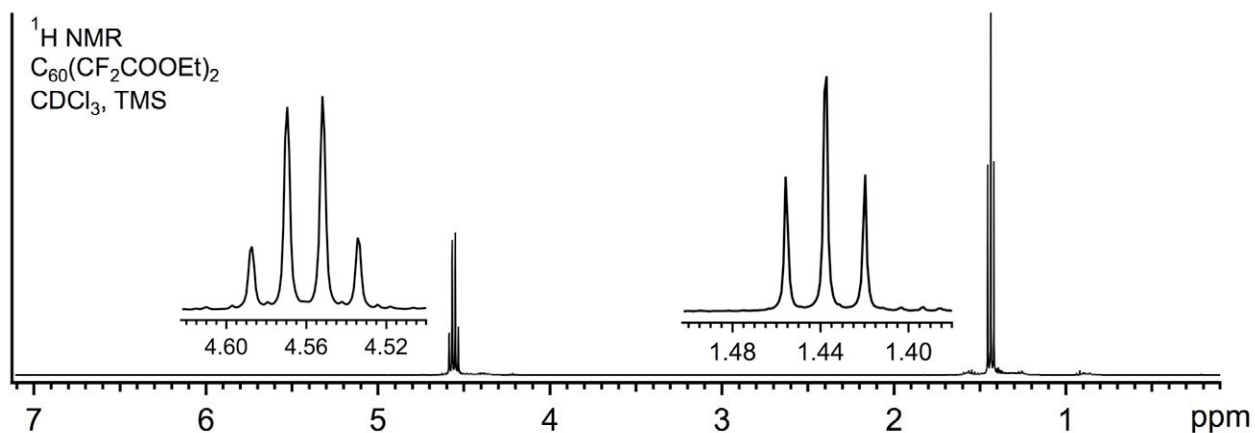


Figure 2.4. The proton NMR spectrum (400 MHz, CDCl₃, TMS internal standard) for C₆₀(CF₂CO₂Et)₂, with spectral expansions of the signals at 4.56 and 1.44 ppm. The integration ratio of the quartet (CH₂ protons) to the triplet (methyl protons) is 2:3.

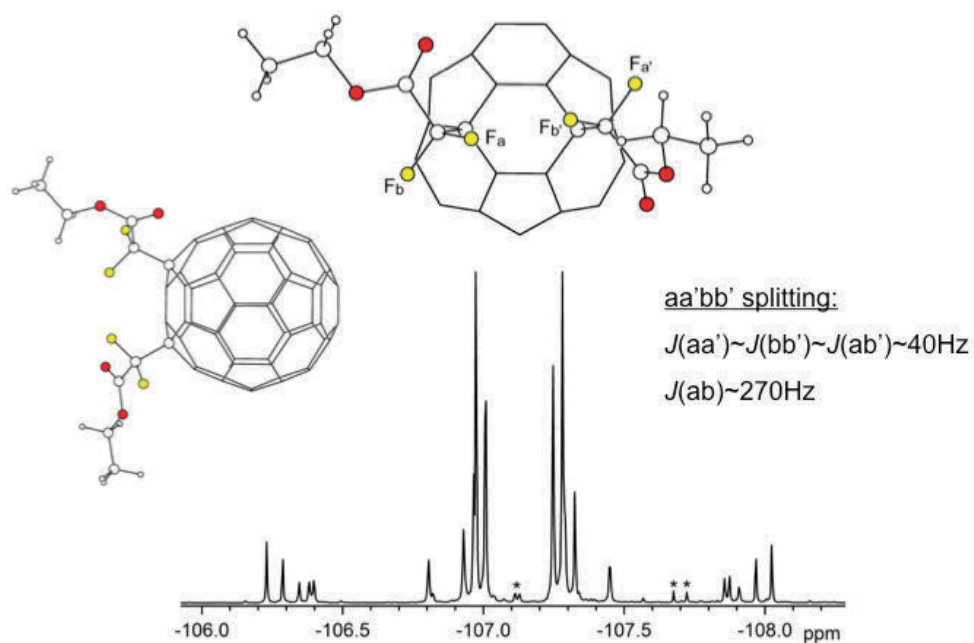


Figure 2.5. The AA'BB' splitting system is shown for C₆₀(CF₂CO₂Et)₂ in the ¹⁹F NMR spectrum (CDCl₃, C₆F₆ std., 376.5 MHz), along with coupling constants. The asterisks mark shifts that are due to slight impurities in the sample. DFT-optimized lowest energy structures are shown (courtesy Dr. Alexey Popov).

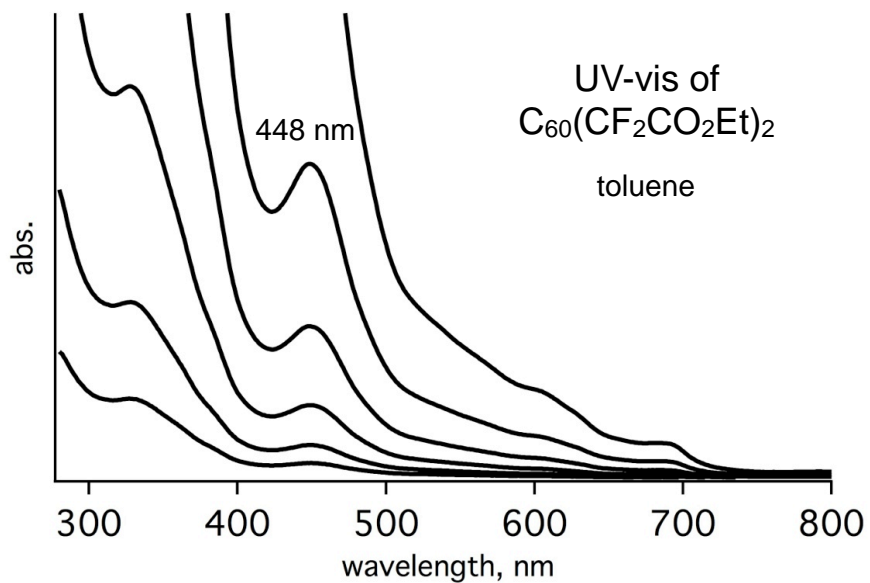


Figure 2.6. The UV-vis spectra in toluene of a serial dilution of a sample of $C_{60}(CF_2CO_2Et)_2$, which has absorption features nearly identical to C_{60} bis-adducts where the substituents are located in *para* position to one another on a cage hexagon (ref 10).

The gas-phase electron affinity was measured by Low-Temperature Photoelectron spectroscopy (LT PES) (by collaborator Dr. Xue-Bin Wang at Pacific Northwest National Laboratory) for the new compound 1,4-C₆₀(CF₂CO₂Et)₂, which is compared to previously recorded measurements for 1,4-C₆₀(CF₃)₂ and 1,4-C₆₀(CF₂CF₃)₂ compounds (the latter compound (1,4-C₆₀(CF₂CF₃)₂) was prepared by Dr. Kuvychko; see Section 2 of Chapter 3 for preparation of C₆₀(CF₃)₂). These data provided insight into the effect of the X substituent on the electron withdrawing strength of CF₂X and thus its influence on the EA of 1,4-C₆₀(CF₂X)₂ compounds when the X moiety changes from F to CF₃ to CO₂Et. For comparison, the EA values are reported relative to the previously measured EA of C₆₀. The trend for increasing electron withdrawing strength is shown in Figure 2.7, by virtue of higher EA of the molecule (shown in parentheses, EA values in eV vs EA(C₆₀)), are: CF₂CO₂Et (2.865) < F (2.900) < CF₃ (2.950). In solution, a similar trend was observed when the electrochemical properties of the three compounds were evaluated by cyclic voltammetry (measurements by Mr. James Whitaker). The first half-wave redox potentials ($E_{1/2}^{0/-}$) relative to the $E_{1/2}^{0/-}$ of C₆₀ are: 0.09(1), 0.13(1), and 0.13(1), respectively. Therefore, this serves as evidence that the ω-X-PFAF molecular design concept can be used to fine-tune the electron accepting properties of C₆₀.

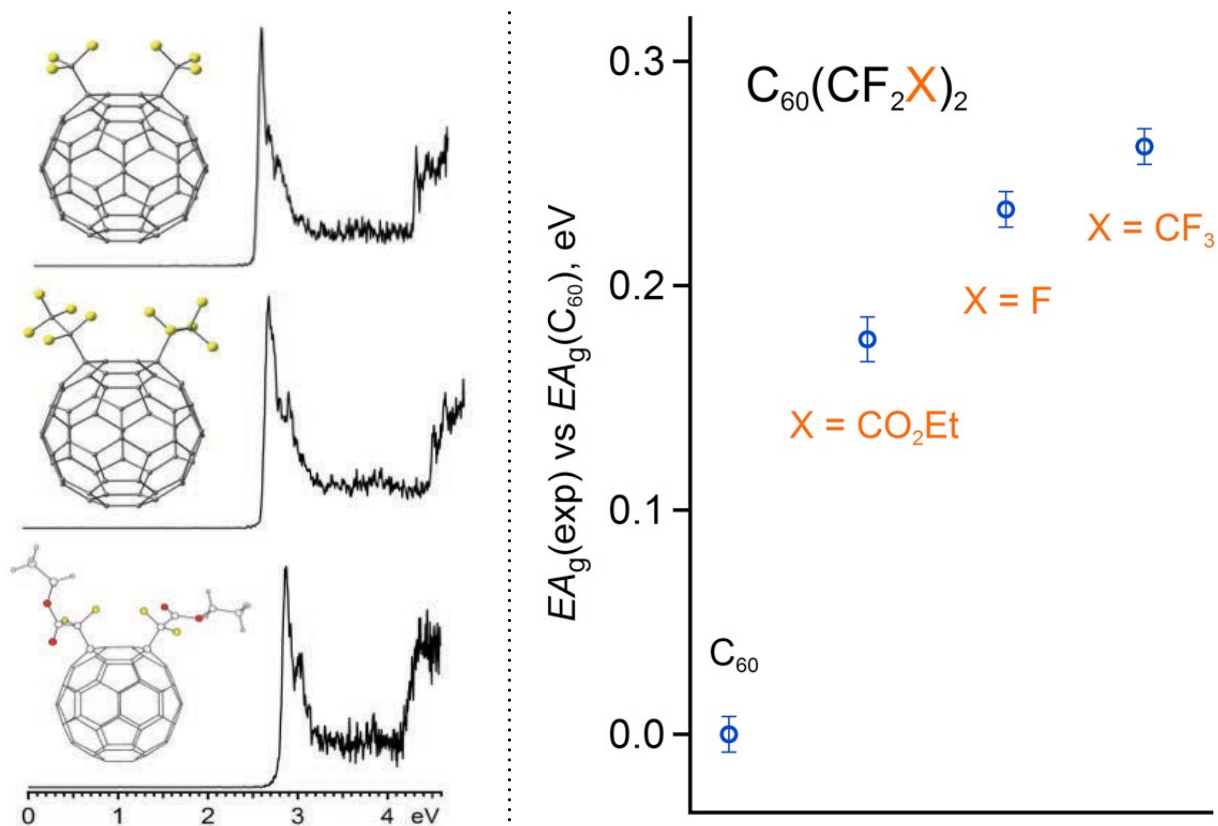


Figure 2.7. Negative ion PES spectra of 1,4-bis-PFAFs¹⁰ and C₆₀(CF₂COOEt)₂ synthesized in this work (left panel). Change in the measured gas-phase electron affinity values for the series of C₆₀(CF₂X)₂ compounds versus C₆₀ (right panel).

The mono-hydride derivative $C_{60}(CF_2CO_2Et)H$, which offers a single ω -X functional moiety, is prepared under similar conditions but requires a slightly higher reaction temperature, fewer equivalents ICF_2CO_2Et , and shorter reactions time, as shown in the HPLC trace in Figure 2.8. The compound $C_{60}(CF_2CO_2Et)H$ was first prepared in 1996 by Yoshida *et al.* by refluxing C_{60} , Bu_3SnH , and $BrCF_2CO_2Et$ in benzene under inert atmosphere for 30 hours, resulting in a yield of 37% based on consumed C_{60} . Yoshida and coworker's reaction relied on radical addition of CF_2CO_2Et to C_{60} followed by abstraction of a hydrogen atom by the $C_{60}(CF_2CO_2Et)$ radical. No mention of $C_{60}(CF_2CO_2Et)_2$ was made in that report. While $C_{60}(CF_2CO_2Et)H$ may serve useful when a single modification is desired on the PFAF synthon, caution is advised on the use of highly acidic reaction medium since the hydrogen atom on the cage is quite acidic. Following the method described here affords $C_{60}(CF_2CO_2Et)H$ in just 1.5 hours in 40% yield based on 60% conversion of starting C_{60} .

An alternative method was developed to more selectively prepare $C_{60}(CF_2CO_2Et)H$, via electrophilic addition instead of thermally-induced radical addition. When 15 equivalents of ICF_2CO_2Et is added to a solution of K_2C_{60} in THF (in an inert atmosphere), $C_{60}(CF_2CO_2Et)H$ is formed in up to 80% yield, albeit with slightly lower conversion of C_{60} , ca. 40%. This method is selective for the mono-hydride compound, as the bis-derivative $C_{60}(CF_2CO_2Et)_2$ was formed in only trace amounts even when up to 60 equivalents of ICF_2CO_2Et were added, Figure 2.9. Interestingly, the conversion of C_{60}^{2-} also does not change when more than 15 equivalents of ICF_2CO_2Et are added. This implies that the attachment of a hydrogen atom is fast and quenching of C_{60}^{2-} to neutral C_{60} also occurs rapidly, possibly due to quenching of C_{60}^{2-} to neutral C_{60} via electron transfer from free iodine in the reaction mixture generated by reacted ICF_2CO_2Et .

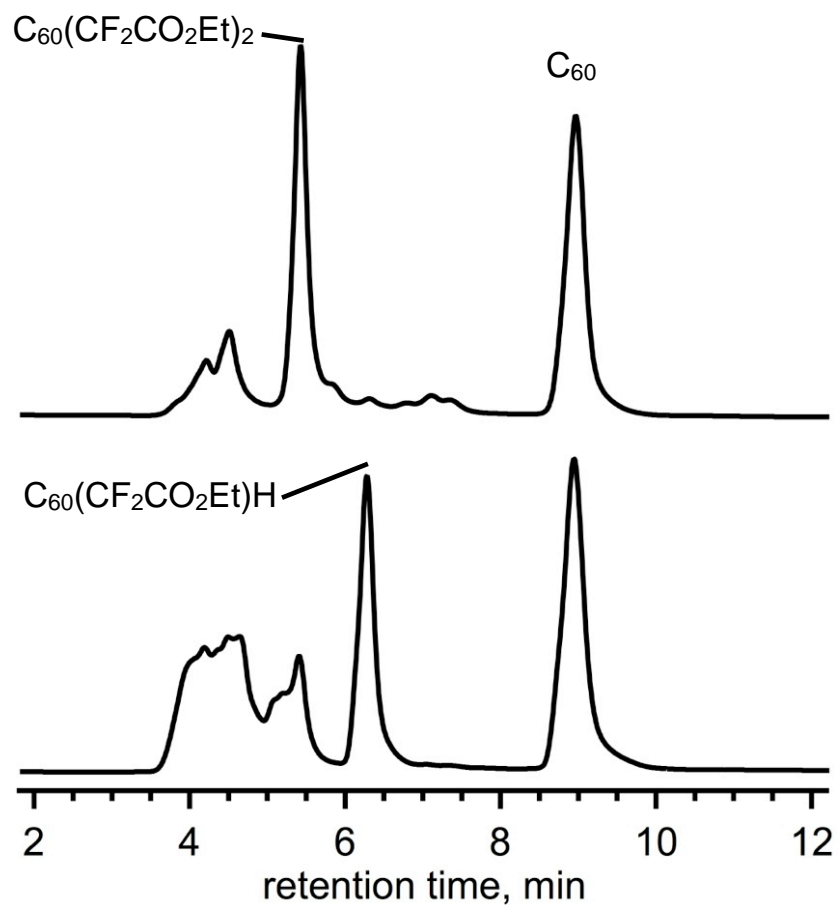


Figure 2.8. HPLC chromatograms are compared for the crude product in the syntheses of $C_{60}(CF_2CO_2Et)_2$ and $C_{60}(C_{60}CO_2Et)H$ (100% toluene eluent, 25 × 250 mm I.D. Cosmosil Buckyprep column, 16 mL/min flow rate, 300 nm detection).

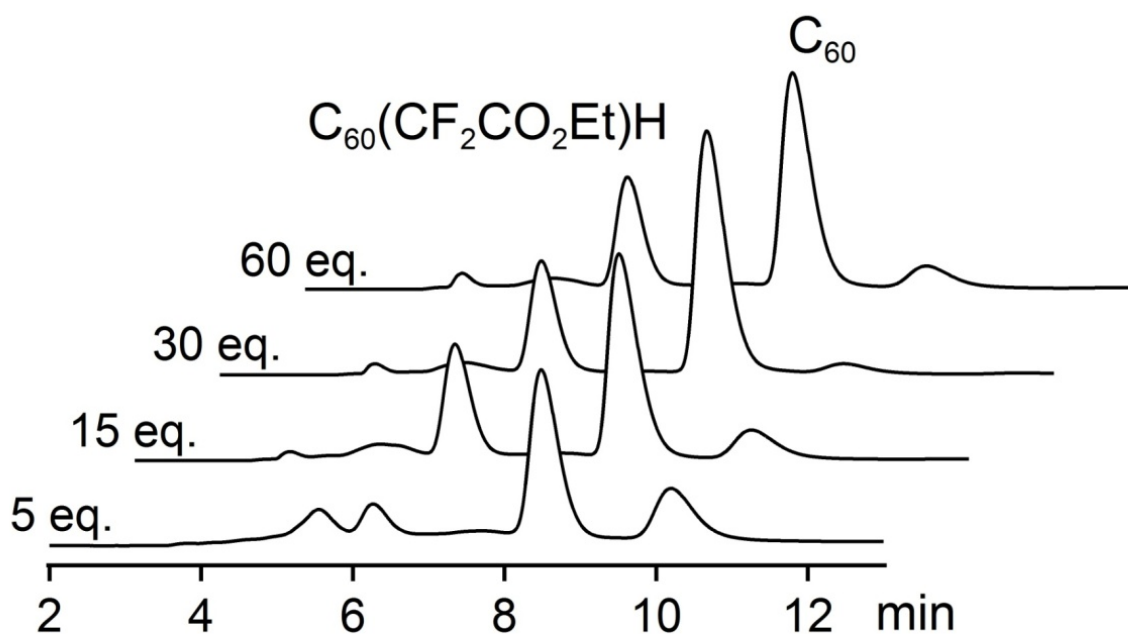


Figure 2.9. A waterfall HPLC plot of the analyses of a series of reactions between K_2C_{60} and the addition of 5–60 molar equivalents of ICF_2CO_2Et (100% toluene eluent, 25×250 mm I.D. Cosmosil Buckyprep column, 16 mL/min flow rate, 300 nm detection).

As mentioned above the $\text{CF}_2\text{CO}_2\text{Et}$ and H likely add to cage carbon atoms 1 and 9 (1,2-positions a hexagon, at a hex-hex junction), as it has a characteristic feature in the UV-vis spectrum at 432 nm, in contrast to the spectrum observed for $\text{C}_{60}(\text{CF}_2\text{CO}_2\text{Et})_2$ shown in Figure 2.10, which has a spectral feature at 448 nm consistent with additions to carbon atoms 1 and 7 (1,4-positions on a hexagon). No F—H through space coupling was observed for this compound; the hydrogen atom on the cage and the two fluorine atoms appear as singlets at δ^{H} 7.06 and δ^{F} –108.8, respectively, which is agreement with the presence of only one $\text{CF}_2\text{CO}_2\text{Et}$ addition to the cage. The singlet in the ^1H NMR spectrum at 7.06 ppm has an integration ratio to the quartet (4.71 ppm) and triplet (1.57 ppm) of 1:2:3, relative to TMS internal standard. Assignment of the structure of this compound is also supported by APCI-MS data (Figure 2.10), which shows a negative mode molecular ion at $m/z = 844.44$; the calculated molecular weight of $\text{C}_{60}(\text{CF}_2\text{CO}_2)\text{H}$ is 844.73 g/mol.

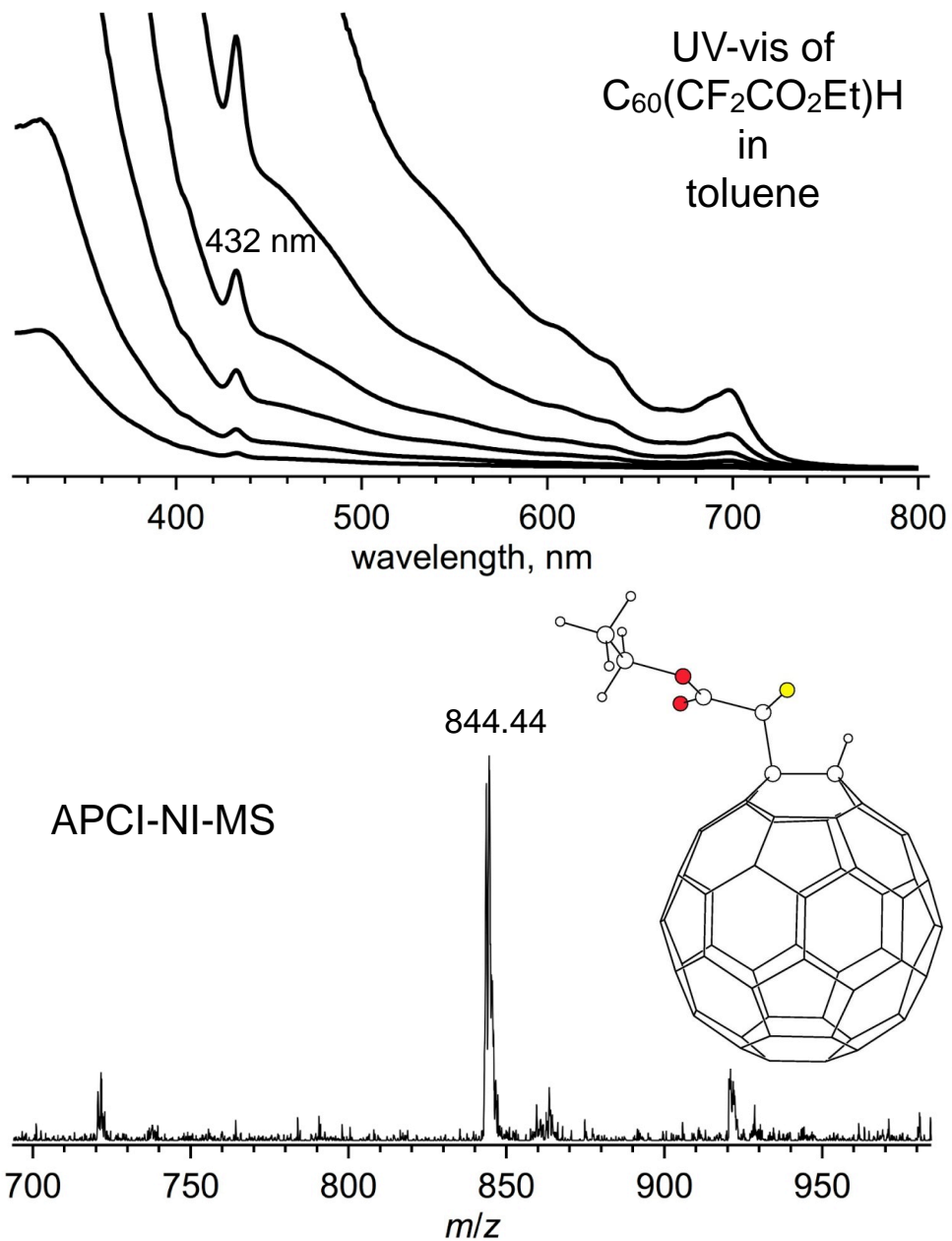


Figure 2.10. UV-vis spectra in toluene of a serial dilution of a sample of the compound assigned as $C_{60}(CF_2CO_2Et)H$, which has a sharp feature in its absorption at 432 nm, characteristic of a 1,2-bisadduct of C_{60} (top), and APCI-MS characterization of the same sample (bottom), and an inset of the DFT-optimized lowest energy structure of the assigned compound $C_{60}(CF_2CO_2Et)H$.

Multiple derivatization routes are possible for further elaboration of the CF_2X functional group, however, transesterification reactions were investigated using $\text{C}_{60}(\text{CF}_2\text{COOEt})_2$ as proof of concept. Typically, addition of a large excess of an alcohol in the presence of a strong protic acid, such as $\text{CF}_3\text{CO}_2\text{H}$, to a substrate containing a carbonyl group should lead to selective transesterification. However, when $\text{C}_{60}(\text{CF}_2\text{CO}_2\text{Et})_2$ was reacted with 20 eq. phenol in ODCB at 100°C and catalyzed by triflic acid under N_2 reflux, no phenyl difluoroacetate groups were observable by APCI-MS. Instead, benzofurano and phenoxy moieties added to the cage. No reaction was observed when a weaker acid, a larger excess of other alcohols, and/or lower reaction temperatures were implemented. Since the acid-catalyzed transesterification was unsuccessful, a base-catalyzed method published by Diederich was used. The reaction of $\text{C}_{60}(\text{CF}_2\text{COOEt})_2$ in 1:1 THF:n-butanol with K_2CO_3 at r.t. overnight gave about 70% conversion of $\text{C}_{60}(\text{CF}_2\text{COOEt})_2$, with about half being $\text{C}_{60}(\text{CF}_2\text{COOBu})_2$ and the other half mixed $\text{C}_{60}(\text{CF}_2\text{COOEt})_2$ and $\text{C}_{60}(\text{CF}_2\text{COOEt})(\text{CF}_2\text{CO}_2\text{Bu})$, estimated from APCI-MS analysis (see Figure 2.11).

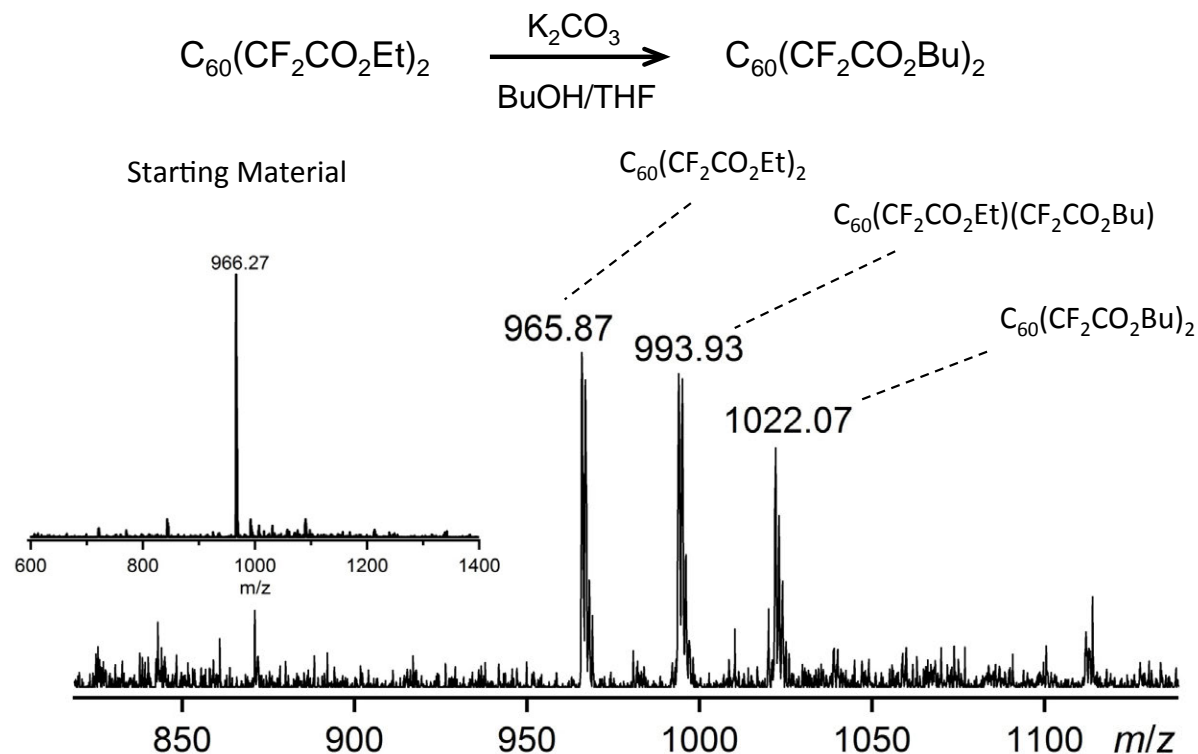


Figure 2.11. APCI-MS negative mode analyses of $\text{C}_{60}(\text{CF}_2\text{CO}_2\text{Et})_2$ starting material and the products of the base-catalyzed transesterification reaction with excess *n*-butanol.

Experimental. A 2.5 cm x 15 cm I.D. glass ampoule reactor equipped with a magnetic stir bar (Figure 2.2.1) was charged with C_{60} (60.2 mg, 0.084 mmol), ICF_2COOEt (49 μL , 0.333 mmol), 603.4 mg Cu powder, and 12.0 mL ODCB. Three cycles of freeze-pump-refill-pump-thaw, backfilling with N_2 , were performed on the ampoule, which was then heated in a 200°C oil bath for 8.5 hours, with an aliquot taken after 2 hrs and each subsequent hour for HPLC analysis. The ampoule was placed in the oil bath to a depth just above the surface of the solution within, whose color changed from clear purple to a murky brown, with the presence of wispy white CuI becoming quite noticeable. The crude product mixture was pumped dry, redissolved in toluene, filtered, and purified by HPLC (25 mm x 250 mm Cosmosil Buckyprep column, Nacalai Tesque,

Inc.; 300 nm UV detector; 16 mL min⁻¹ eluent flow rate) in one stage, with 2.4 mL injections eluted with toluene, to give four fractions. The main product fraction, eluting at 5.05 to 6.06 min, contained 25(5) mg of 90+ mol % pure C₆₀(CF₂COOEt)₂ (ca. 80% overall yield based on converted C₆₀). The monohydride compound was prepared as follows and all operations were carried out using Schlenk technique and a vacuum line: (i) a starting aliquot of ICF₂CO₂Et (Synquest Labs, Inc.) was degassed in a Schlenk flask (ii) followed by cannula transfer of a solution of C₆₀²⁻ in a volume corresponding to a 15:1 ICF₂CO₂Et:C₆₀²⁻ molar ratio (iii) and immediately the wine red C₆₀²⁻ solution turned black and then to brown after 10 minutes; (iv) any remaining dianionic C₆₀ was quenched by adding excess iodine, then the solution was pumped dry, dissolved in a small volume of HPLC grade toluene, filtered, and analyzed by HPLC or separated.

2.3. C₆₀(C₄F₈Br)₂ and C₆₀(C₄F₈I)₂.

Two additional different compounds were prepared to serve as ω-X functionalizable PFAFs, but utilizing a halide (Hal) functionality instead of an ester. The most important reaction parameter on conversion of C₆₀ to these novel bisadducts of C₄F₈Hal₂ was found to be temperature. In reactions performed under identical conditions with varying temperature (i.e. constant amounts of starting C₆₀, 1,4-C₄F₈Hal₂, Cu powder, ODCB solution, etc.), it was found that the same product distribution and conversion of C₆₀ was achieved after heating for 3 hours at 230 °C or 15 hours at 200 °C. This result was interesting because it suggested the higher temperature increases the rate of conversion of C₆₀, but does not appear to affect the rates of individual reaction pathways, since identical products were obtained at those temperatures. Additionally, it was found that increasing the amount of starting C₆₀ from 10 mg to 40 mg only

required a 2 hour increase in reaction time, and no change in the product distribution was observed. As mentioned in the previous section about perfluorocarbocycles, formation of bis-adducts of the C_4F_8 -linked ω -X compound is favored over the formation of C_4F_8 cycles, likely due to the rigidity and length of the perfluoroalkyl chain, which is shown in the HPLC trace in Figure 2.12.

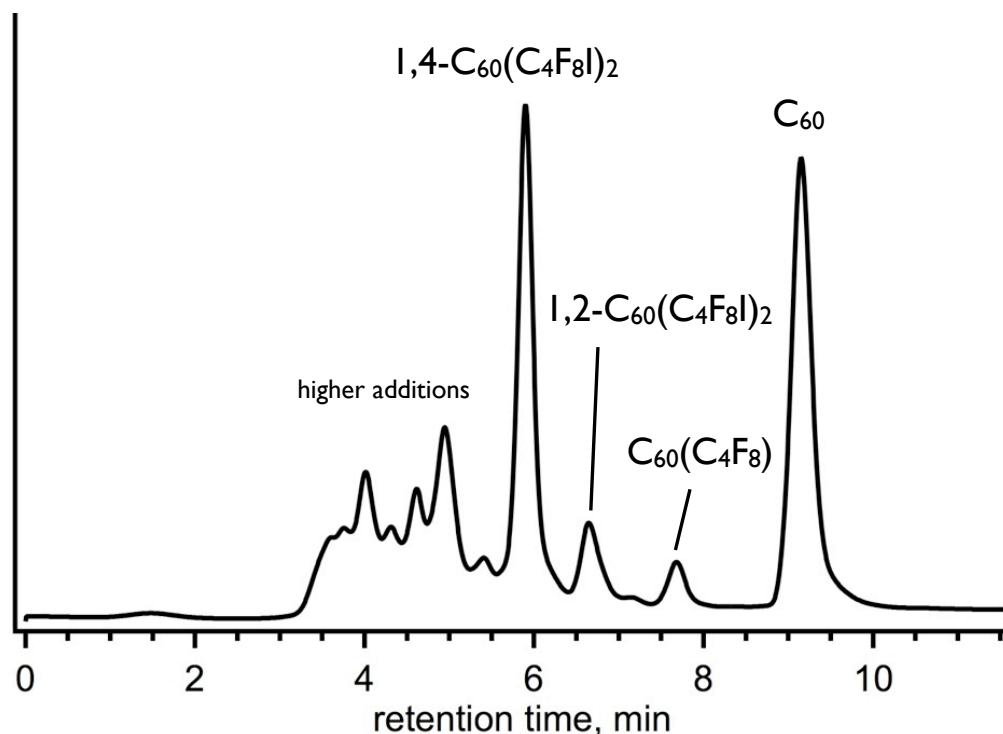


Figure 2.12. HPLC chromatogram of heterogeneous reaction of C_{60} and IC_4F_8I in the presence of Cu powder in a sealed ampoule heated at 230 °C for 3 hours (100% toluene eluent, 25 × 250 mm I.D. Cosmosil Buckyprep column with 25 × 50 mm guard column, 16 mL/min flow rate, 300 nm detection).

Assignment of the compounds to the peaks in the HPLC chromatogram in Figure 2.12 are supported by UV-vis and ^{19}F NMR spectroscopic characterization of the compounds collected from those peaks by HPLC separation. Another piece of supporting evidence for the assignments is the trend observed in HPLC retention times of perfluorocarbocycle compounds, 1,2-

bisadducts, and 1,4-bisadducts of R_F substituents in that the order listed corresponds to decreasing retention time under a set of HPLC conditions (100% toluene mobile phase, 25×250 mm Cosmosil Buckyprep column, 16 mL/min flow rate). The main product formed during the reaction (retention time 5.5 – 6.5 minutes in the HPLC chromatogram in Figure 2.12) is tentatively assigned as 1,4- $C_{60}(C_4F_8I)_2$ and is based on UV-vis spectroscopy and ^{19}F NMR spectroscopy analysis of the compound, shown in Figure 2.13.

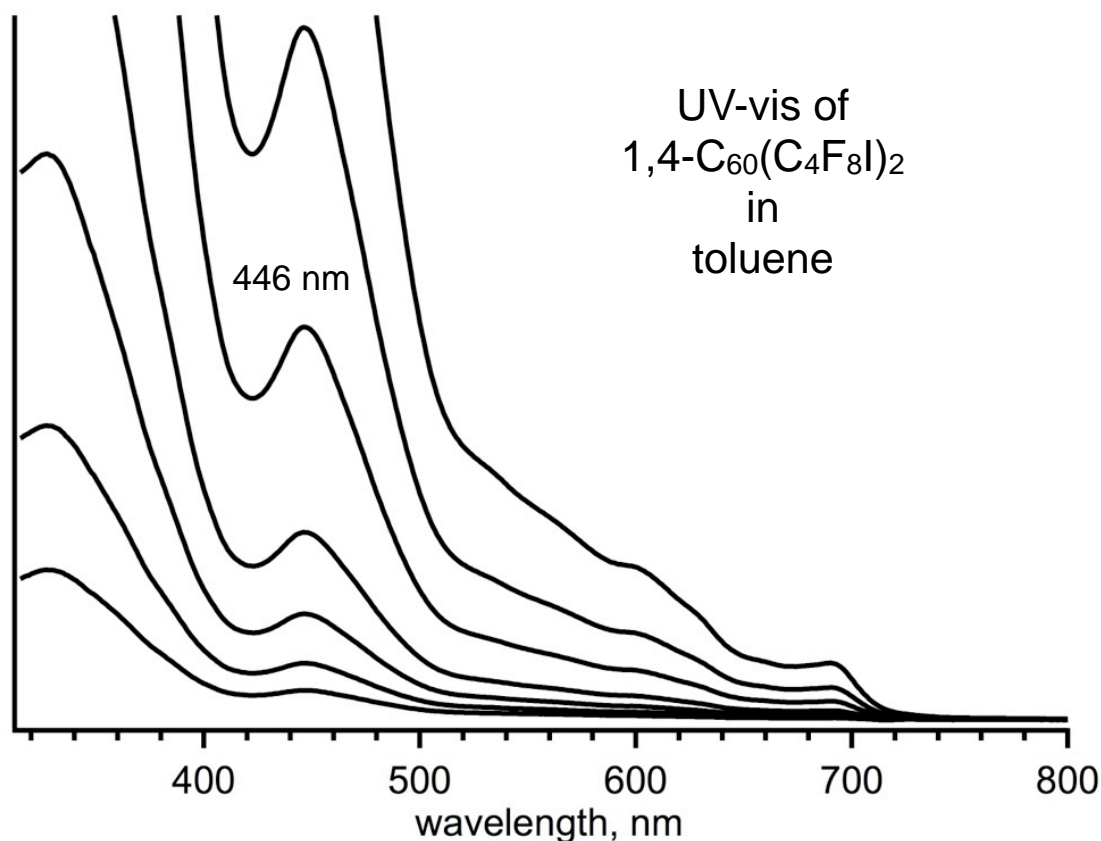


Figure 2.13. The UV-vis spectra in toluene of a serial dilution of a sample of $C_{60}(C_4F_8I)_2$, which has absorption features nearly identical to other C_{60} bis-adducts (including $C_{60}(CF_2CO_2Et)_2$ described above) where the substituents are known to be located in *para* position to one another on a cage hexagon (ref 10).

Two other dihalo- R_F reagents were reacted with C_{60} under similar conditions, BrC_4F_8Br and pseudo-dihalide $IC_4F_8SF_5$, which gave reaction mixtures similar to the one that is shown by its HPLC analysis in Figure 2.12.

Interestingly, the molecular ion for each of these three 1,4- ω -X-bisadducts could not be observed by APCI-MS, possibly due to loss of an ω -X group under the ionization conditions in the spectrometer. In each case, the m/z observed was the molecular ion less the mass of the halide. One possibility is that the compounds actually contain a C_4F_8 cycle, a C_4F_8X , and a hydrogen atom (so it would be a closed shell neutral molecule), which would account for the mass observed in the APCI-MS spectra. However, the UV-vis spectra is strong evidence that there are only two additions to the cage, in *para* position to one another on a hexagon. Another possibility is that these compounds lose one of the ω -X-functional groups under the ionization conditions in the mass spectrometer, and therefore the parent molecule is not observed. Electrochemical measurements by cyclic voltammetry revealed that these compounds also exhibit irreversible redox behavior, which may be due to a similar electrochemical transformation occurring in the mass spectrometer. Additional evidence that supports the assignment of the 1,4-addition pattern is the ^{19}F NMR spectra for each compound. Shown in Figure 2.14 are the ^{19}F NMR spectra of the three derivatives assigned as 1,4-bisadducts, as well as 1,4- $C_{60}(n-C_4F_9)_2$ (prepared by Dr. Igor Kuvycho) for comparison.

A similar AA'BB' splitting pattern is observed in each of the compounds as was for $C_{60}(CF_2CO_2Et)_2$ due to through-space coupling of the fluorine atoms attached to each carbon atom that is directly bonded to the cage. These fluorine atoms have the same resonance in each compound, regardless of the nature of the ω -X group ($X = I, Br, F, SF_5$). A trend is observed for the fluorine atoms attached the terminal carbon atom (carbon D) in the C_4F_8 chain, which is also

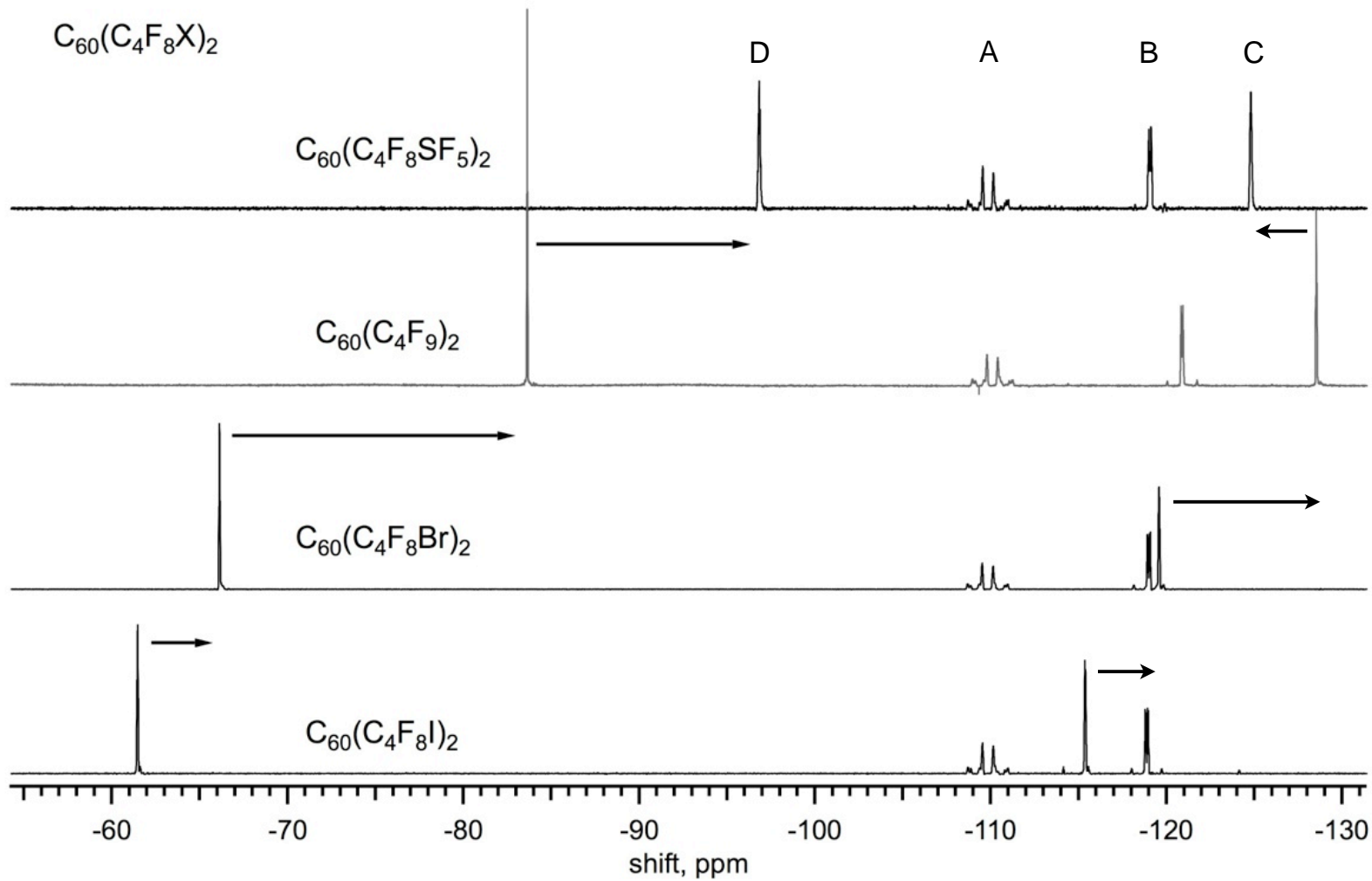


Figure 2.14. Fluorine-19 NMR spectra for a series of $\text{C}_{60}(\text{C}_4\text{F}_8\text{X})_2$ compounds (376.48 MHz, CDCl_3 , C_6F_6 internal standard (-164.9 ppm)). The letters A through D correspond to the fluorine signals due to the two F atoms on each carbon atom in the C_4F_8 chain as it extends from the C_{60} cage.

bound to the X group (refer to Figure 2.14). The trend appears to correlate with the electron withdrawing effect of each ω -X moiety, with SF₅ (a very strong electron withdrawing group) causing the terminal pair of fluorine atoms to be nearly 40 ppm upfield from those in the iodine terminated C₄F₈ chain. The ω -X group also appears to have an effect on the shift of the fluorine atoms on the second to last carbon in the chain (carbon C in the figure). In addition to being useful functionalizable PFAFs, this set of compounds reveals fundamental differences in the deshielding effects specific the nature of a particular terminus for a set of identical substrates.

Experimental. A 20 mL Schlenk tube containing a stirbar was charged with 25 mg C₆₀ (99%; MTR, Ltd.), 405 mg Cu powder (Fisher Labs), and 10 mL *o*-DCB (ACS grade; Aldrich). To the purple solution was added 10-24 equivalents (63-151 μ L) IC₄F₈I (Synquest Labs) via syringe before three cycles of freeze-pump-thaw. The solution was heated with stirring at 230°C for 2-3 hours, at which point its color turned red-brown with wispy white CuI visible. After filtration, the *o*-DCB was pumped off and the crude product mixture was redissolved fully in toluene and analyzed and separated by HPLC (equipped with a Cosmosil Buckyprep column) using 100% toluene mobile phase at 16 mL/min flow rate.

2.4. References.

- (1) Brown, K. L.; Zou, X.; Richardson, M.; Henry, W. P.: Reductive defluorination of (trifluoromethyl) cobamides. *Inorganic Chemistry* **1991**, *30*, 4834-4838.
- (2) Uneyama, K.; Mizutani, G.; Maeda, K.; Kato, T.: Electroreductive Defluorination of Trifluoromethyl Ketones and Trifluoroacetic Acid Derivatives. *J. Org. Chem.* **1999**, *64*, 6717-6723.
- (3) Takano, Y.; Herranz, M. Á.; Martín, N.; de Miguel Rojas, G.; Guldi, Dirk M.; Kareev, Ivan E.; Strauss, Steven H.; Boltalina, Olga V.; Tsuchiya, T.; Akasaka, T.: Electron Donor-Acceptor Interactions in Regioselectively Synthesized exTTF-C₇₀(CF₃)₁₀ Dyads. *Chem. Eur. J.* **2010**, *16*, 5343-5353.
- (4) Takano, Y.; Herranz, M. A.; Kareev, I. E.; Strauss, S. H.; Boltalina, O. V.; Akasaka, T.; Martín, N.: Efficient Regioselective 4+2 Cycloaddition of o-Quinodimethane to C₁-C₇₀(CF₃)₁₀. *J. Org. Chem.* **2009**, *74*, 6902-6905.
- (5) Nardes, A. M., Ferguson, A.J., Whitaker, J. B., Larson, B. W., Larsen, A. E., Maturová, K., Graf, P. A., Boltalina, O. V., Strauss S. H., Kopidakis N.: Beyond PCBM: Understanding the Photovoltaic Performance of Blends of Indene-C60 Multiadducts with Poly(3-hexylthiophene). *Adv. Funct. Mater.* **2012**.
- (6) Shustova, N. B.; Kareev, I. E.; Kuvychko, I. V.; Whitaker, J. B.; Lebedkin, S. F.; Popov, A. A.; Chen, Y. S.; Seppelt, K.; H., S. S.; Boltalina, O. V.: High-temperature and photochemical syntheses of fullerene derivatives with linear perfluoroalkyl chains. *J. Fluorine Chem.* **2010**, *131*, 1198-1212.
- (7) Shustova, N. B.; Peryshkov, D. V.; Kuvychko, I. V.; Whitaker, J. B.; Larson, B. W.; Dunsch, L.; Chen, Y. S.; Seppelt, K.; Popov, A. A.; H., S. S.; Boltalina, O. V.: Chemical tailoring of fullerene acceptors: synthesis, structures and electrochemical properties of perfluoroisopropylfullerenes. *Chem. Commun.* **2010**, *47*, 875-877.
- (8) Popov, A. A.; Kareev, I. E.; Shustova, N. B.; Stukalin, E. B.; Lebedkin, S. F.; Seppelt, K.; Strauss, S. H.; Boltalina, O. V.; Dunsch, L.: Electrochemical, Spectroscopic, and DFT Study of C₆₀(CF₃)_n Frontier Orbitals (*n* = 2-18): The Link between Double Bonds in Pentagons and Reduction Potentials. *J. Am. Chem. Soc.* **2007**, *129*, 11551-11568.
- (9) Shustova, N. B.; Peryshkov, D. V.; Kuvychko, I. V.; Chen, Y. S.; Mackey, M. A.; Coumbe, C.; Heaps, D. T.; Confait, B. S.; Heine, T.; Phillips, J. P.; Stevenson, S.; Dunsch, L.; Popov, A. A.; Strauss Steven, H.; Boltalina, O. V.: Poly(perfluoroalkylation) of Metallic Nitride Fullerenes Reveals Addition-Pattern Guidelines: Synthesis and Characterization of a Family of Sc₃N@C₈₀(CF₃)_n (*n* = 2-16) and Their Radical Anions. *J. Am. Chem. Soc.* **2010**, *133*, 2672-2690.
- (10) Kuvychko, I. V.; Whitaker, J. B.; Larson, B. W.; Folsom, T. C.; Shustova, N. B.; Avdoshenko, S. M.; Chen, Y. S.; Wen, H.; Wang, X. B.; Dunsch, L.; Popov, A. A.; Boltalina, O. V.; Strauss, S. H.: Substituent effects in a series of 1,7-C-60(R-F)(2) compounds (R-F = CF₃, C₂F₅, n-C₃F₇, i-C₃F₇, n-C₄F₉, s-C₄F₉, n-C₈F₁₇): electron affinities, reduction potentials and E(LUMO) values are not always correlated. *Chem. Sci.* **2012**, *3*, 1399-1407.

Chapter 3: Synthesis, Purification, and Characterization of Trifluoromethyl[60]fullerenes

3.1. Isomers of $C_{60}(CF_3)_{10}$.

3.1.1. Background. The first fullerene derivative with multiple CF_3 groups to be structurally characterized by X-ray crystallography was 1,3,7,10,14,17,23,28,31,40- $C_{60}(CF_3)_{10}$.¹ Figure 3.1 shows this structure along with two Schlegel diagrams, one of which shows cage C–C bond distances in pm. The pmp^3mpmp addition-pattern abbreviation denotes a ribbon of edge-sharing *meta* (*m*) and/or *para* (*p*) $C_6(CF_3)_2$ hexagons (note that each shared edge is a $C(sp^3)–C(sp^2)$ bond). This seminal paper and others that followed² showed conclusively that $C_{60}(CF_3)_n$ compounds, in general (there are only two exceptions), have "ribbon" addition patterns with *p-m-p* and/or *p-p-p* (i.e., p^3) segments (as described above) along with, in some cases, one or two isolated *p*- $C_6(CF_3)_2$ hexagons. For example, the only isomer known for the composition $C_{60}(CF_3)_2$ is *p*- $C_{60}(CF_3)_2$ (i.e., 1,7- $C_{60}(CF_3)_2$), and the three known isomers of $C_{60}(CF_3)_4$ are p^3 -, *pmp*-, and *p,p*- $C_{60}(CF_3)_4$.² These observations are in sharp contrast to the earlier prediction of Taylor that the CF_3 groups in $C_{60}(CF_3)_n$ derivatives occupy a string of contiguous cage C atoms.^{3,4}

The six previously known isomers of $C_{60}(CF_3)_{10}$ plus the 21 new isomers isolated and studied in this work are listed in Table 3.1.⁵⁻¹¹ Schlegel diagrams for the six previously known isomers, which are abbreviated 60-10-1 through 60-10-6, are shown in Figure 3.2. The first part of the abbreviation refers to the fullerene, C_{60} . The second part refers to the number of CF_3 groups. The third part is an arbitrary isomer number or letter. Isomer numbers are given for those compounds with experimentally-verified addition patterns (verified by X-ray crystallography except for 60-10-1). The numbered abbreviations refer to both (i) a particular compound of C_{60} with 10 CF_3 groups and (ii) the addition pattern of that compound in general, regardless of substituent. For example, 60-10-7, which is not included in this table, would denote the as-yet-unknown isomer of $C_{60}(CF_3)_{10}$ with the same addition pattern as a structurally-characterized isomer of

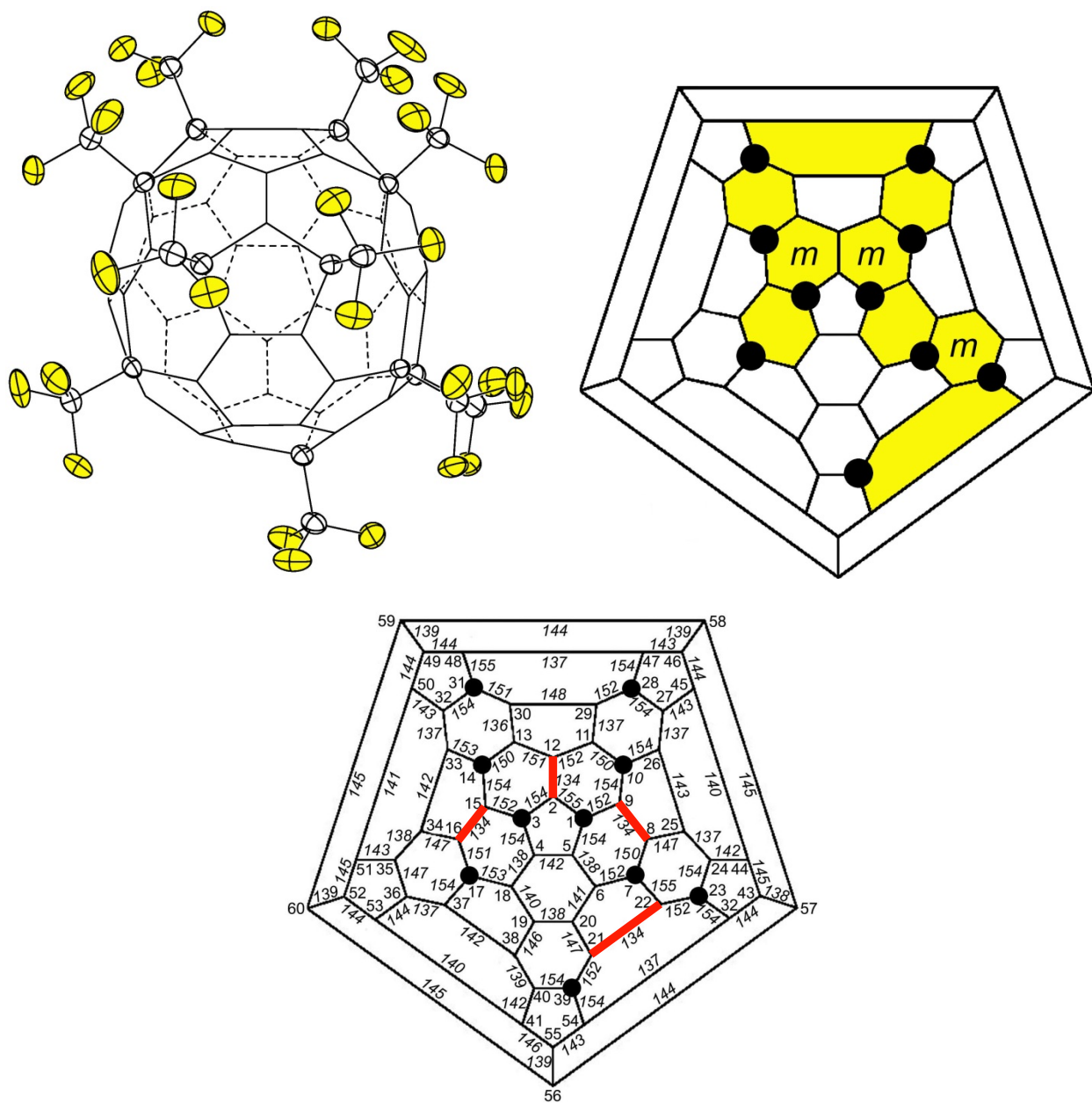


Figure 3.1. Structure and Schlegel diagrams of 1,3,7,10,14,17,23,28,31,40- $C_{60}(CF_3)_{10}$ (60-10-3). The black circles in the Schlegel diagrams indicate the cage C atoms to which the CF_3 groups are attached. The lower Schlegel diagram shows IUPAC locants, cage C–C bond distances in pm, and the four shortest C–C bonds highlighted in red. The standard errors (σ) for the C–C bond distances in this structure are 0.3 pm, so $\pm 3\sigma$ is ca. ± 1 pm. The pmp^3mpmp ribbon is highlighted in yellow in the upper Schlegel diagram, and the *meta*- $C_6(CF_3)_2$ hexagons are indicated with the letter *m*.

Table 3.1. Previously Known and New C₆₀(CF₃)₁₀ Compounds^a

abbreviation ^b	addition-pattern or number of quartets ^c	IUPAC lowest locants ^d	synthesis and isolation ref	X-ray ref	¹⁹ F NMR ref	DFT predictions ^e	
						rel. energy, kJ mol ⁻¹	<i>E</i> (LUMO), eV
60-10-1	<i>C</i> ₁ - <i>p</i> ³ <i>mpmp</i> , <i>p</i>	1,6,11,16,18,24,27,36,41,57 ^f	1	—	1	9.22	-5.129
60-10-2	<i>C</i> ₁ - <i>p</i> ³ <i>mpmpmp</i>	1,6,11,16,18,24,27,36,54,60	1	8	1	0.06	-4.894
60-10-3	<i>C</i> ₁ - <i>pmp</i> ³ <i>mpmp</i>	1,3,7,10,14,17,23,28,31,40	1	1	1	4.56	-4.754
60-10-4	<i>C</i> ₂ -(<i>p</i> ³ <i>m</i> ² -loop) ²	1,6,12,15,18,23,25,41,45,57	6	7	6	7.60	-4.529
60-10-5	<i>C</i> ₁ - <i>pmpmpmpmpmp</i>	1,6,11,16,18,26,36,41,44,57	6	6	6	1.25	-4.638
60-10-6	<i>C</i> ₁ - <i>p</i> ³ <i>mp</i> , <i>pmp</i>	1,6,11,18,24,27,33,51,54,60	6	11	6	0.00	-4.922
60-10-8	<i>C</i> ₁ - <i>p</i> ³ <i>mp</i> , <i>pmp</i>	1,6,11,16,18,28,31,36,44,58	t.w.	t.w.	t.w.	16.03	-4.983
60-10-9	<i>C</i> ₁ - <i>pmpmpmp</i> , <i>p</i>	1,6,11,18,24,27,34,50,52,55	t.w.	t.w.	t.w.	17.36	-4.829
60-10-10	<i>C</i> ₁ - <i>p</i> ³ <i>mpmp</i> , <i>p</i>	1,6,11,16,18,24,27,36,50,60	t.w.	t.w.	t.w.	20.55	-4.924
60-10-11	<i>C</i> ₁ - <i>p</i> ³ <i>mp</i> , <i>p</i> , <i>p</i>	1,6,11,14,18,24,27,31,53,56	t.w.	t.w.	t.w.	29.60	-5.090
60-10-12	<i>C</i> ₁ - <i>pmp</i> ³ <i>mp</i> , <i>p</i>	1,3,7,10,14,17,28,31,43,55	t.w.	t.w.	t.w.	15.41	-4.867
60-10-13	<i>C</i> ₁ - <i>pmpmpmp</i> , <i>p</i>	1,6,11,16,18,26,36,44,47,59	t.w.	t.w.	t.w.	18.46	-4.938
60-10-B	4		t.w.	—	t.w.		
60-10-C	4 plus 1 singlet		t.w.	—	t.w.		
60-10-D	4		t.w.	—	t.w.		
60-10-E	≥ 3		t.w.	—	t.w.		
60-10-G	4		t.w.	—	t.w.		
60-10-H	≥ 3		t.w.	—	t.w.		
60-10-I	≥ 4		t.w.	—	t.w.		
60-10-J	6		t.w.	—	t.w.		
60-10-K	4 ("8 + 2")		t.w.	—	t.w.		
60-10-M	2		t.w.	—	t.w.		
60-10-N	2		t.w.	—	t.w.		
60-10-O	2		t.w.	—	t.w.		
60-10-P	3		t.w.	—	t.w.		
60-10-Q	6		t.w.	—	t.w.		
60-10-S	4		t.w.	—	t.w.		

^a The previously known isomers of $C_{60}(CF_3)_{10}$ are 60-10-1 through 60-10-6. t.w. = this work. ^b The first part of the abbreviation refers to the fullerene, C_{60} . The second part refers to the number of CF_3 groups. The third part is an arbitrary isomer number or letter. Isomer numbers are given for those compounds with experimentally-verified addition patterns (verified by X-ray crystallography except for 60-10-1). Note that the numbered abbreviations refer to (i) a particular compound of C_{60} with 10 CF_3 groups and (ii) the addition pattern of that compound in general. For example, 60-10-7, which is not included in this table, would denote the as-yet-unknown isomer of $C_{60}(CF_3)_{10}$ with the same addition pattern as a structurally-characterized isomer of $C_{60}(C_2F_5)_{10}$, which has been assigned the abbreviation 60-10-7- C_2F_5 . ^c The addition pattern abbreviations refer to a ribbon of edge-sharing *meta*- (*m*) and/or *para* (*p*) $C_6(CF_3)_2$ hexagons (each shared edge is a $C(sp^3)-C(sp^2)$ bond). For the lettered abbreviations with unknown addition patterns, only the number of quartets in the ^{19}F NMR spectrum, indicating CF_3 groups at the end of a ribbon (i.e., terminal CF_3 groups), are given. In one case, for 60-10-C, the presence of a singlet in the ^{19}F NMR spectrum, indicating an isolated CF_3 group (an extremely rare occurrence for any fullerene(CF_3)_n derivative^{2,11}), is also included. ^d According to the Schlegel diagram numbering shown in Figure 3.1 (see ref. ^{9,10} for IUPAC-approved nomenclature rules for C_{60} and C_{70} compounds). ^e The DFT results were obtained by the Strauss-Boltalina Group DFT collaborator Dr. Alexey A. Popov. The methodology he used for these calculations is described in many Popov, Boltalina, Strauss, et al. publications, including refs.² and ⁵. ^f This is the most probable addition pattern based on its ^{19}F NMR spectrum, its DFT relative energy, and its DFT $E(LUMO)$ value (see ref ⁶). ^g The "8 + 2" designation denotes the tentative conclusion that the addition pattern for 60-10-K is most likely a ribbon of eight edge-sharing *m*- and/or *p*- $C_6(CF_3)_2$ hexagons plus an isolated *p*- $C_6(CF_3)_2$ hexagon.

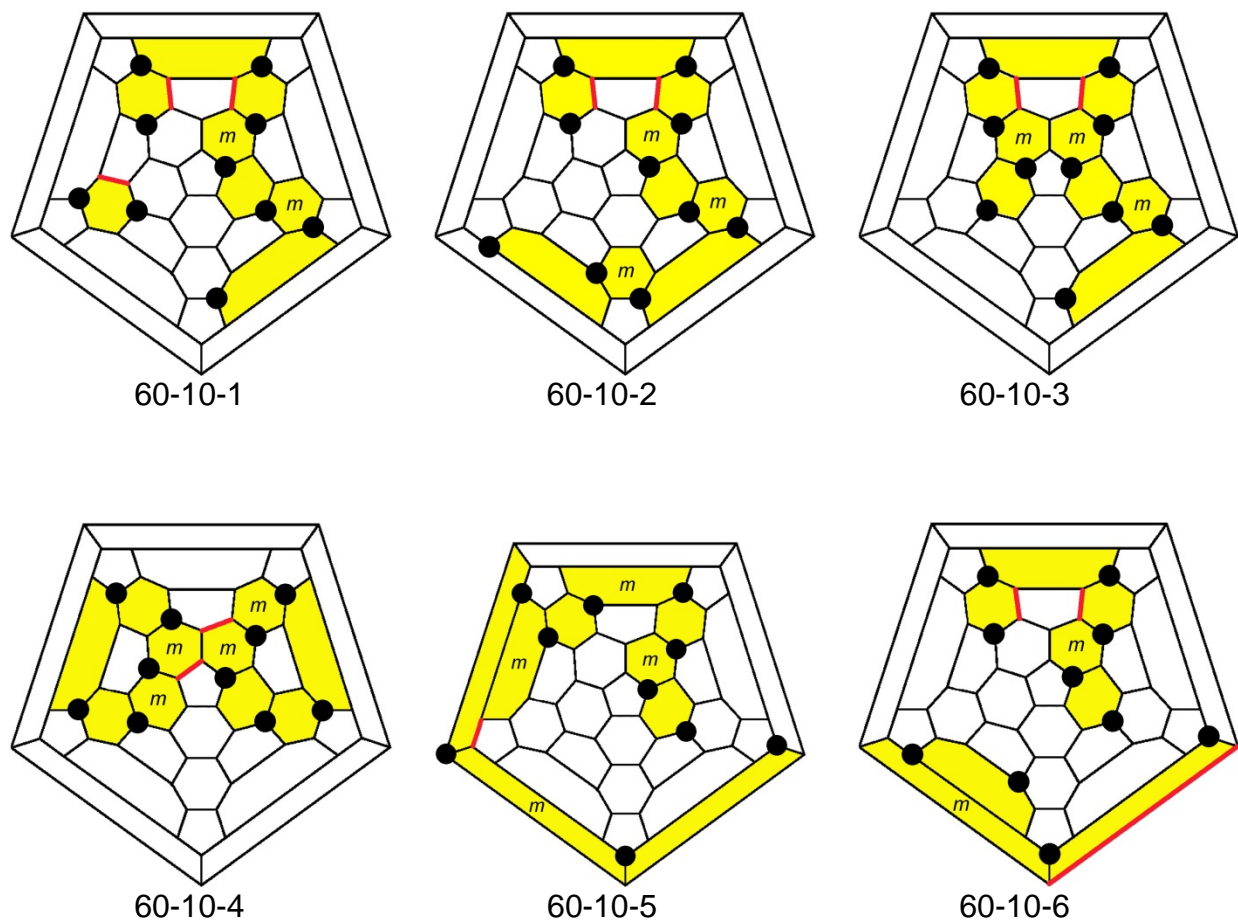


Figure 3.2. Schlegel diagrams for the previously known isomers of $C_{60}(CF_3)_{10}$. The black circles indicate the cage C atoms to which the CF_3 groups are attached. The ribbons or loops of edge-sharing *meta*- or *para*- $C_6(CF_3)_2$ hexagons and isolated *p*- $C_6(CF_3)_2$ hexagons are highlighted in yellow, and the *meta*- $C_6(CF_3)_2$ hexagons are indicated with the letter *m*. The bonds highlighted in red are non-terminal double bonds in pentagons (see text).

$C_{60}(C_2F_5)_{10}$, which has been assigned the abbreviation 60-10-7- C_2F_5 .² As another example, the unknown compound 1,3,7,10,14,17,23,-28,31,40- $C_{10}H_{10}$ would be abbreviated 60-10-3-H. Note that (i) 60-10-1 has an addition pattern consisting of a p^3mpmp ribbon and an isolated $p-C_6(CF_3)_2$ hexagon, (ii) 60-10-3 has an mp^3m segment that surrounds a fulvene-like portion of the fullerene cage that is isolated from the rest of the fullerene π system, (iii) 60-10-6 has an addition pattern consisting of a p^3mp ribbon and a separate pmp ribbon, and (iv) 60-10-4 has an unusual addition pattern consisting of two p^3m^2 loops.

The six previously known isomers of $C_{60}(CF_3)_{10}$ have played an important role in fullerene chemistry for several reasons. First, they comprise the first example of a fullerene(X)_{*n*} composition of *any* fullerene with *any* substituent X with more than four well-characterized isomers for a given value of *n*. Second, their addition patterns were precisely known, in five cases by X-ray crystallography. (This is not a trivial reason; there are literally hundreds of millions of possible isomers for the composition $C_{60}X_{10}$.¹²) Third, their electrochemical properties were studied by cyclic voltammetry in the same laboratory under the same conditions (i.e., identical solvent, electrolyte, electrodes, cell design, and potential-sweep rate), and all six had reversible (i.e., quasi-reversible) first reductions (and some had second and even third reversible reductions).⁶ Fourth, and most importantly, their first reduction potentials (i.e., $E_{1/2}(0/-)$ values) varied over an unexpectedly large range of 0.50 V. The previous largest range of $E_{1/2}(0/-)$ values for *structurally-characterized* isomeric fullerene derivatives was 0.15 V for three isomers of $C_{70}Bn_2$.¹³ Two other examples are three isomers of $C_{60}F_{36}$ ($\Delta E_{1/2}(0/-) = 0.080$ V¹⁴ and two structurally-characterized isomers of $C_{60}(CH_2Ph)_4$ ($\Delta E_{1/2}(0/-) = 0.050$ V.¹⁵ The unprecedented large range of $E_{1/2}(0/-)$ values for $C_{60}(CF_3)_{10}$ isomers (hereinafter known as 60-10 isomers or simply as 60-10's) and a detailed analysis of their addition patterns, their DFT-predicted $E(LUMO)$ values, and the "shapes" of their DFT-predicted LUMOs led to an understanding of what factors most affect $E_{1/2}(0/-)$ values for fullerene derivatives. The unprecedented and surprising conclusion was that the addition pattern, specifically the number and proximity of non-terminal double bonds in pentagons (see below), had a much greater

influence on the reduction potential of a given compound than the number of electron-withdrawing CF_3 substituents.

The distinction between cage C–C single and double bonds in underivatized fullerenes, and the difficulty in distinguishing cage C–C single and double bonds in fullerene derivatives, must be discussed before the conclusion stated in the last sentence of the preceding paragraph can be fully appreciated. Figure 3.3, reproduced from ref 1, shows plots of cage C–C distances in C_{60} (from Balch and Olmstead's precise structure of $\text{C}_{60}\cdot\text{Pt}(\text{OEP})\cdot 2\text{C}_6\text{H}_6$ ¹⁶) and 60-10-3. The terms "single" and "double" bonds are, of course, artificial but useful constructs since all cage C–C bonds in underivatized fullerenes have some double-bond character. All fullerenes have exactly 12 pentagons,¹⁷ and in C_{60} that gives rise to 60 single bonds (pentagon-hexagon edges, also known as 5,6 bonds) and 30 double bonds (hexagon-hexagon edges, also known as 6,6 bonds). However, in 60-10-3 three of the four shortest cage C–C bonds, which are clearly "double" bonds, are 5,6 bonds. Two other short 5,6 bonds, C11–C29 and C13–C30, are "double bonds in pentagons" (DBIPs) that have two $\text{C}(\text{sp}^2)$ nearest neighbors, and they have become known as non-terminal DBIPs, or *nt*-DBIPs.⁶

Figure 3.4 shows that $\text{C}_{60}(\text{CF}_3)_n$ isomers span a wide range of reduction potentials not only for $n = 10$ but for each even value of n from $n = 6$ to $n = 12$. It is possible to pick an isomer for each n such that $E_{1,2}(0/-)$ increases as n increases (this was the expectation of most fullerene scientists before the publication of ref⁶), but it is also possible to pick isomers such that $E_{1/2}(0/-)$ decreases as n increases. (Furthermore, it is possible to pick isomers for $n = 2$ to $n = 12$ that result in a saw-tooth plot as n increases.) One of the main discoveries reported in ref⁶ is that the LUMOs of C_{60}X_n derivatives have large contributions from the $\text{p}-\pi$ orbitals on or near the *nt*-DBIP cage C atoms, and that, all other things being equal, $E(\text{LUMO})$ values decrease (and $E_{1/2}(0/-)$ values increase) as the LUMO becomes more and more delocalized over the fullerene π system. Thus, C_{60}X_n derivatives with multiple *nt*-DBIPs, and especially with *nt*-DBIPs in close proximity, have the most extensively delocalized LUMOs and are the best electron acceptors.

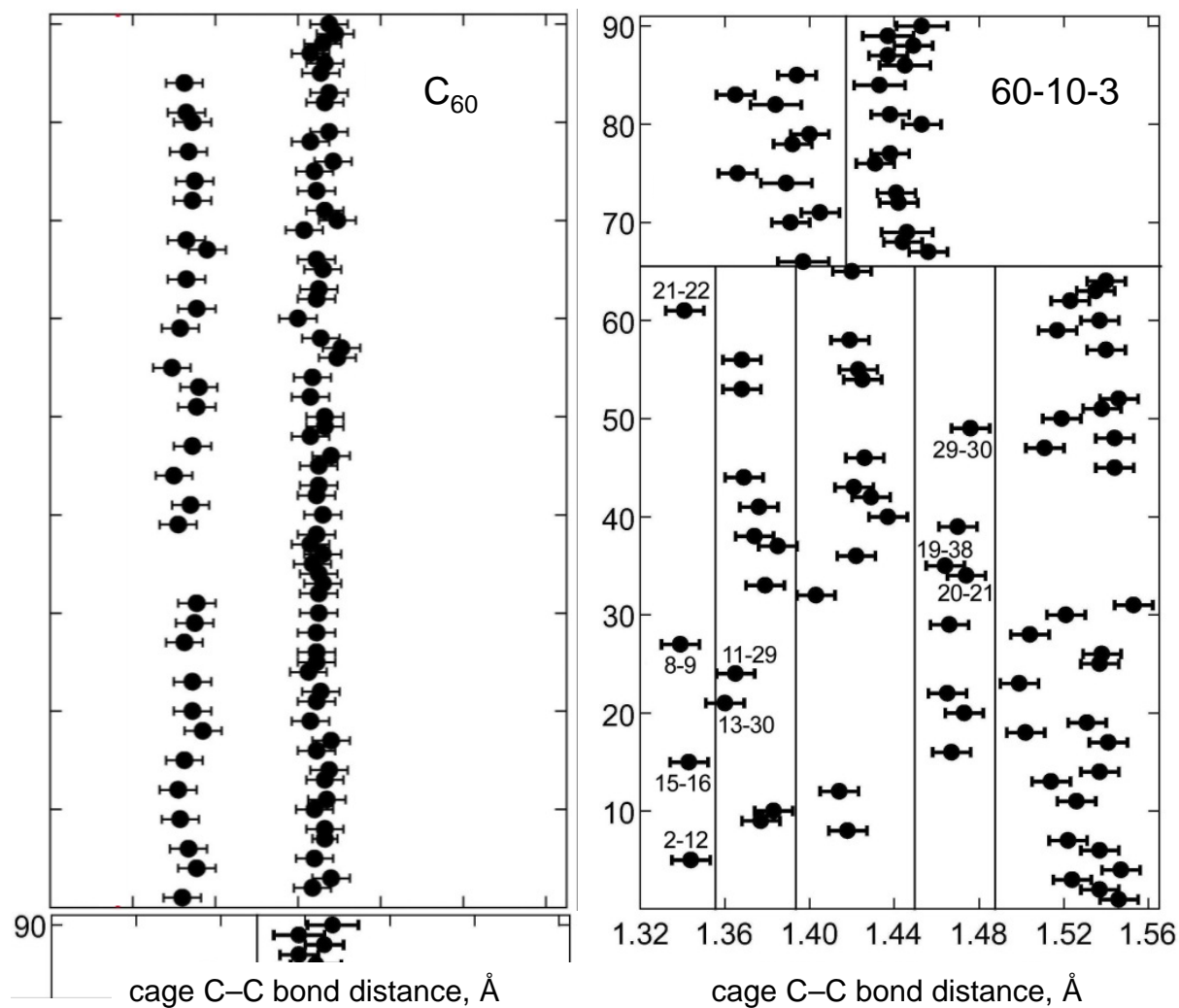


Figure 3.3. The cage C–C bond distances in the C_{60} molecule in $C_{60}\cdot Pt(OEP)\cdot 2C_6H_6$ (ref ¹⁶) and in 1,3,7,10,14,17,23,28,31,40- $C_{60}(CF_3)_{10}$ (60-10-3; ref ¹). The non-terminal double bonds in pentagons in 60-10-3 are C11–C29 and C13–C30, which are part of the isolated fulvene fragment in this compound. The error bars shown in both graphs represent $\pm 3\sigma$.

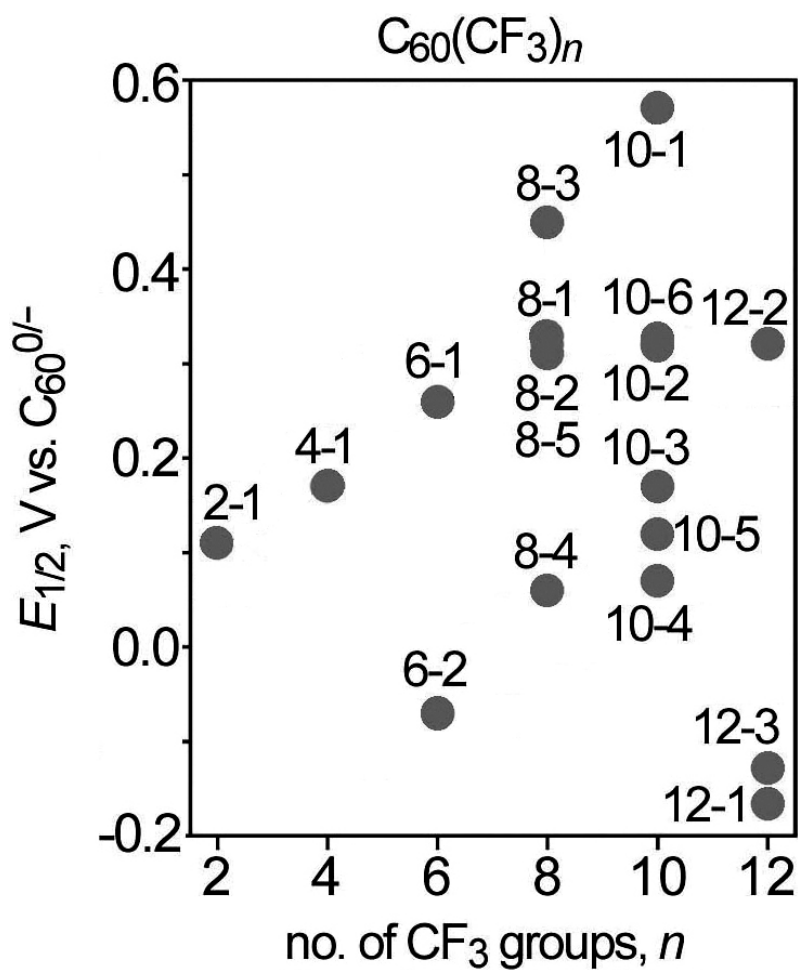


Figure 3.4. Experimental first reduction potentials of 18 $C_{60}(CF_3)_n$ compounds with $n = 2$ (one isomer), 4 (one isomer), 6 (two isomers), 8 (five isomers), 10 (six isomers), and 12 (three isomers). This plot was redrawn using data published in ref ⁶.

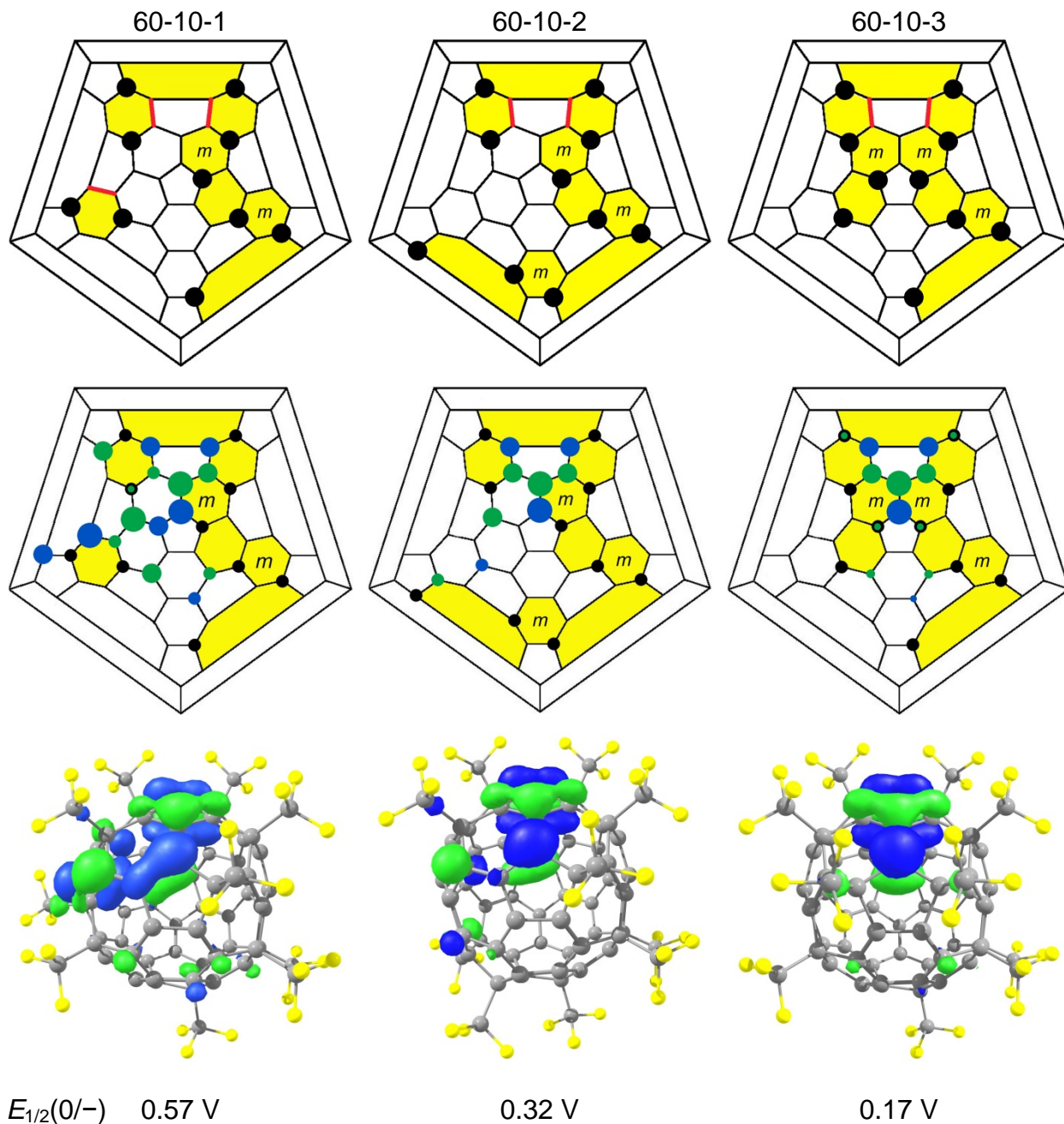


Figure 3.5. Schlegel and LUMO diagrams showing the *nt*-DBIPs (highlighted in red) and the DFT-predicted cage C atom contributions to the LUMOs of 60-10-1, 60-10-2, and 60-10-3. The black circles in the Schlegel diagrams indicate cage C atoms to which the CF₃ groups are attached. The blue (+) and green (-) circles represent the upper lobes of the π atomic orbitals for each cage C atom scaled approximately to its contribution to the LUMO. The $E_{1/2}(0/-)$ values shown are vs. C₆₀^{0/-} (0.1 M N(*n*-Bu)₄BF₄ in CH₂Cl₂; data from ref ⁶).

Figure 3.5 shows Schlegel diagrams with *nt*-DBIPs highlighted in red for 60-10-1, 60-10-2, and 60-10-3 and two representations of their respective DFT-predicted LUMOs. The three LUMOs differ significantly in their degree of delocalization, and the $E_{1/2}(0/-)$ values decrease from 60-10-1 to 60-10-2 to 60-10-3 as the degree of delocalization decreases (i.e., the compounds become harder to reduce as the LUMO becomes more localized, a sensible result if a "particle-in-a-box" analogy is invoked).⁶ The compounds 60-10-2 and 60-10-3 have the same two *nt*-DBIPs. In 60-10-3, however, the LUMO is essentially confined to the isolated fulvene fragment. In 60-10-2, the fulvene fragment is in conjugation with the rest of the fullerene π system. The result is that the LUMO in 60-10-2 is more delocalized than the LUMO in 60-10-3, and 60-10-2 is 0.15 V easier to reduce than 60-10-3. In 60-10-1, the isolated *p*-C₆(CF₃)₂ hexagon gives rise to a third *nt*-DBIP, and the proximity of this double bond to the two *nt*-DBIPs in the fulvene fragment results in a much more extensively delocalized LUMO than in 60-10-2. The net result is that 60-10-1 is 0.25 V easier to reduce than 60-10-2, and 0.40 V easier to reduce than 60-10-3. As the reader will see, the addition patterns of the new 60-10 isomers, their $E_{1/2}(0/-)$ values (measured by the author), and the DFT results of Dr. Alexey A. Popov are entirely consistent with the conclusions published in ref ⁶ regarding LUMOs and *nt*-DBIPs (i.e., regarding LUMOs and addition patterns).

3.1.2 General Comments on New Isomers of C₆₀(CF₃)₁₀. The publication of ref ⁶ alerted the fullerene community that *very minor* changes in C₆₀X_n addition patterns can have profound effects on electronic properties such as reduction potentials. For example, the addition patterns of 60-10-1 and 60-10-3 only differ by shifting a single CF₃ group to a new position only three cage C atoms away, and this difference leads to the aforementioned change in $E_{1/2}(0/-)$ by 0.40 V. In the course of the author's work preparing and isolating larger amounts of the known 60-10 isomers in order to prepare and study 60-10-containing OPV active layers (see Chapter 3), it became apparent that many previously unknown 60-10 isomers were present in small amounts in the high-temperature C₆₀ + CF₃I product mixtures. The working hypothesis for this portion of the

author's work was that the isolation and characterization of new 60-10 isomers would provide not only confirmation of the conclusions discussed above but also additional valuable insights into the links between the addition patterns of $C_{60}X_n$ derivatives and their physicochemical properties. For this reason, a considerable effort was devoted to isolating and characterizing 21 new 60-10 isomers, six of them by single-crystal X-ray diffraction. They are listed in Table 3.1.

3.1.3. Synthesis and Isolation of New $C_{60}(CF_3)_{10}$ Compounds. The gradient-temperature gas-solid (GTGS) reactor, which is shown in Figure 3.6, was used to synthesize more kinetic products. A full description of the reactor and the study of the effects of reaction parameters on preparation of trifluoromethylfullerenes, co-developed along with other members of the Strauss Group, can be found elsewhere. A schematic of the reactor is shown in Figure 3.6. In brief, solid C_{60} , heated to approximately 490 °C, reacts with CF_3 radicals generated by thermal homolytic cleavage of CF_3I molecules in the gas phase under reduced pressure. Since sublimation temperatures of TMFs are lower than for C_{60} , as more CF_3 radicals add to the cage, the products begin to sublime away from the hot zone to a water-cooled thimble, positioned a certain distance from the hot pile of C_{60} , where they condense and no longer react with CF_3 radicals. Therefore, the length of the hot zone, which is where CF_3 addition to C_{60} occurs, can be controlled by the distance of the cold finger to the C_{60} material. Two processes are known to occur in the hot zone of the reactor: attachment of more CF_3 radicals to the subliming $C_{60}(CF_3)_n$ compounds, and rearrangement of the CF_3 groups that are already on the cage to more thermodynamically stable positions. To target more kinetic products, the two most important parameters are the length of the hot zone and the pressure of CF_3I gas in the reactor. When the pressure of CF_3I gas is increased in the

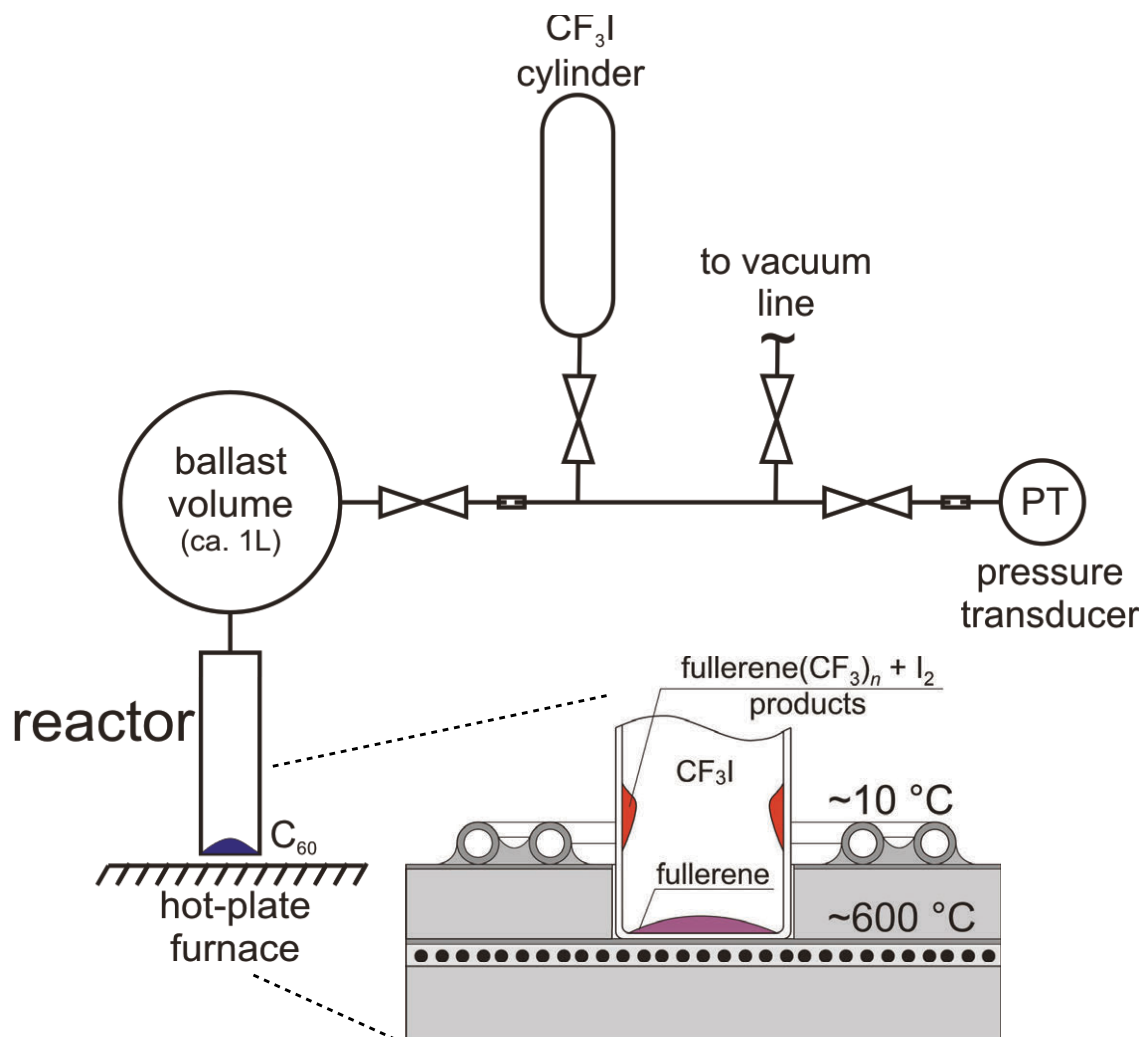


Figure 3.6. Schematic diagram of the gradient-temperature gas-solid reactor and gas-handling system.

reaction, the conversion of C_{60} to higher TMFs, those containing more than 8 CF_3 groups, is observed. When the hot zone is shorter, the residence time of TMFs in the hot zone is decreased, thus allowing less time for CF_3 groups to rearrange and form thermodynamic products. Figure 3.7 shows a comparison of the HPLC chromatograms for the crude product mixture obtained using the previous literature flow-tube method and the current GTGS method. Figure 3.8 shows an expansion of the HPLC traces relevant to $C_{60}(CF_3)_{10}$ compounds. Clearly the flow tube method (with its longer hot-zone) targets more thermodynamic products. Therefore, the reaction parameters chosen for this study to target higher TMFs were a shorter hot zone and more CF_3 radicals present (i.e. – a higher pressure of CF_3I gas was used). Indeed, the difference in the mass of the starting C_{60} and the product mixture corresponded to ca. 9.3 CF_3 groups per molecule. Trifluoromethylation was carried out in four separate reactions using a total of 3.39 g starting C_{60} material, which gave 6.42 g of product. Only approximately 70 mg of unreacted C_{60} was recovered, meaning essentially all of the 6.42 grams of product was due to a mixture of trifluoromethylfullerenes. The purpose of the first stage of HPLC separation was to fractionate the products into four fractions, according to their composition of TMFs by $C_{60}(CF_3)_n$: F1 ($n = 12,10,8$), F2 ($n = 8,6$), F3 ($n = 6,4$), and F4 ($n = 4,2,0$), as shown in Figure 3.9. The fraction F1, containing primarily $C_{60}(CF_3)_{10}$ compounds, weighed ca. 2.41 grams.

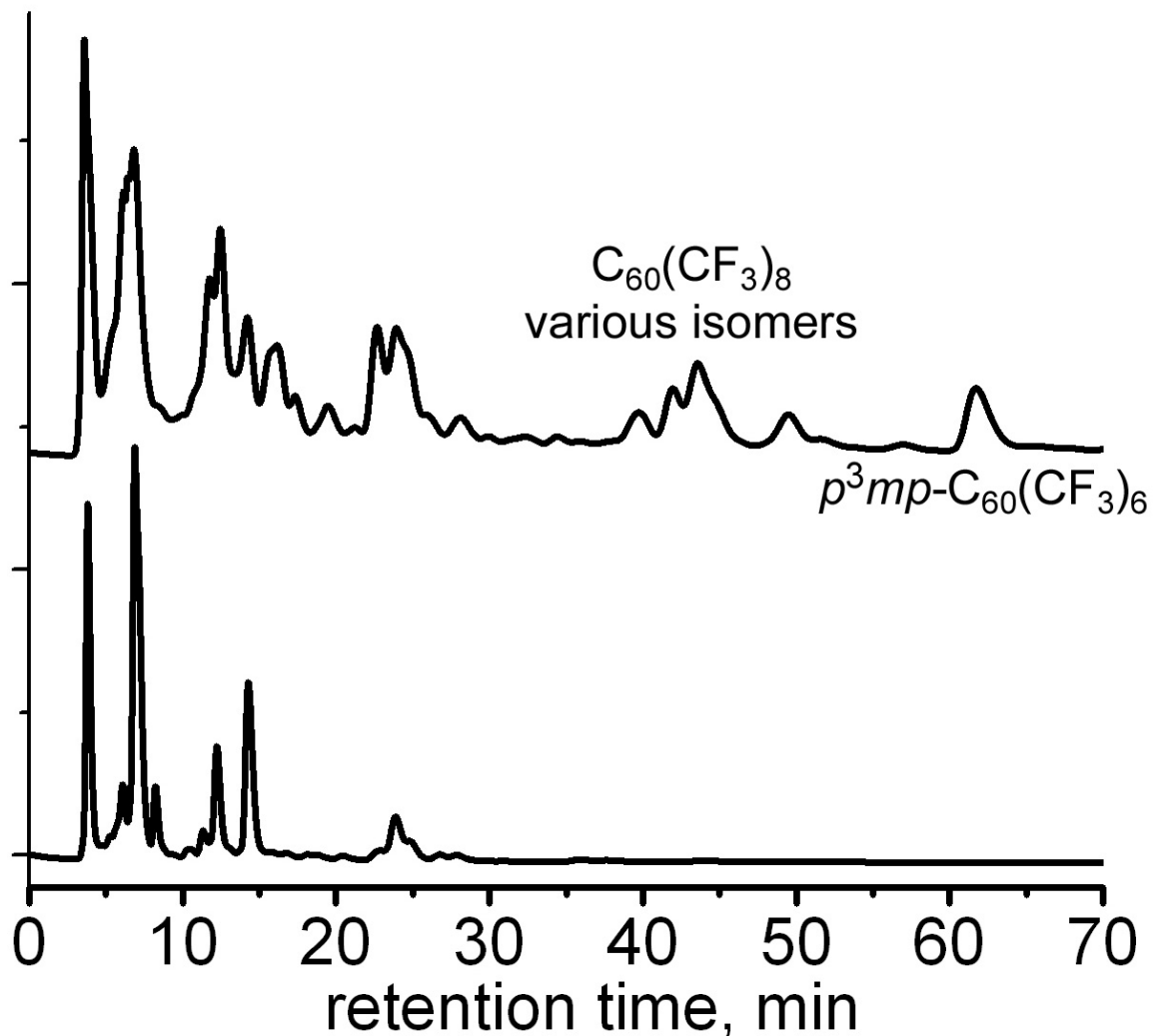


Figure 3.7. Full-scale HPLC traces of two TMF mixtures prepared by trifluoromethylation of C_{60} sample with 640 torr of CF_3I in the GTGS reactor (top trace, $T_{hot\ plate} = 550\ ^\circ C$) and in the flow-tube reactor (bottom trace, $T = 480\ ^\circ C$); 20/80 v/v toluene/heptanes eluent at 5 mL/min flow rate was used for the analysis.

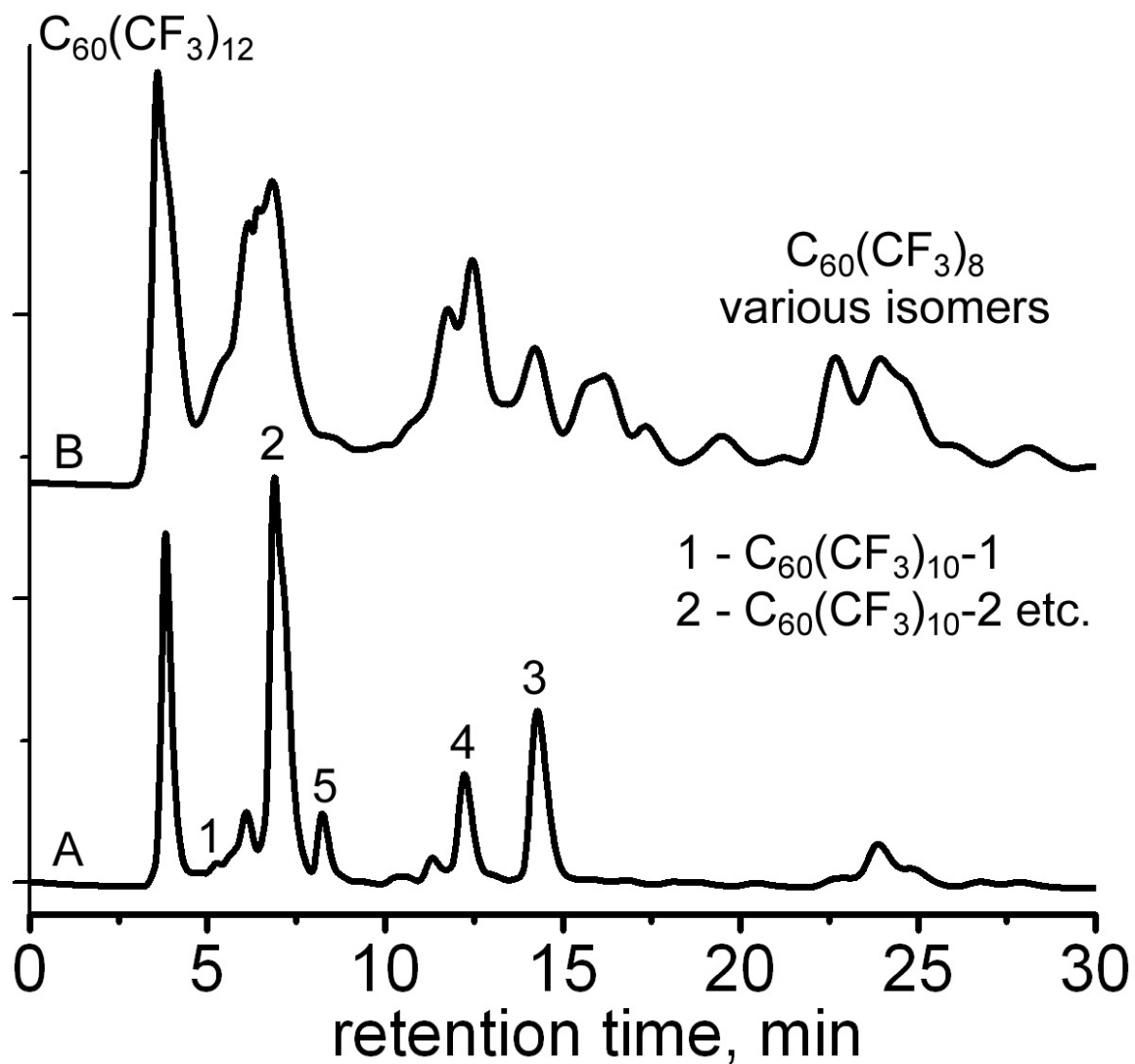


Figure 3.8. Expansions of HPLC traces of two TMF mixtures prepared by trifluoromethylation of C_{60} sample with 640 torr of CF_3I in the GTGS reactor (top trace, $T_{hot\ plate} = 550\ ^\circ C$) and in the flow-tube reactor (bottom trace, $T = 480\ ^\circ C$); 20/80 v/v toluene/heptanes eluent at 5 mL/min flow rate was used for the analysis.

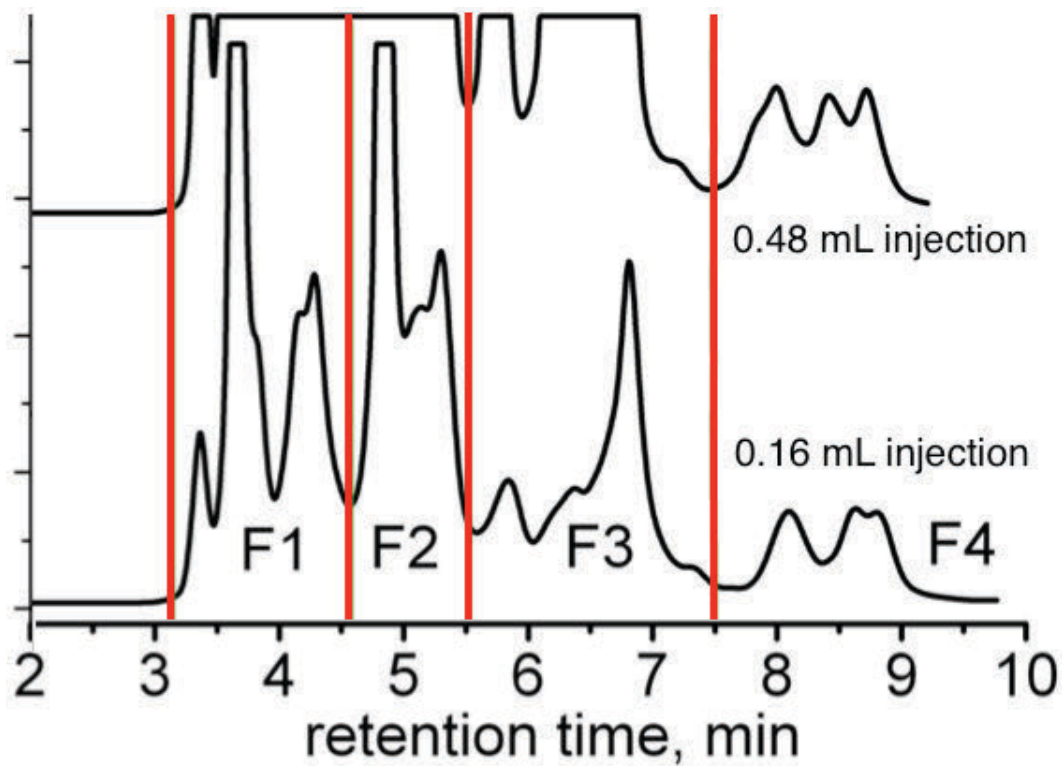


Figure 3.9. HPLC chromatograms are shown for the first-stage separation of the crude product mixture from the combined large-scale GTGS reactions targeting higher- and more isomerically diverse-TMFs. The top chromatogram corresponds to the injection volume used during the separation (all traces: 300 nm detection, 100% toluene mobile phase, and preparative 25 × 250 mm Cosmosil Buckyprep HPLC column).

Fraction F1, which weighed 2.41 g, was the source of all of the $C_{60}(CF_3)_{10}$ compounds discussed in this chapter, and was subjected to extensive multi-stage HPLC separation and other product fractionation techniques. Shown in Figure 3.9 is the HPLC chromatogram of fraction F1 using a 20/80 volume/volume mixture of toluene/hexane. Comparison of this chromatogram to the 0.16 mL injection chromatogram in Figure 3.10 shows the improvement in separation of peaks eluting when a weaker mobile phase is implemented. Fraction F1 was therefore further separated into nine fractions using the 20/80 toluene/hexanes eluent mixture. Even though the appearance of six of the nine fractions suggests relatively pure fractions based on the fact that they elute as sharp peaks with not much shouldering, this was not the case. Figure 3.11 shows the ^{19}F NMR spectra recorded in deuterated chloroform of each of the nine fractions (F1F1 through F1F9). Analysis of these spectra clearly shows that a large number of isomers were produced using the shorter hot zone and higher CF_3I pressure conditions in the GTGS reactor. It also reveals that HPLC conditions had to be further improved to isolate single compounds.

To evaluate the extent to which using a weaker mobile phase could improve separation, the fractions were analyzed using 100% hexane eluent. Figure 3.10 shows the HPLC chromatograms of fractions F1F1 through F1F5; fractions F1F6 – F1F9 showed extremely broad and long-retained peaks, and therefore are not included in the figure. Fraction F1F1 contained primarily TMFs with more than 10 CF_3 groups. These compounds have highly diminished cage pi systems and thus have much lower affinity for the stationary phase of the column, which is why they have such short retention times. HPLC separation of these compounds remains a challenge. Fraction F1F5, as well as F1F6 – F1F9, also could not be effectively separated by additional stages of HPLC under these

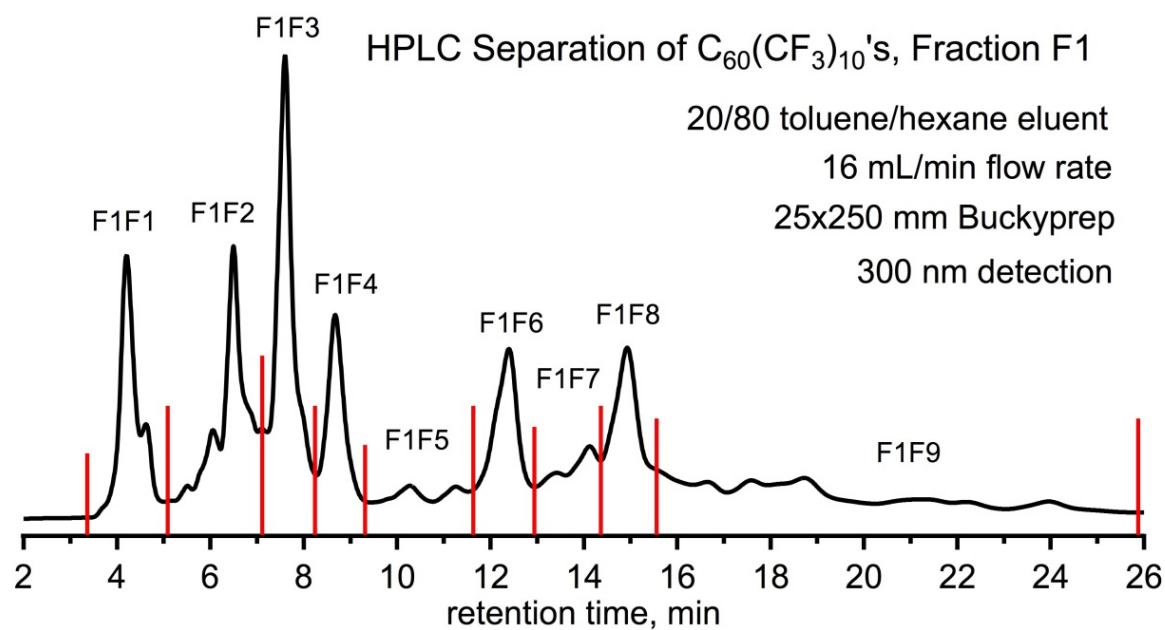


Figure 3.9. The second-stage HPLC separation scheme is shown for fraction F1.

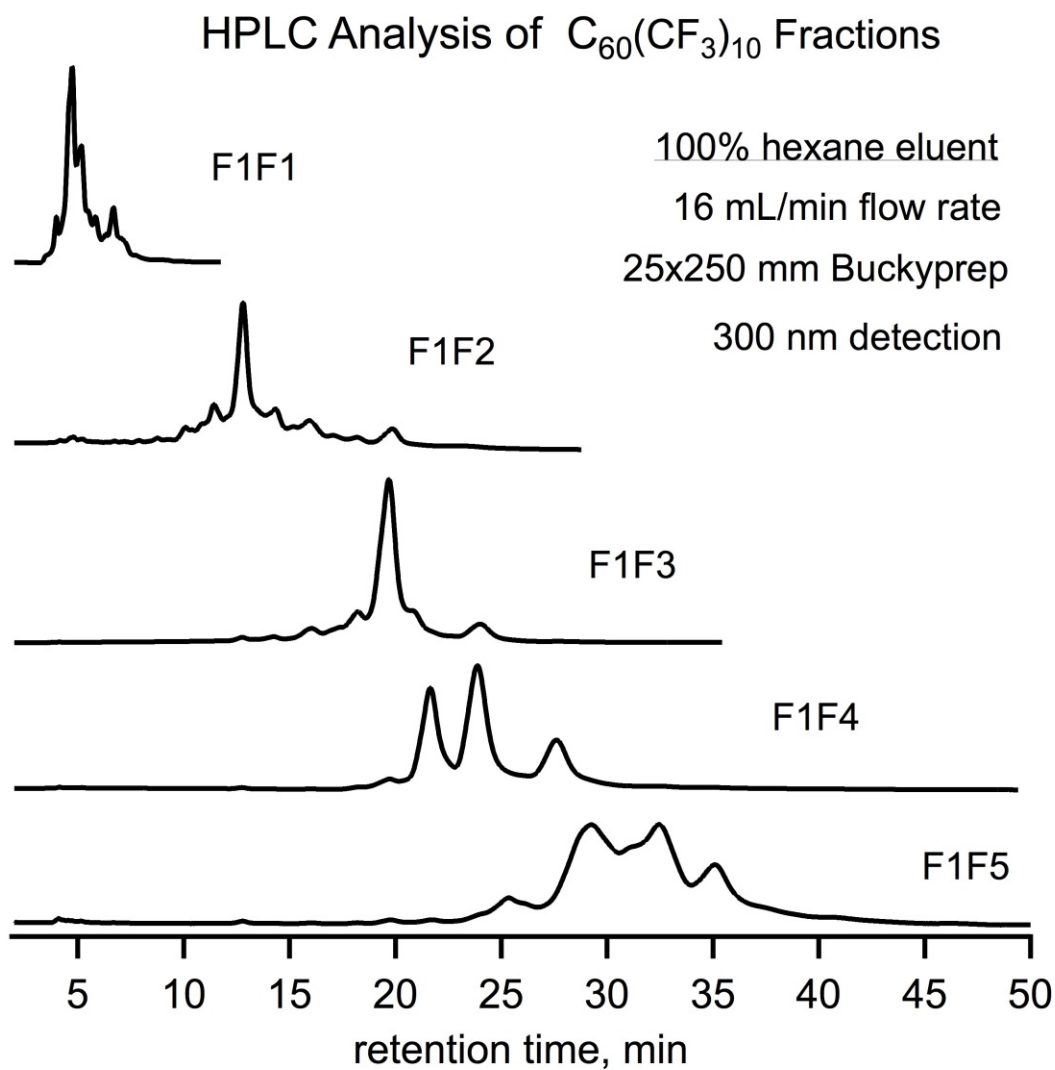


Figure 3.10. HPLC chromatograms are shown for analysis of fractions F1F1 through F1F5 using 100% hexane eluent.

conditions, and therefore an alternative method was developed, which will be discussed in the next section.

In the cases of F1F2, F1F3, and F1F4, use of 100% hexane provided resolution of peaks amenable to further fractionation by a third stage of HPLC separation. However, the total time required between injections under these conditions were prohibitively long considering the large quantity of material in each fraction. Therefore, eluent mixtures of hexanes containing 1-10% by volume of toluene were evaluated. It was found that a 5/95 volume mixture of toluene/hexanes significantly shortened retention times while still maintaining an adequate separation of peaks in fractions F1F2 and F1F3, and a 20/80 mixture was found to be suitable for F1F4. Each of these fractions were then subjected to a third stage of HPLC separation accordingly. However, to demonstrate the method and subsequent additional stages of HPLC separation required to isolate pure $C_{60}(CF_3)_{10}$ isomers, the specific case of $C_{60}(CF_3)_{10-9}$ from F1F2 is discussed. This particular isomer is useful for the discussion because it represents one of the most extreme cases of exhaustive HPLC separation using a Cosmosil Buckyprep column, and also illustrates how difficult and time consuming it can be to isolate pure compounds from complex mixtures of isomers of $C_{60}(CF_3)_{10}$. The third stage of HPLC separation of F1F2 was performed using 5/95 toluene/hexanes eluent. As mentioned, the addition of just 5% by volume of toluene to the eluent significantly shortened the time required between injections compared to 100% hexanes eluent (11 minutes vs. 23 minutes, respectively). Three fractions were collected during this stage of HPLC separation, the third of which, fraction F1F2F3, contained 60-10-9.

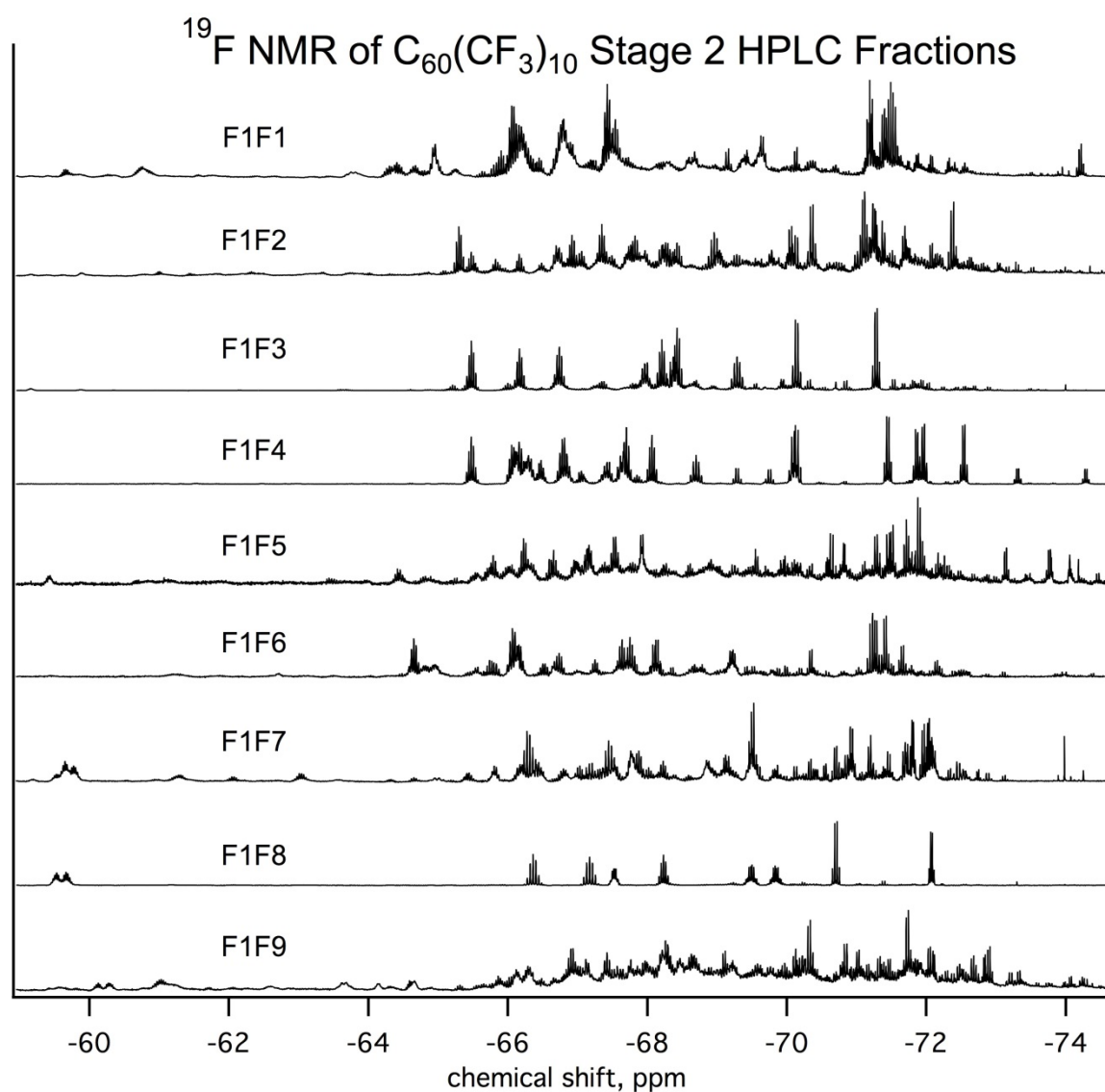


Figure 3.11. The ¹⁹F NMR spectra (CDCl₃, C₆F₆ internal standard, 376.07 MHz) are shown for the fractions from the second-stage HPLC separation of the GTGS product fraction containing C₆₀(CF₃)₁₀ compounds, F1.

This fraction was then subjected to a fourth stage of HPLC separation, using 100% hexanes as eluent, which produced seven fractions. The smallest of these seven fractions contained 60-10-9, but only in about 60% purity according to ^{19}F NMR. Furthermore, under these conditions, the fraction eluted essentially as a single peak. This required application of an even weaker HPLC eluent for fullerenes, 100% *n*-heptane, in a fifth stage of separation that produced some shouldering, which allowed 60-10-9 to be isolated in sufficient purity that upon drying by slow solvent evaporation, crystals suitable for structure elucidation by single-crystal x-ray diffractometry formed. This HPLC separation process, along with the ^{19}F NMR spectrum of the isolated 60-10-9 fraction that was used to grow single crystals, is shown in a stepwise scheme in Figure 3.12. Similar schemes as the one shown in Figure 3.12 were applied to fractions F1F3 and F1F4, resulting in isolation of several more previously unknown isomers of $\text{C}_{60}(\text{CF}_3)_{10}$, the properties and structures of which are described in detail in the next sections of this Chapter.

Although the method described above resulted successfully in isolation of new isomers of $\text{C}_{60}(\text{CF}_3)_{10}$, clearly many improvements could be made to the overall process. Namely, the process to isolate 60-10-9 was massively time consuming. Another major problem is that in many stages of the separation, compounds co-eluted or had overlapping retention times, meaning that when fractions were collected, a significant portion of the target compound becomes an impurity in the fraction that it partially overlaps into. As a result, and an example of the severity of this problem, the mass of the 60-10-9 fraction, F1F2F3F5F1, was less than 2 mg. This problem is inherent to the Cosmosil Buckyprep column stationary phase material; using even one of the weakest HPLC eluents did not produce baseline separation of 60-10-9 from its impurity (which appeared as a single peak but contained a mixture of compounds by ^{19}F NMR).

60-10-9 Roadmap

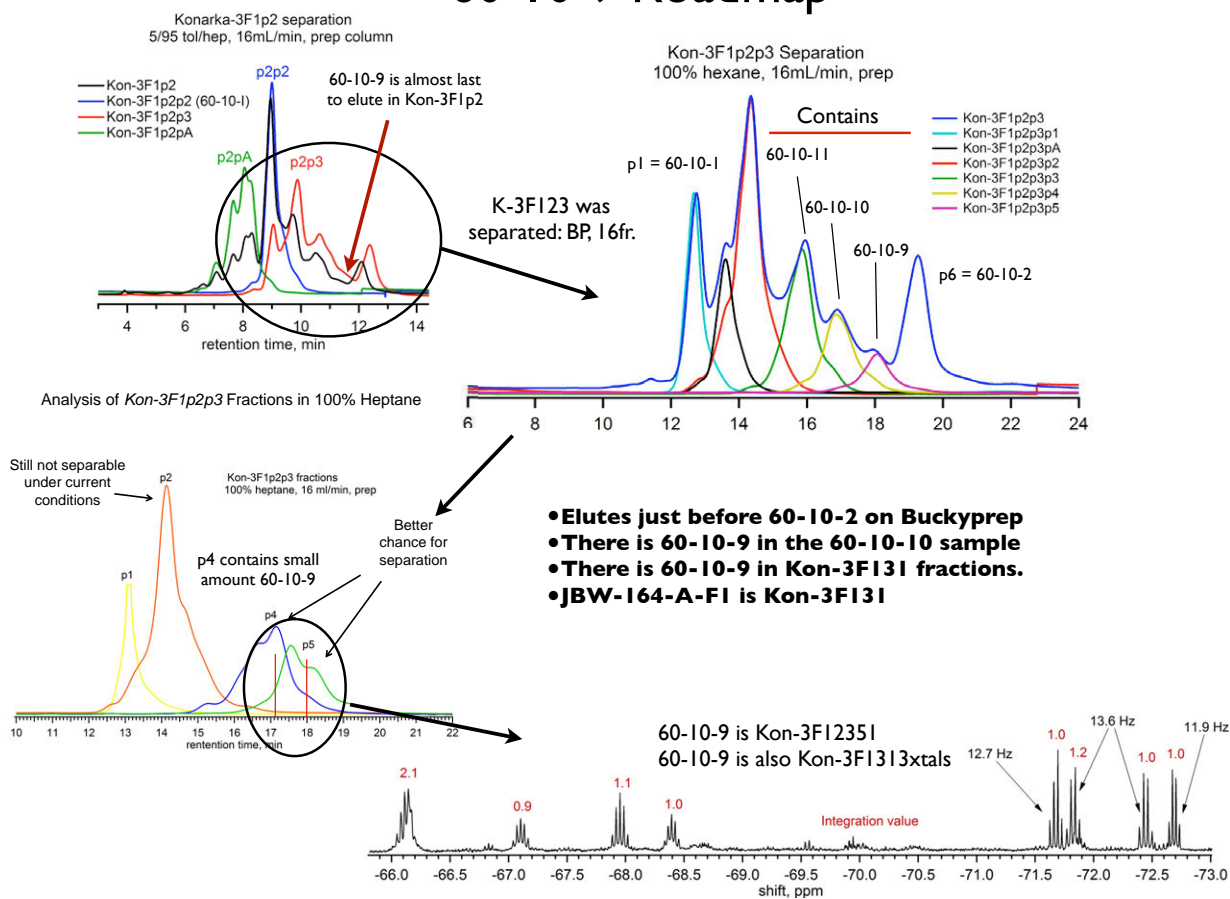
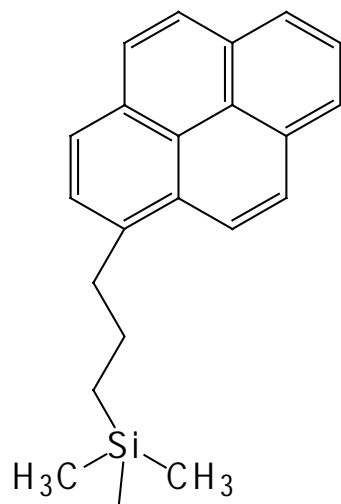


Figure 3.12. The stepwise HPLC separation scheme, continued from F1F2 shown in Figure 3.10, is shown for isolation of $C_{60}(CF_3)_{10}$, including the ^{19}F NMR spectrum of the compound.

The interaction between closely related TMFs and the Cosmosil Buckyprep stationary phase is apparently not distinct enough such that the maximum amount of time that they can be retained on the column still does not result in distinguishable elution times. Nonetheless, Cosmosil Buckyprep is currently advertised as the premier column for separation of fullerene derivatives. The structure of the modified silica Buckyprep stationary phase is shown in Figure 3.13, of which the active component that participates in analyte retention is pyrene. Therefore, the affinity of fullerene molecules for the stationary phase as they pass through the column, and also why Buckyprep is a good column for separation of fullerene derivatives, can be understood by the interaction between the fullerene pi system with the aromatic pyrenylpropyl-coated silica beads. Since the interaction is fundamentally pi-pi, there are two means of resolving power in this case, based on: the size and shape of the cage's pi system, and how much electron density is located within that pi system. The former is determined by the addition pattern of the substituents on the cage, while the latter is determined by the electron induction or withdrawing nature of the substituent. Therefore, it is likely that it is practically impossible to separate certain groups of isomers of $C_{60}(CF_3)_{10}$ if they have similar structures (i.e. – remaining cage pi systems) since they also have the same electron withdrawing CF_3 substituents.

Buckyprep



Buckyprep-M

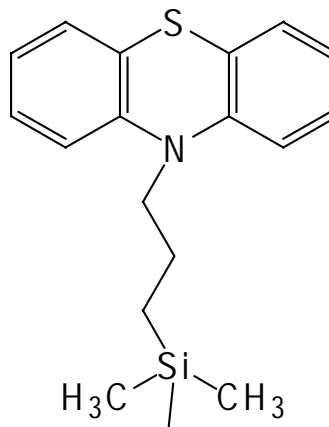


Figure 3.13. The structures of stationary phase materials in Cosmosil HPLC columns are shown for Buckyprep (left) and Buckyprep-M (right).

Recognition of this inherent, albeit very specific, problem made it imperative to look towards the use of different fullerene HPLC columns. One column that stood out was the Buckyprep-M column, which will also be referred to as Buckyprep-M on occasion in this dissertation. The reason that Buckyprep-M stood out from other column options is that the active component in its stationary phase is phenothiazine, which is the only stationary phase material for fullerene HPLC that contains an aromatic component and also atoms with lone electron pairs in addition to the pi cloud ring, sulfur in this case, that can participate directly in interaction with molecules in the mobile phase. Buckyprep-M columns were designed and are sold for separation of endohedral metallofullerenes, which are zwitterionic compounds (the encapsulated metal atoms or clusters actually formally donate electrons to the cage) and hence they possess unique electronic properties. Clearly, having this additional form of interaction between the stationary phase and analyte owes to their successful use in EMF chromatography. It was hypothesized that this additional mode of analyte resolving power (which is in addition the pi-pi interaction modes of separation discussed for Buckyprep) would improve the isolation of $C_{60}(CF_3)_{10}$ compounds. However, to date, there was no precedence in the literature of application of a Buckyprep-M column for separation of derivatives of C_{60} .

The fraction F1F5 was chosen to test this hypothesis since it contained a very large mixture of $C_{60}(CF_3)_{10}$ compounds according to the ^{19}F NMR spectroscopy, and also did not resolve well using a Buckyprep column (Figures 3.11 and 3.10, respectively). Figure 3.14 shows the comparison of HPLC chromatograms of fraction F1F5 using the Buckyprep or Buckyprep-M column, both with 100% hexanes as mobile phase. The only difference between the two analyses is that the Buckyprep column used measures 25 x 250 mm while the Buckyprep-M column

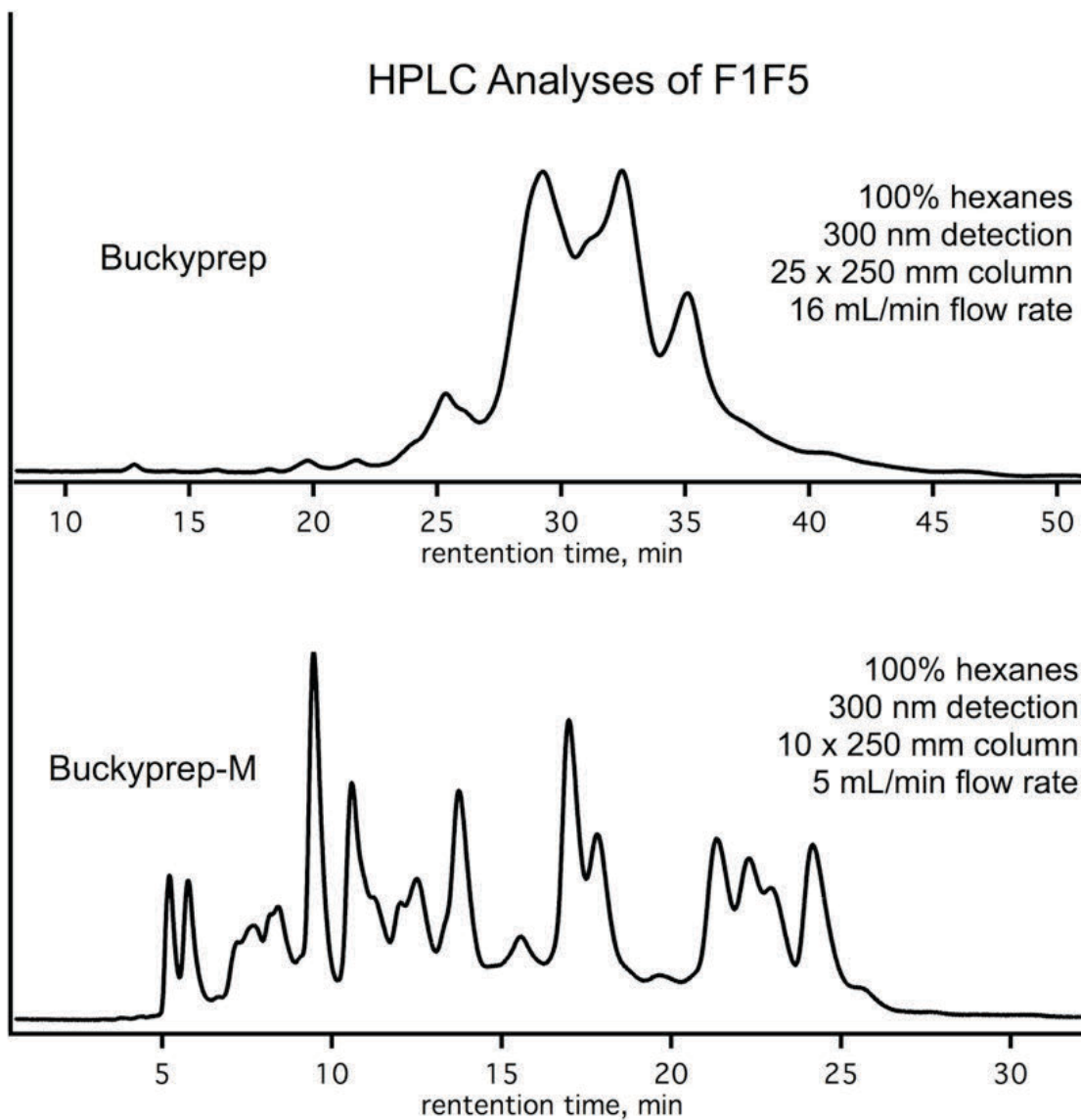
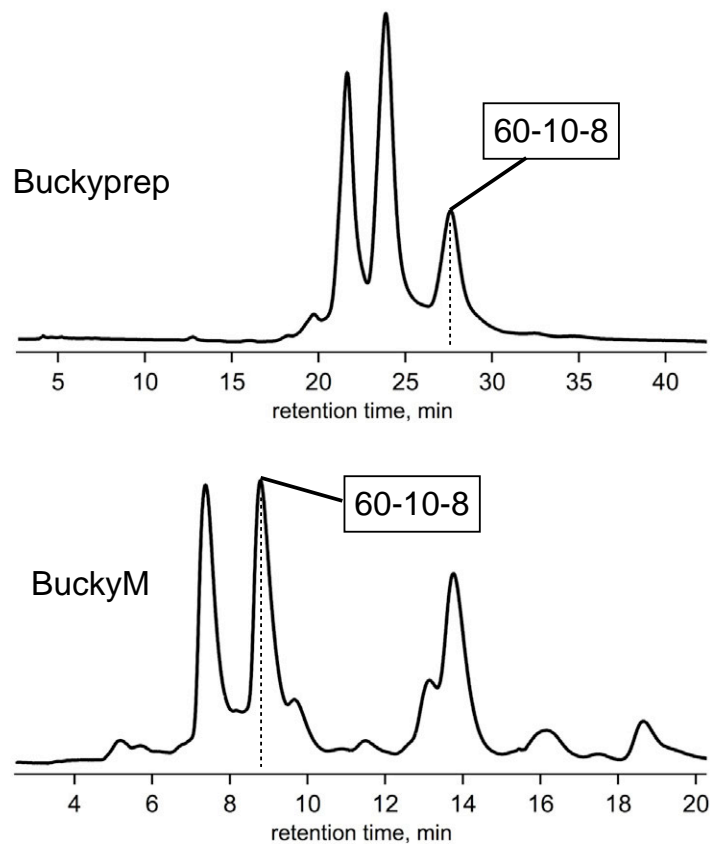


Figure 3.14. HPLC chromatograms are shown for analysis of F1F5, using Cosmosil Buckyprep (top) and Buckyprep-M (bottom) columns.

measures 10 x 250 mm, which was accounted for by accordingly adjusted flow rates. Two drastic differences in the chromatograms are immediately noticeable. First, the sample elutes between 12 – 47 minutes from the Buckyprep column, but elutes between 3 – 27 minutes from the Buckyprep-M column. Second, there are only four main elution features in the Buckyprep chromatogram, as opposed to at least thirteen (more consistent with the ^{19}F NMR spectrum shown in Figure 3.11) in the Buckyprep-M chromatogram and some even appear to contain single compounds (i.e. – the peaks are sharp). An interesting observation is that some isomers of $\text{C}_{60}(\text{CF}_3)_{10}$ were retained for at least 25 minutes on the Buckyprep column, but eluted almost immediately (shortly after elution of dead volume) from the Buckyprep-M column, meaning that these compounds have much greater affinity for pyrene than for phenothiazine.

An added benefit of using Buckyprep-M to separate 60-10's is that total retention times are generally less 30 minutes, even when weak eluents like hexanes or *n*-heptane are used, which tremendously decreases the amount of time that would have otherwise been required using a Buckyprep column. To illustrate this benefit, the case of $\text{C}_{60}(\text{CF}_3)_{10-8}$ will be discussed. Figure 3.15 shows the Buckyprep and Buckyprep-M HPLC chromatograms of F1F4 using 100% hexanes eluent where separation conditions were amenable to isolation of 60-10-8 to some degree of high purity. Using the Buckyprep column, the retention time of 60-10-8 is 27.6 minutes; on a Buckyprep-M column the retention time of 60-10-8 is 8.7 minutes. For preparative HPLC of 60-10-8, however, it is more useful to evaluate the amount of time required between tandem injections of material, since many dozens of injections may be necessary to obtain large

HPLC Separation of F1F4



¹⁹F NMR Spectra of 60-10-8

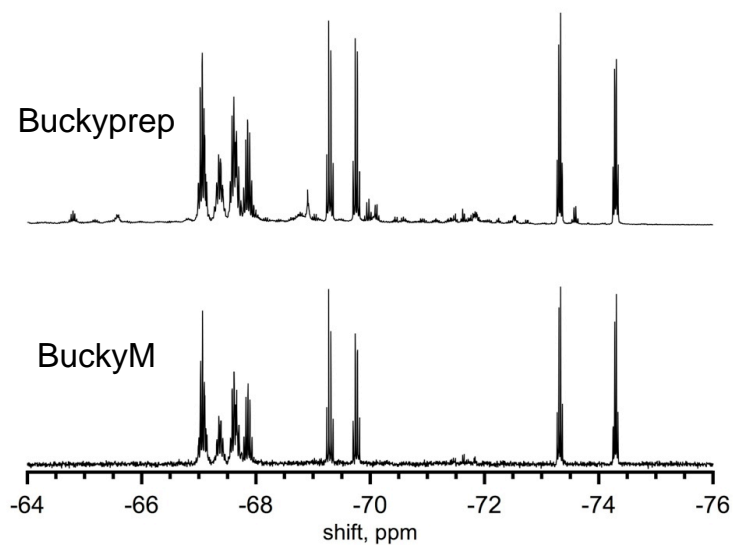


Figure 3.15. HPLC chromatograms (top) and ¹⁹F NMR spectra are shown for isolation of C₆₀(CF₃)₁₀-8 using either a Buckyprep or BuckyM column.

quantities of the compound. In the case Buckyrep-M, injections can be made every 18 minutes and still prevent tailings of the final fraction of the prior injection from contaminating the first fraction of the next injection. In the case of Buckyrep, the time required is 37 minutes. Additionally, since fine resolution of structurally similar $C_{60}(CF_3)_{10}$ compounds can not be achieved on a Buckyrep column, the purity of the 60-10-8 sample using that method was far inferior to the Buckyrep-M isolated sample; this is evident when comparing their corresponding ^{19}F NMR spectra, also shown in Figure 3.15. There are far fewer noise peaks due to impurities in the baseline of the Buckyrep-M isolated sample than the Buckyrep isolated sample. A detailed discussion of ^{19}F NMR spectrum of $C_{60}(CF_3)_{10}$ compounds is given in Section 3.1.5. Here, the purity of the spectrum is what should be gleaned from Figure 3.15.

Use of Buckyrep-M with 100% hexane eluent also enabled HPLC separation of fractions F1F6, F1F7, and F1F8, which produced many of the new isomers of $C_{60}(CF_3)_{10}$ that are discussed in great detail in the following sections after only one stage of HPLC separation. The Buckyrep-M HPLC chromatograms are shown for those fractions in Figure 3.16, and pure compounds isolated from the corresponding peaks are labeled. Other peaks contained simple mixtures of isomers that were further separated either by additional HPLC or selective precipitation. Additional stages of HPLC separation in addition to other non-HPLC isolation methods should enable isolation of even more new compounds when applied to the minor peak components shown in the chromatograms.

Isolation of $C_{60}(CF_3)_{10}$'s by Selective Precipitation. It is important to note that certain compounds that could not be isolated by HPLC using either Buckyrep-M or Buckyrep

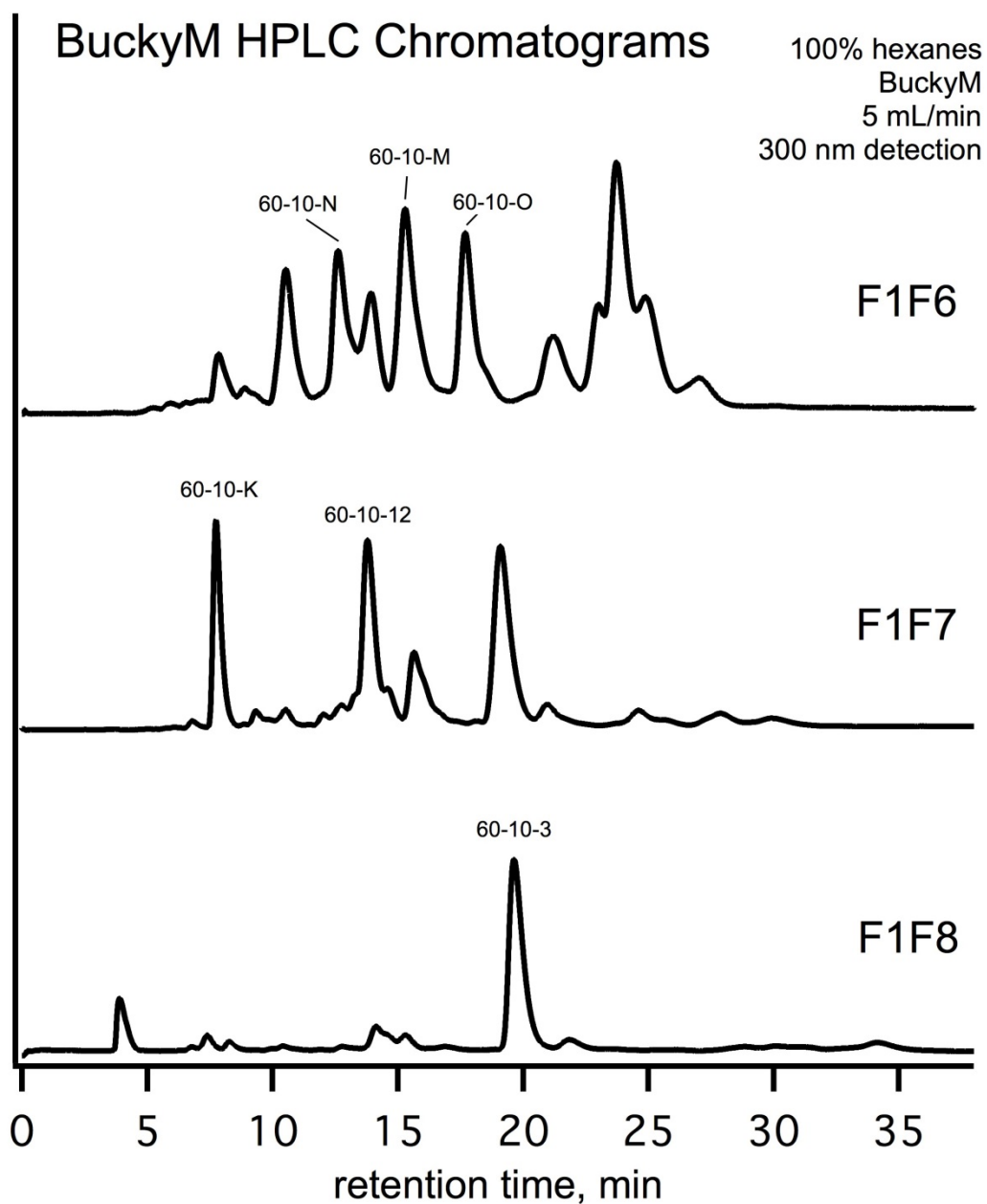


Figure 3.16. Buckyprep-M HPLC chromatograms are shown for fractions F1F6, F1F7, and F1F8. Pure compounds that were isolated from peaks in the corresponding chromatograms are labeled.

columns were obtained by crystallization from a simple mixture of compounds. Therefore, simple mixtures (fractions that contained either primarily one compound or balanced mixtures of just two or three compounds) obtained by HPLC separation were left in solution (100% hexanes) undisturbed and without letting the solvent evaporate for some time to test for selective precipitation. In some cases, a compound would crash out within minutes, while it took days in other cases. Then, the remaining solution was pipetted off, the crystals were washed in hexanes, and then redissolved in toluene.

Applicability of Improved Isolation Methods for Other Higher TMFs. The fractions F2 and F3 shown in Figure 3.9, from the GTGS large-scale synthesis that produced more isomerically-diverse mixtures of $C_{60}(CF_3)_x$ compounds, contained primarily derivatives with eight and six CF_3 groups, respectively. While major synthetic and separation efforts were not directly focused on these two families of compounds in this work, the presence of these fractions in the crude product suggested that they may be also comprised of complex mixtures of isomers, including ones with unknown addition patterns. Therefore, a proof-of-concept study was carried out by the author that would determine whether the improved isolation techniques developed for the $C_{60}(CF_3)_{10}$ family would apply to other compositions of TMFs as well. As was the case in the separation of F1, the second stage of HPLC separation using a Cosmosil Buckyrep column did not produce any pure 60-8-x or 60-6-x compounds. In fact, a third stage of HPLC separation yielded only a few moderately pure fractions. However, separations performed using a Buckyrep-M column resulted in isolation of several new isomers of 60-8 and 60-6, in addition to several known isomers which were isolated in unprecedentedly high purity. The ^{19}F NMR spectra of these compounds are shown in Figures 3.17 and 3.18 as a demonstration of

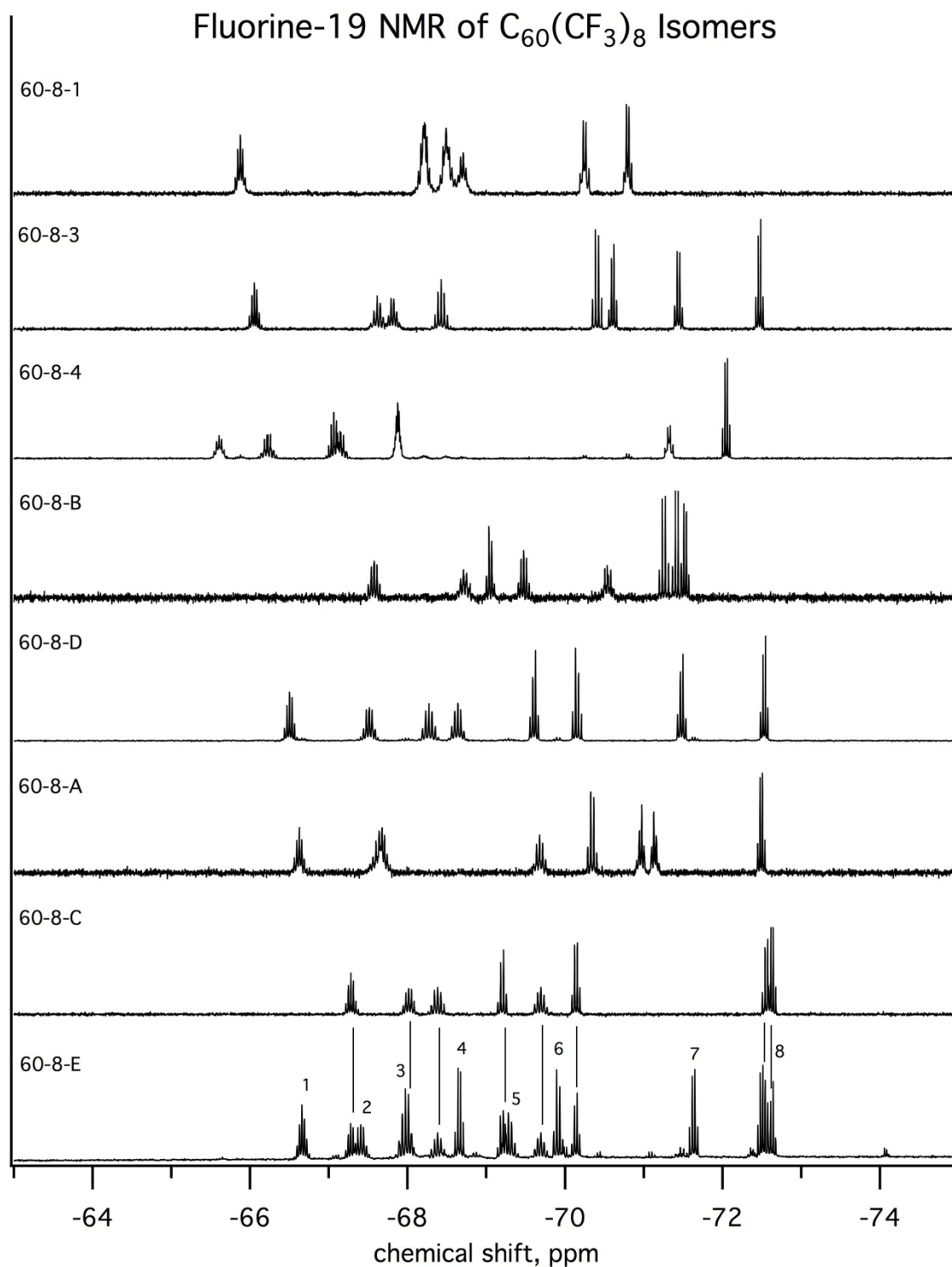


Figure 3.17. The ^{19}F NMR spectra (376.07 MHz, CDCl_3 , C_6F_6 internal standard) are shown for isomers of $C_{60}(CF_3)_8$ compounds that were isolated in this work using new HPLC separation methods. Compounds with letters denote they are new compounds.

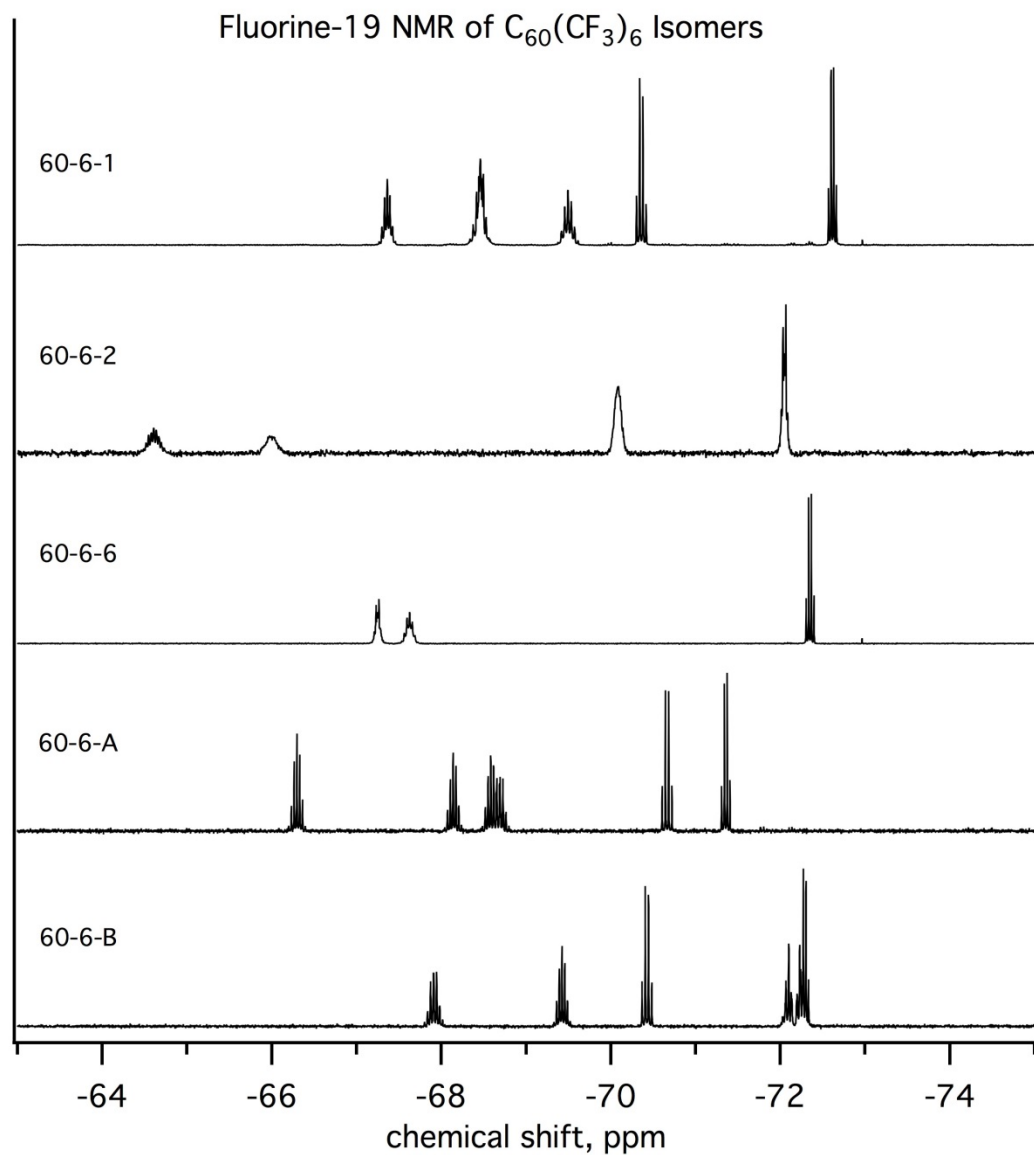


Figure 3.18. The ^{19}F NMR spectra (376.07 MHz, $CDCl_3$, C_6F_6 internal standard) are shown for isomers of $C_{60}(CF_3)_6$ compounds that were isolated in this work using new HPLC separation methods. Compounds with letters denote they are new compounds.

how successful the use of a Cosmosil Buckyprep-M column can be in isolating a variety of compounds from complex mixtures. These results offer promise for studies that may be undertaken in the future by other members of the Strauss group or elsewhere, since the isolation techniques developed for the study of $C_{60}(CF_3)_{10}$ compounds are proven to also be effective for isolation of other TMFs. As a result of the methods developed in this section, the previously known 60-10 isomers were isolated in much higher purity than previous attempts (pre-this work), and 21 new isomers of 60-10 were characterized by ^{19}F NMR spectroscopy; in six cases single crystal X-ray structures were solved, which are discussed in detail in the following section.

3.1.4. X-ray Structures of Six New 60-10's. Thermal ellipsoid plots of the six new 60-10 isomers that were characterized by single-crystal X-ray diffraction are shown in Figure 3.18. X-ray collection and refinement parameters and some derived results (densities, molecular packing arrangements, and ranges of fullerene centroid...centroid ($\odot \cdots \odot$) distances) are listed in Table 3.2). Schlegel diagrams for the six new isomers, designated 60-10-8 through 60-10-13 are shown in Figure 3.19. Crystals for all six structure determinations were grown by the author. Diffraction data were collected, and the structures were initially solved, by the author (with the assistance of Dr. Igor V. Kuvychko) for 60-10-8, 60-10-9, and 60-10-10. Final refinements were performed by Mr. Eric V. Bukovsky. Diffraction data collections, structure solutions, and final refinements for 60-10-11, 60-10-12, and 60-10-13 were performed by Mr. Bukovsky (and, in the case of 60-10-11, with the assistance of Dr. Yu-Sheng Chen at the Advanced Photon Source at Argonne National Lab, where the synchrotron X-ray diffraction data for 60-10-11 were collected by Mr. Bukovsky). All of the structures consist of a complete $C_{60}(CF_3)_{10}$ molecule in the asymmetric unit (i.e., all 100 atoms are unique). All of the structures are asymmetric; only one enantiomer is shown for each structure in Figure 3.18.

The six structures exhibit addition patterns that follow the general trends described above for the previously known 60-10 isomers^{1,6-8,11} and other $C_{60}(CF_3)_n$ derivatives.² For clarity, the

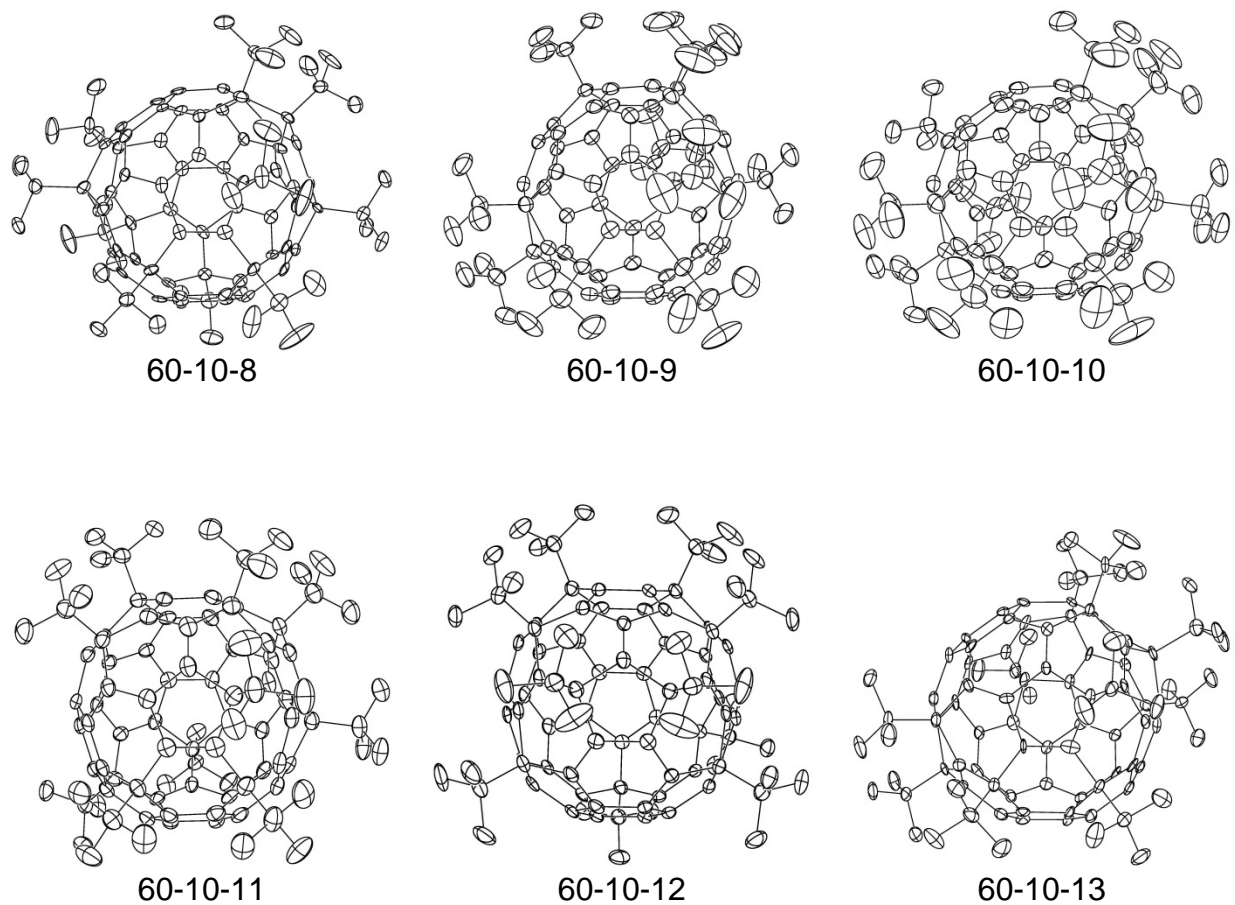


Figure 3.18. X-ray crystallographic 50% thermal ellipsoid plots of the six structurally-characterized new isomers of C₆₀(CF₃)₁₀. The CHCl₃ and CDCl₃ molecules of solvation in the structures of 60-10-8 and 60-10-11, respectively, are omitted for clarity.

Table 3.2. Crystal data, structure refinement parameters, density, and fullerene centroid···centroid ($\odot\cdots\odot$) distances for new $C_{60}(CF_3)_{10}$ isomers^a

compd abbreviation ^b	60-10-8·CHCl ₃	60-10-9	60-10-10	60-10-11·CDCl ₃	60-10-12	60-10-13
crystal system	triclinic	triclinic	monoclinic	triclinic	monoclinic	orthorhombic
space group, <i>Z</i>	$P\bar{1}$, 2	$P\bar{1}$, 2	$C2/c$, 8	$P2_1/c$, 4	$P2_1/n$, 4	$P2_12_12_1$, 4
unit cell dimensions						
<i>a</i> , Å	11.532(1)	12.1441(6)	46.403(6)	12.253(1)	17.794(1)	11.525(1)
<i>b</i> , Å	12.088(1)	12.3855(7)	12.115(2)	24.771(3)	13.1545(8)	19.760(2)
<i>c</i> , Å	19.854(2)	17.3822(9)	17.249(3)	17.001(2)	20.108(1)	20.527(2)
α , deg	72.791(4)	93.614(3)	90	90	90	90
β , deg	74.569(5)	96.249(3)	104.164(7)	106.035(3)	102.099(2)	90
γ , deg	85.305(5)	114.298(2)	90	90	90	90
unit cell volume, Å ³	2548.3(4)	2351.9(2)	9402(2)	4959.2(8)	4602.0(5)	4674.6(9)
density, g cm ⁻³	1.994	1.992	1.993	2.051	2.036	2.004
temperature, K	120(2)	120(2)	120(2)	100(2)	100(2)	120(2)
final <i>R</i> indices [<i>I</i> > 2σ(<i>I</i>)]	<i>R</i> ₁ = 0.0628, <i>wR</i> ₂ = 0.2285	<i>R</i> ₁ = 0.0520, <i>wR</i> ₂ = 0.1556	<i>R</i> ₁ = 0.0458, <i>wR</i> ₂ = 0.1436	<i>R</i> ₁ = 0.0716, <i>wR</i> ₂ = 0.2217	<i>R</i> ₁ = 0.0445, <i>wR</i> ₂ = 0.1123	<i>R</i> ₁ = 0.0401, <i>wR</i> ₂ = 0.1038
goodness-of-fit on <i>F</i> ²	0.975	1.036	1.057	0.985	1.017	1.028
idealized lattice packing ^c	not close packed	HCP	HCP	HCP	CCP	not close packed
$\odot\cdots\odot$ distances, Å	9.852–16.009	9.703–13.741	10.073–14.346	10.078–14.661	10.203–13.958	10.126–14.414
mean $\odot\cdots\odot$ distance, Å (esd)	13.232 (2.110)	12.006 (1.149)	12.121 (1.465)	12.244 (1.268)	11.973 (1.353)	12.455
median $\odot\cdots\odot$ distance, Å	12.198	12.144	12.115	12.327	11.953	11.881

^a Except for 60-10-8·CHCl₃ and 60-10-11·CDCl₃, the chemical formulas and formula weights are C₇₀F₃₀ and 1410.70 g mol⁻¹, respectively. For 60-10-8·CHCl₃, the chemical formula is C₇₀HCl₃F₃₀ and the formula weight is 1530.07 g mol⁻¹. For 60-10-11·CDCl₃, the chemical formula is C₇₀Cl₃DF₃₀ and the formula weight is 1531.07 g mol⁻¹. ^b See Table 3.1 and Figure 3.19 for IUPAC lowest locants and Schlegel diagrams, respectively, for these compounds. ^c HCP = hexagonal close-packed; CCP = cubic close-packed; — = another packing arrangement (see text).

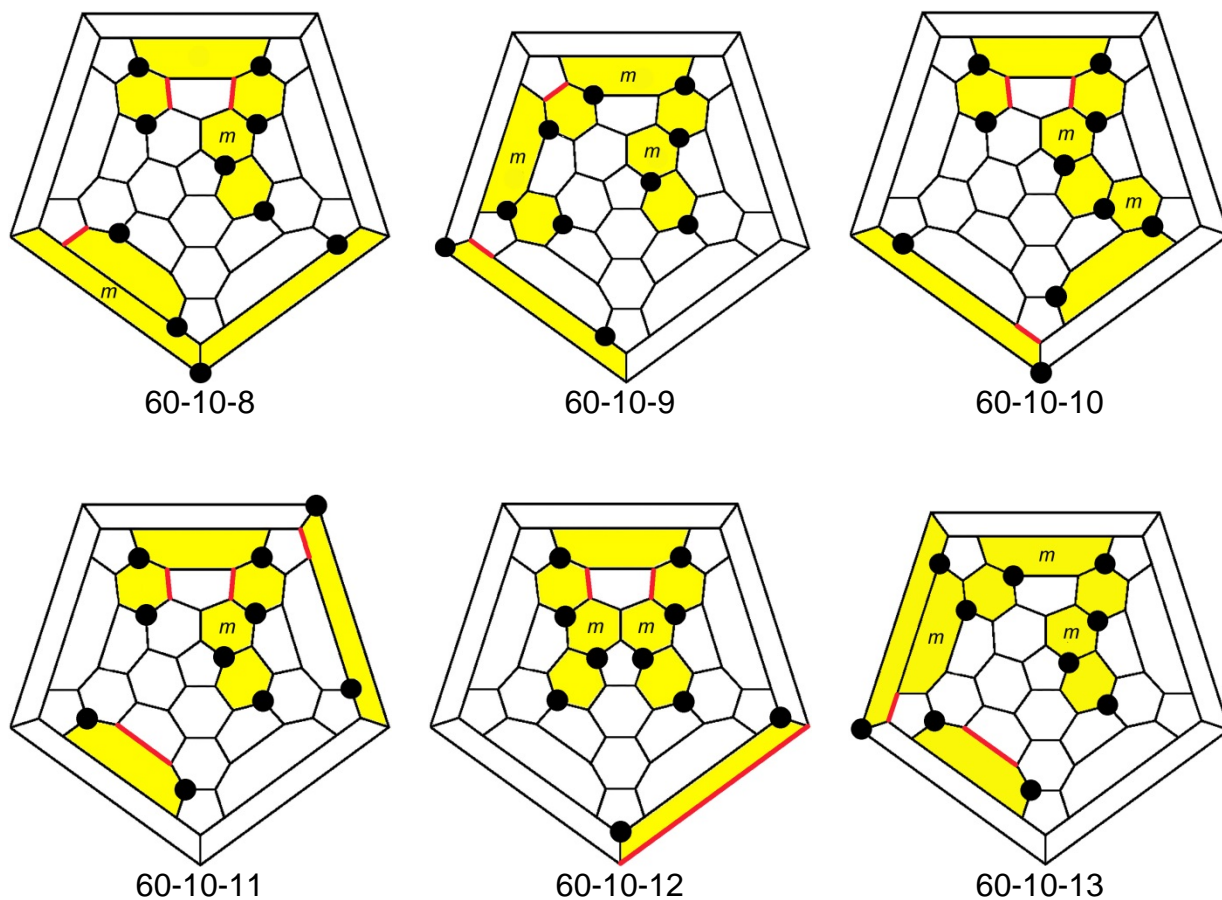


Figure 3.19. Schlegel diagrams for the structurally characterized new isomers of $C_{60}(CF_3)_{10}$. (See Table 1 for a key to the abbreviations 60-10-8 through 60-10-13.) The black circles indicate the cage C atoms to which the CF_3 groups are attached. The ribbons of edge-sharing *meta*- or *para*- $C_6(CF_3)_2$ hexagons and the isolated *para*- $C_6(CF_3)_2$ hexagons are highlighted in yellow, and the *meta*- $C_6(CF_3)_2$ hexagons are indicated with the letter *m*. The bonds highlighted in red are non-terminal double bonds in pentagons (see text).

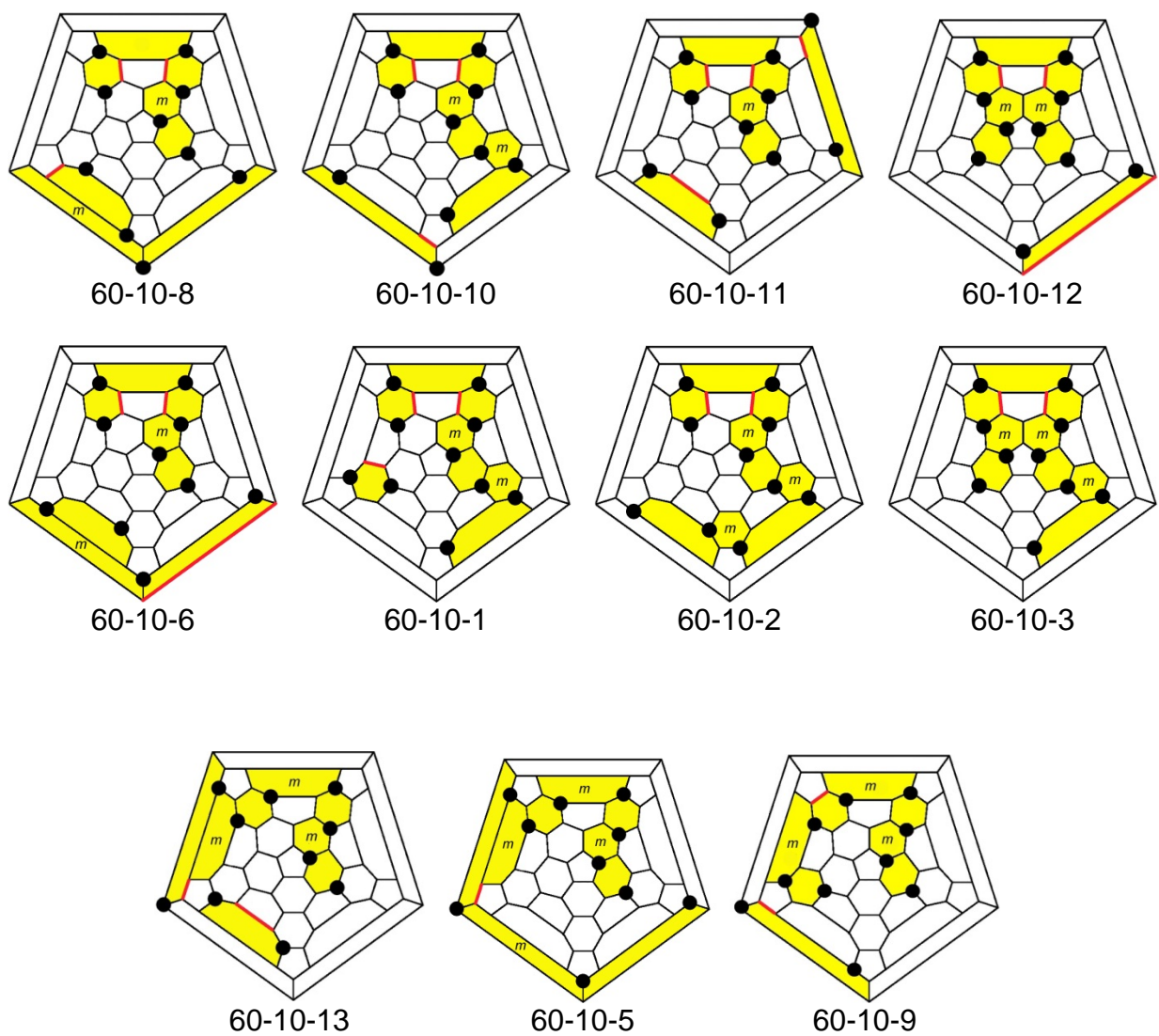


Figure 3.20. Schlegel diagrams arranged to compare and contrast the addition patterns of structurally characterized isomers of $C_{60}(CF_3)_{10}$. The first four relevant comparisons are vertical: 60-10-8 with 60-10-6; 60-10-10 with 60-10-1; 60-10-11 with 60-10-2; and 60-10-12 with 60-10-3. The bottom row allows a horizontal comparison of the addition patterns of 60-10-9, 60-10-5, and 60-10-13 to be made.

comparisons made in the remainder of this paragraph are shown in Figure 3.20. The p^3mp,pmp addition pattern of 60-10-8 is strikingly similar to the addition pattern of 60-10-6. Both molecules have identical p^3mp ribbons, and their pmp ribbons both involve the same three hexagons. The $pmpmpmp,p$ addition patterns of 60-10-9 and 60-10-13 are related to the single-ribbon $pmpmpmpmp$ addition pattern of 60-10-5. Both 60-10-5 and 60-10-13 have the same $pmpmpmp$ fragment, but the "last two" CF_3 groups are on different $p-C_6(CF_3)_2$ hexagons. In the case of 60-10-5, the last $p-C_6(CF_3)_2$ hexagon links up with the $pmpmpmp$ ribbon to generate an additional $m-C_6(CF_3)_2$ hexagon; in the case of 60-10-13, the last $p-C_6(CF_3)_2$ hexagon is an isolated $p-C_6(CF_3)_2$ hexagon.

Unlike a planar molecule such as $m-C_6H_4(CF_3)_2$ and $p-C_6H_4(CF_3)_2$, in which the CF_3 groups are well separated from one another, the curvature of the C_{60} cage, plus the distortions introduced by converting 10 cage $C(sp^2)$ atoms into $C(sp^3)$ atoms, forces the CF_3 groups in $m-C_6(CF_3)_2$ and $p-C_6(CF_3)_2$ hexagons and in 1,3- $C_5(CF_3)_2$ pentagons into close proximity. Furthermore, in general, CF_3 groups in $C_{60}(CF_3)_n$ derivatives exhibit staggered conformations with respect to their three underlying cage C–C bonds. These two structural features result in $F\cdots F$ interatomic distances of ca. 2.5–2.9 Å directly over each shared hexagon or pentagon, as shown in Figure 3.21 for a fragment of the structure of 60-10-12. A more detailed discussion of the $F\cdots F$ distances in the six new structures is in the ^{19}F NMR characterization section, below.

The distortions to the icosahedral C_{60} cage by adding 10 CF_3 groups can be seen in Figure 3.22. Even though molecules of $C_{60}(CF_3)_{10}$ are not as spherically symmetric as C_{60} , most 60-10 isomers that crystallize without lattice solvent molecules adopt either an idealized cubic close-packed (CCP) or hexagonal close-packed (HCP) structure. This is true of new structures 60-10-9, 60-10-10, and 60-10-12, as shown in Figure 3.23, as well as the previously reported structures 60-10-3,¹ 60-10-4,⁷ and 60-10-6.¹¹ When a molecule of chloroform is also present in the asymmetric unit, as in the structure of 60-10-8, the solid-state packing of fullerene moieties is not close packed, as shown in Figure 3.24. In this case each 60-10-8 molecule has 15 nearest-neighbor fullerenes. The range of distances between the fullerene centroids (\odot) is large, from

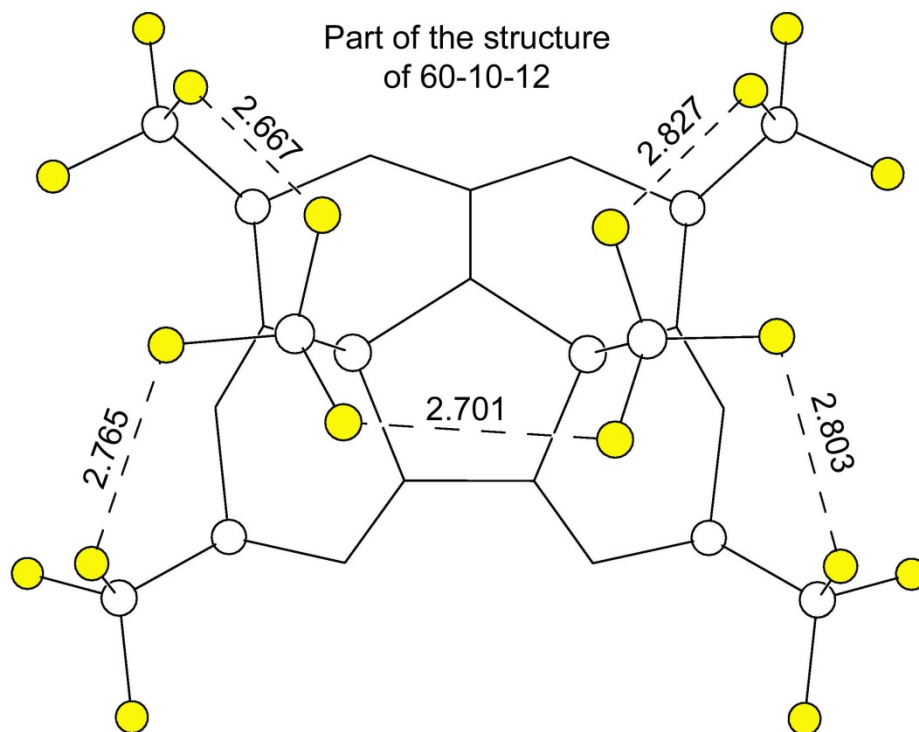


Figure 3.21. A portion of the X-ray structure of 60-10-12. The CF_3 groups that are not on the central pentagon are staggered with respect to the underlying cage $\text{C}-\text{C}$ bonds. Their $\text{F}-\text{C}-\text{C}-\text{C}$ torsion angles are 57.9 – 59.1° . The two CF_3 groups sharing the central pentagon have conformations that are significantly rotated with respect to being staggered. Their torsion angles are 16.1 and 24.0° . The $\text{F}\cdots\text{F}$ interatomic distances shown are in \AA (the standard error for each distance is 0.003 \AA).

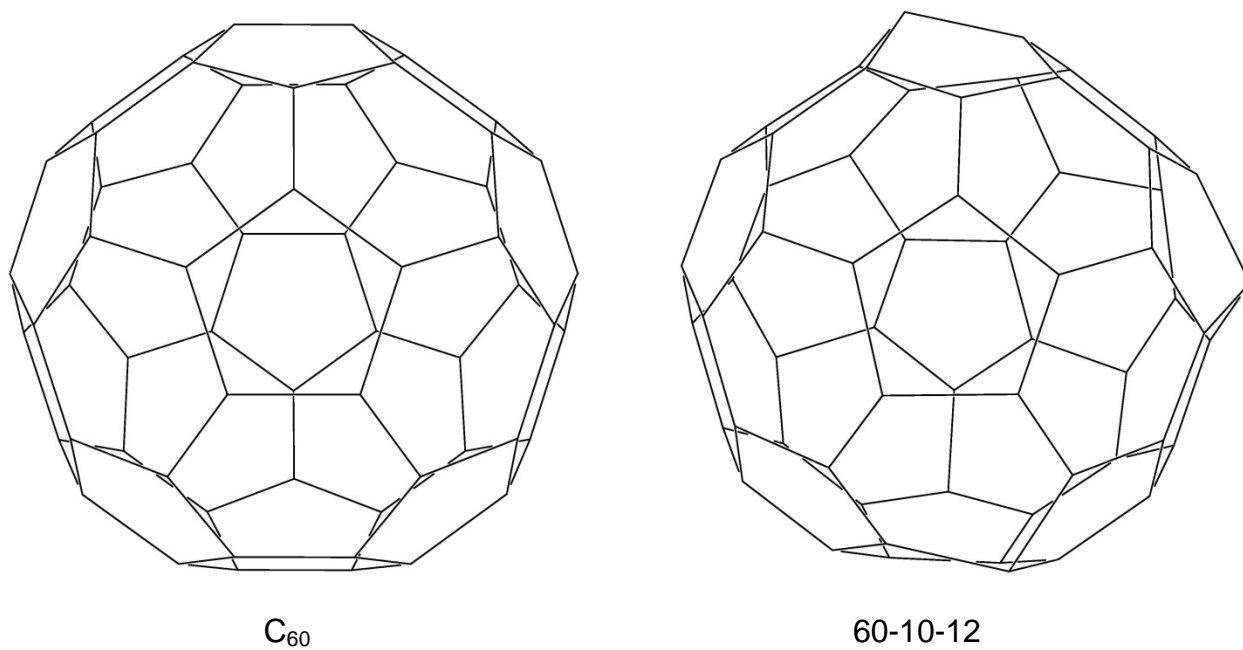


Figure 3.22. Comparison of the structures of underivatized C_{60} (left) and the fullerene cage in the structure of 60-10-12 (right; CF_3 groups omitted for clarity). The coordinates for the 60 unique $C(sp^2)$ atoms in C_{60} (i.e., no crystallographic symmetry) are from ref. 14. Note the significant distortion of the fullerene cage in 60-10-12, which has 50 $C(sp^2)$ and 10 $C(sp^3)$ atoms.

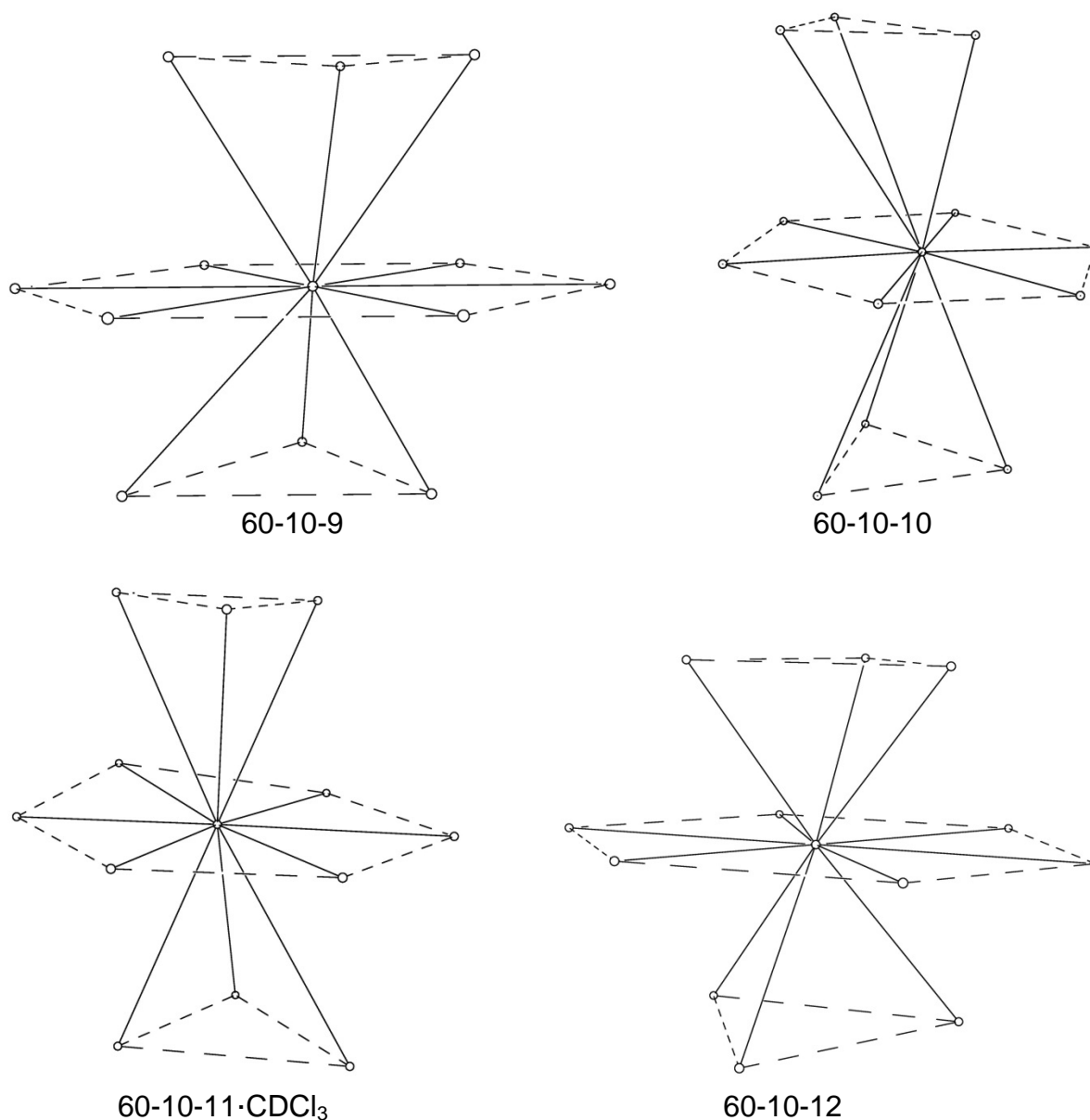


Figure 3.23. Molecular packing in the X-ray structures of four of the new 60-10 isomers. The fullerene centroids (\odot) are shown as spheres of arbitrary size. The CDCl₃ solvent molecules in the structure of 60-10-11·CDCl₃ have been omitted for clarity. The packing pattern for 60-10-12 is cubic close-packed. The packing patterns for the other three structures are hexagonal close-packed. The ranges of $\odot \cdots \odot$ distances are listed in Table 3.2.

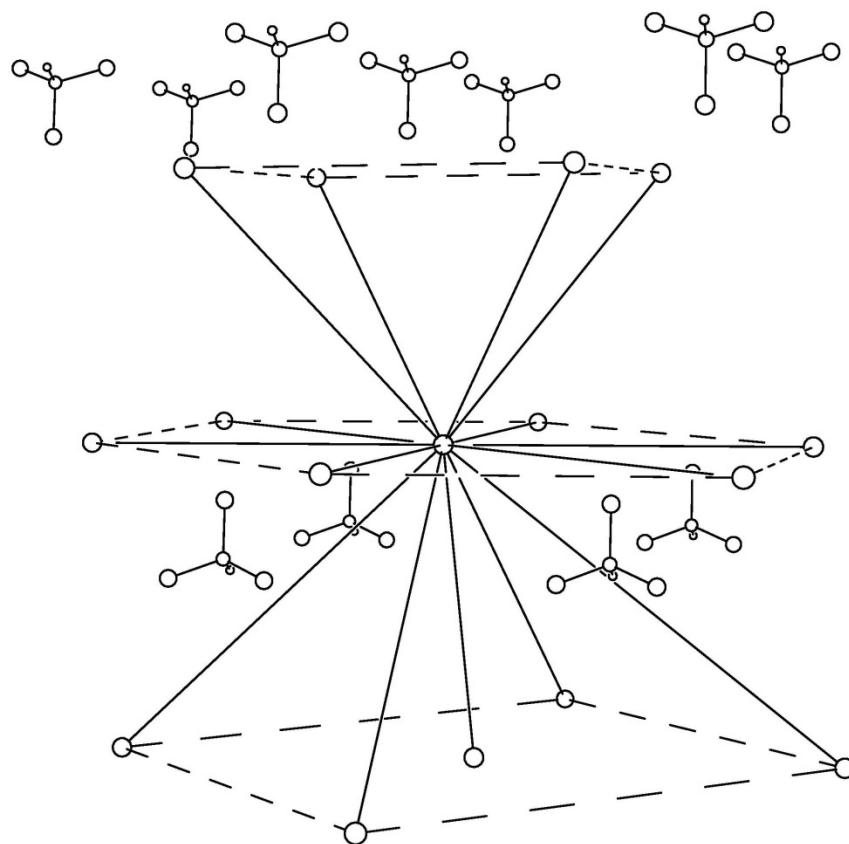


Figure 3.24. Molecular packing pattern for the X-ray structure of $60\text{-}10\text{-}8\cdot\text{CHCl}_3$. The fullerene centroids (\odot) are shown as spheres of arbitrary size. Also shown are 11 molecules of CHCl_3 . The shortest $\odot\cdots\odot$ distance, depicted as a nearly vertical solid line, is 9.852 \AA . The other 14 $\odot\cdots\odot$ distances shown as solid lines span the range $11.271\text{--}16.009\text{ \AA}$.

9.852 to 16.009 Å. Surprisingly, the shortest of these distances is shorter than the unique $\odot \cdots \odot$ distance in cubic C_{60} at 110 K, 9.936 Å.¹⁸ On the other hand, even with a molecule of chloroform-*d* in the asymmetric unit, the 60-10-11 molecules in the structure of 60-10-11·CDCl₃ pack in an HCP array, with only 12 nearest neighbors, as shown in Figure 3.23.

The packing efficiency of fullerene derivatives in the solid state may be one of the factors that controls the mobility of electrons present in fullerene domains in organic photovoltaic active materials (these electrons are produced by exciton dissociation during photoillumination). In this regard, it is interesting that the six solvent-free close-packed structures listed in the preceding paragraph, although they consist of isomer molecules with identical molecular formulas, exhibit subtle differences in their densities, from 1.992 g cm⁻³ for 60-10-9 to 2.073 g cm⁻³ for 60-10-4 (both sets of data were collected at 110 ± 10 K). This must be due to subtle differences in intermolecular interactions, both attractive and repulsive, caused by the different addition patterns. The ranges of $\odot \cdots \odot$ distances for 60-10-9, 60-10-10, and 60-10-12 are listed in Table 3.2. The ranges for 60-10-3, 60-10-4, and 60-10-6 are 10.187–14.232, 9.878–12.634, and 10.952–14.472 Å, respectively. There is a correlation, albeit not a very strong one, between the mean $\odot \cdots \odot$ distance and the crystal density, as shown graphically in Figure 3.25. In contrast, there is no meaningful correlation between the density and either the median $\odot \cdots \odot$ distance or the standard deviation of the 12 $\odot \cdots \odot$ distances (for 60-10-3, 60-10-4, and 60-10-6 these parameters are {12.143 and 1.016 Å}, {12.100 and 0.912 Å}, and {11.441 and 0.988 Å}, respectively).

Finally, the solid-state fullerene packing in the structure of 60-10-13, which does not contain solvent molecules, is not close-packed, as shown in Figure 3.26. Nevertheless, the density of crystals of 60-10-13 is ca. 0.6% higher than the densities of crystals of the HCP structures 60-10-9 and 60-10-10, 1.992 and 1.993 g cm⁻³, respectively. Although HCP and CCP are the most dense ways to pack spheres in three-dimensional space, the nearly equal, if not higher, density of 60-10-13 reinforces the concept that 60-10's are "fuzzy" spheres with "fluorous" patches on parts of the fullerene surface, and the hard sphere (i.e., the surfaces) of the C₆₀ cores does not come

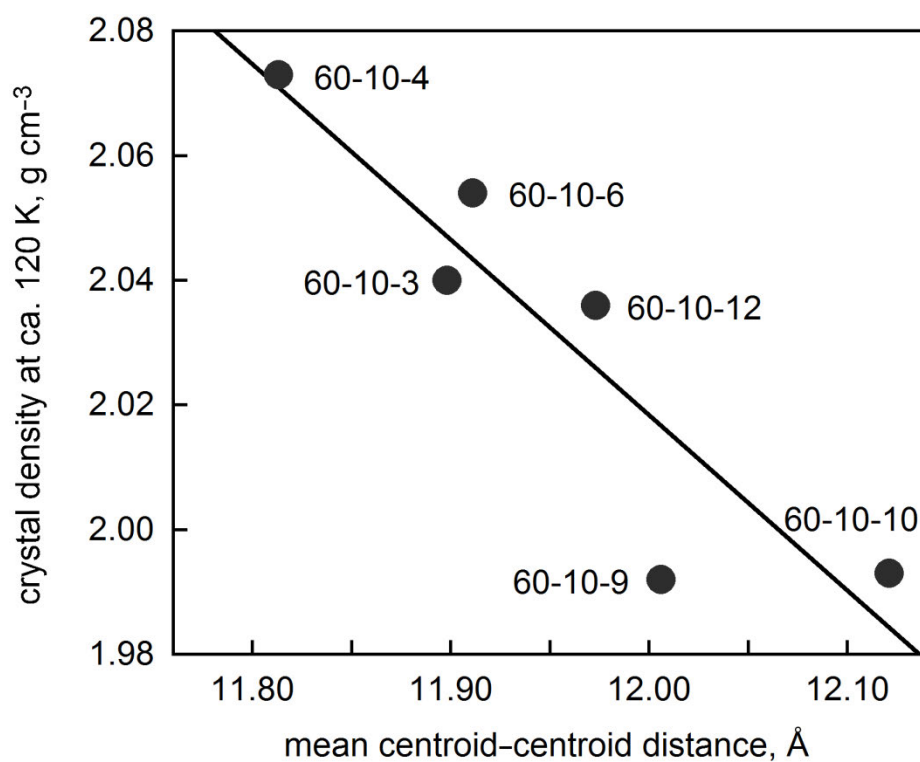


Figure 3.25. Graph showing the approximately linear correlation of crystal density of solvent-free close-packed structures vs. the mean centroid-centroid distance for six 60-10 X-ray structures. The data for all six structures were collected at ca. 120 K (110 ± 10 K). The structures of 60-10-3, 60-10-4, and 60-10-6 were reported in refs ¹, ⁷, and ¹¹, respectively.

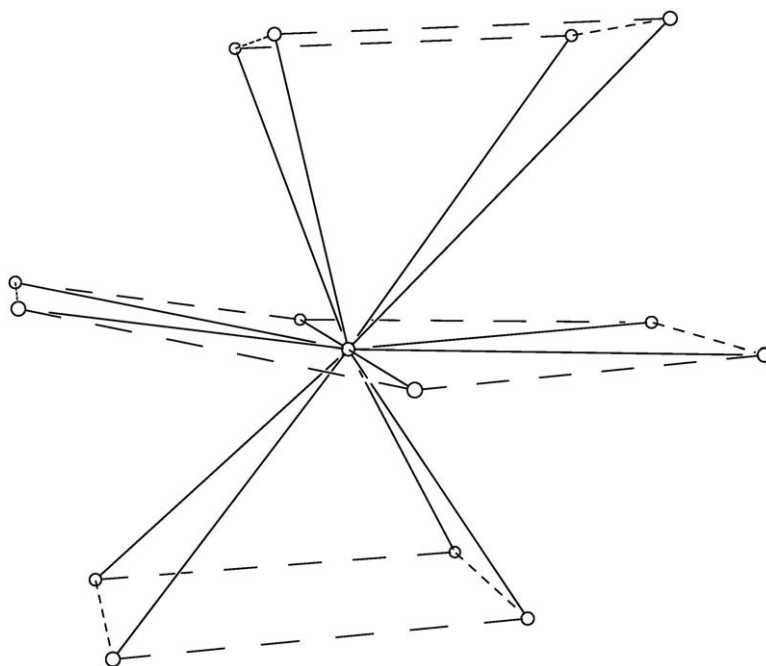


Figure 3.26. Molecular packing in the X-ray structure of 60-10-13. The fullerene centroids (\odot) are shown as spheres of arbitrary size. The range of the $\odot \cdots \odot$ distances shown as 14 solid lines is 10.126–14.414 Å. Even though the molecular packing for 60-10-13 is not close-packed, its density (2.004 g cm^{-3}) is ca. 0.6% higher than the densities of 60-10-9 and 60-10-10, which are close-packed (1.992 and 1.993 g cm^{-3} , respectively).

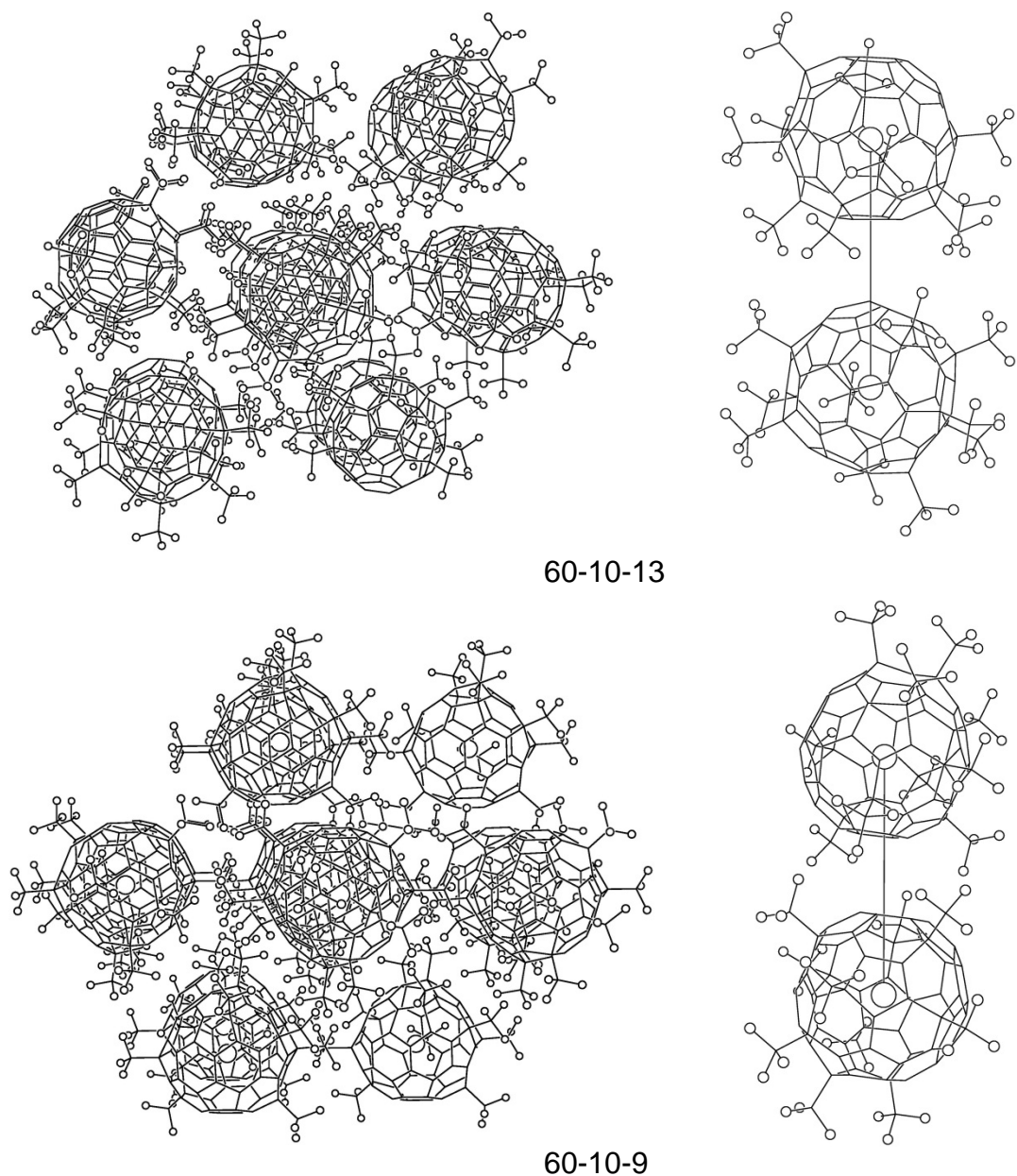


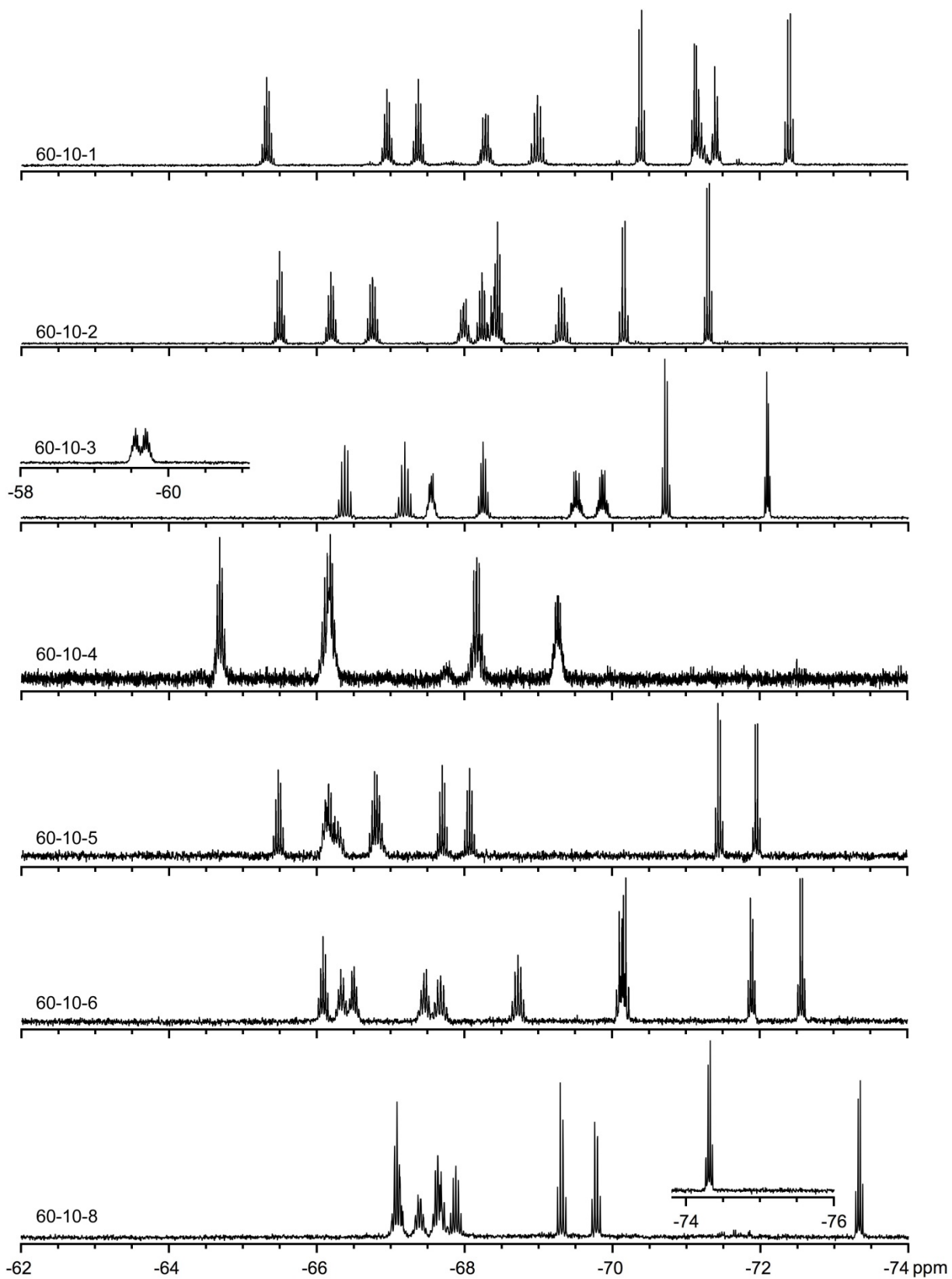
Figure 3.27. Packing of 60-10 molecules in the X-ray structures of 60-10-13 (top) and 60-10-9 (bottom). Only the F atoms and fullerene centroids (\odot) are shown as spheres of arbitrary size (small and large, respectively). The interactions of CF_3 groups on neighboring molecules prevents close π - π interactions in all cases in the structure of 60-10-13 and in all but one case in 60-10-9. Pairs of molecules with the shortest $\odot \cdots \odot$ distance in each structure are also shown ($\odot \cdots \odot = 10.126 \text{ \AA}$ for 60-10-13 and 9.703 \AA for 60-10-9). Note that the pair of neighboring molecules shown for 60-10-9 have an overlapping and rigorously parallel hexagon-hexagon π - π interaction with an interplanar spacing of $3.24 \pm 0.02 \text{ \AA}$.

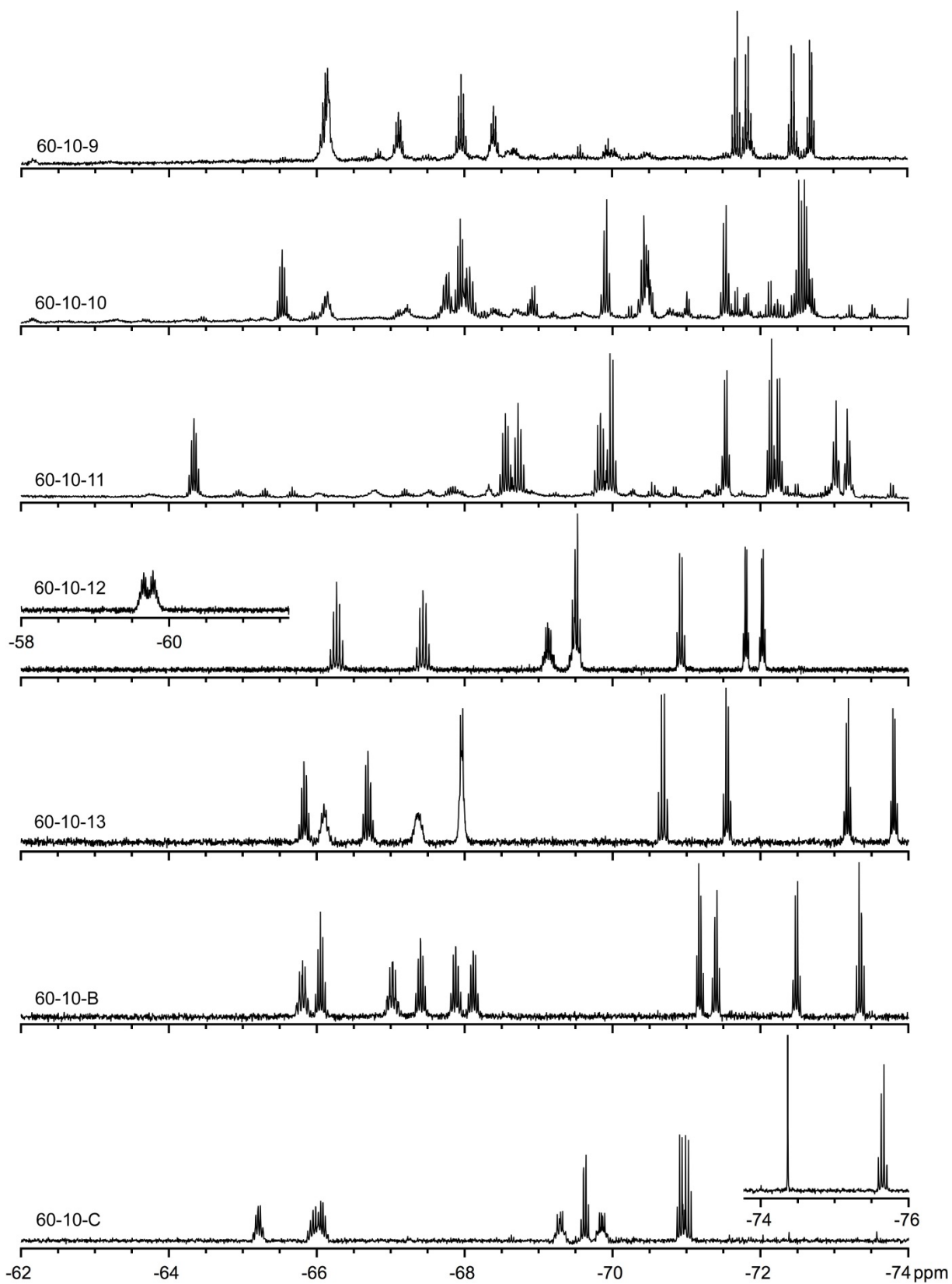
into van der Waals contact with the hard spheres of most of its neighbors in the lattice. This is shown in Figure 3.27, in which the fluorine regions between molecules of 60-10-13 and, for comparison, 60-10-9 are emphasized. Despite the similarities, there is at least one important difference. The closest approach of neighboring molecules in 60-10-13, with a $\odot \cdots \odot$ distance of 10.126 Å, does not involve efficient π - π interactions between parallel polygons on the two molecules. In contrast, in 60-10-9 and in the other close-packed structure, the closest approach has a $\odot \cdots \odot$ distance of 9.703 Å (as mentioned above, shorter than in cubic C_{60}) and does involve a pair of parallel all-C(sp²) hexagons, with perpendicular displacements of 3.24 ± 0.02 Å from the C atoms of one hexagon to the least-squares plane of the other, distances that are shorter than the 3.35 Å separation of the all-C(sp²) hexagonal planes in graphite.

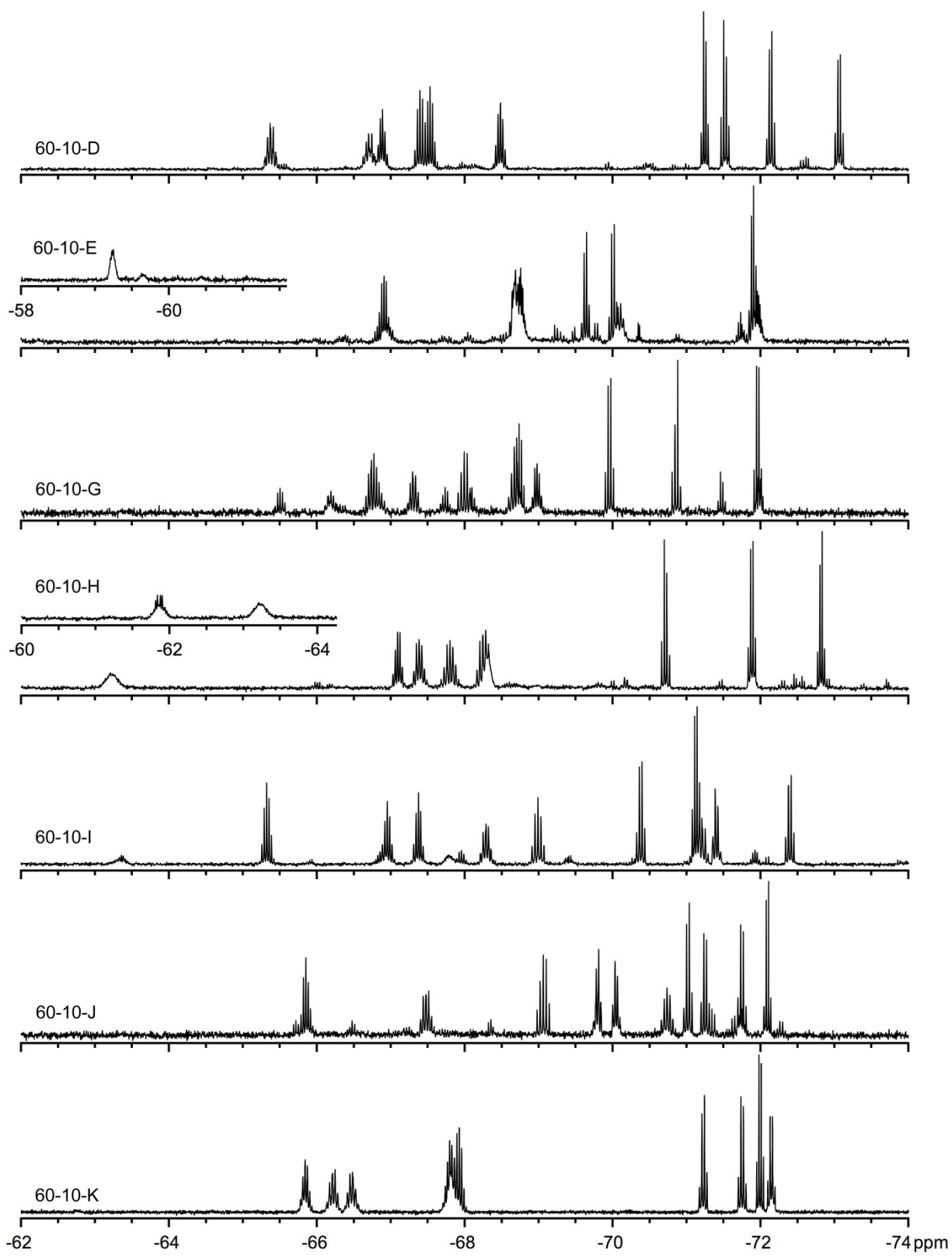
3.1.5. Characterization of New 60-10's by ¹⁹F NMR Spectroscopy and Correlations between $\delta(^{19}\text{F})$ and J_{FF} Values and Addition Patterns. Twenty-seven ¹⁹F NMR spectra recorded at 376.48 MHz in the common solvent CDCl₃ containing a trace amount of C₆F₆ as the internal chemical shift standard (δ -164.9) are shown in Figure 3.27 (the six known 60-10 isomers were re-recorded by the author in this solvent for comparison, and are shown in Figure 3.27 along with the 21 new 60-10 isomers). With one exception, each spectrum for the 21 new isomers consists of 10 multiplets, one for each CF₃ group, demonstrating a C₁ addition pattern (note that the spectrum of 60-10-4 has only five multiplets, and it is known that this compound has a C₂ addition pattern⁶). The exception is the spectrum of 60-10-C, which has nine multiplets and a singlet, the singlet denoting an "isolated" CF₃ group (i.e., a CF₃ group that does not share a hexagon or a pentagon with another CF₃ group). This is the first example of a C₆₀(CF₃)_n compound with any value of $n \leq 12$ with an isolated CF₃ group and only the second example of a fullerene(CF₃)_n compound of any fullerene with $n \leq 12$ and an ¹⁹F NMR singlet (the first example was an isomer of C₇₀(CF₃)₁₀¹⁹). Note that some of the multiplets are accidentally isochronous, or nearly so, resulting in overlapped multiplets with double or triple the integrated

intensity. An example is the double-intensity overlapped multiplets at $\delta -67.1$ and -67.7 in the spectrum of 60-10-8.

The ^{19}F NMR spectra of 60-10 isomers provide the easiest, and probably the most precise, way to estimate the purity of each compound, at least to ≥ 95 mol% purity. The compounds judged to be this pure by NMR are 60-10-1, -2, -3, -5, -6, -8, -12, -13, -B, -C, -K, -M, -O, -P, -Q, and -S. Those compounds that appear to be at least 85 mol% pure are -4, -9, -11, -D, -E, -G, -H,







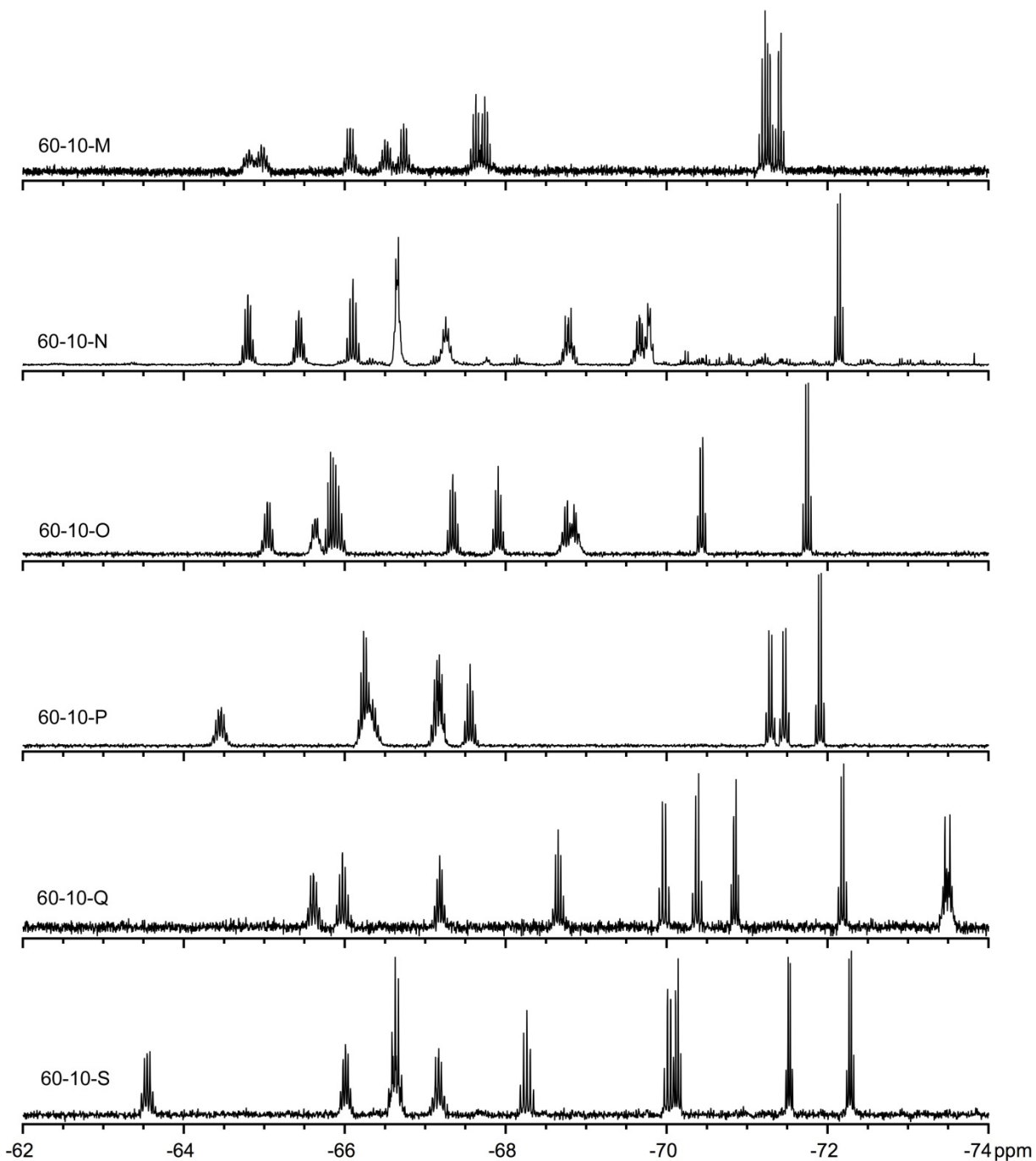


Figure 3.27. Fluorine-19 NMR spectra of 27 isomers of $C_{60}(CF_3)_{10}$ (376.48 MHz, $CDCl_3$, C_6F_6 internal standard ($\delta -164.9$)). See Table 3.1 for a key to the addition patterns of 60-10-1 through 60-10-6 and 60-10-8 through 60-10-13. The other isomers have unknown addition patterns.

-I, -J, and -N. Only 60-10-10 appears to have significantly more than 15 mol% impurities according to its ^{19}F NMR spectrum.

The multiplets are quartets for CF_3 groups that share only a single hexagon or pentagon with another CF_3 group, which are designated "terminal" CF_3 groups (i.e., at the ends of a ribbon or on an isolated $p\text{-C}_6(\text{CF}_3)_2$ hexagon).² The quartets almost always have the largest $-\delta$ values relative to the other multiplets in $\text{C}_{60}(\text{CF}_3)_n$ compounds,² and all of the 21 new 60-10 isomers exhibit ^{19}F NMR spectra with two or more quartets. Since ribbons are common for $\text{C}_{60}(\text{CF}_3)_n$ compounds with $n \leq 12$,² 60-10 spectra with only two quartets are probably due to single-ribbon addition patterns (examples are $p^3mpmpmp$, pmp^3mpmp , and $pmpmpmpmp$ for 60-10-2, 60-10-3, and 60-10-5, respectively). Spectra with four quartets were previously observed for 60-10-1 and 60-10-6,^{1,6} which have p^3mpmp,p and p^3mp,pmp addition patterns, respectively. The two quartets for isolated $p\text{-C}_6(\text{CF}_3)_2$ hexagons must have the same $J(\text{FF})$ value and, when a 2D ^{19}F NMR spectrum is also available, are correlated only with each other. In the absence of a 2D spectrum (2D spectra were not recorded for any of the 21 new 60-10 isomers), it is sometimes possible to unambiguously identify compounds with isolated $p\text{-C}_6(\text{CF}_3)_2$ hexagons when $\Delta\delta$ values for the quartets in question are sufficiently small that the "quartets" exhibit second-order behavior (i.e., when they are not symmetric or nearly-symmetric 1:3:3:1 quartets). This is clearly the case for 60-10-9, 60-10-11, and 60-10-13, which are known to possess isolated $p\text{-C}_6(\text{CF}_3)_2$ hexagons (60-10-11 has two isolated $p\text{-C}_6(\text{CF}_3)_2$ hexagons, but only one can be unambiguously identified in this way), and is also clearly the case for new isomers 60-10-K and 60-10-Q. An example of the second order nature of two quartets in the spectrum of 60-10-11 is shown in Figure 3.29.

The fact that many of the multiplets are quartets, quartets-of-quartets, or, as discussed below, apparent septets, demonstrates that nearly all of the CF_3 groups in 60-10 isomers rotate sufficiently rapidly about their respective $\text{F}_3\text{C}-\text{C}(\text{cage})$ bonds that the spectra are in the fast-exchange limit (the one exception, 60-10-H, will be discussed below). Each CF_3 group is coupled equally to the three F atoms of CF_3 groups with which it shares a hexagon or pentagon

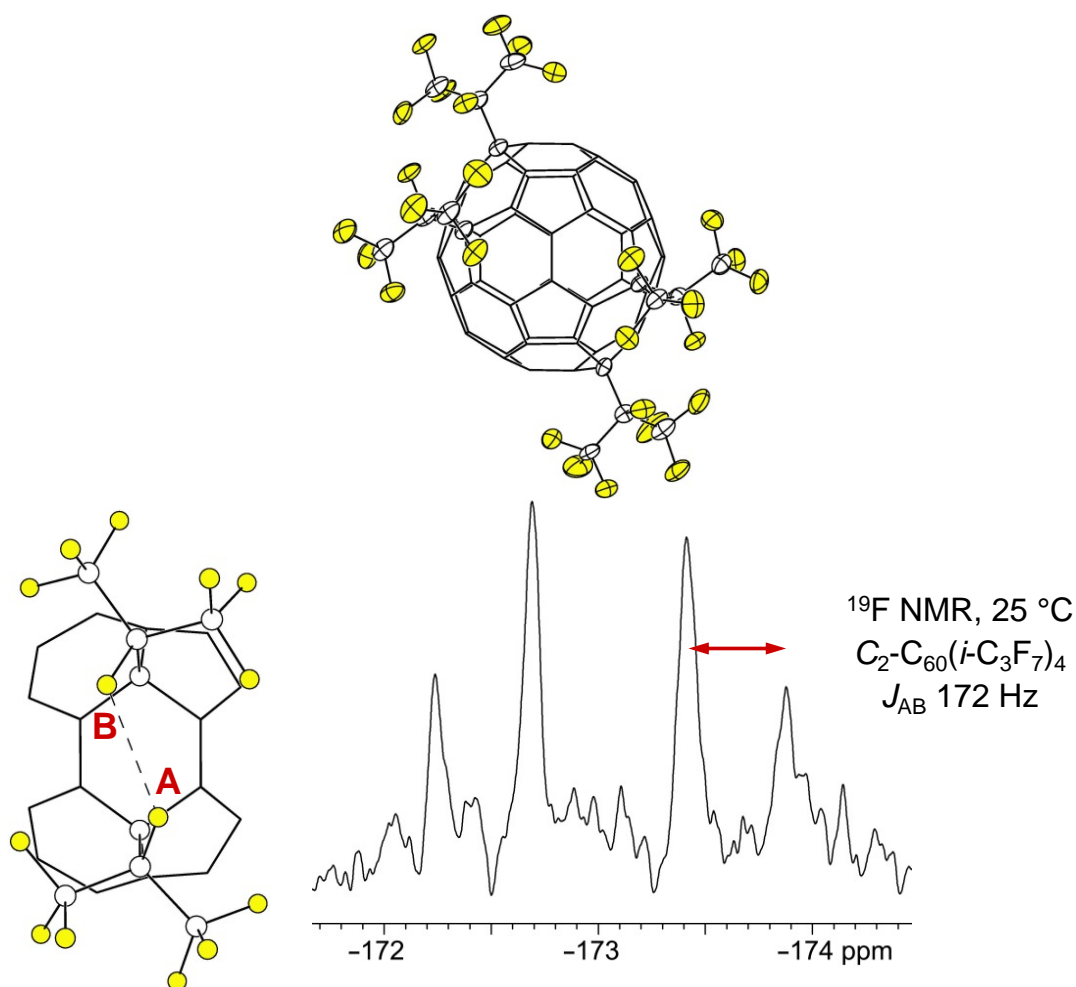


Figure 3.28. Top. The structure of $C_2-C_{60}(i-C_3F_7)_4$ (from ref ²⁹; 50% probability ellipsoids for $i-C_3F_7$ atoms and the cage C atoms to which they are attached; F atoms are shaded yellow). Bottom. A portion of the ^{19}F NMR spectrum of $C_2-C_{60}(i-C_3F_7)_4$ showing the AB quartet for the F atoms indicated in the bird's-eye view of one of the symmetry-related $p-C_6(i-C_3F_7)_2$ hexagons. The $F_A \cdots F_B$ distance is 2.614(5) Å.

(i.e., neighboring CF₃ groups). The observed ${}^7J_{\text{FF}}$ values for the quartets in Figure 3.27 are 8–18 Hz. It has long been recognized that long-range ${}^{\geq 4}J_{\text{FF}}$ coupling, especially for F atoms bonded to C(sp³) atoms, is primarily mediated by a through-space Fermi-contact mechanism (not to be confused with through-space dipolar coupling, which is averaged to zero in liquid NMR).^{20-26,27,28} This Fermi-contact through-space coupling involves the overlap of F atom lone pairs on proximate F atoms (i.e., F⋯F distances ≤ 3 Å). Since there is only one "instantaneous" F⋯F distance ≤ 3 Å for rapidly rotating neighboring CF₃ groups, the observed time-averaged coupling constants indicate that the instantaneous coupling constants for pairs of proximate F atoms in 60–10 isomers are actually nine times larger, 72–162 Hz. This has recently been confirmed for two related compounds in which the perfluoroisopropyl substituents on *p*-C₆(CF(CF₃)₂)₂ hexagons exhibited ${}^7J_{\text{FF}}$ values of 160 and 172 Hz.²⁹ An example is shown in Figure 3.28.

Many multiplets in the ¹⁹F NMR spectra of 60-10 isomers appear to be septets but in reality are quartets of quartets with equal or nearly-equal J_{FF} values.² These multiplets are due to CF₃ groups within a ribbon, so they are independently coupled to the two CF₃ groups with which they share different *m*- and/or *p*-C₆(CF₃)₂ hexagons (and/or possibly a 1,3-C₅(CF₃)₂ pentagon). Two multiplets in the spectrum of 60-10-1, one of which is an apparent septet and one of which is clearly not a septet, but both of which are known to be quartets-of-quartets given the addition pattern and 2D NMR spectrum of 60-10-1, are shown in Figure 3.30. Another pair of quartets-of-quartets, from the spectrum of 60-10-3, and spectral simulations of them, are shown in Figure 3.31. In this case, the J_{FF} values for the simulation of the apparent septet were both set to 11.7 Hz, and the J_{FF} values for the complex multiplet that was also simulated as a quartet-of-quartets were set to 9 and 14 Hz.

The ¹⁹F NMR spectrum of a new fullerene(CF₃)_{*n*} isomer that has not, or cannot, been studied by X-ray crystallography can frequently be used to narrow down the number of possible addition patterns. As discussed above, the number of quartets indicates the number of CF₃ groups with only one nearest-neighbor CF₃ group. But there is much more information in the chemical shifts

and ^{19}F - ^{19}F coupling constants that can be used to elucidate the most likely structure, or at least eliminate many possible addition patterns from consideration. For example, consider the addition

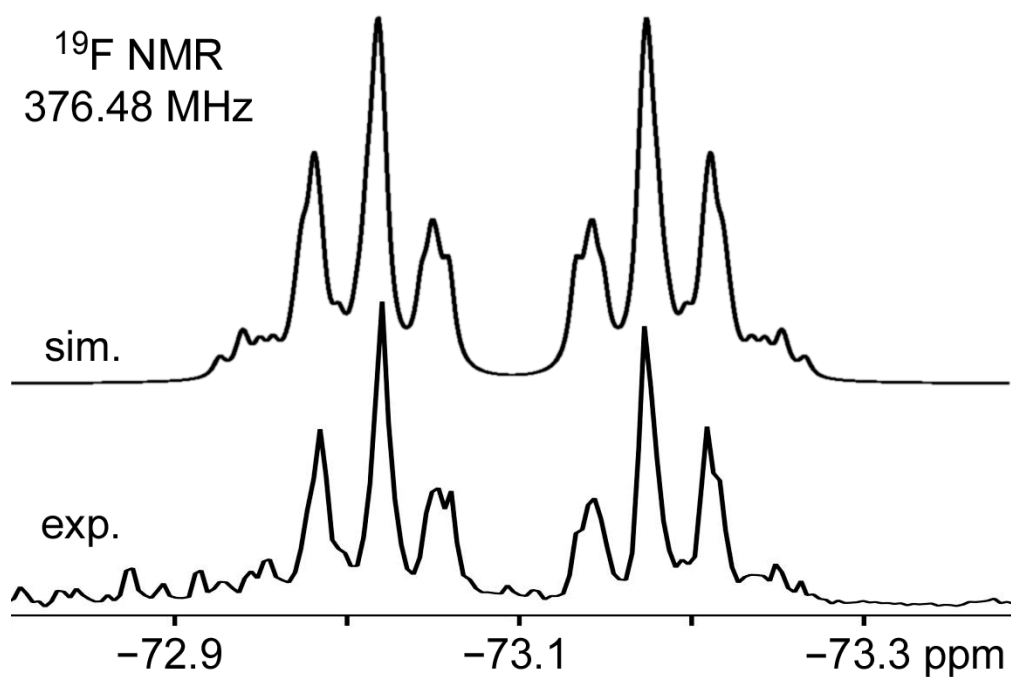


Figure 3.29. Part of the experimental ^{19}F NMR spectrum of 60-10-11 showing the second order nature of the multiplets assigned to the CF_3 groups on one of the two $p\text{-C}_6(\text{CF}_3)_2$ hexagons (376.48 MHz, CDCl_3 , C_6F_6 internal chemical shift standard (δ -164.9)). Also shown is the simulated spectrum calculated with the NMR program MNova version 8.1. The simulation parameters were $\delta(^{19}\text{F}) = -69.97$ and -70.05 and $J_{\text{FF}} = 14$ Hz.

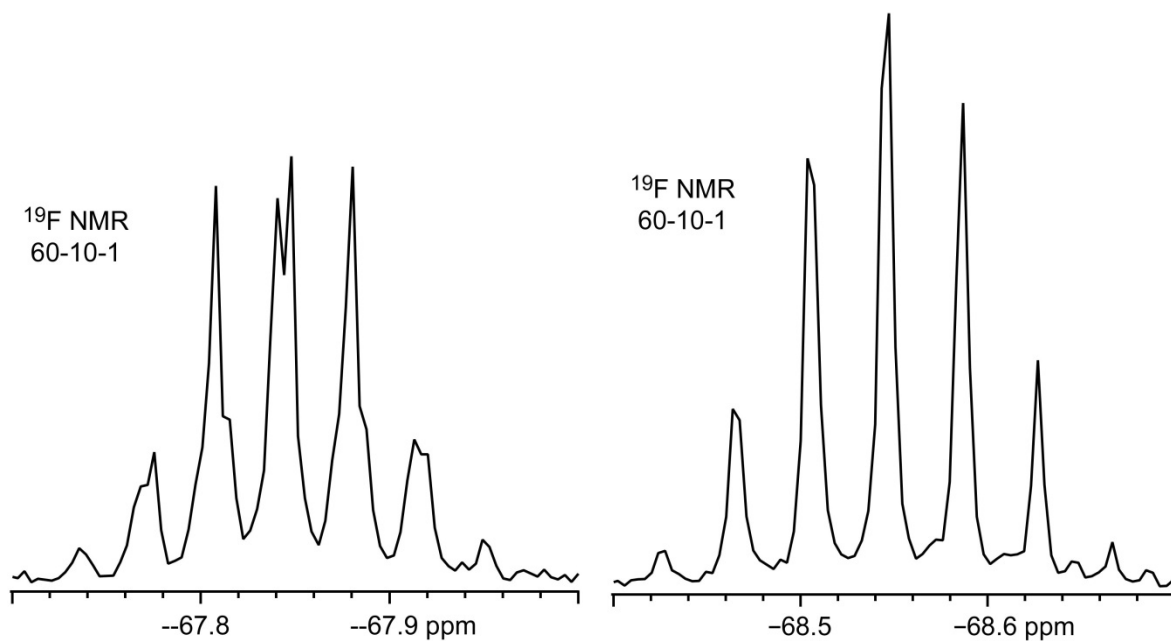


Figure 3.30. Expansions of two of the quartet-of-quartets in the ^{19}F NMR spectrum of 60-10-1. For the quartet-of-quartets on the right, the two J_{FF} values are sufficiently similar that it has the appearance of a 1:6:15:20:15:6:1 septet.

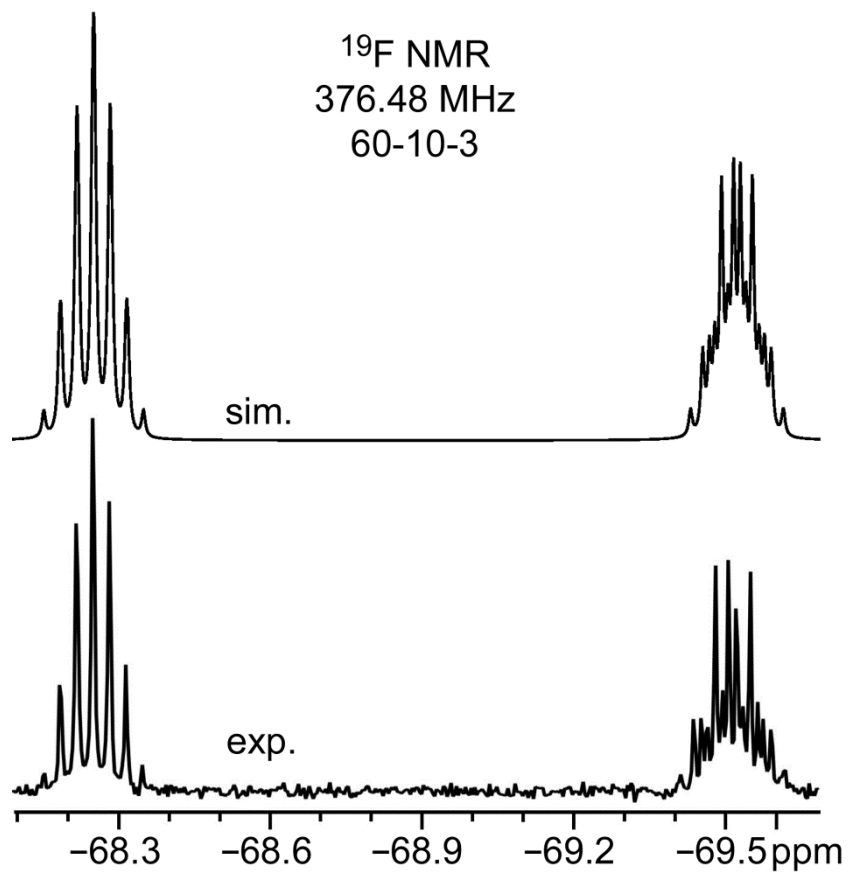


Figure 3.31. Expansion of two of the quartet-of-quartets in the ^{19}F NMR spectrum of 60-10-3. For the quartet-of-quartets on the left, the two J_{FF} values are sufficiently similar that it has the appearance of a 1:6:15:20:15:6:1 septet. It was simulated using the NMR program MNova version 8.1 with two equal J_{FF} values of 11.7 Hz. The simulation of the quartet-of-quartets on the right was made with unequal J_{FF} values, 9 and 14 Hz, and this multiplet is not easily recognizable as a quartet of quartets or an apparent septet.

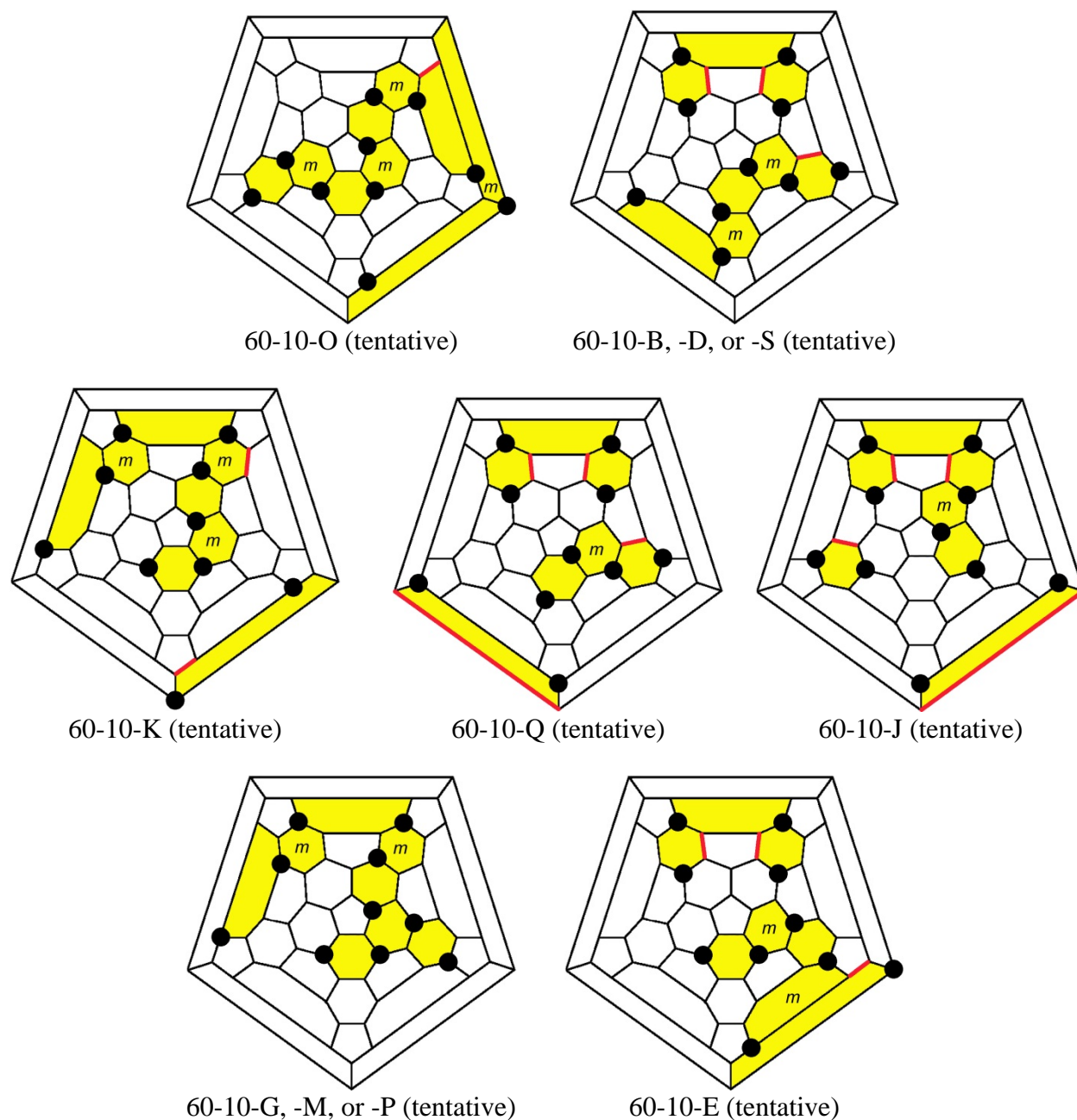


Figure 3.32. Schlegel diagrams of possible addition patterns for some of the 21 new $C_{60}(CF_3)_{10}$ isomers (see Table 3.3). The assignments are based on DFT-predicted relative energies and ^{19}F NMR spectroscopy and are tentative. Non-terminal double bonds in pentagons (*nt*-DBIPs; see text) are highlighted in red. Note that the addition pattern proposed for either 60-10-G, -M, or -P does not have any *nt*-DBIPs.

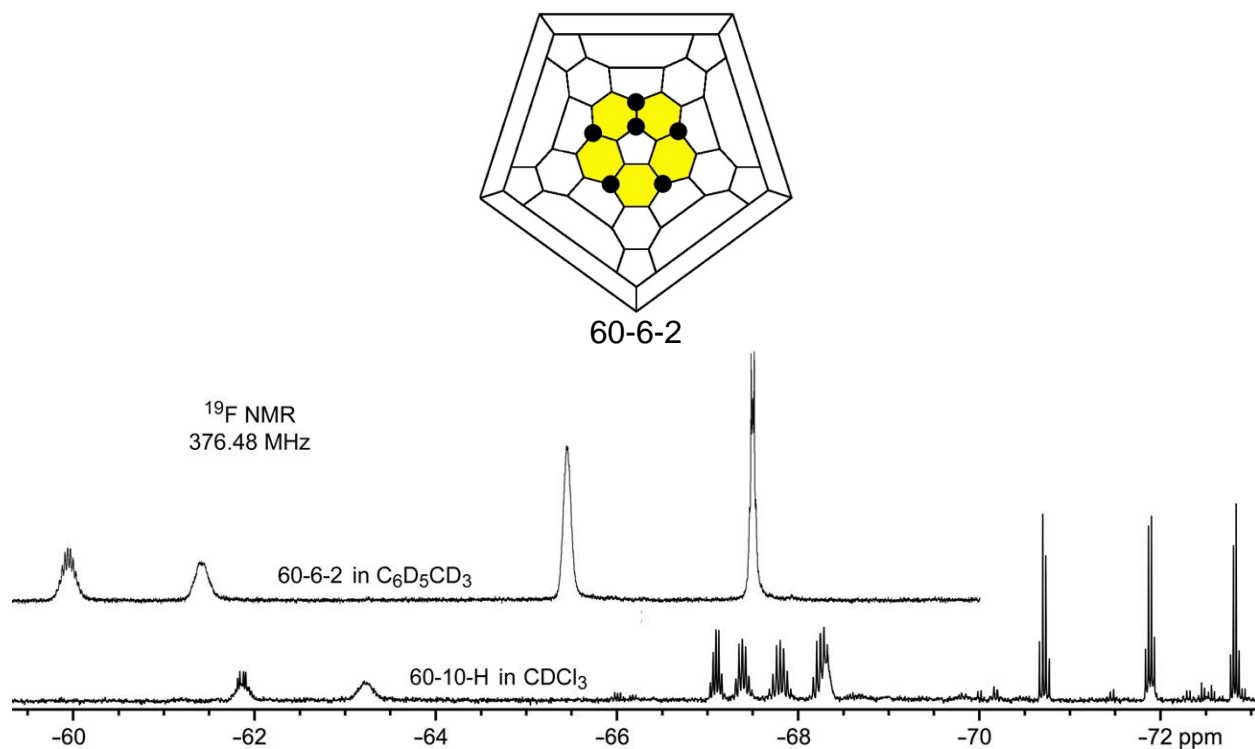


Figure 3.33. (Top) The skew-pentagonal pyramidal (SPP) addition pattern for the six CF₃ groups in C_s-1,6,9,12,15,18-C₆₀(CF₃)₆ (60-6-2; see ref ³⁰) is shown in the Schlegel diagram. (Bottom) The 376.48 MHz ¹⁹F NMR spectra of 60-6-2 in toluene-d₈ (ref 30) and 60-10-H in chloroform-d. Note that δ(¹⁹F) values for fullerene(CF₃)_n derivatives are, in general, ca. 2 ppm higher in chloroform-d than in toluene-d₈. Note also that the presence of 10 multiplets in the spectrum 60-10-H requires that the proposed SPP,*p,p* addition pattern is asymmetric.

patterns of 60-10-3 and 60-10-12, shown as Schlegel diagrams in Figure 3.32, their respective ^{19}F NMR spectra, and the fragment of the structure of 60-10-12 shown in Figure 3.21. Both compounds have a pmp^3mp ribbon (60-10-12) or ribbon fragment (60-10-3) that results in a 1,3- $\text{C}_5(\text{CF}_3)_2$ pentagon. Each CF_3 group on this pentagon has three CF_3 nearest neighbors, and that results in $-\delta$ values lower than 60 ppm. Furthermore, they have rotational conformations (at least in the solid state) that are closer to being eclipsed than to fully staggered, and this results in longer $\text{F}\cdots\text{F}$ distances to their respective $p\text{-C}_6(\text{CF}_3)_2$ hexagon partner and a concomitant smaller $^7J_{\text{FF}}$ value. In 60-10-3, only one of these $p\text{-C}_6(\text{CF}_3)_2$ hexagon partners is a terminal CF_3 group, and its quartet coupling constant is 8.4 Hz, a characteristically small value.^{1,6} In 60-10-12, both $p\text{-C}_6(\text{CF}_3)_2$ hexagon partners are terminal CF_3 groups, so the two quartets with small coupling constants, 8.5 and 8.9 Hz, are assigned to these CF_3 groups. That means that the other two quartets in the 60-10-12 spectrum belong to the isolated $p\text{-C}_6(\text{CF}_3)_2$ hexagon, which could not have been deduced from their multiplet intensities alone because they have different enough chemical shifts and appear to be first-order quartets. To further confirm this, these two quartets have the same J_{FF} value, 12.9 Hz, which is a typical value for isolated $p\text{-C}_6(\text{CF}_3)_2$ hexagons in $\text{C}_{60}(\text{CF}_3)_n$ derivatives.

Experience has shown that the addition patterns of more than 100 structurally characterized fullerene(CF_3) $_n$ derivatives prepared at temperatures exceeding 300 °C, like the 27 60-10's discussed here, have DFT-predicted relative energies within 40 kJ mol^{-1} of one another, and nearly all of them are within the first 30 kJ mol^{-1} .^{5,6,31-34} Some of the DFT-predicted relative energies for 60-10 isomers, calculated by Dr. Alexey A. Popov in 2007 and included in the Supporting Information for ref⁶, are reproduced in Table 3.3. Assuming that the 21 new 60-10 isomers have energies within 30 kJ mol of 60-10-6 (which is predicted to be the most stable isomer), the insights gained by analyzing the ^{19}F NMR spectra have even more predictive power as far as possible addition patterns are concerned.

Seven such predictions are shown as Schlegel diagrams in Figure 3.32. There are only four possible single-ribbon addition patterns for 60-10 isomers consisting of *m*- and *p*- $\text{C}_6(\text{CF}_3)_2$

Table 3.3. DFT-Predicted Relative Energies of C₆₀(CF₃)₁₀ Isomers^a

addition pattern ^b	relative energy, kJ mol ⁻¹	definite or tentative assignment ^c
<i>p</i> ³ <i>mp,pmp</i>	0.00	60-10-6
<i>p</i> ³ <i>mpmpmp</i>	0.06	60-10-2
<i>pmpmpmpmp</i> ^d	1.25	[60-10-O]
<i>p</i> ³ , <i>pmpmp</i> ^d	5.93	[60-10-B, 60-10-D, 60-10-K, or 60-10-S]
<i>pmp</i> ³ <i>mpmp</i>	4.56	60-10-3
C ₂ -(<i>p</i> ³ <i>m</i> ² -loop) ²	7.60	60-10-4
<i>pmpmpmpmp</i>	8.01	60-10-5
<i>p</i> ³ <i>mpmp,p</i>	9.22	60-10-1
<i>pmpmpmp,p</i>	13.57	[60-10-K]
<i>p</i> ³ <i>mp,pmp,p</i>	13.95	[60-10-Q]
<i>p</i> ³ <i>mp,p,p</i> ^d	14.08	[60-10-J]
<i>pmp</i> ³ <i>mp,p</i>	15.41	60-10-12
<i>p</i> ³ <i>mp,pmp</i>	16.03	60-10-8
<i>pmpmpmp,p</i>	17.36	60-10-9
<i>pmpmpmp,p</i>	18.46	60-10-13
<i>p</i> ³ <i>mpmp,p</i>	20.55	60-10-10
1,3,5-C ₆ (CF ₃) ₃ - <i>pmpmp,p,p</i> ^{d,e}	22.61	[60-10-G, 60-10-M, or 60-10-P]
<i>p</i> ³ , <i>pmpmp</i> ^{d,f}	28.40	[60-10-E]
<i>p</i> ³ <i>mp,p,p</i>	29.60	60-10-11

^a Calculated by Dr. Alexey A. Popov and published, in part, in the Supporting Information for ref 6. See Table 3.1 for a key to the abbreviations. ^b Note that there can be different addition patterns with the same abbreviation. For example, there are two *pmpmpmpmp* addition patterns, and many possible *p*³*mpmp,p* addition patterns (i.e., the isolated *p*-C₆(CF₃)₂ hexagon can occupy several different positions relative to the *p*³*mpmp* ribbon; compare the Schlegel diagrams for 60-10-1 and 60-10-10 in Figure 3.2). All addition patterns have C₁ symmetry except as noted. ^c Definite assignments were made by X-ray crystallography (see Table 3.1) or, in the case of 60-10-1, on the basis of ¹⁹F NMR spectroscopy, cyclic voltammetry, and its DFT-predicted relative energy and *E*(LUMO) value. Tentative assignments based on relative energy and ¹⁹F NMR spectroscopy are shown in square brackets. ^d See Figure 3.32 for a Schlegel diagram of this addition pattern. ^e This addition pattern includes three CF₃ groups on one hexagon and does not fit the abbreviation scheme used here. ^f This addition pattern is unusual because the two ribbons are connected with a 1,3-C₅(CF₃)₂ pentagon, and one of the CF₃ groups on the pentagon has three CF₃ nearest neighbors.

hexagons (i.e., with no 1,3-C₅(CF₃)₂ pentagons), and three of them are accounted for with the compounds 60-10-2, 60-10-3, and 60-10-5. The fourth is the 1.25 kJ mol⁻¹ *pmpmpmpmp* ribbon, and the most likely candidate for this addition pattern is 60-10-O. Another low-energy structure that was not assigned to a 60-10 isomer before this work is the 5.93 kJ mol⁻¹ two-ribbon addition pattern *p*³*pmpmp*, and spectra for 60-10-B, -D, and -S, with four quartets having different *J*_{FF} values, are consistent with this structure (cf. the two-ribbon addition patterns of 60-10-6 and 60-10-8). The four-quartet spectrum of 60-10-K indicates a ribbon of eight CF₃ groups and an isolated *p*-C₆(CF₃)₂ hexagon, and this compound may have the as-yet-unassigned 13.57 kJ mol⁻¹ *pmpmpmp,p* addition pattern. The spectrum of 60-10-Q exhibits six quartets. The two that are nearly isochronous, at δ -73.5, are due to an isolated *p*-C₆(CF₃)₂ hexagon. The other four have different *J*_{FF} values, 15.0, 14.0, 11.4, and 12.3 Hz from left to right. Therefore, 60-10-Q must have a two-ribbon-plus-an-isolated-hexagon addition pattern. Dr. Popov's DFT calculations predicted a 13.95 kJ mol⁻¹ *p*³*mp,pmp,p* addition pattern, and it is tentatively assigned to this isomer. New isomer 60-10-J exhibits an ¹⁹F NMR spectrum with six quartets, but in this case two pairs with equal *J*_{FF} values represent two isolated *p*-C₆(CF₃)₂ hexagons. There is a missing 14.08 kJ mol⁻¹ *p*³*mp,p,p* addition pattern that may be the structure of this new 60-10 (note that 60-10-11 has a higher-energy version of this addition pattern). An interesting 22.61 kJ mol⁻¹ addition pattern contains a 1,3,5-C₆(CF₃)₃ hexagon and should give rise to three quartets (an *odd* number in both senses of the word) with different *J*_{FF} values. Therefore, one of the three compounds 60-10-G, -M, or -P may have this particular structure. There is another interesting structure that is predicted to have a relative energy of 28.40 kJ mol⁻¹. It consists of a 1,3-C₅(CF₃)₂ pentagon joining *p*³ and *pmpmp* ribbons, resulting in a situation in which only one CF₃ group on that pentagon has three nearest neighbor CF₃ groups. The spectrum of 60-10-E, with only one multiplet that has a -δ value lower than 60, is consistent with such a situation. Therefore, this addition pattern, the lowest-energy structure consistent with the spectrum of 60-10-E, is tentatively assigned to this compound. Note that the DFT-predicted relative energy of 29.60 kJ mol⁻¹ for the *p*³*mp,p,p* addition pattern proven by X-ray crystallography for 60-10-11

demonstrates that 60-10 isomers with energies this high are real possibilities as products of the high-temperature reactions used to form the 21 new 60-10's.

Finally, the ^{19}F NMR spectrum of 60-10-H is unique in the following way. The $-\delta$ values of 61.8 and 63.2 for the two very broad multiplets are too high to be attributed to CF_3 groups on a 1,3- $\text{C}_5(\text{CF}_3)_2$ pentagon with three nearest CF_3 neighbors. The shapes and chemical shifts of these multiplets are reminiscent of the spectrum of an isomer of $\text{C}_{60}(\text{CF}_3)_6$ that has the so-called skew pentagonal pyramid structure shown as a Schlegel diagram in Figure 3.33. Therefore, it is possible that 60-10-H has an addition pattern with at least one 1,2,4- $\text{C}_6(\text{CF}_3)_3$ hexagon, and the two broad multiplets are due to the *ortho* pair of CF_3 groups. No 60-10 addition patterns of this type have been calculated to date, so it is not possible to know how stable they might be. Note that the structure of 60-10-H must also be consistent with three quartets with different coupling constants (14.2, 12.3, and 11.8 Hz, from left to right), requiring three terminal CF_3 groups.

3.1.6. Electrochemical Study of New 60-10's. As discussed in the Background to this section, reduction potentials of 60-10 isomers, with their unprecedented large range of 0.50 V, led to the discovery that, more than anything else, non-terminal double bonds in pentagons (*nt*-DBIPs) determine the position, shape, and energy of the LUMO, the most important orbital of a fullerene derivative as far as its electron-acceptor properties are concerned. For this reason, cyclic voltammograms were recorded by the author for as many of the new 60-10's as possible given the limitations imposed by solubility and the availability of a sufficient amount of pure compound.

It is generally the case that cyclic voltammograms (CVs) recorded in relatively low-dielectric solvents, such as 1,2-dichlorobenzene (*o*DCB; $\epsilon = 9.9$) and dichloromethane (DCM; $\epsilon = 8.9$), do not exhibit truly reversible, or Nernstian, behavior.³⁵ Instead, the faradaic response is superimposed on an approximately constant charging current, making it difficult to measure reduction or re-oxidation peak potentials (usually denoted as E_{pc} and E_{pa} , respectively) and peak

currents (i_{pc} and i_{pa} , respectively) from an uncorrected "baseline."³⁵ For this reason, half-wave potentials ($(E_{pc} + E_{pa})/2$), known as $E_{1/2}$ values, are measured instead of E^0 values, and successive one-electron reductions are referred to as quasireversible as long as i_{pc} and i_{pa} are approximately equal and $|E_{pc} - E_{pa}| \leq 200$ mV.³⁵ However, following common usage, and for convenience, reduction/re-oxidation processes that behave in this way will be referred to as reversible. Another issue with nonaqueous cyclic voltammetry is that the internal resistance in the electrochemical cell can be high, also because of the low dielectric medium, resulting in a so-called iR drop and the concomitant potential shift from the "true" potential at which current is being measured. The magnitude of the potential shift depends, in part, on the distance between the electrodes, which is not always possible to keep constant from one experiment to the next. In addition, stable reference electrodes that can be used under strictly anhydrous conditions are generally not available. The standard way to overcome these problems,³⁶ and the one that has been recommended by the IUPAC,³⁷ is to use a wire, either silver or platinum, as the "reference" electrode and, as soon as a CV is recorded, to add a small amount of ferrocene (FeCp₂; bis(η^5 -cyclopentadienyl)iron(II)) to the solution and re-record the CV. In this way, the Fe(Cp)₂⁺⁰ couple acts as an electrochemical internal standard. The $E_{1/2}$ value for the first reduction of C₆₀ in *o*DCB (i.e., $E_{1/2}(0/-)$) vs. internal Fe(Cp)₂⁺⁰ was determined to be $-1.08(1)$ V (this value was re-determined periodically). It was also determined that E_{pc} for the reduction of C₆₀ was $-1.08(1)$ V vs. E_{pc} for the reduction of Fe(Cp)₂⁺. Potentials for 60-10 compounds measured vs. $E_{1/2}$ or E_{pc} for Fe(Cp)₂⁺⁰ in *o*DCB were converted to potentials vs. C₆₀^{0/-} by adding 1.08 V to the measured value.

Many, but not all, of the new 60-10 isomers studied by cyclic voltammetry in this work had reversible first reductions (and some had reversible second and third reductions). However, some had irreversible first reductions. The CVs are shown in Figure 3.34. The $E_{1/2}$ values for reversible reductions and the E_{pc} values for both the reversible and irreversible first reductions for all compounds studied by CV are listed in Table 3.4. Note that the solvent used for the CV experiments was 1,2-dichlorobenzene (*o*DCB) instead of dichloromethane (DCM), the solvent

used to study the six previously-known 60-10 isomers.⁶ This was done because some of the new isomers were more soluble in *o*DCB than in DCM. Note also that five of the six previously-known isomers were also studied in *o*DCB in this work for comparison (however, highly purified samples of 60-10-4 were found to be insufficiently soluble in *o*DCB for this purpose). Finally, note that the electrolyte used in this work was N(*n*-Bu)₄PF₆, not N(*n*-Bu)₄BF₄ as in the previous study, because it was found that the addition of N(*n*-Bu)₄BF₄ to some of the new 60-10's dissolved in *o*DCB resulted in a color change and probably a chemical transformation (this was not pursued further).

Although the comparison of E_{pc} values for reversible and irreversible reductions is not always justified, a plot of $E_{1/2}(0/-)$ vs. E_{pc} , shown in Figure 3.35, indicates that it may be justified for this particular set of compounds. That is, the correlation of the two electrochemical measurements for 11 60-10's and for C₆₀ was very close to 1:1 with only a modest offset of 0.008

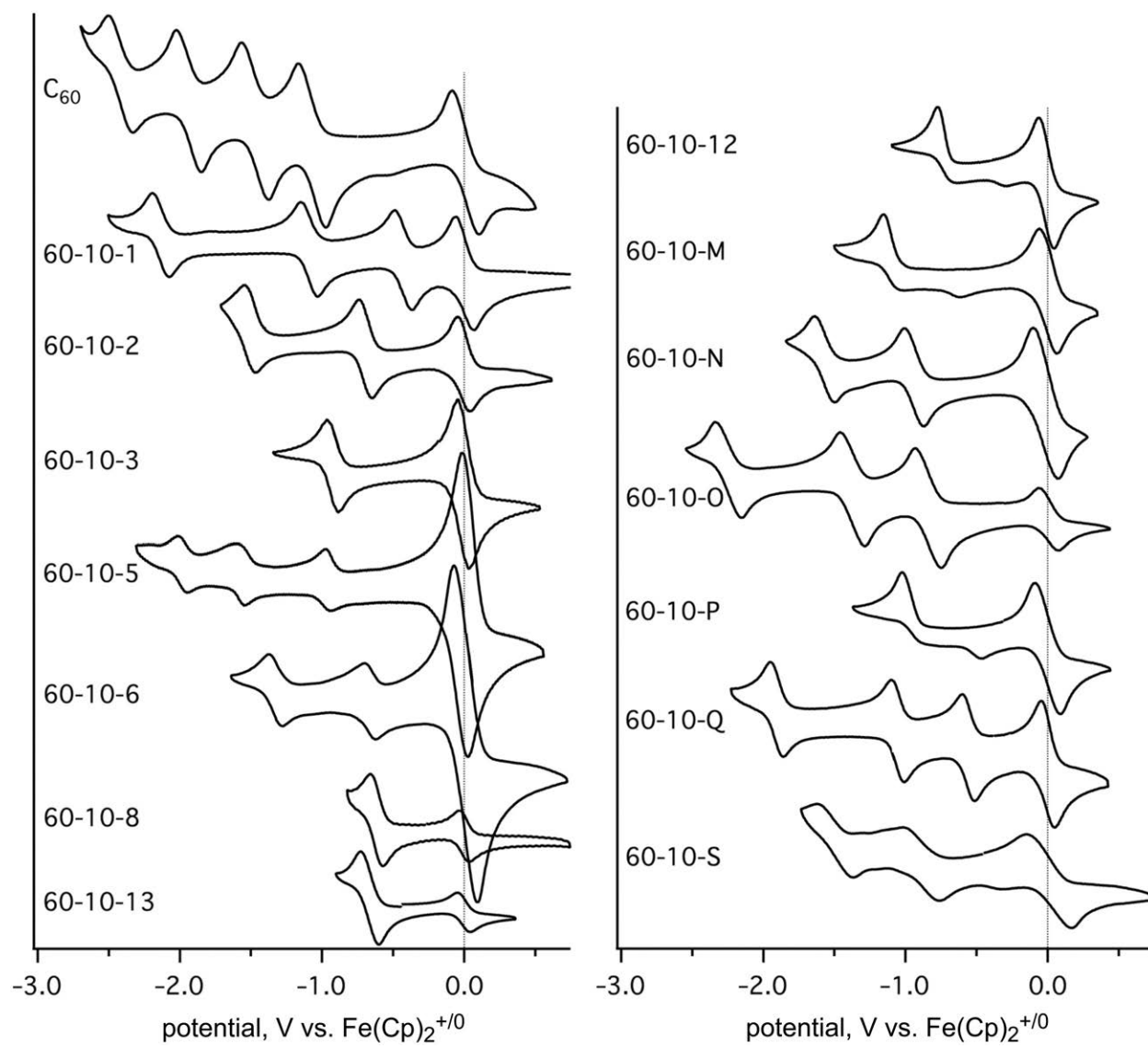


Figure 3.34. Cyclic voltammograms of selected 60-10 isomers (0.1 M $N(n\text{-Bu})_4\text{PF}_6$ in 1,2-dichlorobenzene, $\text{Fe}(\text{Cp})_2$ internal standard ($E_{1/2}(\text{C}_{60}^{0/-}) = -1.08$ V vs. $\text{Fe}(\text{Cp})_2^{+/0}$), platinum working and counter electrodes, silver-wire quasi-reference electrode).

Table 3.4. Electrochemical Results for C₆₀(CF₃)₁₀ Isomers^a

compd	potentials, V vs. C ₆₀ ^{0/-}			
	<i>E</i> _{1/2} (0/-)	<i>E</i> _{pc} (0/-)	<i>E</i> _{1/2} (-/2-)	<i>E</i> _{1/2} (2-/3-)
C ₆₀	0.00 {0.00}	0.00	-0.40 {-0.40}	-0.86 {-0.84}
60-10-1	0.65 {0.57}	0.66	-0.02	-1.06
60-10-2	0.38 {0.32}	0.38	-0.44	irrev. {irrev.}
60-10-3	0.16 {0.17}	0.16	irrev. {-0.44}	{irrev.}
60-10-5	0.12 {0.12}	0.13	-0.50 {-0.46}	-0.91 {-0.90}
60-10-6	0.41 {0.33}	0.45	-0.26 {-0.34}	irrev. {irrev.}
60-10-8	0.47	0.47	-0.19	-0.81
60-10-12	irrev.	0.37		
60-10-13	0.42	0.40	-0.12	-1.01
60-10-M	irrev.	-0.02		
60-10-N	0.16	0.18	-0.47	irrev.
60-10-O	0.20	0.19	-0.28	-1.14
60-10-P	irrev.	0.15		
60-10-Q	0.52	0.52	-0.01	-0.83
60-10-S	0.19	0.22	irrev.	

^a Potentials were measured in 1,2-C₆H₄Cl₂ containing 0.1 M N(*n*-Bu)₄PF₆ vs. the internal standard Fe(Cp)₂ (*E*_{1/2}(Fe(Cp)₂⁺⁰) = 1.08 V vs. C₆₀^{0/-}); irrev. = irreversible. Potentials enclosed in braces were measured in CH₂Cl₂ containing 0.1 M N(*n*-Bu)₄BF₄ and were previously reported in ref. ⁶. The uncertainty for all potential measurements is ±0.01 V.

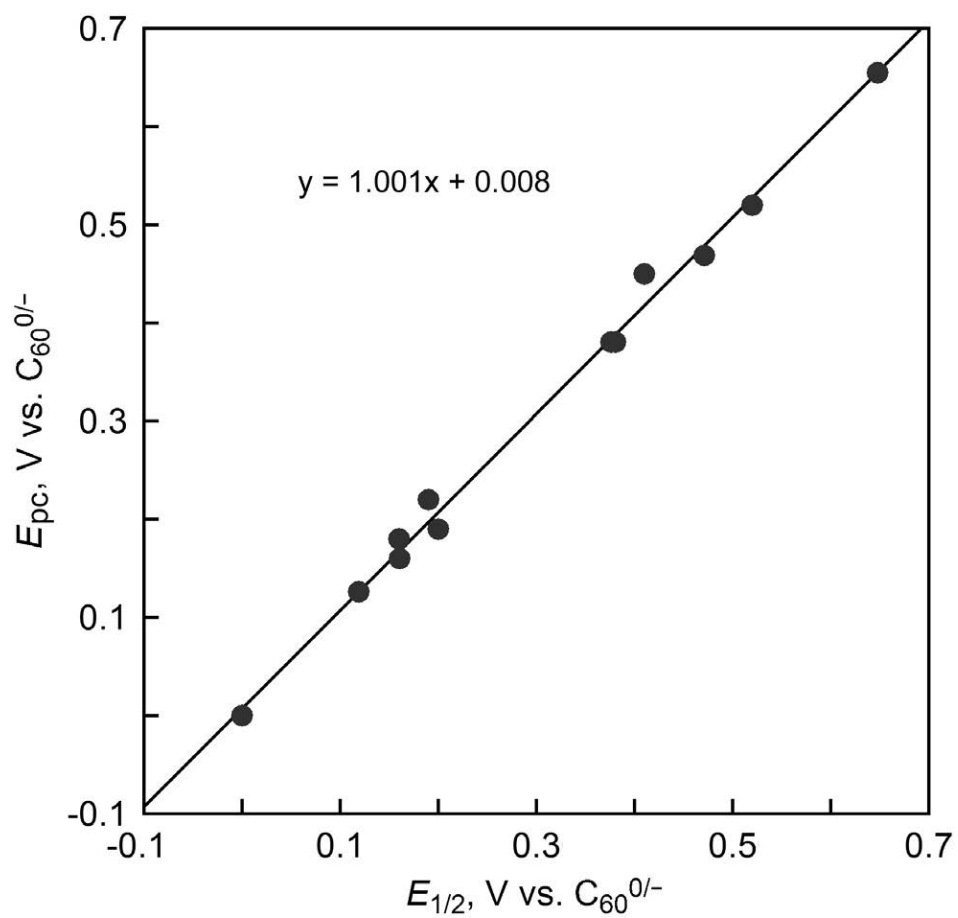


Figure 3.35. Plot of cyclic voltammetry $E_{1/2}(0/-)$ vs. $E_{pc}(0/-)$ potentials for C_{60} and 12 of the 60-10 isomers listed in Table 3.4. The correlation is almost exactly 1:1, with only an 8 mV offset, which is smaller than the ± 10 mV uncertainty in the measured potentials. Note that the ± 10 mV error bars are smaller than the diameter of the data points on the plot.

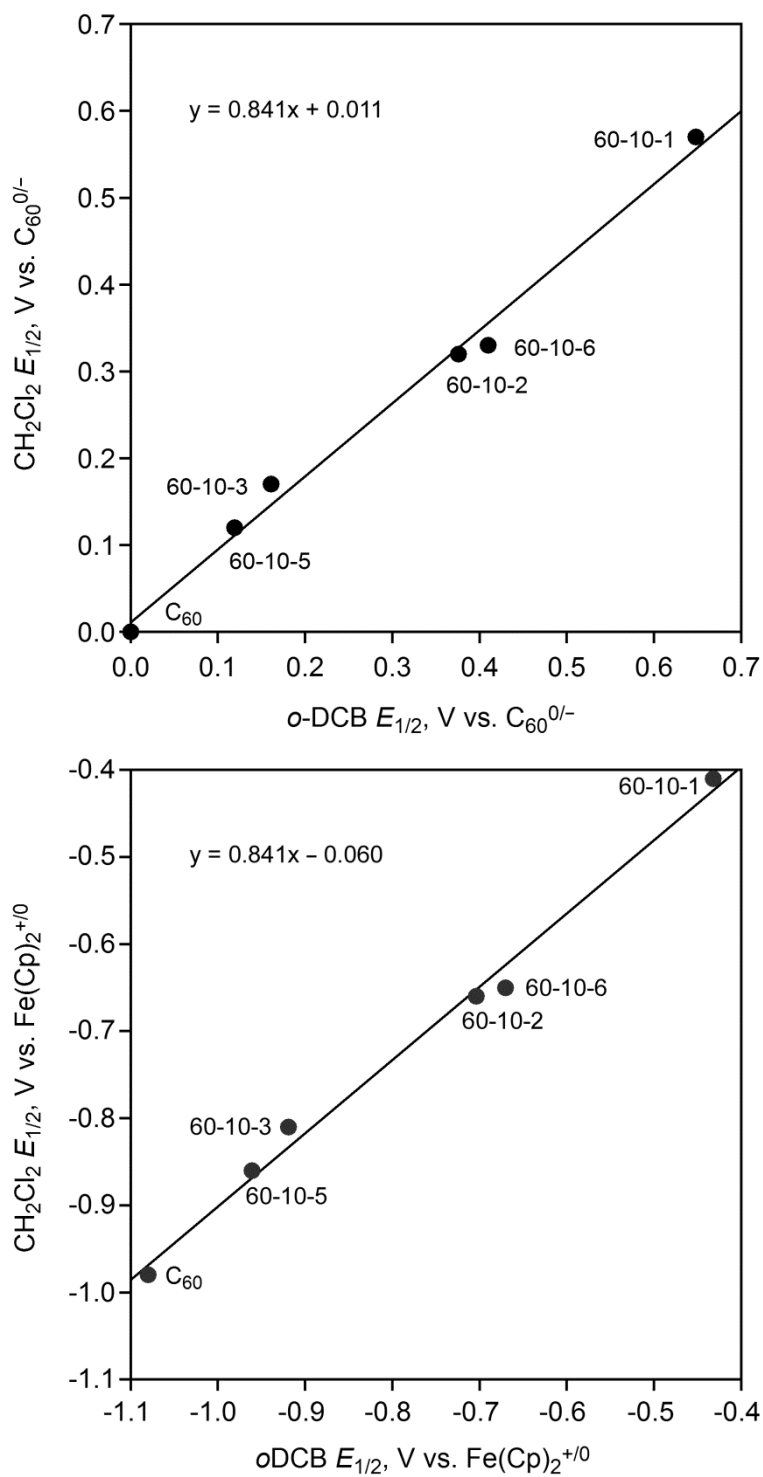


Figure 3.36. Plots of $E_{1/2}$ values recorded in CH_2Cl_2 vs. $E_{1/2}$ values recorded in $1,2\text{-C}_6\text{H}_4\text{Cl}_2$ for C_{60} and six 60-10 isomers. The difference between the two plots are that the values in the upper plot are referenced to $E_{1/2}(\text{C}_{60}^{0/-})$ and the values in the lower plot to the $E_{1/2}(\text{Fe(Cp)}_2^{+/0})$.

V, which is smaller than the ± 0.01 V uncertainty in the individual potential measurements. This will allow two additional compounds with irreversible first reductions, 60-10-12 and 60-10-M, to be included in the discussion of electron affinities and LUMO energies in the next section.

An interesting observation was made when the $E_{1/2}(0/-)$ values measured in *o*DCB in this work for the previously known 60-10 isomers were compared with the previously reported $E_{1/2}(0/-)$ values measured in DCM.⁶ The plots in Figure 3.36 show this comparison in two ways. Consider the upper plot, in which the potentials are shown vs. the $C_{60}^{0/-}$ $E_{1/2}$ value. The spread of $E_{1/2}$ values, from C_{60} , which is the hardest to reduce of these six compounds, to 60-10-1, the easiest to reduce, is 0.57 V in DCM but 0.65 V in *o*DCB. The difference, 80 mV, is not insignificant. This difference is equivalent to changing an equilibrium constant by a factor of 20 at 25 °C. Furthermore, there is a linear relationship between $E_{1/2}$ in DCM and $E_{1/2}$ in *o*DCB, so that the difference in potentials appears to increase from C_{60} to 60-10-1. The slope of the linear least-squares fit to the data is 0.84, which means that the difference in electron-accepting properties of these compounds is attenuated in DCM relative to *o*DCB. But is this because the electron-accepting ability of 60-10-1 is reduced in DCM relative to *o*DCB or because the electron-accepting ability of C_{60} is increased in DCM relative to *o*DCB?

Now consider the lower plot, in which the potentials are shown vs. the $Fe(Cp)_2^{+/0}$ $E_{1/2}$ value (ferrocene was the internal standard used in ref⁶ and in this work). Relative to the ferrocene redox couple, 60-10-1 has the same electron-accepting ability in the two solvents (i.e., its $E_{1/2}$ value is ca. -0.4 V in both solvents). The parent fullerene C_{60} is a better electron acceptor in DCM than in *o*DCM with respect to the ferrocene internal standard potential. Similar results for the electrochemical behavior of C_{60} in a variety of solvents were summarized in an important review by Reed and Bolskar,³⁸ but the observations just described for the relative redox potentials of a series of fullerene compounds, five of which are isomers, is unprecedented. In other words, it was known that the potential of $C_{60}^{0/-}$ redox couple was solvent dependent relative to the $Fe(Cp)_2^{+/0}$ $E_{1/2}$ value, but it was not known that the solvent dependence varied from one fullerene derivative to another, and did so linearly.

The electrochemical community has generally regarded the standard electrode potential of the $\text{Fe}(\text{Cp})_2^{+/0}$ couple to be solvent-independent.^{36,37,39} The metal center, which undergoes the formal change in oxidation state from 2+ to 3+ when ferrocene is oxidized, is believed to be shielded from specific solvent effects by the large cyclopentadienyl ligands. With this in mind, decamethylferrocene ($\text{Fe}(\text{Cp}^*)_2$) was proposed as an even better internal standard than ferrocene because its ligands are larger.³⁹ In fact, the difference in $E_{1/2}$ values for the two ferrocene compounds did show a solvent dependence, but importantly, there was no measureable difference between DCM and *o*DCB.

Therefore, the differences observed for the fullerenes cannot be explained by a solvation energy difference for the internal standard relative to which the fullerene potentials were measured. It is not clear why the difference in the spread of $E_{1/2}$ values for the six fullerene compounds is solvent dependent, nor is it clear why the differences should change linearly. It may be due to differential changes in solvation energies or it may be due to differential changes in ion-pairing energies, since the electrolyte anion was BF_4^- in DCM (ref⁶) and PF_6^- in *o*DCB (this work). Although the dielectric constants of the two solvents are essentially the same (see above), specific solvation effects, not bulk dielectric-continuum effects, may be the critical factor. This certainly deserves further study.

3.1.7. Links Between Addition Patterns, 60-10 $E_{1/2}$ Values, Electron Affinities, and DFT-Predicted LUMOs and LUMO Energies. There were two reasons for spending the time and effort to isolate and characterize so many new isomers of $\text{C}_{60}(\text{CF}_3)_{10}$. One reason was so that their different physicochemical properties might find use in one or another type of practical application such as organic photovoltaics, molecular electronics, fluorescence microscopy, etc. The other reason was the expectation that new insights into the physicochemical effects of changing the addition pattern of a fullerene derivative. As a result of the work described in this chapter, there are now 27 isomers of the composition $\text{C}_{60}(\text{CF}_3)_{10}$. In 11 cases, the exact placement of the CF_3 groups is known from X-ray crystallography, including six of the 21 new

isomers. Fluorine-19 NMR spectra are now available for all 27 isomers, 21 of which are the result of this work, and in many cases the spectra greatly narrow down the possible addition patterns for particular isomers. This collection of 60-10 isomers not only far exceeds the number of separable and relatively pure isomers of any other fullerene composition (i.e., pure enough to distinguish and analyze individual spectral properties), it almost certainly exceeds the number of separable and relatively pure isomers of *any* molecular (i.e., stoichiometric) composition.

Table 3.5 lists the $E_{1/2}(0/-)$ and/or $E_{pc}(0/-)$ for the new isomers studied by cyclic voltammetry, low-temperature gas-phase electron affinities (measured at Pacific Northwest National Lab by Dr. Xue-Bin Wang and co-workers using samples provided by the author), and the results of DFT calculations (using the PBE functional⁴⁰) performed by Dr. Alexey A. Popov at the Leibniz Institute for Solid-State and Materials Research Dresden (energies of the LUMO for compounds with known addition patterns). Electronic files provided by Dr. Popov were used to make the LUMO diagrams shown in the figures below.

The addition patterns of six of the new isomers, 60-10-8, -9, -10, -11, -12, and -13, have been established beyond doubt by X-ray crystallography. They are shown as Schlegel diagrams in Figures 3.19 and 3.20. The links between fullerene derivative addition patterns, *nt*-DBIPs, and measured and calculated electron-accepting properties (i.e., experimental and DFT-predicted

Table 3.5. First Reduction Potentials, Gas-Phase Electron Affinities, and DFT-Predicted LUMO Energies for C₆₀(CF₃)₁₀ Isomers^a

compd	$E_{1/2}(0/-)$ [$E_{pc}(0/-)$], V vs. C ₆₀ ^{0/-}	EA, eV ^b	DFT $E(\text{LUMO})$, eV ^c
C ₆₀	0.00	2.684(8)	-4.379
60-10-1	0.65	3.61(1)	-5.129
60-10-2	0.38	3.36 (1)	-4.894
60-10-3	0.16	3.17(2)	-4.754
60-10-4			-4.529
60-10-5	0.12		-4.638
60-10-6	0.41	3.40(2)	-4.922
60-10-8	0.47	3.45(1)	-4.983
60-10-12	[0.37]	3.32(1)	-4.867
60-10-13	0.42		-4.938
60-10-C		3.51(1)	
60-10-H		3.44(2)	
60-10-K		4.09(1)	
60-10-M	[-0.02]	3.01(1)	
60-10-O	0.20		
60-10-P	[0.15]		
60-10-Q	0.52		

^a Uncertainties for electrochemical measurements are ± 0.01 V. ^b EA = gas phase electron affinity. The uncertainties shown in parentheses are in the least significant figure. These values were measured by Dr. Xue-Bin Wang at Pacific Northwest National Lab. Samples of the new 60-10 isomers for these experiments were prepared by the author. See the Experimental Section for more details. ^c Calculated by Dr. Alexey A. Popov.

$E_{1/2}(0/-)$ values and DFT-predicted LUMO energies ($E(\text{LUMO})$'s), respectively) established in 2007/2008 for $\text{C}_{60,70}(\text{CF}_3)_n$ derivatives^{6,31} are completely supported by the results reported in this dissertation. Those links, and their use to predict the electronic properties of some of the new 60-10 isomers with tentative addition patterns (i.e., those shown as Schlegel diagrams in Figure 3.32) but not yet characterized by X-ray crystallography, will be discussed in the remainder of this chapter. Note, however, that the underlying theoretical explanation for the association of a fullerene derivative's LUMO at cage C atoms that are close to or themselves comprise *nt*-DBIPs has not been published and is beyond the scope of the research reported herein.

A comparison of the addition patterns of 60-10-8 and 60-10-6 shows that they have two *nt*-DBIPs in common in the p^3 portion of their respective addition patterns. These *nt*-DBIPs are in conjugation and, together with a 6:6 double bond, form a fulvene-like moiety on the surface of the cages. The compound 60-6-1, with a p^3mp , has the same fulvene moiety with two *nt*-DBIPs.⁶ This fulvene moieties "anchor" the LUMO to that portion of each molecule, as shown in Figure 3.37. The remaining *nt*-DBIP in each molecule is remote from the fulvene and does not appear to influence the location or cage-C atom contributions to the LUMOs, unlike the situation in 60-10-1, where the third *nt*-DBIP is close to the fulvene moiety and produces a more delocalized LUMO. In harmony with the similar remote location of the third *nt*-DBIP and similarly shaped LUMO for 60-10-8 and 60-10-6, their $E(\text{LUMO})$, $E_{1/2}(0/-)$, and gas-phase EA values are all very similar, -4.983 eV, $0.47(1)$ V, and $3.45(1)$ eV, respectively, for 60-10-8 and -4.922 eV, $0.41(1)$ V, and $3.40(1)$ eV, respectively, for 60-10-6. However, note that 60-10-1, with its more extensively delocalized LUMO, is a significantly better electron acceptor. The corresponding three values for this compound are -5.129 eV, $0.65(1)$ V, and $3.61(1)$ eV, respectively.

The isolated fulvene moiety in 60-10-3, a key to its much poorer electron accepting properties, was discussed above (see Figure 3.3). Its $E(\text{LUMO})$, $E_{1/2}(0/-)$, and gas-phase EA are -4.754 eV, $0.16(1)$ V, and $3.17(2)$ eV, respectively. New isomer 60-10-12 also has an isolated fulvene moiety, but in addition it has another *nt*-DBIP that contributes to its LUMO, as

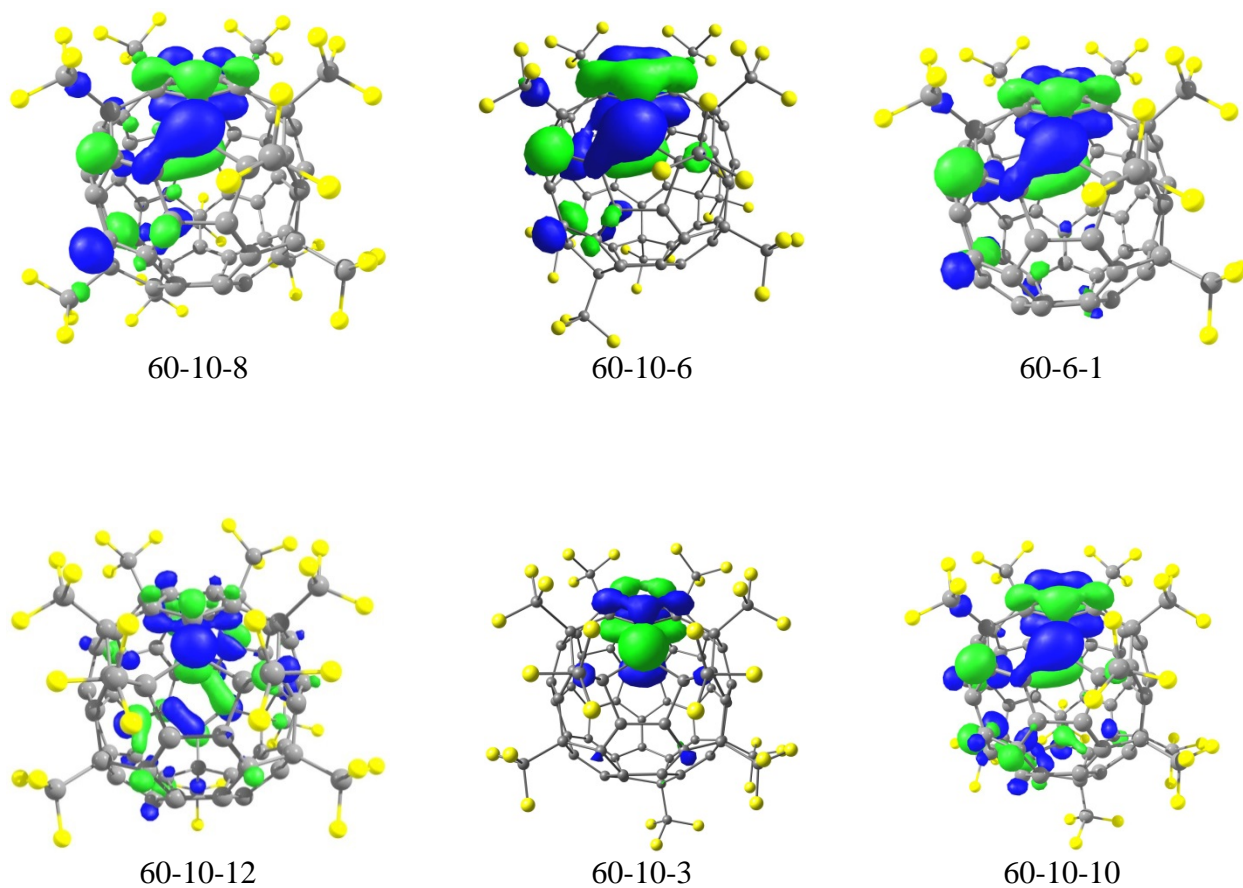


Figure 3.37. (Top) Comparison of the DFT-predicted LUMOs of new compound 60-10-8 with the previously reported compounds 60-10-12 and 60-6-1. (Bottom) Comparison of the DFT-predicted LUMOs of new compounds 60-10-12 and 60-10-10 with the previously reported compound 60-10-3.

shown in Figure 3.37, unlike the situation in 60-10-3. Therefore, it comes as no surprise that 60-10-12 is a better electron acceptor (-4.867 eV, 0.37 V, and $3.32(1)$ eV) than 60-10-3. Note that the third *nt*-DBIP in 60-10-12 contributes to the LUMO but the third *nt*-DBIP in 60-10-6 does not, in spite of the fact that the location of the third *nt*-DBIP relative to the fulvene moieties is exactly the same in both compounds.

The DFT-predicted $E(\text{LUMO})$ for 60-10-11 is -5.090 eV, only 39 meV higher than 60-10-1. Based on this, it should be the second-best electron acceptor of the structurally characterized 60-10 isomers, and that prediction will be tested when more compound becomes available in the future and CV and EA measurements are made. It is easy to see why this compound is predicted to be such a good electron acceptor. Its addition pattern gives rise to four *nt*-DBIPs, three of which are spatially similar to the three *nt*-DBIPs in 60-10-1. These three *nt*-DBIPs in 60-10-11 combine to form a very delocalized LUMO, as shown in Figure 3.38. Interestingly, the fourth *nt*-DBIP in 60-10-11, which is spatially closer to the fulvene *nt*-DBIPs than the third but is actually more remote than the third as far as π conjugation is concerned, does not contribute to the LUMO. For this reason, Dr. Popov was asked to calculate the LUMO+1 orbital for 60-10-11. It is also shown in Figure 3.38, and clearly shows that this orbital is "anchored" to the fourth *nt*-DBIP. This is a satisfying result as far as the link between *nt*-DBIPs and a 60-10's LUMO (and now LUMO+1) is concerned.

The links can now be applied to some of the new 60-10's with tentative addition patterns (see Figure 3.32). These were picked on the basis of their relative energies and their ^{19}F NMR spectra (Dr. Popov has not calculated LUMO figure files for these addition patterns, only their relative energies). The tentative addition pattern for 60-10-O has only one *nt*-DBIP, and its $E_{1/2}$ value is relatively low, only $0.20(1)$ V vs. $\text{C}_{60}^{0/-}$, as expected. The tentative addition pattern for either 60-10-B, 60-10-D, or 60-10-S has three *nt*-DBIPs, two in the fulvene moiety and the third only three double bonds away. As such, this addition pattern should belong to a very good electron acceptor, and on that basis, isomer 60-10-S can be ruled out because its $E_{1/2}$ value is only 0.19 V.

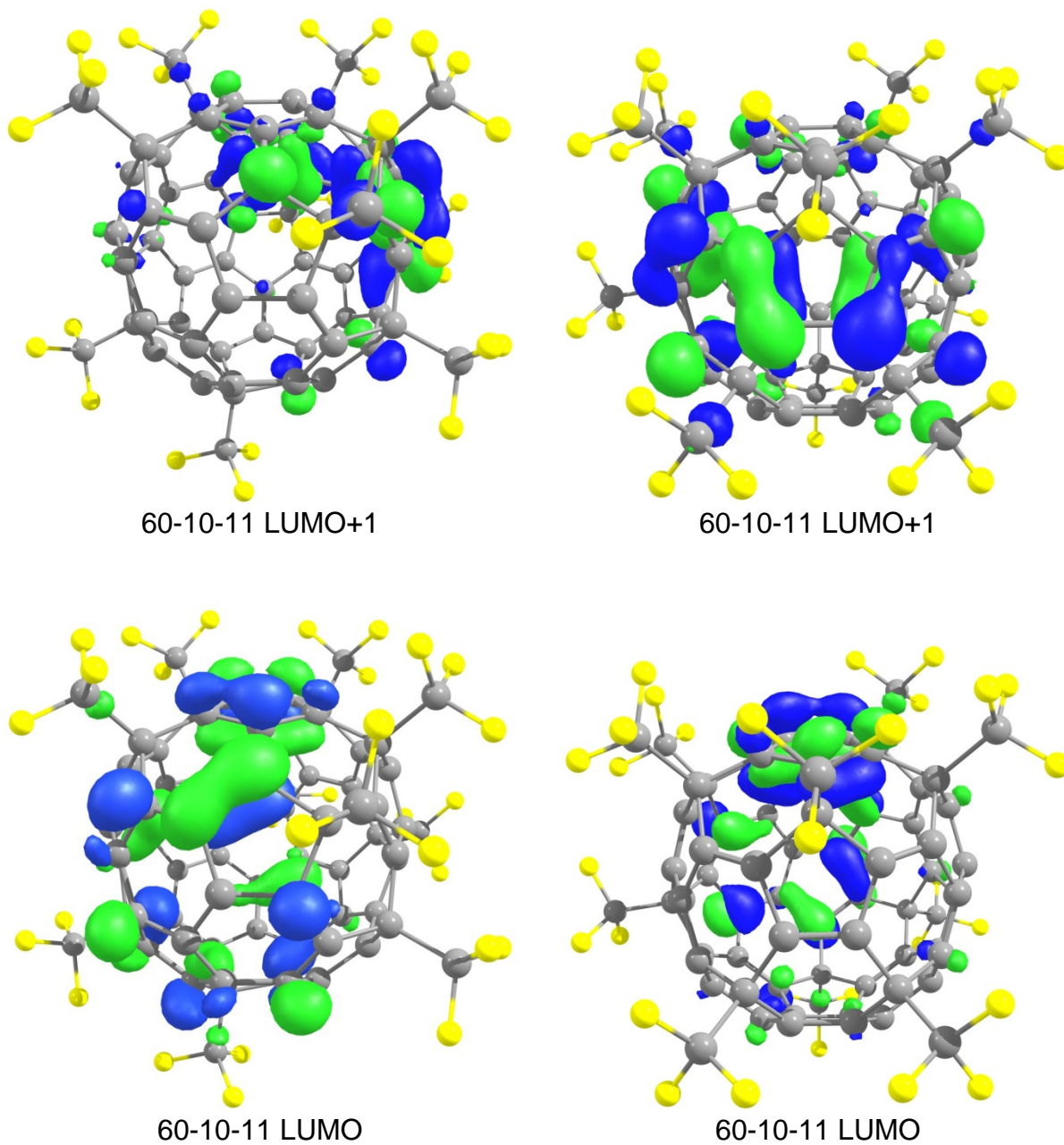


Figure 3.38. Drawings of two orientations of the LUMO and LUMO+1 for isomer 60-10-11. These drawings are based on DFT calculations by Dr. Alexey A. Popov.

This addition pattern is no longer a viable possibility for 60-10-S. When CV and EA measurements are made for 60-10-B and 60-10-D, it may be possible to rule out one or the other in a similar way. The addition pattern tentatively assigned to 60-10-K based on its ^{19}F NMR spectrum can also be ruled out for this compound, since it has only one *nt*-DBIP but its gas-phase EA, at 4.09(1) eV, is even higher than for 60-10-1. Isomer 60-10-Q was tentatively assigned an addition pattern with four *nt*-DBIPs that would make this compound a strong electron acceptor, and this is in harmony with its $E_{1/2}$ value of 0.52 V. Finally, isomers 60-10-M and 60-10-P are poor electron acceptors ($E_{1/2}$ values of -0.02 and 0.15 V, respectively), so they are still reasonable candidates for their tentatively assigned addition pattern, which has no *nt*-DBIPs.

3.2. Synthesis and Improved Isolation of Lower Trifluoromethylfullerenes.

3.2.1. Introduction. Preparation of practical amounts of fullerene(CF_3) $_n$ with $n \leq 4$ (referred to as “lower TMFs” in this section) is particularly challenging, partly because lower TMFs are typically prepared in the flow tube reactor at higher temperature when sublimation of fullerenes or even their partial thermal degradation lead to low yields and conversions. At the same time, lower TMFs have promise to become valuable for future PFAF studies and especially their practical application, these compounds are good electron acceptors, highly thermally stable, and a large portion of the π -system of the parent fullerene is preserved allowing for (i) efficient charge delocalization (for photo- and electrochemical applications) and (ii) fairly unrestricted further derivatization aiming at new advanced materials and polymers with specific properties.^{41,42} As discussed in the previous section of this chapter, the development of the GTGS reactor by the author and other members of the Strauss group (pioneered by Dr. Igor Kuvychko) enabled the large-scale preparation and study of a family of *higher* TMFs. A method for

preparation of *lower* TMFs was also developed by our team; Dr. Kuvychko, Mr. James Whitaker, and the author investigated many of the tunable reaction parameters of the GTGS reactor (effect of presence of copper powder, temperature, pressure of CF₃I gas, and use of a buffer gas) that are described elsewhere.⁴³ These exploratory reactions were all performed on a scale of starting fullerene material of about 5 mg. Therefore, the GTGS reaction parameters optimized for preparation of lower TMFs on a 5 mg scale were evaluated by the author in attempts to push the reaction scale to up to or more than 1 gram of starting material. Several modifications to the GTGS reactor design (the large-scale reactor-quartz thimble) were built by Dr. Igor Kuvychko in order to accommodate 1+ g starting material and to optimize the synthetic method parameters necessary to achieve similar (or higher) conversion and yield after scale-up.

Two main challenges had to be overcome in this work to realize this goal: (i) previously developed GTGS reaction conditions (by other members of the Strauss group) for selective synthesis of lower TMFs were performed on a <10mg scale, so the method needed to be scaled up by orders of magnitude, and (ii) the separation (primarily HPLC) methods used to isolate pure lower TMFs were extremely time consuming, and/or were ineffective at producing TMFs in very high purity (better than 95 mol%). The achievement of these goals enabled a number of fundamental and applied studies to be undertaken, examples of which for OPV research are discussed in Chapter 3. Described here is the scale-up of fullerene trifluoromethylation using the GTGS reactor for preparation of lower TMFs and improved separation techniques for obtaining pure compounds; the combination of both achievements should provide rapid and facile access to large quantities of these compounds for applied studies.

3.2.2. Large-scale Synthesis and Improved Isolation Methods. The method developed for synthesis of lower TMFs using the GTGS reactor on a less than 10 mg scale⁴³ was used as an

entry point for scaling up the reaction. The HPLC traces of the products prepared by trifluoromethylation of C_{60} samples of different size (other reaction conditions were the same) are shown in Figure 3.39. The molar yield of a single-isomer $C_{60}(CF_3)_2$ (**2-1**) was ca. 30% when 4.0 mg of C_{60} was used, but as the scale of the reaction was increased to 10.8 mg and then to 21.1 mg, the yield dropped to ca. 15%. When the size of the C_{60} sample was increased further to 105 mg, less than 10 mg of **2-1** was obtained (corresponding to less than 8% molar yield). During this experiment an extensive formation of iodine crystals on the walls of the quartz thimble just outside of the hot zone was observed; compared to smaller-scale reactions carried out under identical conditions, the amount of iodine was much larger.

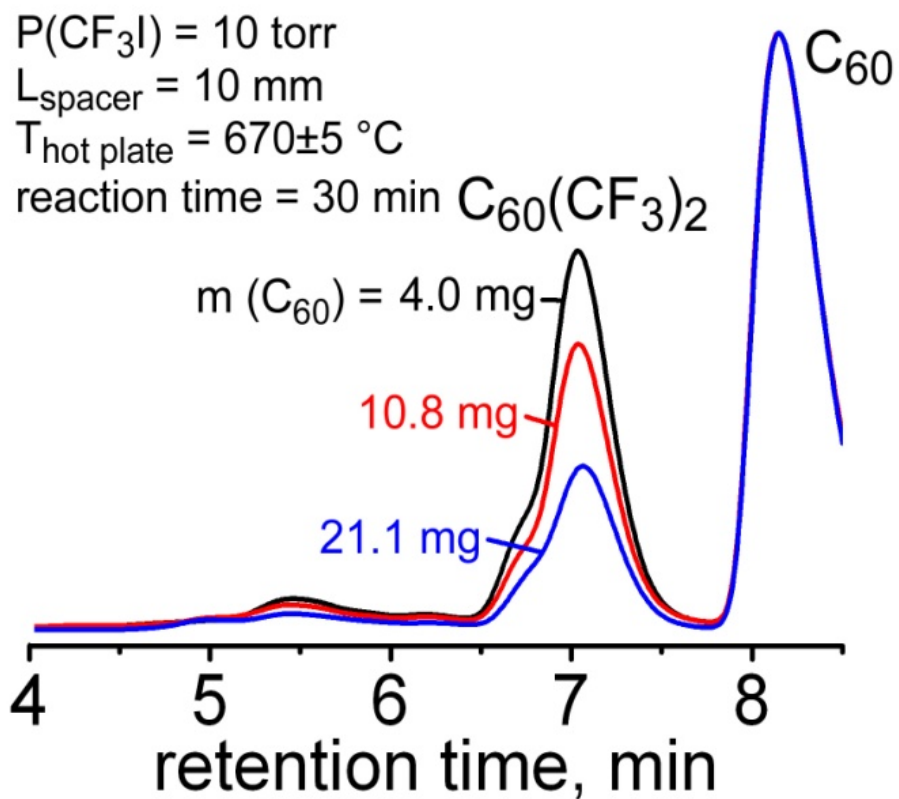


Figure 3.39. Comparison of the trifluoromethylation of C_{60} samples of different size in GTGS reactor. The HPLC traces are normalized so that the peaks corresponding to C_{60} have equal intensity.

It was hypothesized that the decrease of the C_{60} conversion was caused by the accumulation of the substantial amounts of gaseous iodine in the reaction zone which would decrease the concentration of CF_3 radicals and decrease the partial pressure of CF_3I . In order to test this hypothesis several larger scale experiments were repeated with a cold finger condenser positioned 20 mm above the fullerene sample and serving as iodine trap. It was found that the presence of the cold finger increases the yield of TMFs dramatically: 20–25% molar yields of 85+% pure **2-1** based on the starting C_{60} were achieved for 65–150 mg samples of C_{60} or fullerene extract during 2-hour reaction (Figure 3.40). These reaction conditions can be used for a highly economical selective synthesis of 85+% pure **2-1** from the crude fullerene extract.

Further scale up of the trifluoromethylation required a construction of a larger quartz thimble and removal of the water-cooled cold plate (air-cooling of the large reactor thimble is sufficiently effective without it). This larger version of the GTGS reactor can process 1+ gram samples of fullerene substrate in a single run, resulting in TMF mixtures with compositions very similar to the ones prepared in the original version of the reaction, demonstrating an excellent scalability. Depending on the particular reaction conditions the composition of the resulting crude mixture is easily adjusted: from the product containing selectively synthesized **60-2-1** to a mixture enriched with other lower TMFs $C_{60}(CF_3)_4$ and $C_{60}(CF_3)_6$. Like the original GTGS reactor, the large version of it relies on the internal cold finger condenser in order to remove iodine from the hot zone. It is also notable that a bakeout of fullerene substrates at ca. 400 °C (T_{hp} = ca. 500 °C) under dynamic vacuum for at least one hour is critical for large-scale runs. Several attempts to trifluoromethylate a large (ca. 250+ mg) fullerene sample without a proper bakeout resulted in a formation of a small amount of a brown tar-like sublimate and an effective termination of the trifluoromethylation process (only trace amounts of TMFs were

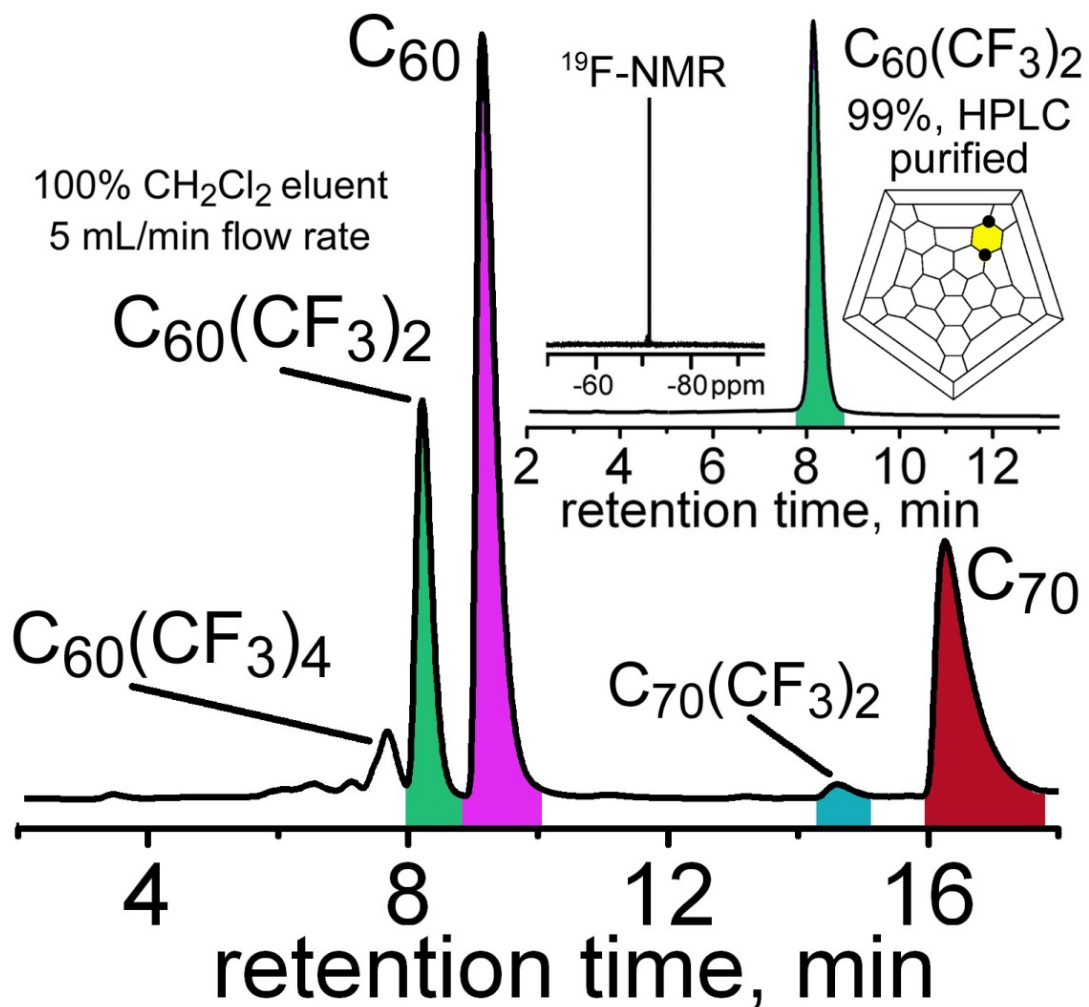


Figure 3.40. HPLC analysis of the crude product obtained from 120 mg of fullerene extract in the GTGS reactor (10 torr of CF₃I, T_{hz} = 480 °C, L_{spacer} = 10 mm, cold finger used to capture the iodine). Pure C₆₀(CF₃)₂ was isolated from the crude using HPLC and analyzed by ¹⁹F NMR spectroscopy and HPLC, see inserts.

formed). This phenomenon can be connected with the presence of solvated organic solvent in the commercial samples that are known to catalyze thermal degradation of fullerenes at elevated temperatures. Passivation of the fullerene surface may involve partial polymerization hampering reactions with CF_3 radicals, which is supposedly mitigated by bake-out described above.

Isolation of 60-2-1 was historically difficult due to it having similar retention time to 60-4-1 and 60-4-2 (and its epoxidized form, 60-4-2-O). Even though it was first reported in 2003,⁴⁴ it was not until 2007 that it was isolated in sufficient purity for growth of crystals suitable for single-crystal x-ray diffractometry confirmation of its molecular structure.⁴⁵ In that report, 60-2-1 was isolated by multiple stages of HPLC separation, the authors mentioned the impurity 60-4-2-O was present, but in sufficiently low amounts as not to hinder formation of crystalline 60-2-1 used for that x-ray study. Unfortunately, the authors did not report any ^{19}F NMR spectroscopy data, which is the best diagnostic tool for TMF purity. An improved scheme for obtaining baseline-resolved 60-2-1 by HPLC that was used internally in the Strauss group to isolate those compounds (before this work) is shown in Figure 3.41. While these methods do enable 60-2-1 to be obtained in +99mol% purity, they both require up to three stages up HPLC purification, the last of which relies on a mobile phase in which 60-2-1 has low solubility (limiting the concentration of sample injections) and requires over 70 minutes for the sample to elute fully. These ineffective and laborious separation procedures could not be practically applied to the large quantities of TMFs produced from scaled-up GTGS trifluoromethylation reactions.

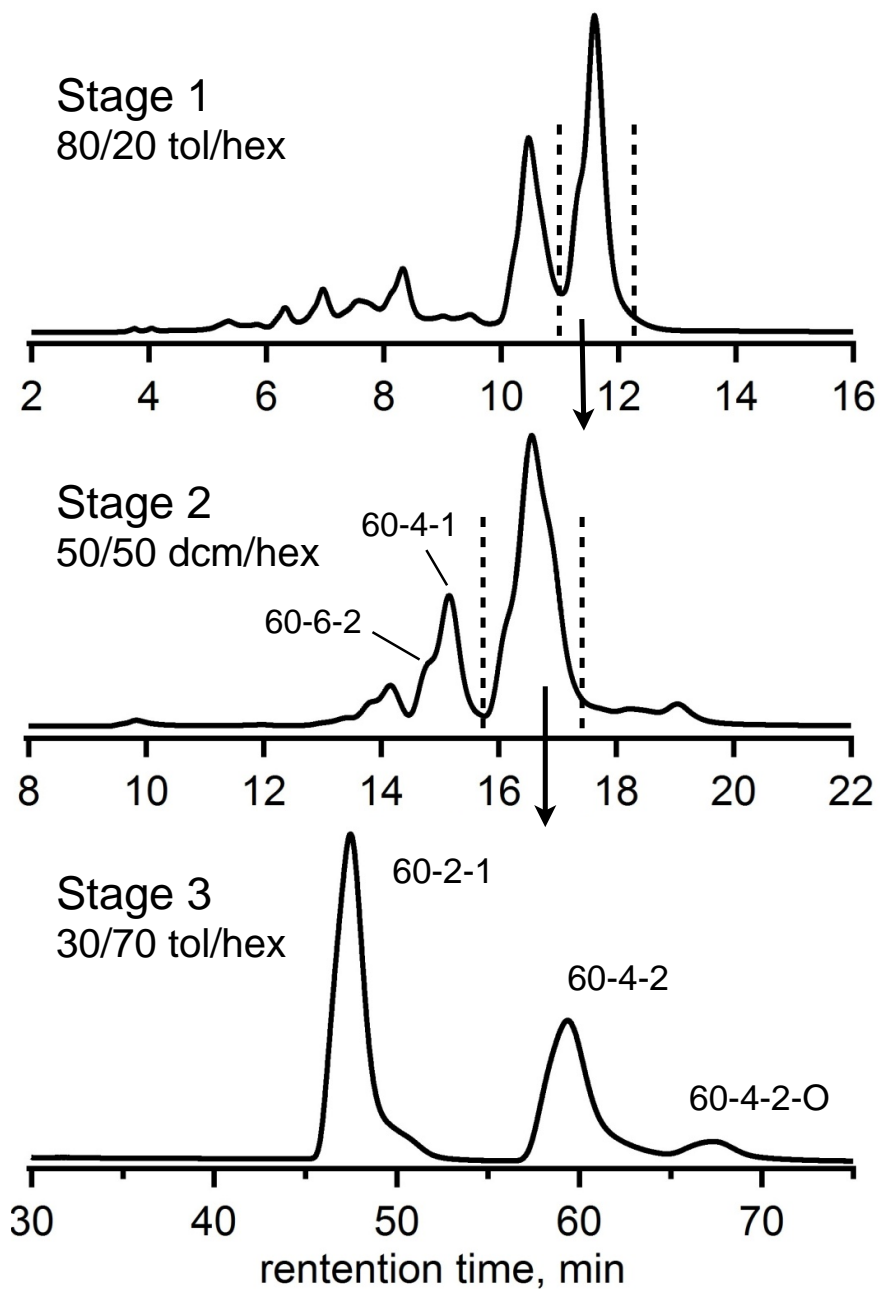


Figure 3.41. The best HPLC separation scheme for isolation of lower TMFs before this work is shown (300 nm detection, 25 x 250 mm Cosmosil Buckyprep, 16 mL/min flow rate).

Two greatly improved methods of isolating 60-2-1 in very high purity (as high as 99+ mol%) by single-stage HPLC were developed in this work. The first method was developed by investigating mobile phase options outside of toluene, hexanes, and their mixtures, which are the standard eluents used in the literature for separation of fullerene derivatives, and were the staple eluents in the Strauss group prior to this work. It was hypothesized that using a weaker solvating mobile phase that was also polar, would assist in separation of lower TMFs with different dipole moments. A sample of the crude lower TMF reaction mixture was analyzed in this work using a Cosmosil Buckyprep column and a variety of eluents; the chromatograms are shown in Figure 3.42. When 100% toluene is used to elute the TMF mixture from the column, C_{60} is baseline resolved from the TMF products, but 60-2-1, 60-4-1, 60-4-2 all co-elute. When chloroform is used as an eluent, no separation of peaks is observed, and nothing is retained on the column after 7 minutes. When dichloromethane (DCM) is used as eluent, C_{60} and the TMFs are resolved, but also 60-2-1 is separated from isomers of $C_{60}(CF_3)_4$. In this case, the retention times of C_{60} and the TMFs increase compared to 100% toluene eluent, but only by a few minutes. Under these conditions, 60-2-1 was obtained in high purity using single-stage HPLC. For preparative HPLC the time between injections was reduced to only 7.5 minutes using this method, compared to 11, 10, and 25 minutes for the first, second, and third stages of the previous isolation method (Figure 3.41). Furthermore, mixtures of DCM/hexanes added an additional facet to the new method, since they provided different separations of $C_{60}(CF_3)_4$ isomers than analogous toluene/hexanes mixtures. However, shifting retention times due to recycling solvent (it is nearly impossible to rotovap used DCM/hexanes mixtures without changing the solvent ratio) compromised the chromatogram reproducibility throughout the course of the separation and hence prevented the use of automated fraction collector.

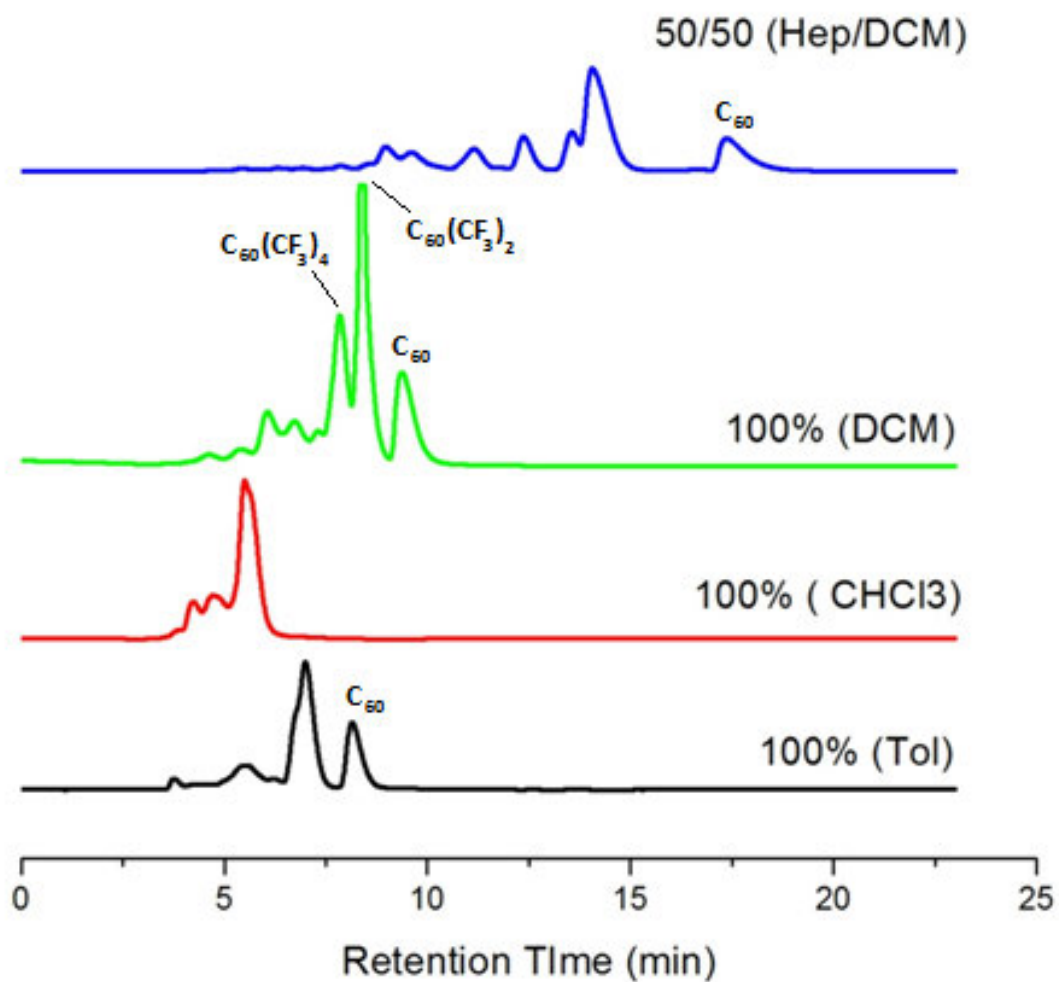


Figure 3.42. The HPLC chromatograms are shown for a crude mixture of lower TMFs using different mobile phases (25 x 250 mm Buckyprep, 16 mL/min flow rate, 300 nm detection).

There are other disadvantages to using DCM as an HPLC eluent: (i) crude lower TMF product mixtures have significantly lower solubility in DCM and DCM/hexanes mixtures than in aromatic solvents such as toluene (a single stage separation is achieved, but more injections are required), (ii) high vapor pressure of DCM (a degassing unit is necessary for optimal HPLC performance), (iii) use of 100% DCM eluent only provides a single-step isolation method for 60-2-1 (other lower TMFs require additional stages of HPLC). Even so, as a single-step method, this process significantly improves and simplifies isolation of 60-2-1 over previously reported methods in that a shorter time is required and a higher purity of isolated compound is achieved (+98 mol%).

The second method involved using a different stationary phase for separation, Cosmosil Buckyrep-M column. During the development of better techniques to separate complex mixtures of higher TMFs, it was found that this column, which is advertised for chromatography of endohedral metallofullerenes, was far superior to Buckyrep in separating not only different isomers of $C_{60}(CF_3)_{10}$, but higher TMFs in general (see Section 3.1.3 of this chapter). Therefore, the use of Buckyrep-M was evaluated for isolation of lower TMFs, too. A comparison of Buckyrep and Buckyrep-M HPLC chromatograms for a crude product mixture of lower TMFs is shown in Figure 3.43, both with an 80/20 toluene/hexanes eluent mixture. The Buckyrep-M chromatogram shows baseline separation of 60-2-1 from a crude mixture of TMFs and C_{60} ; +99 mol% 60-2-1 can be isolated using high concentration sample injections (80% toluene mobile phase) with this single-step HPLC method. Furthermore, the retention time of 60-2-1 is only 6.1 minutes using Buckyrep-M (under the same conditions, it is 7.0 minutes using Buckyrep *and* requires additional stages of separation). Use of Buckyrep-M column with 50/50 toluene/hexanes eluent results in baseline separation of 60-2-1 and 60-4-2, near

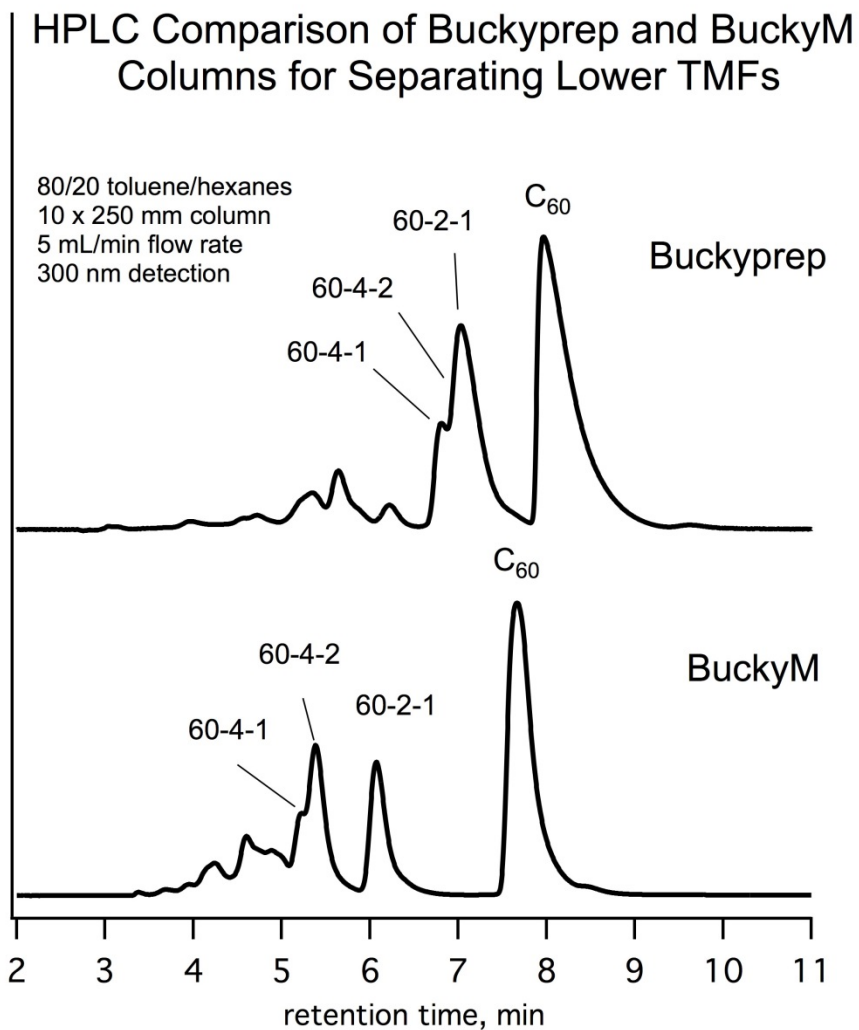


Figure 3.43. HPLC chromatograms of the crude product picture from a synthesis of lower TMFs using Buckyprep and Buckyprep-M columns. Lower TMFs are labeled in each chromatogram.

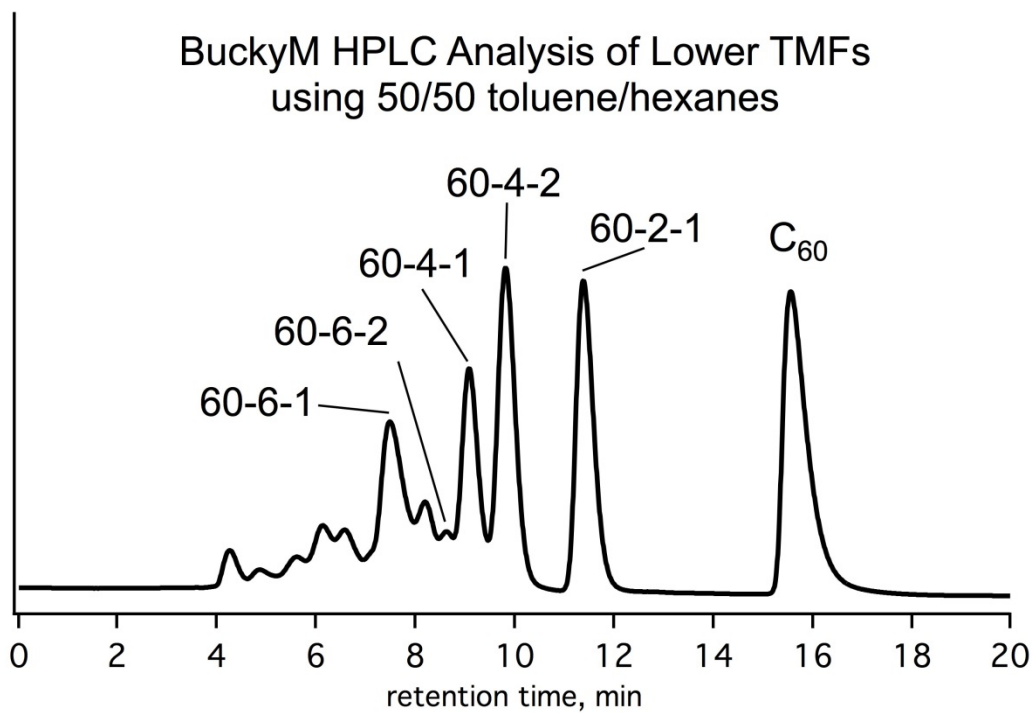


Figure 3.44. The use of 50/50 v/v mixture of toluene/hexanes as mobile phase allows for rapid single-stage isolation of lower TMFs in high purity.

baseline separation of 60-4-1, and even near baseline separation of some isomers of $C_{60}(CF_3)_6$, enabling collection of all three lower TMFs in high purity during the same HPLC collection scheme, with only a modest increase in retention time. The primary disadvantage of this method is the required use of a solvent mixture for single-stage isolation of **60-2-1**, meaning injection concentration is the limiting factor in mass production. Even so, hundreds of milligrams of pure compounds can be isolated in high purity over the course of one day. Also, in the case of toluene/hexanes eluent mixtures, fluctuations in retention time due to solvent recycling is not as much of a concern as when DCM/hexanes mixtures are recycled, since toluene has a significantly lower vapor pressure than DCM.

As shown in Figure 3.44, when using Buckyrep-M and 50/50 toluene/hexanes solvent mixture, 60-4-2 can be isolated in very high purity in a single step. It is noted here that 60-4-2 undergoes epoxidization quickly in highly polar solvents when O_2 is also present and slowly in nonpolar solvents, and that this TMF epoxide (60-4-2-O; characterized and reported on elsewhere by Mr. James Whitaker of the Strauss group) has nearly the same retention time as 60-4-2. Therefore, it is necessary to carry out additional characterization when this fraction is collected to evaluate purity, especially if a significant amount of time passes between the GTGS reaction work-up and HPLC separation. Concerning 60-4-1 purity, the primary impurity is 60-6-2 when HPLC separation utilizes the conditions shown in Figure 3.44. One option for isolating 60-4-1 in high purity after such first stage is a second stage of Buckyrep-M HPLC implementing a 30/70 toluene/hexanes eluent, which allows to separate 60-6-2. One problem then arises that is the solubility of 60-4-1 is very low in that solvent mixture, which necessitates significantly more injections for preparative HPLC. A simpler, non-HPLC second step was developed as an alternative. Simply, the fraction containing a mixture of 60-4-1 and 60-6-2 (from

the first stage of HPLC separation) is allowed to dry slowly. Upon drying, 60-4-1 and 60-6-2 totally phase separate: 60-4-1 forms dense black crystals and 60-6-2 forms orange less crystalline domains. The degree of crystallinity depends on the presence of other TMF impurities in the fraction, which co-precipitate together with the orange 60-6-2 solid domains. Then, the 60-6-2 (and other impurities) are washed away by rinsing the crystals first with hexanes and then briefly with toluene; 60-4-1 crystals remain intact. This selective precipitation followed by solvent washing method yields highly pure 60-4-1 crystals and does not require additional HPLC purification. It is noted that the 60-4-1 crystals do require gentle heating and stirring to be fully redissolved later.

In summary, large-scale syntheses of lower C_{60} TMFs were achieved using judiciously chosen reaction parameters in the GTGS reactor. Several new separation methods (both HPLC-based and non-chromatographic) were developed that significantly improve the efficacy of isolating lower TMFs of C_{60} . This work enables easy access to these compounds in large quantity and high purity, which makes them much more amenable to use in applied and fundamental studies. Examples of such studies are discussed in Chapter 3.

3.3. Experimental.

Description of the Reactor. The plate furnace of the reactor is built locally. The magnesia refractory brick is used as heat insulation (except for 10 mm spacer that is made of fused silica wool); the heating element from Corning hot plate is used as a heater (it is powered using Variac autotransformer). K-type thermocouples were used for all temperature measurements. Both the cold and the hot plate of the furnace are made of 1.25 mm brass. The

quartz thimble is attached to the ballast volume using Ace Glass compression joint with Viton O-ring (see Figure S-9 for the technical drawings of small- and large-scale quartz thimbles). The ballast volume of the reactor is made of a 1 L pyrex glass flask equipped with two Ace Glass compression joint lying on the same axis, and a right-angle Teflon valve. The reactor is connected to the gas-handling system through this valve using 1/2" Cajon connector. The gas-handling system is equipped with 0-1000 torr range Baratron (capacitance manometer) for pressure measurements.

Description of a typical large-scale synthesis. A sample of starting material (400 – 650 mg of ground C_{60}) was placed in the center of the quartz thimble of the GTGS reactor, and then heated at ca. 400 °C for 1 hour under dynamic vacuum. The system was isolated and allowed to cool, then filled with 30-45 torr of trifluoromethyl iodide, and the system was isolated. The preheated plate heater/cooling plate assembly was put in place; therefore, the temperature ramp-up was very fast, taking only 2-4 minutes. To target lower TMFs, and high conversion of C_{60} , the pressure of CF_3I gas in the reactor was monitored with an equipped baratron, and as more CF_3I gas was introduced into the reactor throughout the course of the 5 – 6 hour reaction, as needed to maintain a pressure of 30 – 45 torr. Then the plate heater/cooling plate assembly was removed and the reactor was allowed to cool off for about 10 minutes. The quartz thimble was removed and thoroughly washed with toluene; this solution was evaporated (in order to remove iodine) and then redissolved in either toluene or the solvent mixture that was used for HPLC separation. Molar yields of 20-25% were generally achieved for $C_{60}(CF_3)_2$.

High-performance liquid chromatography. HPLC Grade toluene, heptanes (Fisher Scientific), CH_2Cl_2 (Fisher Scientific), C_{60} (99.9%, Term-USA), and CF_3I gas (SynQuest Labs) were used as received. HPLC analysis and separation was done using Shimadzu liquid

chromatography instrument (CBM-20A control module, SPD-20A UV-detector set to 300 nm detection wavelength, LC-6AD pump, manual injector valve) equipped with 10-mm I.D. × 250 mm Cosmosil Buckyprep of Buckyprep-M column, Nacalai Tesque, Inc.). Fluorine-19 NMR spectra were recorded in CDCl₃ using a Varian RM spectrometer at 376 MHz, and chemical shifts were referenced to a C₆F₆ internal standard (^Fδ −164.9).

3.4. References.

- (1) Kareev, I. E.; Kuvychko, I. V.; Lebedkin, S. F.; Miller, S. M.; Anderson, O. P.; Seppelt, K.; Strauss, S. H.; Boltalina, O. V.: Synthesis, Structure, and ^{19}F NMR Spectra of 1,3,7,10,14,17,23,28,31,40- $\text{C}_{60}(\text{CF}_3)_{10}$. *J. Am. Chem. Soc.* **2005**, *127*, 8362-8375.
- (2) Boltalina, O. V. K., I. V.; Shustova, N. B.; Strauss, S. H. : Perfluoroalkylation of Fullerenes. In *Handbook of Carbon Nanomaterials, Volume 1, Syntheses and Supramolecular Systems*; Desouza, F., Kadish, K. M., Ed.; World Scientific Singapore, 2011; pp 101-143 and references therein.
- (3) Darwish, A. D.; Avent, A. G.; Abdul-Sada, A. K.; Taylor, R.: [60]- and [70]Fullerenes are trifluoromethylated across 5:6-bonds. *Chem. Commun.* **2003**, 1374-1375.
- (4) Darwish, A. D.; Abdul-Sada, A. K.; Avent, A. G.; Martsinovich, N.; Street, J. M.; Taylor, R.: Novel addition in trifluoromethylation of [70]fullerene. *J. Fluorine Chem.* **2004**, *125*, 1383-1391.
- (5) Kareev, I. E.; Popov, A. A.; Kuvychko, I. V.; Shustova, N. B.; Lebedkin, S. F.; Bubnov, V. P.; Anderson, O. P.; Seppelt, K.; Strauss, S. H.; Boltalina, O. V.: Synthesis and X-ray or NMR/DFT Structure Elucidation of Twenty-One New Trifluoromethyl Derivatives of Soluble Cage Isomers of C_{76} , C_{78} , C_{84} , and C_{90} . *J. Am. Chem. Soc.* **2008**, *130*, 13471-13489.
- (6) Popov, A. A.; Kareev, I. E.; Shustova, N. B.; Stukalin, E. B.; Lebedkin, S. F.; Seppelt, K.; Strauss, S. H.; Boltalina, O. V.; Dunsch, L.: Electrochemical, Spectroscopic, and DFT Study of $\text{C}_{60}(\text{CF}_3)_n$ Frontier Orbitals ($n = 2-18$): The Link between Double Bonds in Pentagons and Reduction Potentials. *J. Am. Chem. Soc.* **2007**, *129*, 11551-11568.
- (7) Kareev, I. E.; Lebedkin, S. F.; Popov, A. A.; Miller, S. M.; Anderson, O. P.; Strauss, S. H.; Boltalina, O. V.: 1,6,12,15,18,23,25,41,45,57-Decakis(trifluoromethyl)-1,6,12,15,18,23,-25,41,45,57-decahydro($\text{C}_{60}\text{-I}_h$)[5,6]fullerene. *Acta Crystallogr.* **2006**, *E62*, o1501-o1503.
- (8) Kareev, I. E.; Lebedkin, S. F.; Miller, S. M.; Anderson, O. P.; Strauss, S. H.; Boltalina, O. V.: 1,6,11,16,18,26,36,44,48,58-Decakis(trifluoromethyl)-1,6,11,16,18,26,36,44,48,58-decahydro($\text{C}_{60}\text{-I}_h$)[5,6]fullerene benzene 2.5-solvate. *Acta Crystallogr.* **2006**, *E62*, o1498-o1500.
- (9) Cozzi, F.; Powell, W. H.; Thilgen, C.: Numbering of Fullerenes. *Pure Appl. Chem.* **2005**, *77*, 843-923.
- (10) Powell, W. H.; Cozzi, F.; Moss, G. P.; Thilgen, C.; Hwu, R. J. R.; Yerin, A.: Nomenclature for the $\text{C}_{60}\text{-I}_h$ and $\text{C}_{70}\text{-D}_{5h(6)}$ Fullerenes (IUPAC Recommendations 2002). *Pure Appl. Chem.* **2002**, *74*, 629-695.
- (11) Shustova, N. B.; Peryshkov, D. V.; Popov, A. A.; Boltalina, O. V.; Strauss, S. H.: 1,6,11,18,24,27,33,51,54,60-Decakis(trifluoromethyl)-1,6,11,18,24,27,33,51,54,60-decahydro-($\text{C}_{60}\text{-I}_h$)[5,6]fullerene. *Acta Cryst.* **2007**, *E63*, o3129.
- (12) Fujita, S.: Soccerane Derivatives of Given Symmetries. *Bull. Chem. Soc. Japan* **1990**, *63*, 3215-3223.
- (13) Kadish, K. M.; Gao, X.; Gorelik, O.; Van Caemelbecke, E.; Suenobu, T.; Fukuzumi, S.: Electrogeneration and characterization of $(\text{C}_6\text{H}_5\text{CH}_2)_2\text{C}-70$. *J. Phys. Chem. A* **2000**, *104*, 2902-2907.
- (14) Paolucci, D.; Paolucci, F.; Marcaccio, M.; Carano, M.; Taylor, R.: Electrochemistry of perfluorinated fullerenes: the case of three isomers of $\text{C}_{60}\text{F}_{36}$. *Chem. Phys. Lett.* **2004**, *400*, 389-393.

- (15) Kadish, K. M.; Gao, X.; Caemelbecke, E. V.; Suenobu, T.; Fukuzumi, S.: Electrosynthesis and Structural Characterization of Two (C₆H₅CH₂)₄C₆₀ Isomers. *J. Am. Chem. Soc.* **2000**, *122*, 563-570.
- (16) Olmstead, M. M.; de Bettencourt-Dias, A.; Lee, H. M.; Pham, D.; Balch, A. L.: Interactions of metalloporphyrins as donors with the electron acceptors C₆₀, tetracyanoquinomethane (TCNQ) and trinitrofluorenylidene malonitrile. *Dalton Trans.* **2003**, 3227-3232.
- (17) Fowler, P. W.; Manolopoulos, D. E.: *An Atlas of Fullerenes*; Dover: Mineola, NY, 2006.
- (18) Liu, S. L., Y.-J.; Kappes, M.; Ibers, J. A. : The Structure of the C₆₀ Molecule: X-Ray Crystal Structure Determination of a Twin at 110 K. *Science* **1991**, *254*, 408-410.
- (19) Kareev, I. E.; Lebedkin, S. F.; Miller, S. M.; Anderson, O. P.; Strauss, S. H.; Boltalina, O. V.: 1,4,10,14,19,25,35,41,49,60,66,69-Dodecakis(trifluoromethyl)-1,4,10,14,19,25,35,41,49,60,66,69-dodecahydroC₇₀-D_{5h}(6))[5,6]-fullerene benzene disolvate. *Acta Crystallogr.* **2006**, *E62*, o620-o622.
- (20) Ernst, L.; Ibrom, K.: A New Quantitative Description of the Distance Dependence of Through-Space F-19,F-19 Spin-Spin Coupling. *Angew. Chem. Int. Ed.* **1995**, *34*, 1881-1882.
- (21) Arnold, W. D.; Mao, J.; Sun, H.; Oldfield, E.: Computation of Through-Space ¹⁹F-¹⁹F Scalar Couplings via Density Functional Theory. *J. Am. Chem. Soc.* **2000**, *122*, 12164-12168.
- (22) Peralta, J. E.; Barone, V.; Contreras, R. H.; Zaccari, D. G.; Snyder, J. P.: Through-Bond and Through-Space J_{FF} Spin-Spin Coupling in Perdifluoronaphthalenes: Accurate DFT Evaluation of the Four Contributions. *J. Am. Chem. Soc.* **2001**, *123*, 9162-9163.
- (23) Peralta, J. E.; Contreras, R. H.; Snyder, J. P.: Natural bond order dissection of fluorine-fluorine through-space NMR coupling ($J_{F,F}$) in polycyclic organic molecules. *Chem. Commun.* **2000**, 2025-2026.
- (24) Bryce, D. L.; Wasylishen, R. E.: Ab initio Characterization of Through-Space Indirect Nuclear Spin-Spin Coupling Tensors for Fluorine-X (X = F, C, H) Spin Pairs. *J. Mol. Struct.* **2002**, *602*, 463-472.
- (25) Alkorta, I.; Elguero, J. E.: Fluorine-Fluorine Interactions: NMR and AIM Analysis. *Struct. Chem.* **2004**, *15*, 117-120.
- (26) Tuttle, T.; Grafenstein, J.; Cremer, D.: Analysis of NMR through-space coupling mechanism between ¹⁹F atoms. *Chem. Phys. Lett.* **2004**, *394*, 5-13.
- (27) San Fabian, J.; Westra Hoekzema, A. J. A.: Vicinal fluorine-fluorine coupling constants: Fourier analysis. *J. Chem. Phys.* **2004**, *121*, 6268-6276.
- (28) Kareev, I. E.; Santiso-Quinones, G.; Kuvychko, I. V.; Ioffe, I. N.; Goldt, I. V.; Lebedkin, S. F.; Seppelt, K.; Strauss, S. H.; Boltalina, O. V.: Synthesis of 1,7- and 1,9-C₆₀F(CF₃): Sterically Hindered CF₃ Rotation and Through-Space J_{FF} Coupling in 1,9-C₆₀F(CF₃) and in C₁- and C_s-C₆₀F₁₇(CF₃). *J. Am. Chem. Soc.* **2005**, *127*, 11497-11504.
- (29) Shustova, N. B.; Peryshkov, D. V.; Kuvychko, I. V.; Whitaker, J. B.; Larson, B. W.; Dunsch, L.; Chen, Y. S.; Seppelt, K.; Popov, A. A.; H., S. S.; Boltalina, O. V.: Chemical tailoring of fullerene acceptors: synthesis, structures and electrochemical properties of perfluoroisopropylfullerenes. *Chem. Commun.* **2010**, *47*, 875-877.
- (30) Kareev, I. E.; Shustova, N. B.; Kuvychko, I. V.; Lebedkin, S. F.; Miller, S. M.; Anderson, O. P.; Popov, A. A.; Strauss, S. H.; Boltalina, O. V.: Thermally-Stable

Perfluoroalkylfullerenes With the Skew-Pentagonal Pyramid Pattern: $C_{60}(C_2F_5)_4O$, $C_{60}(CF_3)_4O$, and $C_{60}(CF_3)_6$. *J. Am. Chem. Soc.* **2006**, *128*, 12268-12280.

(31) Popov, A. A.; Kareev, I. E.; Shustova, N. B.; Lebedkin, S. F.; Strauss, S. H.; Boltalina, O. V.; Dunsch, L.: Synthesis, Spectroscopic and Electrochemical Characterization, and DFT Study of Seventeen $C_{70}(CF_3)_n$ Derivatives ($n = 2, 4, 6, 8, 10, 12$). *Chem. Eur. J.* **2008**, *14*, 107-121.

(32) Shustova, N. B.; Popov, A. A.; Newell, B. S.; Miller, S. M.; Anderson, O. P.; Seppelt, K.; Bolskar, R. D.; Boltalina, O. V.; Strauss, S. H.: Discovering New Fullerene Cages with CF_3 Radicals. Structures of $C_2-p^{11}-(C_{74}-D_{3h})(CF_3)_{12}$ and $C_2-p^{11}-(C_{78}-D_{3h}(5))(CF_3)_{12}$. *Angew. Chem. Int. Ed.* **2007**, *46*, 4111-4114.

(33) Kareev, I. E.; Shustova, N. B.; Peryshkov, D. V.; Lebedkin, S. F.; Miller, S. M.; Anderson, O. P.; Popov, A. A.; Boltalina, O. V.; Strauss, S. H.: X-ray structure and DFT study of $C_1-C_{60}(CF_3)_{12}$. A high-energy kinetically-stable isomer prepared at 500 °C. *Chem. Commun.* **2007**, 1650-1652.

(34) Shustova, N. B.; Kuvychko, I. V.; Bolskar, R. D.; Seppelt, K.; Strauss, S. H.; Popov, A. A.; Boltalina, O. V.: Trifluoromethyl Derivatives of Insoluble Small-HOMO-LUMO-Gap Hollow Higher Fullerenes. NMR and DFT Structure Elucidation of $C_2-(C_{74}-D_{3h})(CF_3)_{12}$, $C_s-(C_{76}-T_d)(CF_3)_{12}$, $C_2-(C_{78}-D_{3h}(5))(CF_3)_{12}$, $C_s-(C_{80}-C_{2v}(5))(CF_3)_{12}$, and $C_2-(C_{82}-C_2(5))(CF_3)_{12}$. *J. Am. Chem. Soc.* **2006**, *128*, 15793-15798.

(35) Bard, A. J. F., L. R. ; : *Electrochemical Methods: Fundamentals and Applications*; 2nd ed.; Wiley: New York, 2001.

(36) Geiger, W. E.: Organometallic Electrochemistry: Origins, Development, and Future. *Organometallics* **2007**, *26*, 5738-5765.

(37) Gritzner, G. K., J.: IUPAC Commission on Electrochemistry: Recommendations on Reporting Electrode Potentials in Nonaqueous Solvents. *Electrochim. Acta* **1984**, *29*, 869-873.

(38) Reed, C. A.; Bolskar, R. D.: Discrete fulleride anions and fullerenium cations. *Chem. Rev.* **2000**, *100*, 1075-1120.

(39) Noviandri, I. B., K. N.; Fleming, D. S.; Gulyas, P. T.; Lay, P. A.; Masters, A. F.; Phillips, L. : The Decamethylferrocenium/Decamethylferrocene Redox Couple: A Superior Redox Standard to the Ferrocenium/Ferrocene Redox Couple for Studying Solvent Effects on the Thermodynamics of Electron Transfer. *J. Phys. Chem. B* **1999**, *103*, 6713-6722

(40) Kuvychko, I. V.; Whitaker, J. B.; Larson, B. W.; Folsom, T. C.; Shustova, N. B.; Avdoshenko, S. M.; Chen, Y. S.; Wen, H.; Wang, X. B.; Dunsch, L.; Popov, A. A.; Boltalina, O. V.; Strauss, S. H.: Substituent effects in a series of 1,7-C-60(R-F)(2) compounds (R-F = CF_3 , C_2F_5 , n-C $_3$ F $_7$, i-C $_3$ F $_7$, n-C $_4$ F $_9$, s-C $_4$ F $_9$, n-C $_8$ F $_{17}$): electron affinities, reduction potentials and E(LUMO) values are not always correlated. *Chem. Sci.* **2012**, *3*, 1399-1407.

(41) Ovchinnikova, N. S.; Ignateva, D. V.; Tamm, N. B.; Avdoshenko, S. M.; Goryunkov, A. A.; Ioffe, I. N.; Markov, V. Y.; Troyanov, S. I.; Sidorov, L. N.; Yurovskaya, M. A.; Kemnitz, E.: Regioselective synthesis and crystal structure of $C_{70}(CF_3)_{10}[C(CO_2Et)_2]$. *New J. Chem.* **2008**, *32*, 89.

(42) Troyanov, S. I.; Kemnitz, E.: Mixed chlorotrifluoromethyl fullerene $C_{60}(CF_3)_{12}Cl_{12}$. *Mendeleev Commun.* **2008**, *18*, 27.

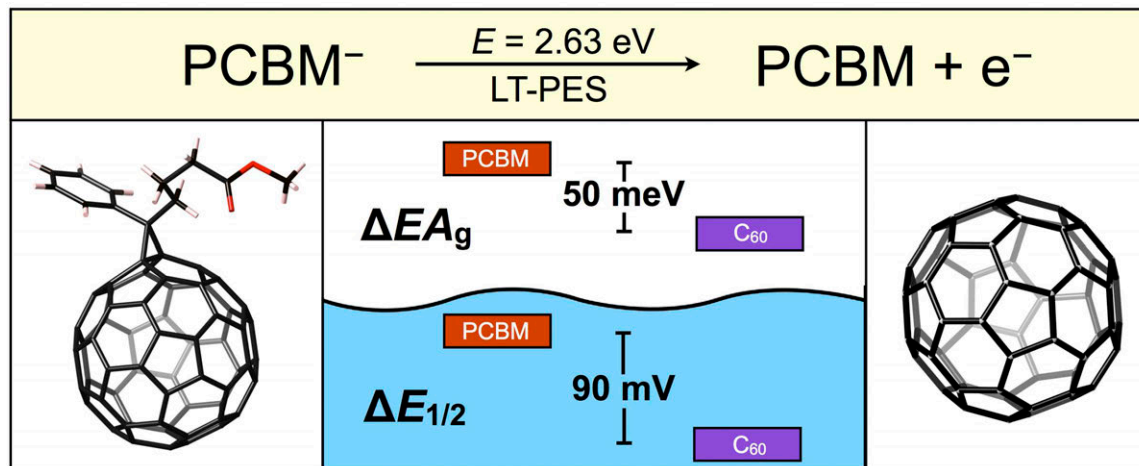
- (43) Kuvychko, I. V.; Whitaker, J. B.; Larson, B. W.; Raguindin, R. S.; Suhr, K. J.; Strauss, S. H.; Boltalina, O. V.: Pressure effect on heterogeneous trifluoromethylation of fullerenes and its application. *J. Fluorine Chem.* **2011**, *132*, 679-685.
- (44) Goryunkov, A. A.; Kuvychko, I. V.; Ioffe, I. N.; Dick, D. L.; Sidorov, L. N.; Strauss, S. H.; Boltalina, O. V.: Isolation of C-60(CF₃)_n (n=2, 4, 6, 8, 10) with high compositional purity. *Journal of Fluorine Chemistry* **2003**, *124*, 61-64.
- (45) Dorozhkin, E. I.; Goryunkov, A. A.; Ioffe, I. N.; Avdoshenko, S. M.; Markov, V. Y.; Tamm, N. B.; Ignat'eva, D. V.; Sidorov, L. N.; Troyanov, S. I.: Synthesis, structure, and theoretical study of lower trifluoromethyl derivatives of 60 fullerene. *Eur. J. Org. Chem.* **2007**, 5082-5094.

Chapter 4: Phenyl-C₆₁-Butyric Acid Methyl Ester (PCBM).

4.1. General Remarks.

In the past decade, a singular organic derivative, phenyl-C₆₁-butyric acid methyl ester, which is commonly abbreviated PCBM, has been in the focus of many research groups, as evidenced by its prominent presence in the literature. According to a web search using SciFinder Scholar at the time this dissertation was written, the keywords “PCBM”, “PC61BM”, and “PC60BM” produced 7,030 hits refined to only the last ten years. Although PCBM was originally designed and synthesized in 1995 for use as an HIV treatment drug,¹ it is now known widely for its major role in organic electronics and especially organic photovoltaics. PCBM was used in the first certified record-efficiency polymer solar cell,² and has continued to be among the champion fullerene acceptors in OPV research. Despite this extensive PCBM-based research activity, many fundamental properties of the compound itself remain either unknown or determined with low accuracy or precision. For example, its gas-phase electron affinity had been unknown until this work, random non-validated DFT values notwithstanding (see below). Furthermore, information on the thermal behavior, and particularly, temperature range of its thermal stability was difficult to find in the literature. This was surprising, since both these properties have direct implications for fabrication and performance of photoactive materials that contain PCBM. The two sections of this chapter are dedicated to the studies of electronic properties of PCBM in solution and in the gas-phase (Section 4.2) and thermal stability of PCBM in the solid phase (Section 4.3).

4.2. Electronic Properties of PCBM



4.2.1. Introduction

The search for fossil fuel alternatives as sources of energy has sparked a rapid expansion of the field of organic photovoltaics (OPVs), owing to their low cost, facile processing, and high material abundance relative to inorganic solar cells. However, if power conversion efficiencies greater than 15% in single-junction research-scale devices are to be achieved by rational design,^{1,2} precise determination of electronic properties of OPV donor and acceptor materials is of key importance, especially since the maximum open-circuit voltage of a device is limited by the offset of the donor highest occupied molecular orbital (HOMO) and acceptor lowest unoccupied molecular orbital (LUMO) energies.^{3,4} Surprisingly, for one of the best performing and most commonly used fullerene acceptors, phenyl-C₆₁-butyric acid methyl ester (PCBM),⁵ there is little agreement in the literature regarding its LUMO energy. The LUMO energy is commonly estimated from correlations or conversions from the data obtained experimentally by cyclic voltammetry (CV), gas-phase photoelectron spectroscopy of negative ions, or solid-state inverse photoelectron spectroscopy (IPES), as well as from DFT calculations. In fact, a thorough literature search revealed that E(LUMO) values for PCBM derived from original experiments

(mostly from CV) by different authors did not agree well. Clearly, such a discrepancy causes confusion when scientists have to select a reliable E(LUMO) value for energy level modeling/design of OPV active layers. We have investigated the sources of this E(LUMO) inconsistency in the literature and propose a simple and reliable protocol for comparison of fullerene acceptors.

More importantly, our literature search revealed that even a fundamental molecular property, the gas-phase electron affinity (EA), is not known for PCBM. In this work, we report the adiabatic EA data for PCBM measured by low-temperature photoelectron spectroscopy (LT-PES) for the first time. Additionally, we address the question of reliability and precision of currently available data regarding solid-state EA measurements for PCBM.^{6,7}

4.2.2. Experimental.

Low-Temperature Photoelectron Spectroscopy (LT-PES). Dr. Xue-Bin Wang conducted LT-PES measurements at the Pacific Northwest National Laboratory (PNNL). The gas-phase EA of PCBM was directly measured from the 0–0 transition in the corresponding anion photoelectron spectrum. The PES experiments were performed with a low-temperature apparatus that couples an electrospray ionization (ESI) source and a temperature-controlled ion trap to a magnetic-bottle time-of-flight photoelectron spectrometer previously described in detail.⁸ Fresh spray solutions were prepared by adding an aliquot of an acetonitrile solution of an electron-donor compound, tetrakis(dimethylamino)ethylene (TDAE), to a 10⁻³ M toluene stock solution of PCBM. The anions produced by the ESI source were guided by two RF-only quadrupoles and directed by a 90° ion bender into a 3-D ion trap, where they were accumulated and thermalized via collisions with a background gas (ca. 0.1 mTorr 20/80 H₂/ He) for a period of 20 to 100 ms before being pulsed out into the extraction zone of a time-of-flight mass

spectrometer at a repetition rate of 10 Hz. The trap was attached to the cold head of a closed-cycle helium cryostat equipped with a feedback heating system that allows the temperature to be controlled from 10 to 350 K. In this work, the trap was operated at 12 K in order to achieve optimal instrument resolution, as well as to eliminate vibrational hot bands.

During the PES experiment, the negative ions were mass-selected and decelerated before being intercepted by a probe laser beam from a Nd:YAG laser (266 nm; 4.661 eV) in the photodetachment zone of the magnetic bottle photoelectron analyzer. The laser was operated at a 20 Hz repetition rate with the ion beam off at alternating laser shots for shot-by-shot background subtraction. Photoelectrons were collected at nearly 100% efficiency by the magnetic bottle and analyzed in a 5.2 m flight tube. Time-of-flight photoelectron spectra were collected and converted to kinetic energy spectra, calibrated by the known spectra of I^- and ClO_2^- . The electron binding energy spectrum was obtained by subtracting the kinetic energy spectrum from the detachment photon energy used. The energy resolution ($\Delta E/E$) was ca. 2% (i.e., ca. 20 meV for 1 eV electrons).

Cyclic Voltammetry. Mr. James Whitaker of the Strauss group performed the electrochemical measurements on PCBM and C_{60} . All electrochemical experiments were controlled with a PAR 263 potentiostat/galvanostat at a scan rate of 100 mV/s. Each experiment was conducted in a dinitrogen filled glovebox (oxygen and water < 1 ppm). The electrolyte was $\text{N}(n\text{-Bu})_4\text{BF}_4$ (Fluka puriss grade) dried under vacuum at 70 °C for 24 h. A 0.1 M solution of $\text{N}(n\text{-Bu})_4\text{BF}_4$ in *o*-dichlorobenzene (*o*-DCB) that had been freshly dried with 3 Å molecular sieves and vacuum distilled was used for each measurement. Both $\text{Fe}(\text{Cp}^*)_2$ and $\text{Fe}(\text{Cp})_2$ were used as internal standards. A three electrode, one compartment electrochemical cell was used.

Both the working and auxiliary electrodes were platinum wires (0.5 mm diameter). A silver wire (0.5 mm diameter, Alfa Aesar Premion, 99.99%) served as the quasi-reference electrode.

Density Functional Theory (DFT) Calculations. Dr. Alexey Popov of the IFW in Dresden, Germany performed theoretical calculations for this study. The DFT gas-phase electron affinity of PCBM was calculated in this work using the PBE functional⁹ and a TZ2P-quality (6, 3, 2)/ (11s, 6p, 2d) basis set implemented in the PRIRODA code,¹⁰ and B3LYP/def2-TZVP//PBE/TZ2P levels of theory using ORCA suite employing the RIJCOSX algorithm.¹¹

4.2.3. Results and Discussion.

4.2.3.1. Gas-phase Electron Affinity. Figure 4.1 shows low-temperature PES spectra of the singly charged gas-phase molecular anions of PCBM and C₆₀. The PCBM anions were generated by mixing a toluene solution of PCBM with a donor compound (TDAE) and introducing the solution into the electrospray ion source of the PES setup. Cooling molecular ions to 12 K allowed for recording PES spectra with finely resolved features (see ref 14 for interpretation of the observed features for C₆₀) and high-accuracy EA measurements (typically 0.01 eV uncertainty). The peak at binding energy of 2.63(1) eV corresponds to the gas-phase adiabatic EA of PCBM, which is lower than the adiabatic EA value of 2.683(8) eV for C₆₀, measured previously under similar conditions by Dr. Xue-Bin Wang.⁸ To our knowledge, it is the first direct measurement of the gas-phase EA of PCBM. It reveals that PCBM is only a slightly weaker electron acceptor (by ca. 0.05 eV) in the gas phase than C₆₀.

4.2.3.2. DFT Study. A few theoretical studies on the gas-phase EA of PCBM are available in the literature. For example, in two DFT studies, the EA values for PCBM were reported as 2.004¹² and 2.3 eV.¹³ Those values are greatly underestimated compared to the

experimental value obtained in this work; furthermore, the corresponding DFT-derived EA values for C_{60} are also significantly lower (2.094¹² and 2.4 eV¹³) than the gas-phase EA value from the LT-PES measurement (2.683(8) eV).¹⁴ The DFT gas-phase electron affinity values for PCBM were calculated in this work at the PBE/TZ2P and B3LYP/def2-TZVP//PBE/TZ2P levels as 2.741 and 2.336 eV, respectively, whereas the corresponding EA values for C_{60} are 2.924 and 2.642 eV. Thus, GGA functional (PBE) overestimates experimental EA values, whereas usually more reliable hybrid functional (B3LYP) underestimates experimental EA values. Furthermore, both methods predict a much greater difference in the EA values between gas-phase C_{60} and PCBM than found experimentally in this study. Similarly, we observed a poor correlation between DFT-calculated and experimental EA values for C_{60} and $C_{60}(R_F)_2$ compounds.¹⁵ It has been long recognized that DFT gives much less accurate predictions of EAs than ionization potentials (IPs);¹⁶ these new results call for caution when using DFT-calculated EAs (and even Δ EA calculated by the same DFT method) for comparing different acceptor materials, and specifically selecting them for donor:acceptor pairing for OPV applications on the basis of their estimated electronic properties. We also recently

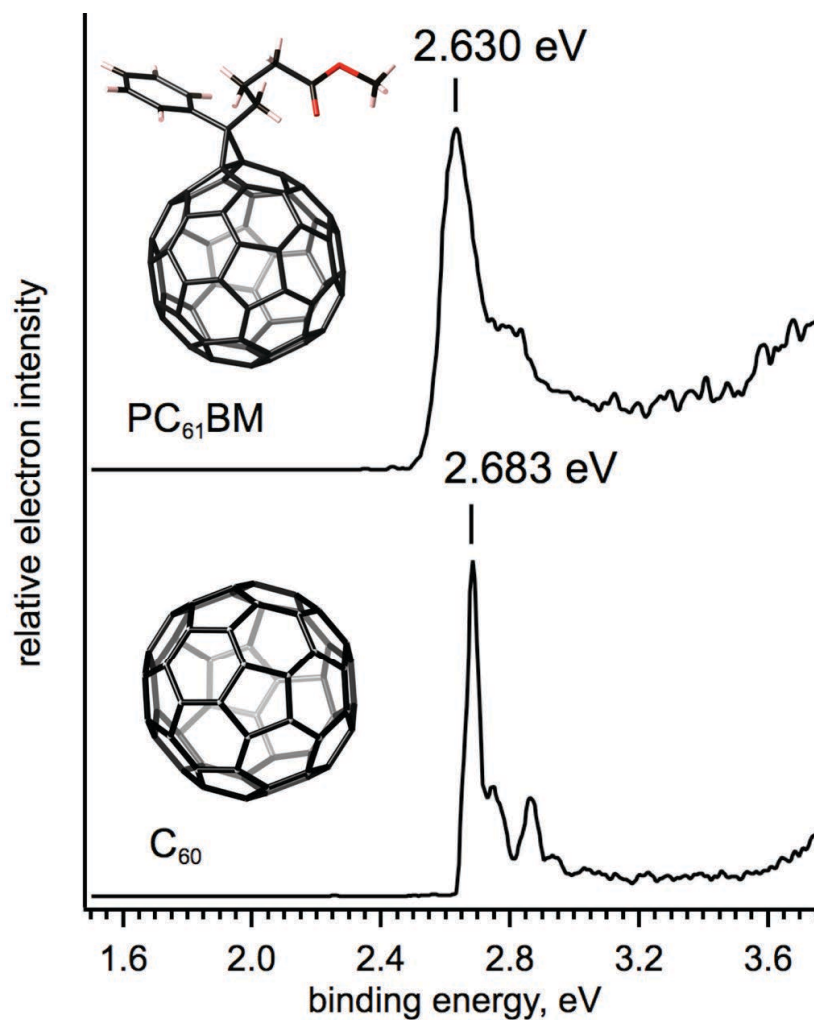


Figure 4.1. Low temperature (12 K) photoelectron spectrum of PCBM at 266 nm is shown (top), with a peak maximum at 2.63(1) eV corresponding to its gas-phase electron affinity, EA. For comparison, the low temperature (68 K) PE spectrum of C₆₀ is also shown (bottom), at 266 nm, first reported in ref 14.

demonstrated that widely used correlations between EA, E(LUMO), and reduction potentials for fullerene derivatives are not always observed, even for the group of very closely related compounds.¹⁵

4.2.3.3. Cyclic Voltammetry and E(LUMO) Approximations. Cyclic voltammetry (CV) is commonly used to characterize acceptor and donor properties of different organic materials and polymers. PCBM has good solubility in organic solvents, is reasonably stable in solution, and exhibits reversible redox behavior, so cyclic voltammetry is an appropriate, convenient, and rather precise (± 10 mV is the usual uncertainty) method for evaluation of its acceptor properties in solution and, in some instances, in the solid phase.¹⁷ Indeed, as mentioned above, we found over 30 original CV measurements for PCBM that were reported in the past seven years (see Table 4.1). However, an analysis of these data revealed some disconcerting facts: (i) a large range in the reported electrochemical potentials caused by variations in the experimental conditions and differences in the methods of derivation of electrochemical potentials from cyclic voltammograms (i.e., onset, peak, or half-wave potentials) was found, (ii) in many studies reduction potentials are reported, but the relevant CV experimental conditions are not provided, (iii) in some works, E_{red} -derived estimates of E(LUMO) are reported but original electrochemical potentials or cyclic voltammograms are not given, and (iv) E(LUMO) estimates derived from CV data also vary over a wide range of values (-3.62 to -4.38 eV).

All this prompted us to carry out an independent CV measurement of a sample of PCBM under controlled conditions. We observed three quasi-reversible reductions, in agreement with some earlier reports (entries 11, 16, 20, 25, and 33–36 in Table 4.1). For

Table 4.1
Compilation of the data on the electrochemical potentials, conditions of the CV experiments, and $E(\text{LUMO})$ estimates for PCBM

entry	$E(\text{CV})$, V	vs.	$\Delta E/C_{60}$	std.	E_{LUMO} , eV	E_{LUMO} conversion	CV conditions solvent	electrodes ^b	electrolyte	ref.
1	n/a ^c	n/a	n/a	n/a	-4.1	$-e(E_{\text{red on}} - 4.71)$	n/a	GCE ^d /Pt/Ag	TBP ^e	45
2	n/a	n/a	n/a	FeCp ₂	-4.3	$-(E_{\text{red on}} + 4.75)$	n/a	Pt/Pt/Ag	TBAPF ₆ ^f	46
3	n/a	n/a	n/a	FeCp ₂	-3.80	n/a	CH ₂ Cl ₂	Pt/Pt/Ag	TBAPF ₆	47
4	n/a	n/a	n/a	FeCp ₂	-3.8	n/a	<i>o</i> DCB/ACN(4/1)	n/a	TBAPF ₆	48
5	n/a	n/a	n/a	FeCp ₂	-3.70	$-(E_{\text{red on}} + 4.71)$	n/a	n/a	n/a	49
6	n/a	n/a	n/a	FeCp ₂	-4.3	$-(E_{\text{red on}} - E_{1/2} + 4.8)$	n/a	Pt/Pt/Ag	TBAPF ₆	50
7	--	--	n/a	--	-3.9	$E_{\text{opt on}} + IP_{\text{PES}}$	n/a	--	--	51
8	--	--	n/a	--	-4.30	$E_{\text{opt on}} + E_{\text{HOMO}}$ (UPS)	<i>o</i> DCB	--	--	44
9	-0.64 ^g	SCE	-0.09	n/a	n/a	n/a	<i>o</i> DCB	GCE/Pt/SCE	TBAPF ₆	52
10	-0.69 ^g	NHE	-0.09	FeCp ₂	n/a	n/a	<i>o</i> DCB/ACN(4/1)	Pt/Pt/Ag	TBAPF ₆	2
11	-0.57 ^g	Ag ⁺⁰	-0.08	n/a	-3.73	$-(E_{\text{red on}} - E_{\text{red on}}^{\text{FeCp}_2} + 4.8)$	<i>o</i> DCB/ACN(4/1)	Pt/Pt/Ag	TBAPF ₆	53
12	-0.58 ^g	Ag ⁺⁰	n/a	FeCp ₂	-3.75	$[-e(E_{\text{red on}} - E_{\text{red on}}^{\text{FeCp}_2})] - 4.8$	<i>o</i> DCB/ACN(4/1)	Pt/Pt/Ag	TBAPF ₆	54
13	-0.60 ^g	Ag ⁺⁰	n/a	FeCp ₂	-3.81	$-(E_{\text{red on}} - E_{\text{red on}}^{\text{FeCp}_2} + 4.8)$	CH ₂ Cl ₂	GCE/Pt/Ag	TBAPF ₆	55
14	-0.75 ^g	Ag ⁺⁰	n/a	n/a	-3.95	$-q(E_{\text{red}} + 4.7)$	n/a	GCE/Pt/Ag	TBAPF ₆	56
15	-0.80 ^g	Ag ⁺⁰	n/a	n/a	-3.91	$-(E_{\text{red on}} + 4.71)$	<i>o</i> DCB/ACN(5/1)	Pt/Pt/Ag	TBAPF ₆	57
16	-0.84 ^g	Ag ⁺⁰	-0.08	FeCp ₂	-3.70	$-(E_{\text{red on}} - E_{\text{red on}}^{\text{FeCp}_2} + 4.8)$	<i>o</i> DCB	GCE/Pt/Ag	TBABF ₄ ^h	58
17	-0.87 ^{ij}	Ag ⁺⁰	n/a	n/a	-3.92	$-e(E_{\text{red on}} - 4.71)$	<i>o</i> DCB/ACN(5/1)	Pt/Pt/Ag	TBAPF ₆	59
18	-0.88 ⁱ	Ag ⁺⁰	n/a	n/a	-3.91	$-(E_{\text{red on}} + 4.71)$	<i>o</i> DCB/ACN(5/1)	Pt/Pt/Ag	TBAPF ₆	60
19	-0.9 ^f	FeCp ₂ ⁺⁰	n/a	FeCp ₂	-4.2	$-(E_{\text{red on}} + 5.1)$	n/a	Pt/Pt/Ag	TBAPF ₆	61
20	-0.921 ^k	FeCp ₂ ⁺⁰	-0.097	FeCp ₂	-3.88	$-(E_{\text{red}} + 4.8)$	<i>o</i> DCB/ACN(4/1)	Pt/Pt/Ag	TBAPF ₆	62
21	-0.98 ^g	Ag ⁺⁰	n/a	FeCp	-3.70	$-4.8 - (E_{\text{red on}} - E_{1/2}^{\text{FeCp}_2})$	n/a	GCE/Pt/Ag	TBAPF ₆	63
22	-1.00 ⁱ	FeCp ₂ ⁺⁰	n/a	FeCp ₂	-3.80	$-(E_{1/2} + 4.80)$	THF	GCE/Pt/Ag	TBAClO ₄	64

23	-1.00 ⁱ	FeCp ₂ ⁺⁰	n/a	FeCp ₂	-3.80	-(E _{1/2} + 4.80)	THF	GCE/Pt/Ag	TBAClO ₄	65
24	-1.05 ^g	FeCp ₂ ⁺⁰	n/a	FeCp ₂	-3.74	E _{opt on} + E _{red on}	oDCB	n/a/Pt/Ag	TBAPF ₆	66
25	-1.06 ^g	FeCp ₂ ⁺⁰	-0.08	FeCp ₂	-3.73	-[(E _{red on} + E _{ox on})/2] + 4.8	oDCB/ACN(4/1)	n/a/Pt/Ag	TBABF ₄	67
26	-1.07 ⁱ	FeCp ₂ ⁺⁰	n/a	FeCp ₂	-3.73	-(E _{1/2} + 4.8)	oDCB/ACN(5/1)	n/a	TBAClO ₄	68
27	-1.078 ⁱ	FeCp ₂ ⁺⁰	n/a	FeCp ₂	-3.722	E _{1/2}	oDCB/ACN(4/1)	n/a	TBAPF ₆	69
28	-1.08 ⁱ	FeCp ₂ ⁺⁰	n/a	FeCp ₂	-3.72 ^l	-(E _{1/2} + 4.8)	oDCB/ACN(4/1)	Ti/Ti/Ag	TBAPF ₆	70
29	-1.084 ⁱ	FeCp ₂ ⁺⁰	n/a	FeCp ₂	n/a	n/a	oDCB/ACN(4/1)	n/a	TBAPF ₆	71
30	-1.09 ^g	FeCp ₂ ⁺⁰	n/a	FeCp ₂	-4.38 ^m	-5.23 - eE _{red on} + 1/2(E _{CV} ^{sol} - E _g)	oDCB	Pt/Pt/Ag	TBAPF ₆	72
31	-1.13 ⁱ	FeCp ₂ ⁺⁰	n/a	FeCp ₂	-3.67	-(E _{1/2} + 4.8)	CB/ACN(5/1)	Pt/n/a/n/a	TBAPF ₆	73
32	-1.15ⁱ	FeCp₂⁺⁰	-0.09	FeCp₂	n/a	n/a	oDCB	Pt/Pt/Ag	TBABF₄	tw
33	-1.158 ⁱ	FeCp ₂ ⁺⁰	-0.087	FeCp ₂	n/a	n/a	oDCB	Pt/Pt/Ag	TBAClO ₄	74
34	-1.163 ⁱ	FeCp ₂ ⁺⁰	-0.086	FeCp ₂	n/a	n/a	oDCB	Pt/Pt/na	TBAClO ₄	75
35	-1.169 ⁱ	FeCp ₂ ⁺⁰	-0.113	FeCp ₂	n/a	n/a	oDCB	Pt/Pt/Ag	TBABF ₄	1
36	-1.18 ⁱ	FeCp ₂ ⁺⁰	-0.08	FeCp ₂	-3.62	-(E _{1/2} + 4.8)	oDCB	GCE/Pt/Ag	TBAPF ₆	76
37	-1.21 ⁱ	FeCp ₂ ⁺⁰	n/a	FeCp ₂	-3.80	E _{red on} + 4.835	oDCB	GCE/Pt/Ag	TBAPF ₆	77

^aΔE/C₆₀ = E_{PCBM} - E_{C60} ^bElectrodes reported as working/counter/(quasi)reference electrode. ^cn/a = not reported or available. ^dGCE is a glassy carbon electrode. ^eTBP is 4-*tert*-butylpyridine. ^fTBAPF₆ is tetrabutylammonium hexafluorophosphate. ^gOnset of the first reduction. ^hTBABF₄ is tetrabutylammonium tetrafluoroborate. ⁱE_{1/2} of the first reduction. ^jThe authors also report reduction onset potentials for PCBM, C₆₀, and ferrocene, which were used for the E_{LUMO} conversion (see ref.⁵⁹). ^kPeak reduction potential. ^lGiven as electron affinity, EA. ^mReported as “effective” LUMO, see reference ⁷⁸ for details.

a reversible (or quasi-reversible) redox event, the first half-wave potential, $E_{1/2}$, is defined as $1/2(E_{pa} + E_{pc})$, where E_{pa} and E_{pc} are anodic and cathodic peak potentials, respectively. In our hands, the $E_{1/2}$ for PCBM in *o*-DCB is $-1.15(1)$ V vs $\text{Fe}(\text{Cp})_2^{+/0}$. This result is in good agreement with some literature values (entries 31, 33–36 in Table 4.1) but is significantly different from other reports (entries 19, 20, 22–30, 37). Detailed analysis of the experimental conditions listed in Table 4.1 reveals that variations in solvent composition, supporting electrolyte, and electrodes are the most likely sources of the observed differences, as shown previously for C_{60} .¹⁸ For example, changing the solvent from dimethylformamide to dichloromethane to *o*-DCB changes the $E_{1/2}$ value for C_{60} from -312 to -468 to -535 mV vs $\text{Fe}(\text{Cp}^*)_2^{+/0}$, respectively.¹⁸ It appears that the solvent has an effect on the $E_{1/2}$ of PCBM, too; the value measured in tetrahydrofuran differs by ca. 60 mV from that in *o*-DCB (entries 22 and 30 or 31). The CV measurement in dichloromethane (entry 13) cannot be used for such a comparison because the $E_{1/2}$ value was not reported. Use of reduction potentials versus different references (e.g., NHE, $\text{Ag}^{+/0}$) in entries 10–18 and 21 in Table 4.1 results in further E(LUMO) dispersion due to the use of different conversion factors (see the ELUMO conversion column in Table 4.1). All of the E(LUMO) values in Table 4.1 were derived from electrochemical measurements with the exception of entries 9 and 10, which were calculated by adding the optical absorption onset energy to the measured IP. This method, however, ignores the exciton binding energy contribution to the electronic gap. It is noteworthy that these two values differ by 400 meV (i.e., -3.9 and -4.3 eV).

Cardona et al. recently discussed in detail the many considerations that must be taken into account when determining HOMO/LUMO levels for conjugated polymers from cyclic voltammetry, with emphasis on the origin of conversion factors.¹⁹ For measurements on polymer films deposited on an electrode, it is common that the reduction or oxidation events are

irreversible, and therefore the onset or peak potentials are often evaluated. However, fullerenes and their derivatives normally show several reversible or quasi-reversible redox events by CV. In contrast to a well-defined electrochemical half potential, $E_{1/2}$, there is no well-defined equation for the determination of onset reduction or oxidation potentials (E_{on}) in cyclic voltammetry, which leads to arbitrary assignments and discrepancies between the data from different laboratories when different evaluation methods are used.

Variations in the conversion factors (from 4.7 to 5.23 eV, see Table 4.1, which correspond to onset potentials for ferrocene converted to the gas-phase (see ref 19 for full details)) used by different authors to evaluate the E(LUMO) of PCBM contribute to the wide range of values found in the literature. Additionally, the inconsistent use of onset, peak, or half-wave potentials for the E(LUMO) conversion also leads to the great deal of uncertainty in the E(LUMO) value for PCBM. It can easily be seen how rapidly errors can propagate if the appropriate conversion factor and CV data evaluation methods are not chosen carefully. We urge caution to researchers when selecting a literature E(LUMO) value for applications where frontier orbital energy matchups are vital for device operations.

In order to minimize accumulation of discrepancies in the CV-derived electronic level characteristics of fullerenes and their derivatives due to differences in data interpretation and experimental conditions used from lab to lab, we propose adopting a practice of measuring CVs for new fullerene acceptors using two references: (i) ferrocene (or decamethylferrocene if appropriate, both of which are universally accepted internal standards) and (ii) fullerene C_{60} . The latter compound exhibits reversible reductions, it is ubiquitously present in all laboratories dealing with fullerenes, and it is relatively inexpensive and commercially available with a reasonable purity of 99.5%. When C_{60} is measured in the same laboratory (and under identical

conditions), it should provide researchers with a simple but effective and fairly reliable approach to the construction of a universal electrochemical scale for fullerene-based electron acceptors that will be usable by other researchers across different laboratories as well. For example, nine of ten entries (not including our own) in Table 4.1 (9–11, 16, 20, 25, 33–36) represent studies in which reduction potentials were measured for C_{60} under the same conditions as for PCBM. The resulting ($E(\text{PCBM}) - E(C_{60})$) values are equal to within 10 mV, with PCBM being 80–90 mV more difficult to reduce (i.e., it is a weaker electron acceptor) than C_{60} . At the same time, the absolute values of reduction potentials reported in these studies differ by more than 300 mV (this does not include the potential measured vs $\text{Ag}^{+/0}$, entry 16, which needs to be converted to the $\text{Fe}(\text{Cp})_2^{+/0}$ scale if included). This suggests that while the absolute values of the reduction potentials for PCBM and C_{60} can vary significantly with varying experimental conditions and methods of data derivation, their difference remains nearly constant. As shown in Figure 4.2, we have measured the first four quasi-reversible reductions of C_{60} under the same experimental conditions as PCBM and determined the $E_{1/2}(\text{PCBM})$ value to be -0.09 V versus C_{60} , in excellent agreement with the literature data discussed above. Evaluations of fullerene acceptor strength based on gas- or solution-phase measurements or DFT calculations have been used by researchers with the understanding that such approaches are only indirect methods since

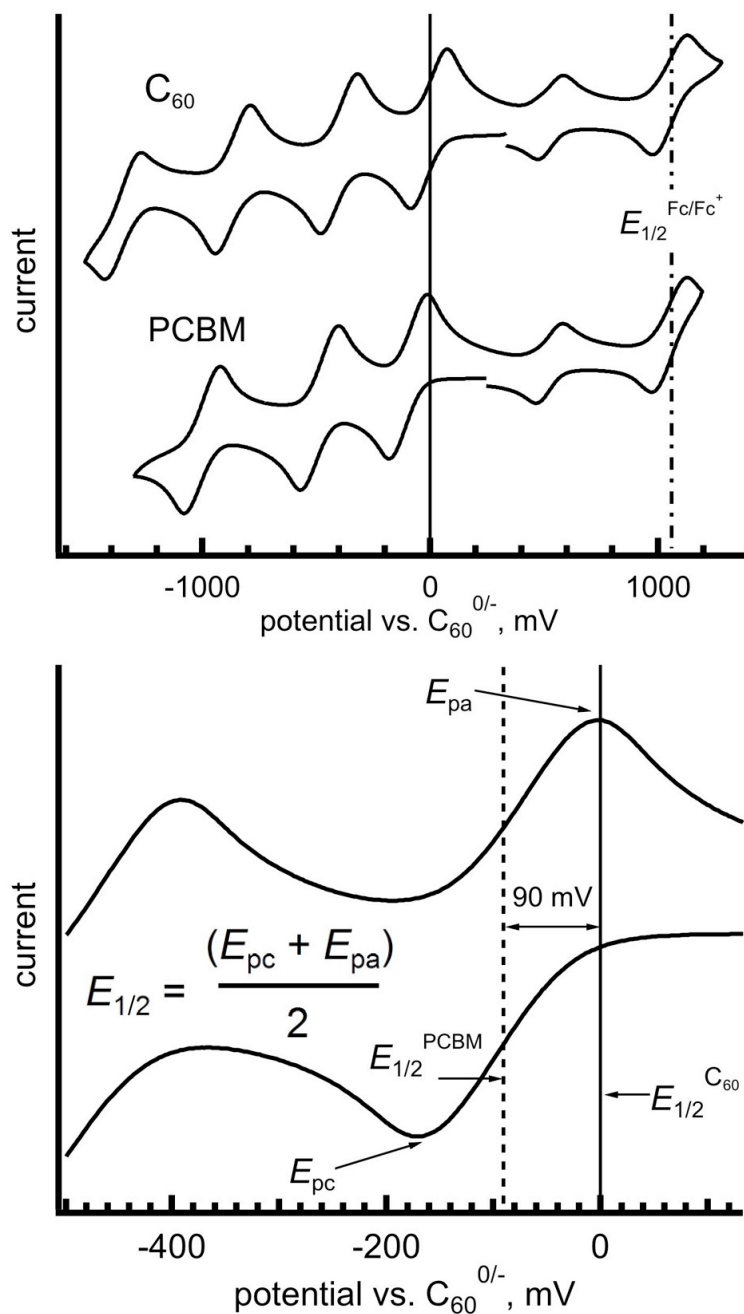


Figure 4.2. Top: cyclic voltammograms for C_{60} and PCBM in *o*-DCB with $Fe(Cp^*)_2$ and $Fe(Cp)_2$ internal standards (see experimental section for full details). The $E_{1/2}$ of $Fe(Cp)_2$ is represented by the vertical dash-dotted line at 1.05 V vs $C_{60}^{0/-}$. Bottom: an expansion of the CV with the first reduction of PCBM is shown, with cathodic (E_{pc}) and anodic (E_{pa}) peak potentials labeled. The $E_{1/2}$ is the midpoint of E_{pa} and E_{pc} and is represented by the vertical dashed line. The vertical black solid line corresponds to the $E_{1/2}$ of C_{60} , referenced at 0.00 mV in both the inset and main figure.

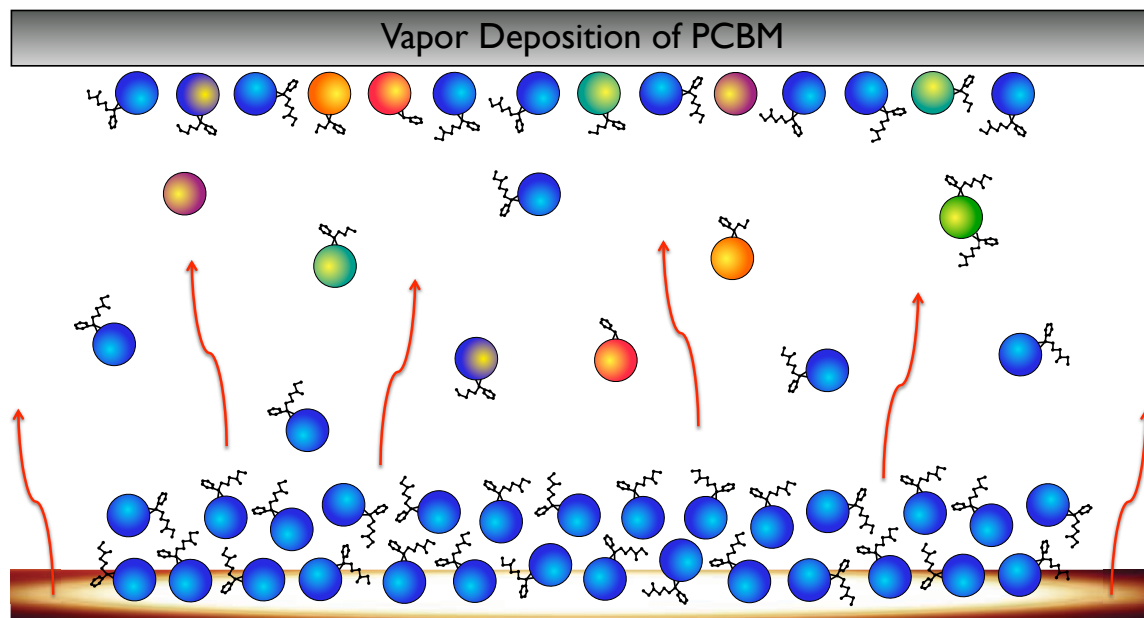
they do not account for effects of the condensed phase. Therefore, efforts continue, both on experimental and theoretical fronts, to develop techniques that would provide reliable data on solid-state EAs of organic materials.

Inverse photoelectron spectroscopy (IPES) is considered a promising tool for direct determination of the solid-state EA.²⁰ Another approach involves solid-state electrochemical measurements, in which solid films deposited on an electrode are studied.¹⁷ Recently, the EA of a spin-cast PCBM film, measured by IPES, was reported to be 3.80 eV (no error reported; spectrometer resolution = 0.45 eV).²⁰ In 2008, a value of 3.9 ± 0.1 eV (spectrometer resolution = 0.4 eV)²¹ was reported for a similar experiment, but using a film of PCBM that had been vapor deposited. Typically, vapor deposition performed under high vacuum allows for preparation of high-quality films of thermally stable compounds. However, PCBM has not been considered as a thermally stable compound. In 2003, Rispen and Hummelen wrote “PCBM (like virtually all fullerene derivatives) cannot be evaporated without substantial decomposition.”²² However, no relevant study supporting this statement about PCBM can currently be found in the literature. Therefore, the feasibility of the vapor deposition method for PCBM in IPES studies remains under question until thorough studies are carried out to address the thermal stability of PCBM (these studies were carried out and are discussed in the following section of this dissertation). Furthermore, because of the large uncertainties in solid-state EA values caused by the low resolution of IPES spectrometers, use of this technique for evaluation of the relative strengths of acceptors from families of chemically closely-related compounds are currently problematic.

4.2.4. Summary and Conclusions. This work reports the first experimentally determined EA value for PCBM in the gas-phase, which may serve as a reference for further elaboration of the theoretical methods for EA calculations because currently DFT methods do not agree well

with experimental data. Compilation and analysis of the available data on solution electrochemical studies of PCBM revealed a large discrepancy in reported reduction potentials, whereas the difference in the $E_{1/2}$ values between PCBM and C_{60} is shown to remain nearly constant regardless of the experimental conditions. We therefore propose to construct a scale of relative acceptor strength for new fullerene acceptor molecules based on CV measurements in which C_{60} and ferrocene/decamethylferrocene are used as standards. The current solid-state EA data for PCBM and many other organic acceptors suffer from low precision and large experimental uncertainties, and this calls for further improvements in the relevant experimental techniques.

4.3. Thermal Properties of PCBM



4.3.1. Introduction

High thermal stability is one of the desired properties of fullerenes and fullerene derivatives that lends well towards applications in organic-electronic technologies such as OPVs, OLEDs, and OFETs. Of all fullerene derivatives, PCBM is the best studied and also one of the

best performing materials in these devices,³ and has been widely used in both fundamental and applied organic semiconductor studies.^{4,5,6,7,8,9} However, no reports to date have been dedicated to studying the thermal stability limits of this technologically important compound. At the same time, post-fabrication thermal annealing treatments of PCBM-containing OPV devices have been shown to drastically improve device efficiency and are now common practices in polymer solar cell research.^{10,11} In contrast, it was shown that prolonged thermal treatments decrease cell performance¹² and that high-temperature annealing leads to decreased charge carrier lifetimes in microcrystalline PCBM.¹³ Some remarks that PCBM thermally decomposes have been made in the literature (though without compelling relevant supporting data).^{14,15} Furthermore, the decomposition temperatures that have been mentioned in the literature for PCBM and PCBM-like fullerene derivatives are inconsistent, ranging from 200 °C to 400 °C.^{13,16,17,18,19,20} At the same time, numerous studies involve films of PCBM prepared by high-vacuum thermal evaporation for layered organo-electronic applications^{21,22,23,24,25} or to study the solid-state properties of the film.^{26,27} There is a general consensus among the researchers that organic fullerene derivatives are more susceptible to decomposition during thermal evaporation than bare-cage fullerenes such as C₆₀ or C₇₀. For example, detrimental effects of thermal treatment on the molecular composition were clearly demonstrated for hydrofullerenes,²⁸ whereas fluorofullerenes were shown to sublime without decomposition.²⁹

In this section, the physical, chemical, and electrochemical effects of (i) thermal annealing of PCBM films or powders over a temperature range of 180–380 °C and (ii) vapor deposition of PCBM are described, which are based on high-performance liquid chromatography, cyclic voltammetry, NMR spectroscopy, thermogravimetric analysis, and mass spectrometry. In addition, the major product of thermal decomposition of PCBM has been

isolated, characterized, and identified as a new isomer of PCBM that forms at high temperatures in the PCBM melt.

4.3.2. Experimental Section.

Commercially available PCBM powder (Nano-C, 99%) and all solvents (Fisher Scientific, HPLC grade) were used as received. Vacuum sublimation was carried out in an Edwards Auto306 vapor deposition chamber by resistively heating the sample in a tungsten boat at a base pressure of 7×10^{-6} Torr and deposition rate of 0.7 \AA s^{-1} as monitored by an LQC crystal mass balance. HPLC analysis and separation was performed using Shimadzu instrumentation (CBM-20A control module, SPD-20A UV-detector set to 300 nm detection, LC-6AD pump, manual injector valve) equipped with a 20-mm I.D. \times 250 mm preparative Cosmosil Buckyprep column (Nacalai Tesque, Inc.) with toluene as eluent at a flow rate 16 mL min^{-1} . Negative and positive ion APCI mass spectra were recorded using a Finnigan LCQ-DUO mass spectrometer with acetonitrile carrier solvent (samples injected in toluene:acetonitrile mixtures) at a flow rate of 0.3 mL min^{-1} . Proton-1 NMR spectra were recorded using a Varian INOVA 400 MHz spectrometer with samples in CDCl_3 (TMS internal standard). Cyclic voltammograms were recorded using an in-house one-compartment electrochemical cell with a PAR 273 potentiostat/galvanostat at room temperature in a dinitrogen atmosphere glovebox. Thermogravimetric analysis was accomplished using a TA Instruments 2950 Series TGA at a heating rate of $3 \text{ }^\circ\text{C min}^{-1}$ in He atmosphere using a platinum sample boat. Cyclic voltammetry experiments were carried out as described in the previous section.

4.3.3. Results and Discussion

4.3.3.1. Thermal Behavior of PCBM

Thermogravimetric analysis (TGA) is a useful technique for determining thermally induced changes in physical and chemical properties of a compound, and therefore was used to study the thermal behavior of PCBM. Figure 4.3 shows the TGA thermogram of PCBM heated to 600 °C. A gradual mass loss of about 0.5% was observed up to 345 °C, followed by a mass loss of 9.6% out to 600 °C. This result is consistent with the literature TGA thermograms for PCBM^{13,16,18,20,30} and PCBM-like^{16,17} derivatives. The calculated mass change associated with decomposition by full loss of PCBM's methano-adduct to C₆₀ is a loss of 20.9%, which is not consistent with the mass loss of 9.6% observed. The char-like, mostly insoluble, residue remaining after the TGA experiment was extracted with toluene and analyzed by HPLC (Figure 4.3. inset), and was found to contain primarily C₆₀ based on color, its UV-vis spectrum, and having the same HPLC retention time as a C₆₀ reference. This means that while C₆₀ was indeed formed as a decomposition product, the majority of the mass of the sample was retained. This suggests that fragments of the adduct must have participated in inter- or intra-molecular bonding (likely some complex cross linking) of the fullerene network forming

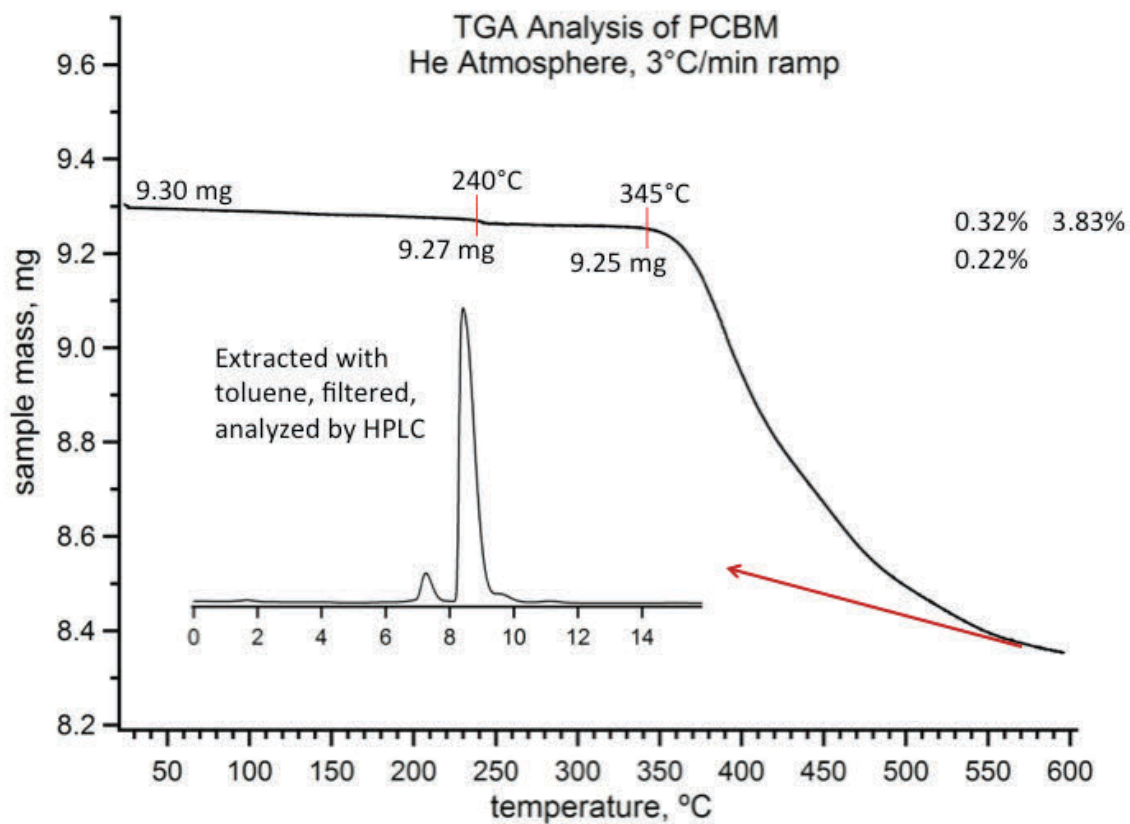


Figure 4.3. Thermogravimetric analysis of PCBM. Inset: HPLC chromatogram of the solvent-extracted char after the TGA experiment.

oligomers and polymers, which is consistent with the fact that a significant portion of the sample was insoluble after the TGA experiment and also with the lower mass loss (9% vs. predicted 20.9%). The results also indicate that chemical transformation takes place when PCBM is heated to high temperatures.

To determine the nature and onset temperature threshold of these thermally induced chemical changes to PCBM, a series of experiments involving its thermal treatment were carried out in the temperature range of 180 to 380 °C. This range was chosen for two reasons: (i) it includes the temperature range within which mass loss was seen in the TGA thermogram, and (ii) it practically covers annealing temperatures commonly applied for studies related to PCBM thermal properties, especially phase behavior studies. Each PCBM sample (approximately 1 mg) was heated for 20 minutes in a TGA instrument at constant temperature under N₂ flush and then analyzed by HPLC and ¹H NMR spectroscopy. No detectable decomposition of PCBM was found by HPLC or proton NMR spectroscopy in the samples heated at 260 °C or below (Figures 4.4 and 4.5). This indicates that the mass loss feature observed in the thermogram in Figure 4.3 at 240 °C is not due to a chemical change in PCBM, but more likely a loss of trace solvent molecules. Interestingly, heating at 300 °C resulted in some decomposition as evidenced by appearances of new peaks in the HPLC chromatogram and ¹H NMR spectrum (see Figures 4.4 and 4.5), however, the entire sample dissolved readily in toluene after the heating treatment (i.e., no insoluble material was formed). When heated to 340 °C, massive decomposition was observed by HPLC analysis and by ¹H NMR spectroscopy, and insoluble char was formed as observed after extraction with toluene. Additionally, effects of duration of thermal treatment were tested. Heating PCBM for 60 minutes at

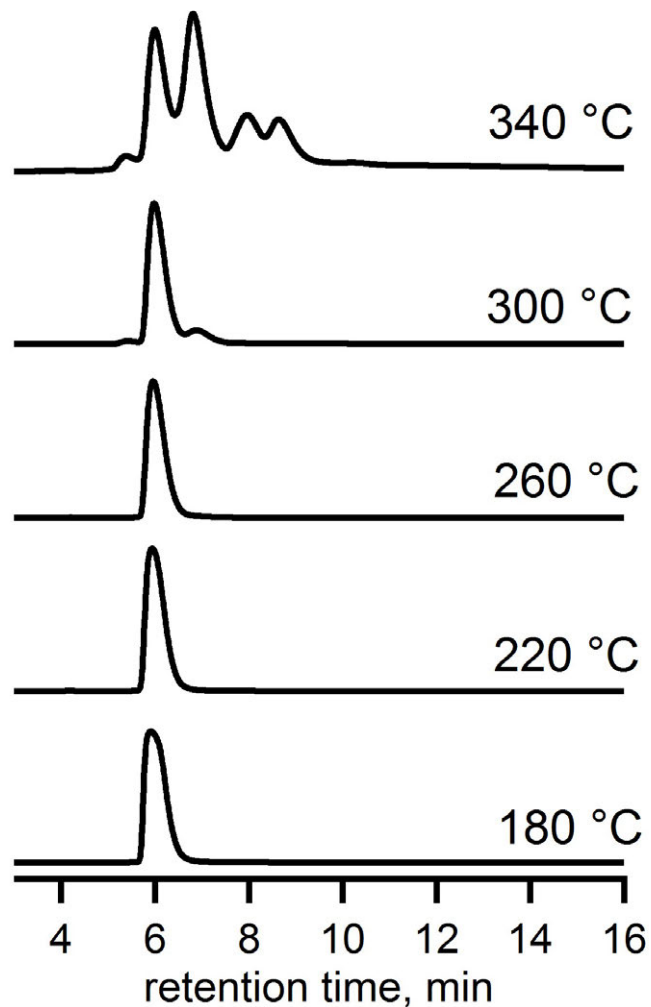


Figure 4.4. HPLC chromatograms for a series of PCBM samples that were heated for 20 minutes at temperatures in the range of 180–340 °C. Toluene eluent and 5 mL min⁻¹ flow rate was used for each analysis (10 x 250 mm Cosmosil Buckyprep column) at 300 nm detection.

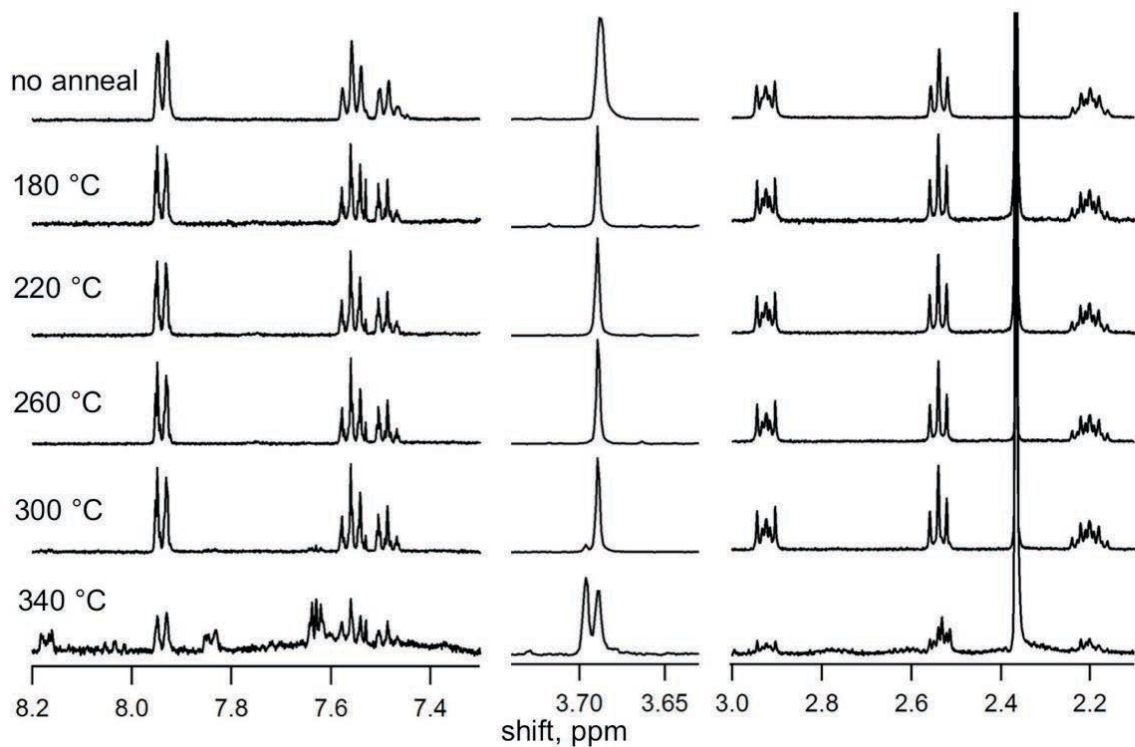


Figure 4.5. Relevant portions of the ^1H NMR spectra (400 MHz, CDCl_3 , TMS std.) are shown for commercial PCBM (top) and samples heated over the temperature range of 180–340 °C.

280 °C resulted in the same degree of decomposition as when the sample was heated for 20 minutes at 300 °C (Figure 4.4), indicating decomposition does occur at lower temperatures during longer periods of heating. The rate of degradation appears to increase drastically as temperatures exceed 300 °C. This observation merits caution be taken when PCBM-containing devices or sample preparation techniques require prolonged heating at elevated temperatures (i.e. $T > 280$ °C). In an experiment aimed to determine the long-term thermal stability of PCBM, we heated a PCBM sample in the TGA instrument for 6 hours at 220 °C and found negligible decomposition (<1% by HPLC chromatogram integration).

It is noteworthy that the samples heated below 300 °C remained as powders while the samples heated above 300 °C appeared glassy after heating, indicative of melting. This is consistent with the reported melting temperatures of PCBM in the literature that range 273 °C to 290 °C.^{20,31,32} Apparently, the observed decomposition of PCBM occurs when the sample is in liquid phase.

4.3.3.2. Formation, Isolation, and Characterization of a New Isomer of PCBM.

Presence of several discrete peaks in the HPLC chromatogram of the 340 °C sample prompted a larger scale experiment in order to isolate individual decomposition products. A 20.13 mg sample of PCBM was annealed at 340 °C for 20 minutes under constant N₂ flush in a TGA instrument and subsequently separated by HPLC. Better resolution of peaks was achieved by using a volume/volume mixture of 80/20 toluene/hexanes that facilitated single-stage isolation of decomposition products in higher purity. Indeed, as shown in the chromatogram in Figure 4.6, this procedure improved separation of peaks since additional peaks that co-elute in toluene eluent (Figure 4.6 top vs. Figure 4.6 bottom) were revealed. The two major components of the sample isolated by HPLC were Fraction 1 (r.t. = 7.9–9.0 min) and Fraction 2 (r.t. = 9.9–10.9 min).

Fraction 1 (confirmed as PCBM by ^1H NMR, UV-Vis, and APCI-MS, see below) constituted 22% of the chromatogram by total area integration, while Fraction 2 represented 41%. Five other minor peaks were also present having both longer and shorter r.t.'s than PCBM and were also collected. Each fraction, as well as a sample of pristine commercial PCBM, was then analyzed by atmospheric pressure chemical ionization mass spectrometry (APCI-MS) and ^1H NMR spectroscopy. The five smaller fractions were also characterized, but structures could not be completely assigned. Figures 4.7 and 4.8 show the APCI-MS spectra and ^1H NMR, respectively, for those fractions.

Negative ion APCI-MS is a useful technique for analysis of fullerenes, since in general they readily get ionized by accepting an electron and have good solubility; it is also suitable for analysis of fullerene derivatives due to soft ionization conditions that suppress fragmentation. The case for PCBM is no different, even though its electron affinity is slightly lower than that of C_{60} .³³ The mass spectrum of Fraction 1 (PCBM) is shown on the left in Figure 4.7 and reveals the singly charged molecular ion, at m/z 910. To our surprise, APCI-MS also revealed that the major decomposition product, Fraction 2, has the same molecular mass as PCBM, indicating isomerization is the main pathway of thermally-induced chemical transformation. The only other known isomer of PCBM is the [5,6]-fulleroid, which is known to thermally isomerize to the more stable [6,6]-methanofullerene PCBM at fairly low temperatures in solution.³⁴ The [5,6]-isomer was ruled out as based on its ^1H NMR spectrum (see below) and color ([5,6]-PCBM and C_{60} are both purple in toluene, while Fraction 2 was red-brown). Collision-induced dissociation

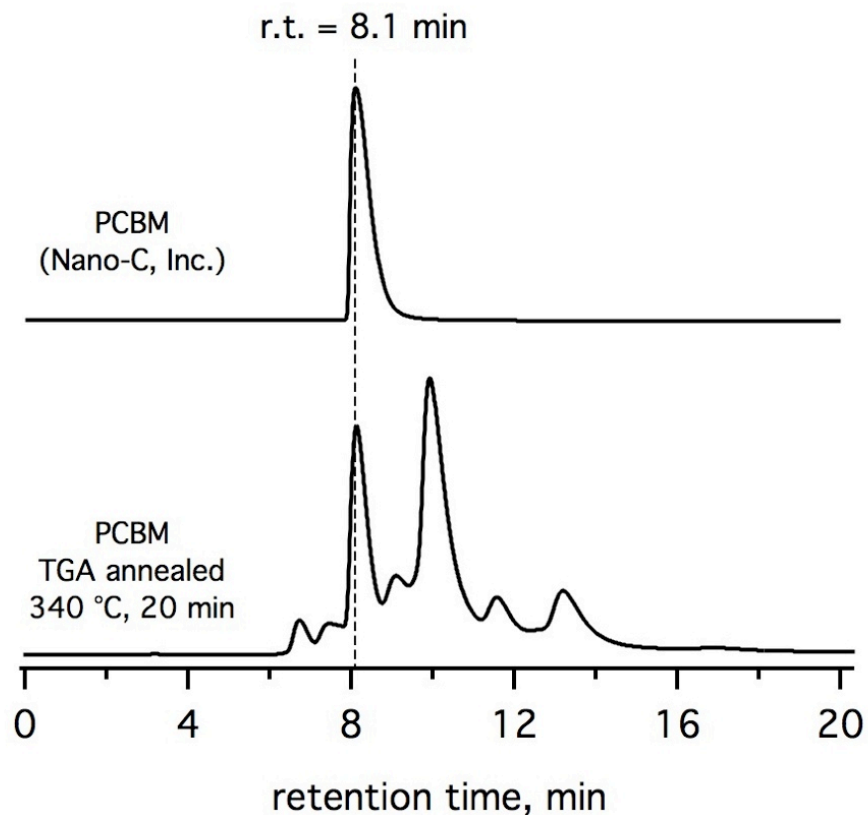


Figure 4.6. HPLC chromatograms (300 nm detection) are shown for a commercial sample of PCBM (top) and a sample that was annealed at 340 °C for 20 minutes under dinitrogen atmosphere using a thermogravimetric analysis instrument (bottom). The retention time of PCBM using a Cosmosil Buckyprep column (10 x 250 mm) is 8.1 minutes at a flow rate of 5.0 mL min⁻¹ with 80/20 V/V toluene/hexanes eluent mixture.

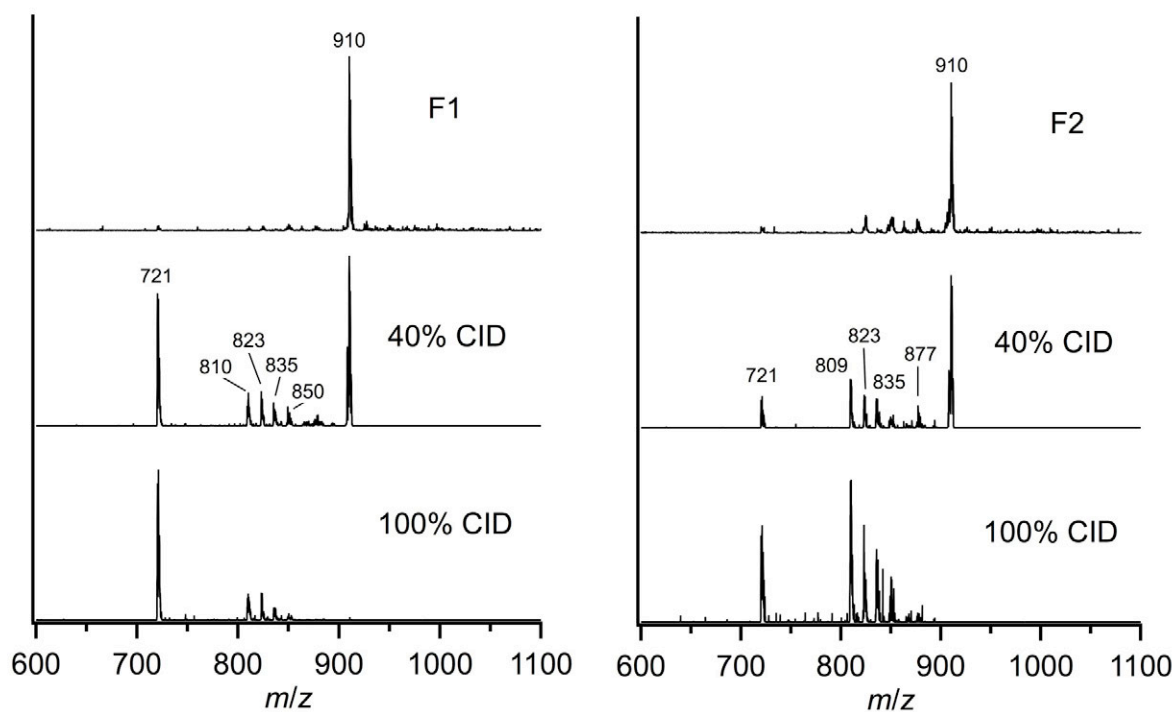


Figure 4.7. The negative ion mass spectra shown correspond to the fractions isolated by HPLC from the heated PCBM sample. The left panel is Fraction 1 (identical to commercial PCBM, not shown) and the right panel is Fraction 2. Top to bottom for each panel shows the parent molecule, 40% collision energy, and 100% collision energy, respectively, in MS/MS mode.

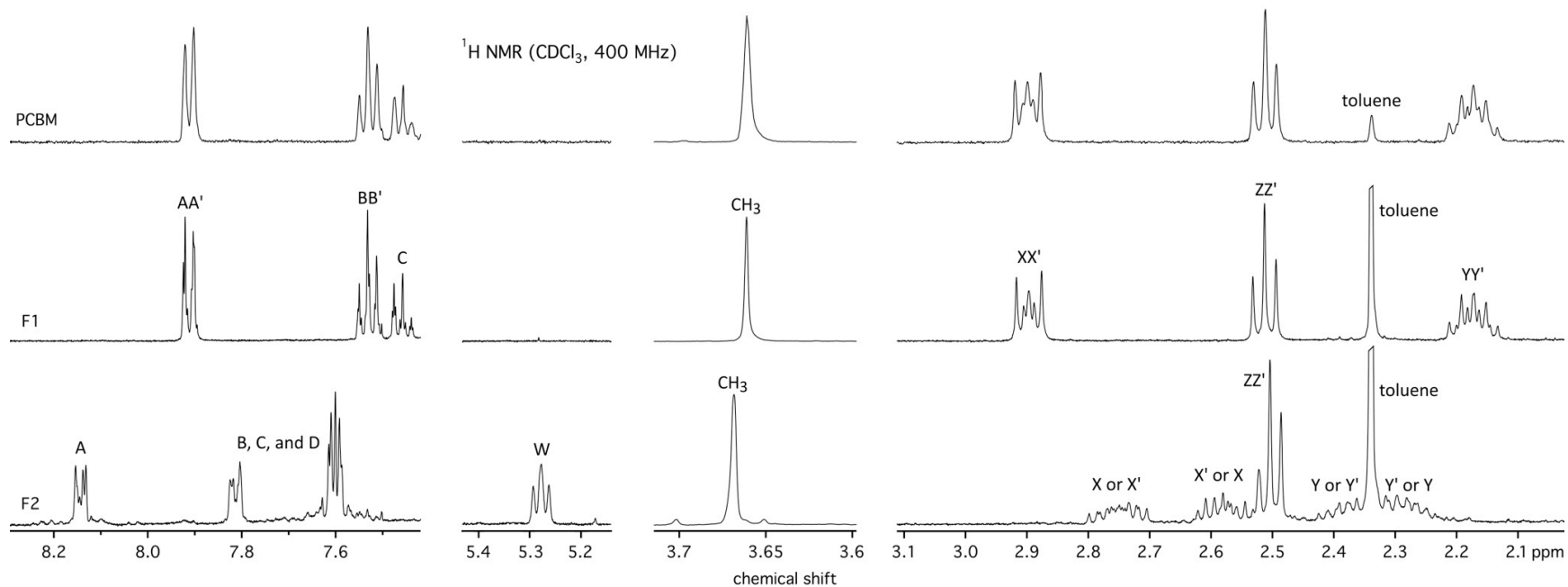


Figure 4.8. Relevant portions of the $^1\text{H NMR}$ spectra for PCBM, Fraction 1, and Fraction 2 (top to bottom, respectively) in CDCl_3 using a 400 MHz instrument. Relative integration values are shown above each shift. The large off-scale singlets in each spectrum at approximately 2.36 ppm belong to methyl protons of a toluene impurity.

(CID or MS/MS) experiments were performed on the 910 m/z signal in Fraction 1 (PCBM) and Fraction 2, giving insight into the possible structure of the isomer of PCBM. At 40% CID energy, the key difference between PCBM and its isomer is the intensity of the signal at m/z 721 due to full cleavage of the methano-adduct corresponding to the $C_{60}H^-$ ion. For Fraction 2, this signal is over three times lower than for Fraction 1, meaning the isomer of PCBM does not cleave to bare C_{60} as readily as PCBM does in the mass spectrometer under identical conditions.

At 100% CID energy, 721 m/z is again the largest signal for Fraction 1, but not for Fraction 2. Instead, the CID spectrum of m/z 910 from Fraction 2 contains high intensity anions due to fragmentation following loss of methoxy, carbonyl, and butyl chain (ca. 877 to 810 m/z). Noteworthy, all of the fragment masses observed down to C_{60} appear in both samples. This means that little or no structural change occurs to the butyl methyl ester chain upon isomerization. These findings also suggest that for the new isomer of PCBM (i.e., Fraction 2), the exohedral adduct is more strongly bound to the C_{60} cage *and* all of the functional moieties (i.e. methoxy, carbonyl, butyl chain, and phenyl ring) are present and intact.

Analysis of the 1H NMR data recorded for Fractions 1 and 2 revealed the following. The proton NMR shifts in Fraction 1 are identical to those observed for the commercial PCBM sample (Figure 4.8). Due to free rotation of the phenyl ring portion of PCBM's adduct, the *ortho*- and *meta*-position protons are equivalent, giving rise to only three signals in the phenyl region of the spectrum for PCBM, including the *para*-proton's signal. However, in the phenyl region of Fraction 2, there are four signals accounting for four protons: two overlapping triplets and two doublets. The apparent doublet at δ 8.15 represents a highly deshielded nucleus in the AA'BB' arene system, which likely arises due to close proximity of that proton to the pi network on the

C_{60} cage, as has been shown for rigid methylene protons in indene- C_{60} -monoadduct.³⁵ The A' proton signal at δ 7.81 ppm is shifted 0.34 ppm upfield compared to PCBM.

These experimental data are consistent with the formation of a new five-membered carbocycle at the 1,2-positions of the phenyl ring in the new isomer of PCBM (Figure 4.9, right). Consistent with this proposed structure is the triplet observed at ca. 5.30 ppm accounting for one proton, which is typical chemical shift for protons on five-membered rings on C_{60} (5.0–7.0 ppm).^{36,37} The methoxy protons of PCBM are at ca. 3.66 ppm, and are only slightly different in the compound from Fraction 2, at 3.67 ppm. The analysis of the alkyl region of the spectra reveals more stark differences between two isomers. Due to the broken symmetry in the new isomer, four signals (i.e., three multiplets and one triplet), account for 6 protons versus three signals (i.e., two multiplets and one triplet) in the spectrum of PCBM with effective C_s symmetry. Clearly, the protons on the butyl chain of PCBM, that are closer to the cage, exhibit more second-order coupling due to the cage pi-system. This effect is observed to an even greater extent in the spectrum of Fraction 2, so much so that the alpha and beta protons on the first carbon atom extending from the cage are not equivalent (shifts at 2.75 and 2.59 ppm). Consistent with the new five-membered ring formation would be the sterics introduced that inhibits rapid free-rotation about the C-C(cage) bond, considering that would demand very close proximity of protons on the adjacent carbon atom to the cage. These protons

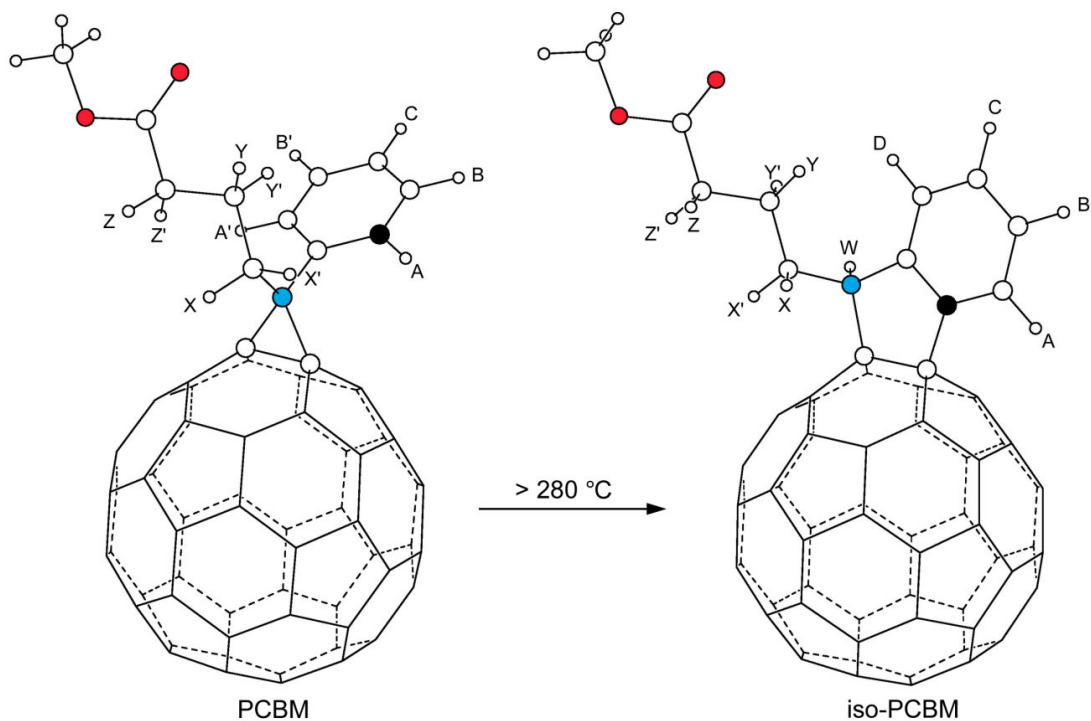


Figure 4.9. DFT-optimized structures of PCBM and the proposed isomer iso-PCBM (red atoms are O atoms). The labeled H atoms correspond to their NMR assignments (see Figure 4.8). The H_W atom in iso-PCBM was one of the H_{AA} atoms in PCBM, and the methinyl C atom to which H_W is attached in iso-PCBM (blue) was the quaternary methano C atom in PCBM.

do indeed experience a different chemical environment and more second-order coupling than those in PCBM, resulting in a broader multiplet at 2.20–2.43 ppm as opposed to a smaller multiplet at 2.19 ppm. Finally, the methoxy protons, which are six positions along the butyl methyl ester chain away from C₆₀ show up in nearly the same position as in PCBM and classic first-order coupling as a triplet at 2.50 ppm. Therefore, the proposed structure of the compound in Fraction 2 is an isomer of PCBM is a five-membered ring attached to the cage and fused to a phenyl ring, with the butyl methyl ester moiety unchanged in the structure. The exact mechanism of this thermally induced isomerization is unclear at this point, but certainly involves opening of the cyclopropyl (methano-addition) ring, abstraction of a hydrogen atom from the phenyl ring and formation of the cyclopentyl ring addition to the cage. The proposed structure (Figure 4.9) is also consistent with the APCI-MS data in that a compound with a five-membered ring attachment motif to C₆₀ is expected to be a more stable than one with a three-membered cycle, and therefore would show less fragmentation of the parent molecule to C₆₀ under identical mass-spectrometer conditions (as seen in Figure 4.7).

4.3.3.3. Sublimation Study of PCBM. Low-pressure vapor deposition is a technique well suited for preparation of high quality and impurity-free thin films and has been successfully implemented in the fabrication of OPVs containing C₆₀ and copper(II) phthalocyanine.³⁸ thermal evaporation has been utilized for fabrication of organic electronic devices such as OPVs^{21,22,24,25} and OLEDs,²³ as well as for fundamental property measurements such as solid state EA.^{26,27} However, consequences of using this technique for molecular composition of thin films of the C₆₀ derivative PCBM have not been addressed in the literature.

A series of experiments were designed and implemented in this work that tested viability of vapor deposition technique for preparation of thin films of PCBM with preserved uniform molecular composition. For this purpose, a vapor deposition chamber, similar to those commonly found in OPV research laboratories, was used to prepare vapor-deposited PCBM samples in order to determine if thermal evaporation leads to the same decomposition observed in the thermal treatment experiments. After the sublimed material was deposited onto a substrate in the vacuum chamber, it was exposed to air and then dissolved in toluene for subsequent analyses. First, this sublimate was analyzed by HPLC. Likewise, the evaporation boat residue material was extracted with toluene and analyzed by HPLC. The residue material was comprised of a significant amount of gray insoluble char (see Figure 4.10 for photos). The temperature of the evaporation boat during the sublimation was not known, but estimated to be at least 340 °C based on the fact that the heating process produced insoluble char, which was not observed in thermal annealing experiments below that temperature (discussed in Section 4.2.3.2.). A sample of PCBM was also analyzed by HPLC for reference, exhibiting a single peak eluting at r.t. 5.5 minutes (Figure 4.11). In contrast, many peaks eluting between 5 and 10 minutes were present in the HPLC chromatogram of the sublimate; integration of the total chromatogram area reveals that the 5.5-min peak (assigned as PCBM) constitutes only 41%¹. In the HPLC chromatogram of the residue, several peaks eluting between 4.5 and 11 minutes were also observed, of which the PCBM peak at 5.5 minutes constituted only

¹ We note that these percentages rely on the assumptions that each compound eluting has the same or a very similar absorption coefficient at 300 nm and that the PCBM peaks in the sublimate and residue are not co-eluting with other decomposition products.

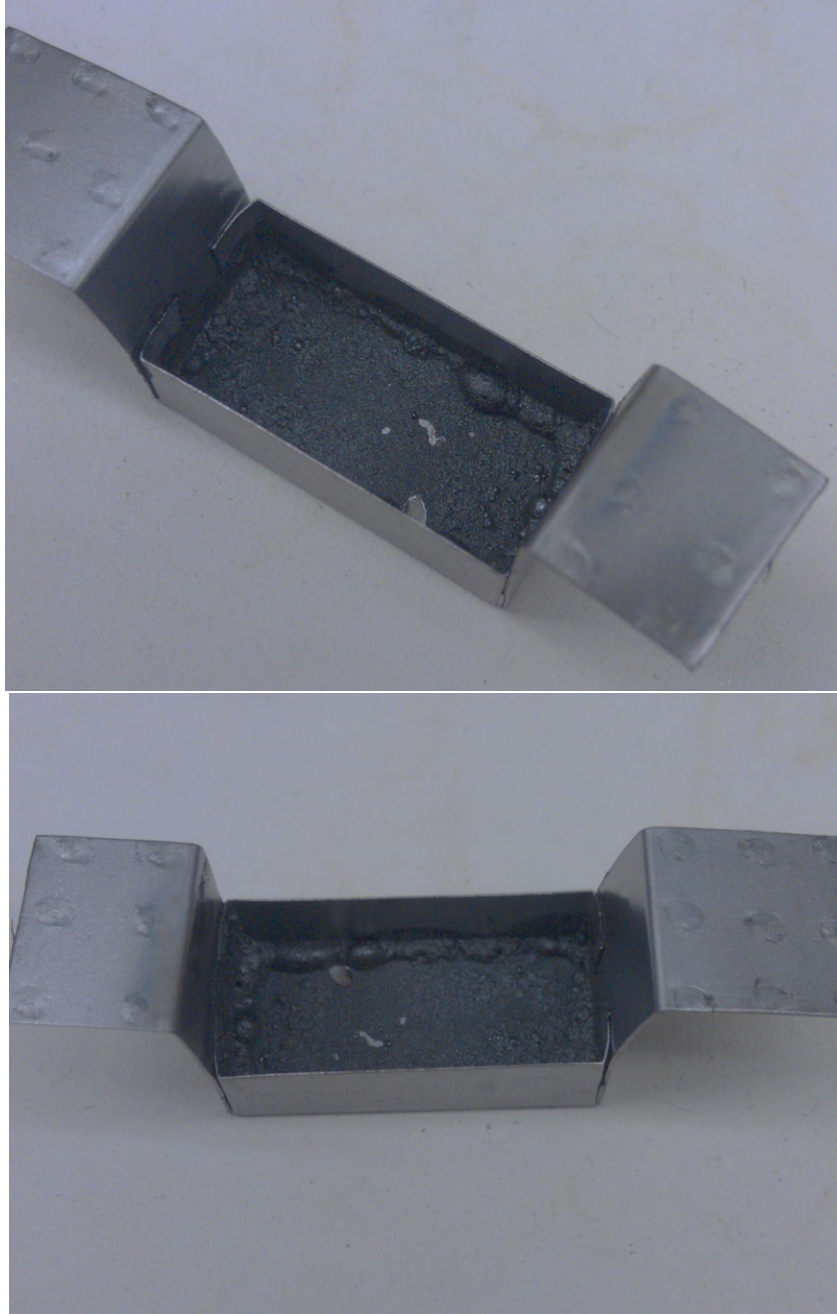


Figure 4.10. Pictures of the tungsten evaporation boat, showing black molten char residue, remaining after the PCBM evaporation experiment.

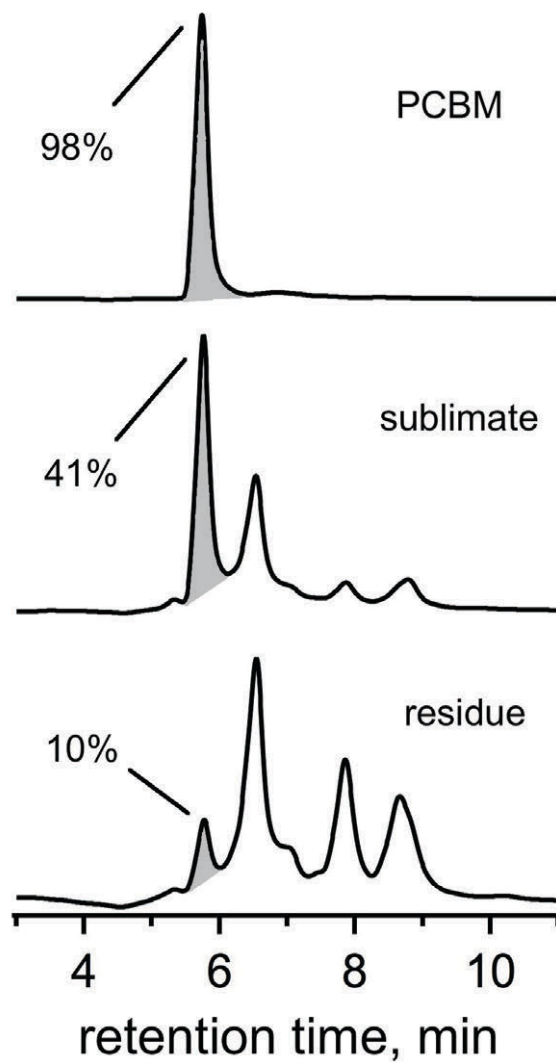


Figure 4.11. HPLC chromatograms of PCBM, its sublimate, and residue (top to bottom, respectively) using a 25 x 250 mm Cosmosil Buckyrep column with toluene eluent at 16 mL/min flow rate and 300 nm detection. Percentages given correspond to the PCBM peak area of the integrated chromatogram.

10%. Interestingly, the HPLC chromatogram of the 340 °C thermally treated sample shown in Figure 4.11 resembles an HPLC chromatogram simulated (Figure 4.12) by averaging the sublimate and residue chromatograms that are shown in Figure 4.6. The main difference between the two experiments is that the vapor deposition sample was heated under vacuum, not N₂ flush, which may have allowed for better separation of sublimate and residue at that temperature. Additionally, the proton-NMR spectrum of the sample heated at 340 °C is a good match to that of the PCBM sublimate, suggesting that the decomposition products formed during annealing of PCBM are similar, if not identical to the decomposition products from the vapor deposition of PCBM (Figure 4.13).

Typical vapor deposition chambers such as the one used in this experiment do not allow for post-deposition air-free handling of the sample, since these instruments are unpractical to house within a glovebox, and therefore a new experiment had to be designed to determine whether post-deposition air exposure affected the observed results. This led to use of a tube furnace and an evacuated glass ampoule to sublime PCBM in a manner that intentionally prevented contact of the sublimed films with air by performing all manipulations under air-free conditions. Based on HPLC and ¹H NMR analyses, no significant differences were observed when comparing the products from both experiments, and thus the thermal decomposition products of PCBM are not air-sensitive, at least not on the time-scale of the subsequent sample preparations and analyses. The temperature of the PCBM sample within the tube furnace was monitored, and its sublimation temperature was measured to be 340 ± 5 °C. These results indicate that it is during the heating and/or vapor deposition of PCBM that substantial

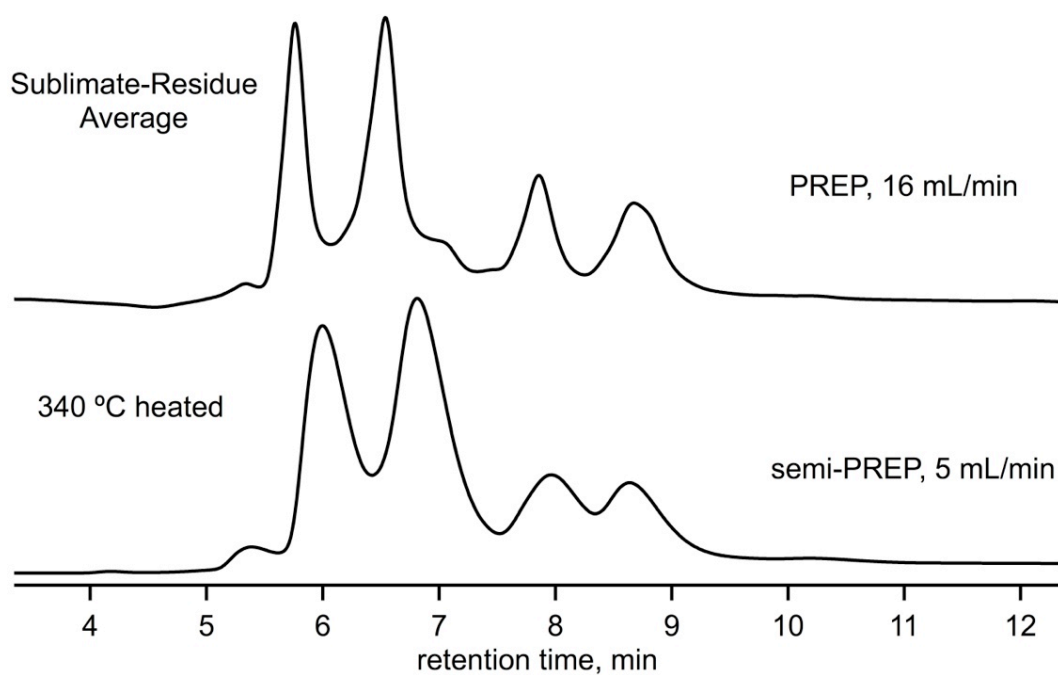


Figure 4.12. Shown top is the HPLC chromatogram that was simulated by averaging the HPLC chromatograms of the PCBM sublimate and residue samples. Shown on bottom is the HPLC chromatogram of the PCBM sample that was thermally annealed for 20 minutes at 340 °C under N₂ flow.

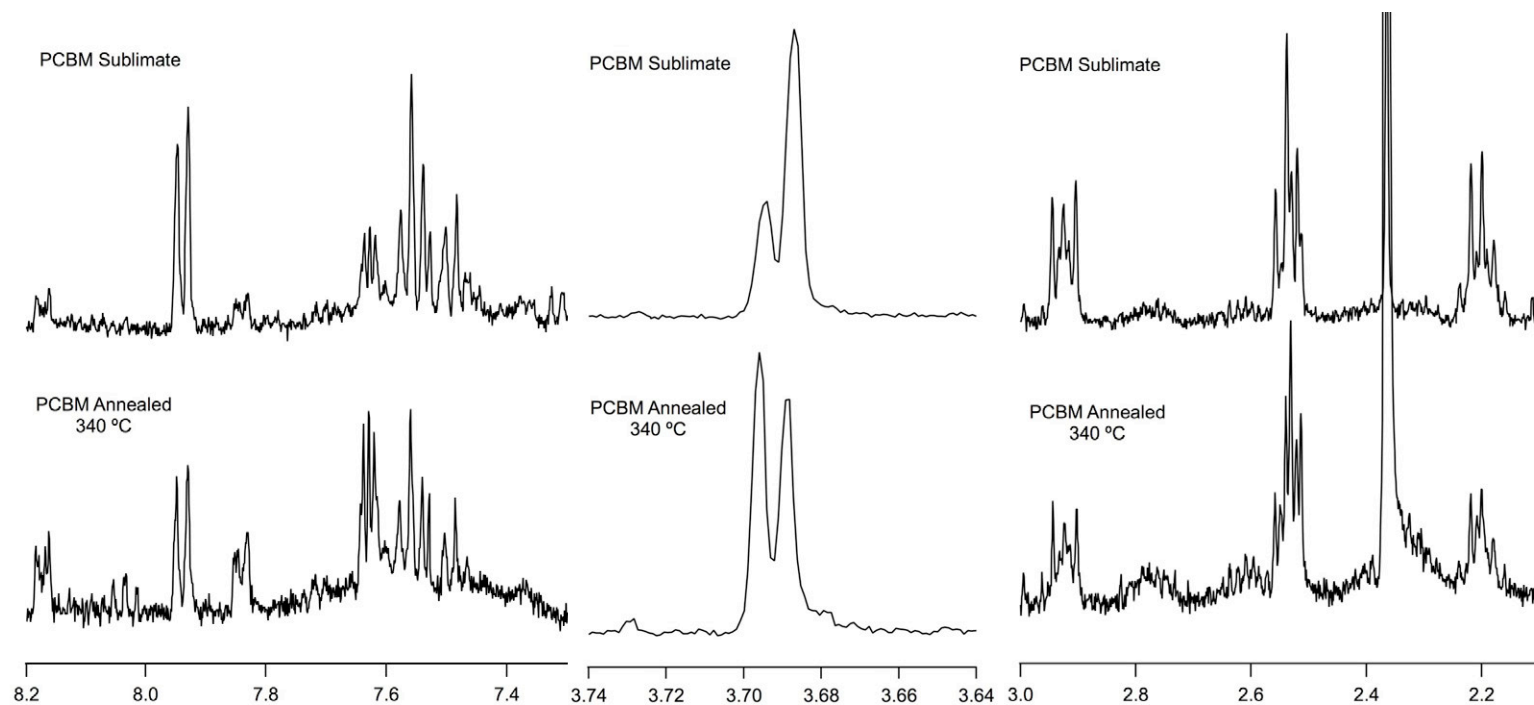


Figure 4.13. The ^1H NMR spectra recorded at 400 MHz, (CDCl_3 , TMS std.) are shown for PCBM heated for 20 minutes at 340 °C and the sublimate material from the vapor deposition chamber experiment. PCBM and iso-PCBM are the two main compounds in each sample.

degradation/chemical modification occurs. To date, this stands as the first experimental evidence characterizing and quantifying the decomposition of PCBM accompanying vapor deposition. These results indicate that while it is possible to vapor deposit PCBM under these conditions, the sublimate only contains at best 40-50% of PCBM, the rest being its isomer, and other decomposition products.

The electronic properties of the sublimed mixture of PCBM isomers and other decomposition products were of interest since thermal evaporation has been utilized for fabrication of organic electronic devices such as OPVs as well as for fundamental physical properties measurements such as solid state EA.^{26,27} It is known that presence of small amounts of impurities that possess different electrochemical properties have drastic and detrimental effects on mobility and recombination rates of free carriers in OPV materials. For example, the efficiency of a PCBM-based OPV device was shown recently to be greatly reduced when the active layer was doped with small amounts of PC₈₄BM, whose $E_{1/2}$ is anodically shifted 350 mV relative to PCBM (PC₈₄BM is 350 mV easier to reduce than PCBM).^{39,40} On the other hand, the mixture of isomers comprising indene-C₆₀-bisadducts results in some of the best performing photovoltaic devices.^{41,42}

To study the electrochemical properties of the components present in the thermally evaporated films of PCBM, the sublimate was separated by HPLC into three fractions (Figure 4.11 middle): **A** (retention time 5.5 – 6.0 minutes), **B** (retention time 6.0 – 6.8 minutes), and **C** (the rest of the material eluting at 2.8 – 5.5 min. and 6.8 – 12.0 min.). These fractions, along with PCBM and C₆₀ for reference, were studied by cyclic voltammetry. The voltammograms are depicted in Figure 4.14. Fraction **A** and **B** were confirmed as PCBM and its cyclo-pentyl isomer,

respectively, by ^1H NMR spectroscopy. Fraction **A** (PCBM) had three sharp quasi-reversible reductions while **B** exhibited sharp quasi-reversible first and second reductions, but a less well-defined third quasi-reversible reduction due to peak shouldering, likely due to differing third reduction properties of minor impurities that co-eluted during HPLC separation. Broader peaks and only two defined redox events were found for fraction **C**, as expected, because this fraction contained a complex mixture of compounds (Figure 4.11, middle). Even so, there is no observable difference in the $E_{1/2}^{0/-}$ potentials of these three fractions as compared with pristine PCBM, within the ± 10 mV experimental error.

This result has two important implications. First it supports the assignment of the thermal decomposition products, including the isomer of PCBM, as having a [6,6]-linkage to the C_{60} cage. Numerous reports have demonstrated that the first reduction potential of fullerene derivatives are mostly determined by the nature and the addition pattern of the exohedral modification.^{43,44} Second, it indicates that the electrochemical properties of the thermally evaporated PCBM film remain mostly unaltered even though only about 40% of it is composed of PCBM molecules.

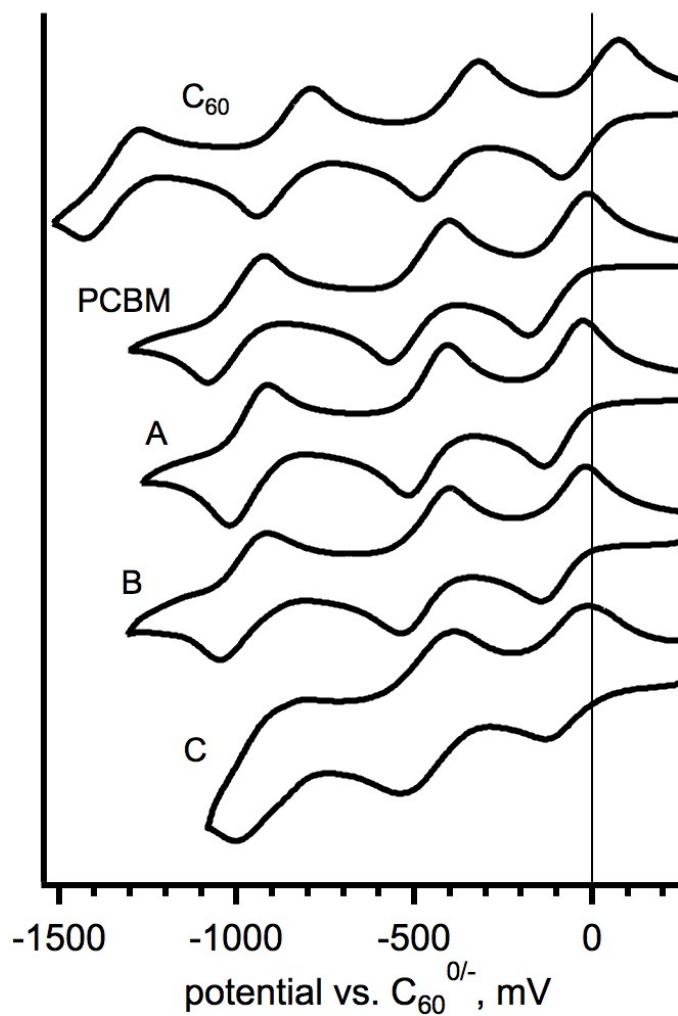


Figure 4.14. Cyclic voltammograms of C₆₀, PCBM, and the sublimation fractions.

4.3.4. Summary and Conclusions. In this study, the behavior of PCBM during thermal annealing and thermal evaporation was studied, and decomposition products were characterized and quantified. It was found that PCBM decomposes after brief (20 minutes) thermal treatment at 300 °C, but also decomposes to the same degree when heated for one hour at 280 °C. Above 300 °C, decomposition is massive; a 20 minute thermal treatment of PCBM at 340 °C results in nearly 80% sample degradation. The main product of thermal decomposition is a new and more thermally stable isomer of PCBM, characterized here for the first time, which contains a five-membered cycloadduct.

PCBM can be thermally evaporated, but with significant decomposition, as the sublimate only contains about 41% PCBM, in addition to the cyclo-pentyl isomer and other decomposition products. Even so, the [6,6]-addition motif is retained in nearly all of the decomposition products and therefore, the electrochemical properties of the sublimation products remain unchanged from PCBM, measured here by cyclic voltammetry. Future studies are warranted, though, to determine the effects of having such a mixture on bulk material properties such as microcrystalline domain morphology and long-range electron mobility. These findings offer consideration to future studies involving PCBM or other fullerene derivatives that may demand high temperatures or high-quality impurity free thin films for which vapor deposition is usually well suited.

4.4. References.

- (1) Hummelen, J.; Knight, B.; Lepeq, F.; Wudl, F.; Yao, J.; Wilkins, C.: Preparation and Characterization of Fulleroid and Metallofullerene Derivatives. *J. Org. Chem.* **1995**, *60*, 532-538.
- (2) Brabec, C.; Cravino, A.; Meissner, D.; Sariciftci, N.; Fromherz, T.; Rispens, M.; Sanchez, L.; Hummelen, J.: Origin of the Open Circuit Voltage of Plastic Solar Cells. *Adv. Funct. Mater.* **2001**, *11*, 374-380.
- (3) Dang, M. T.; Hirsch, L.; Wantz, G.: P3HT:PCBM, Best Seller in Polymer Photovoltaic Research. *Advanced Materials* **2011**, *23*, 3597-3602.
- (4) He, Y.; Li, Y.: Fullerene derivative acceptors for high performance polymer solar cells. *Physical chemistry chemical physics : PCCP* **2011**, *13*, 1970-83.
- (5) Tiwari, S. P.; Namdas, E. B.; Ramgopal Rao, V.; Fichou, D.; Mhaisalkar, S. G.: Solution-Processed n-Type Organic Field-Effect Transistors With High on-off Current Ratios Based on Fullerene Derivatives. *Electron Device Letters, IEEE* **2007**, *28*, 880-883.
- (6) Yan, G.; Zhao, S.; Xu, Z.; Zhang, F.; Kong, C.; Liu, X.; Gong, W.; Xu, X.: The effect of PCBM doping on the electroluminescent performance of organic light-emitting diodes. *physica status solidi (a)* **2011**, *208*, 2317-2320.
- (7) Chochos, C. L.; Tagmatarchis, N.; Gregoriou, V. G.: Rational design on n-type organic materials for high performance organic photovoltaics. *RSC Advances* **2013**, *3*, 7160.
- (8) Tang, M. L.; Bao, Z.: Halogenated Materials as Organic Semiconductors†. *Chemistry of Materials* **2011**, *23*, 446-455.
- (9) Anthony, J. E.; Facchetti, A.; Heeney, M.; Marder, S. R.; Zhan, X.: n-Type organic semiconductors in organic electronics. *Adv Mater* **2010**, *22*, 3876-92.
- (10) Padinger, F.; Rittberger, R. S.; Sariciftci, N. S.: Effects of Postproduction Treatment on Plastic Solar Cells. *Advanced Functional Materials* **2003**, *13*, 85-88.
- (11) Verploegen, E.; Mondal, R.; Bettinger, C. J.; Sok, S.; Toney, M. F.; Bao, Z.: Effects of Thermal Annealing Upon the Morphology of Polymer-Fullerene Blends. *Advanced Functional Materials* **2010**, *20*, 3519-3529.
- (12) Pearson, A. J.; Wang, T.; Jones, R. A. L.; Lidzey, D. G.; Staniec, P. A.; Hopkinson, P. E.; Donald, A. M.: Rationalizing Phase Transitions with Thermal Annealing Temperatures for P3HT:PCBM Organic Photovoltaic Devices. *Macromolecules* **2012**, *45*, 1499-1508.
- (13) Warman, J. M.; de Haas, M. P.; Anthopoulos, T. D.; de Leeuw, D. M.: The Negative Effect of High-Temperature Annealing on Charge-Carrier Lifetimes in Microcrystalline PCBM. *Advanced Materials* **2006**, *18*, 2294-2298.
- (14) Kaur, M.; Gopal, A.; Davis, R. M.; Heflin, J. R.: Concentration gradient P3OT/PCBM photovoltaic devices fabricated by thermal interdiffusion of separately spin-cast organic layers. *Solar Energy Materials and Solar Cells* **2009**, *93*, 1779-1784.
- (15) Rispens, M. T.; Hummelen, J. C.: Photovoltaic Applications. In *Fullerenes: From Synthesis to Optoelectronic Properties*; Guldi, D. M., Martin, N., Eds.; Kluwer Academic Publishers Dordrecht, 2002; pp 387-435.
- (16) Kim, S.-T.; Cho, S. Y.; Lee, C.; Baek, N. S.; Lee, K.-S.; Kim, T.-D.: Synthesis and characteristics of a solution-processable fullerene derivative for n-type organic field-effect transistors. *Thin Solid Films* **2010**, *519*, 690-693.

- (17) Lee, J. U.; Jung, J. W.; Emrick, T.; Russell, T. P.; Jo, W. H.: Synthesis of C60-end capped P3HT and its application for high performance of P3HT/PCBM bulk heterojunction solar cells. *Journal of Materials Chemistry* **2010**, *20*, 3287.
- (18) Ngo, T. T.; Nguyen, D. N.; Nguyen, V. T.: Glass transition of PCBM, P3HT and their blends in quenched state. *Advances in Natural Sciences: Nanoscience and Nanotechnology* **2012**, *3*, 045001.
- (19) Azimi, H.; Fournier, D.; Wirix, M.; Dobrocka, E.; Ameri, T.; Machui, F.; Rodman, S.; Dennler, G.; Scharber, M. C.; Hingerl, K.; Loos, J.; Brabec, C. J.; Morana, M.: Nano-morphology characterization of organic bulk heterojunctions based on mono and bis-adduct fullerenes. *Organic Electronics* **2012**, *13*, 1315-1321.
- (20) Hopkinson, P. E.; Staniec, P. A.; Pearson, A. J.; Dunbar, A. D. F.; Wang, T.; Ryan, A. J.; Jones, R. A. L.; Lidzey, D. G.; Donald, A. M.: A Phase Diagram of the P3HT:PCBM Organic Photovoltaic System: Implications for Device Processing and Performance. *Macromolecules* **2011**, *44*, 2908-2917.
- (21) Tseng, W.-H.: Enhancement of poly(3-hexylthiophene)-based solar cell with thermal-evaporated [6,6]-phenyl-C60 butyric acid methyl ester layers. *Journal of Photonics for Energy* **2012**, *2*, 021009.
- (22) Reddy, V. S.; Karak, S.; Ray, S. K.; Dhar, A.: Photovoltaic properties of pentacene/[6,6]-phenyl C61butyric acid methyl ester based bilayer hetero-junction solar cells. *Journal of Physics D: Applied Physics* **2009**, *42*, 145103.
- (23) Charas, A.; Ferreira, Q.; Farinhas, J.; Matos, M.; Alcácer, L. s.; Morgado, J.: Insoluble Patterns of Cross-Linkable Conjugated Polymers from Blend Demixing in Spin Cast Films. *Macromolecules* **2009**, *42*, 7903-7912.
- (24) Kumar, A.; Li, G.; Hong, Z.; Yang, Y.: High efficiency polymer solar cells with vertically modulated nanoscale morphology. *Nanotechnology* **2009**, *20*, 165202.
- (25) Chu, C.-W.; Shrotriya, V.; Li, G.; Yang, Y.: Tuning acceptor energy level for efficient charge collection in copper-phthalocyanine-based organic solar cells. *Applied Physics Letters* **2006**, *88*, 153504.
- (26) Akaike, K.; Kanai, K.; Yoshida, H.; Tsutsumi, J. y.; Nishi, T.; Sato, N.; Ouchi, Y.; Seki, K.: Ultraviolet photoelectron spectroscopy and inverse photoemission spectroscopy of [6,6]-phenyl-C[sub 61]-butyric acid methyl ester in gas and solid phases. *Journal of Applied Physics* **2008**, *104*, 023710.
- (27) Kanai, K.; Akaike, K.; Koyasu, K.; Sakai, K.; Nishi, T.; Kamizuru, Y.; Nishi, T.; Ouchi, Y.; Seki, K.: Determination of electron affinity of electron accepting molecules. *Applied Physics A* **2008**, *95*, 309-313.
- (28) Dorozhko, P. A.; Lobach, A. S.; Popov, A. A.; Senyavin, V. M.; Korobov, M. V.: Sublimation of hydrofullerenes C60H36 and C60H18. *Chemical Physics Letters* **2001**, *336*, 39-46.
- (29) Boltalina, O. V.; Markov, V. Y.; Borschevskii, A. Y.; Galeva, N. A.; Sidorov, L. N.; Gigli, G.; Balducci, G.: Saturated vapor pressure and sublimation enthalpy of fluorine derivatives of C-60. *Journal of Physical Chemistry B* **1999**, *103*, 3828-3832.
- (30) Zhao, J.; Bertho, S.; Vandenbergh, J.; Van Assche, G.; Manca, J.; Vanderzande, D.; Yin, X.; Shi, J.; Cleij, T.; Lutsen, L.; Van Mele, B.: Phase behavior of PCBM blends with different conjugated polymers. *Physical chemistry chemical physics : PCCP* **2011**, *13*, 12285-92.

- (31) Zhao, J.; Swinnen, A.; Van Assche, G.; Manca, J.; Vanderzande, D.; Mele, B. V.: Phase Diagram of P3HT/PCBM Blends and Its Implication for the Stability of Morphology. *The Journal of Physical Chemistry B* **2009**, *113*, 1587-1591.
- (32) Müller, C.; Ferenczi, T. A. M.; Campoy-Quiles, M.; Frost, J. M.; Bradley, D. D. C.; Smith, P.; Stingelin-Stutzmann, N.; Nelson, J.: Binary Organic Photovoltaic Blends: A Simple Rationale for Optimum Compositions. *Advanced Materials* **2008**, *20*, 3510-3515.
- (33) Larson, B. W.; Whitaker, J. B.; Wang, X.-B.; Popov, A. A.; Rumbles, G.; Kopidakis, N.; Strauss, S. H.; Boltalina, O. V.: Electron Affinity of Phenyl-C61-Butyric Acid Methyl Ester (PCBM). *J. Phys. Chem. C* **2013**, *117*, 14958-14964.
- (34) Hummelen, J. C.; Knight, B. W.; LePeq, F.; Wudl, F.; Yao, J.; Wilkins, C. L.: Preparation and Characterization of Fulleroid and Methanofullerene Derivatives. *The Journal of Organic Chemistry* **1995**, *60*, 532-538.
- (35) Puplovskis, A.; Kacens, J.; Neilands, O.: New route for [60]fullerene functionalisation in [4+2] cycloaddition reaction using indene. *Tetrahedron Letters* **1997**, *38*, 285-288.
- (36) Numata, Y.; Kawashima, J.; Hara, T.; Tajima, Y.: One-pot Synthesis of Indolino[20,30:1,2][60]fullerenes from Fullerene Epoxide: Lewis Acid-assisted Nucleophilic Addition Followed by Intramolecular Cyclization. *Chemistry Lett.* **2008**, *37*, 1018-1019.
- (37) Su, Y.-T.; Wang, Y.-L.; Wang, G.-W.: Palladium-catalysed heteroannulation of [60]fullerene with N-benzyl sulfonamides and subsequent functionalisation. *Chem. Commun.* **2012**, *48*, 8132-8134.
- (38) Kim, J. W.; Kim, H. J.; Lee, H. H.; Kim, T.; Kim, J.-J.: Formation of Bulk Heterojunctions by Alternative Thermal Deposition and Its Structure Analysis for High Efficiency Small Molecular Organic Photovoltaics. *Advanced Functional Materials* **2011**, *21*, 2067-2071.
- (39) Cowan, S. R.; Leong, W. L.; Banerji, N.; Dennler, G.; Heeger, A. J.: Identifying a Threshold Impurity Level for Organic Solar Cells: Enhanced First-Order Recombination Via Well-Defined PC84BM Traps in Organic Bulk Heterojunction Solar Cells. *Advanced Functional Materials* **2011**, *21*, 3083-3092.
- (40) Kooistra, F. B.; Mihailetchi, V. D.; Popescu, L. M.; Kronholm, D.; Blom, P. W. M.; Hummelen, J. C.: New C84 Derivative and Its Application in a Bulk Heterojunction Solar Cell. *Chemistry of Materials* **2006**, *18*, 3068-3073.
- (41) Kang, H.; Cho, C. H.; Cho, H. H.; Kang, T. E.; Kim, H. J.; Kim, K. H.; Yoon, S. C.; Kim, B. J.: Controlling number of indene solubilizing groups in multiadduct fullerenes for tuning optoelectronic properties and open-circuit voltage in organic solar cells. *ACS applied materials & interfaces* **2012**, *4*, 110-6.
- (42) Nardes, A. M.; Ferguson, A. J.; Whitaker, J. B.; Larson, B. W.; Larsen, R. E.; Maturová, K.; Graf, P. A.; Boltalina, O. V.; Strauss, S. H.; Kopidakis, N.: Beyond PCBM: Understanding the Photovoltaic Performance of Blends of Indene-C60Multiadducts with Poly(3-hexylthiophene). *Advanced Functional Materials* **2012**, *22*, 4115-4127.
- (43) Popov, A. A.; Kareev, I. E.; Shustova, N. B.; Stukalin, E. B.; Lebedkin, S. F.; Seppelt, K.; Strauss, S. H.; Boltalina, O. V.; Dunsch, L.: Electrochemical, spectroscopic, and DFT study of C-60(CF3)(n) frontier orbitals (n=2-18): The link between double bonds in pentagons and reduction Potentials. *J. Amer. Chem. Soc.* **2007**, *129*, 11551-11568.

- (44) Kuvychko, I. V.; Whitaker, J. B.; Larson, B. W.; Folsom, T. C.; Shustova, N. B.; Avdoshenko, S. M.; Chen, Y. S.; Wen, H.; Wang, X. B.; Dunsch, L.; Popov, A. A.; Boltalina, O. V.; Strauss, S. H.: Substituent Effects in a Series of 1,7-C₆₀(R_F)₂ Compounds (R_F = CF₃, C₂F₅, n-C₃F₇, i-C₃F₇, n-C₄F₉, s-C₄F₉, n-C₈F₁₇): Electron Affinities, Reduction Potentials and E(LUMO) Values are not Always Correlated. *Chem. Sci.* **2012**, *3*, 1399-1407.
- (45) Mikroyannidis, J. A.; Sharma, S. S.; Vijay, Y. K.; Sharma, G. D.: Novel Low Band Gap Small Molecule and Phenylenevinylene Copolymer with Cyanovinylene 4-Nitrophenyl Segments: Synthesis and Application for Efficient Bulk Heterojunction Solar Cells. *Applied Mater. Interfaces* **2010**, *2*, 270 - 278.
- (46) Scharber, M.; Wuhlbacher, D.; Koppe, M.; Denk, P.; Waldauf, C.; Heeger, A.; Brabec, C.: Design rules for donors in bulk-heterojunction solar cells - Towards 10 % energy-conversion efficiency. *Adv. Mater.* **2006**, *18*, 789-794.
- (47) Li, Z.; Dong, Q.; Li, Y.; Xu, B.; Deng, M.; Pei, J.; Zhang, J.; Chen, F.; Wen, S.; Gao, Y.; Tian, W.: Design and Synthesis of Solution Processable Small Molecules towards High Photovoltaic Performance. *J. Mater. Chem.* **2011**, *21*, 2159-2168.
- (48) Lenes, M.; Wetzelaer, G.-J. A. H.; Kooistra, F. B.; Veenstra, S. C.; Hummelen, J. C.; Blom, P. W. M.: Fullerene Bisadducts for Enhanced Open-Circuit Voltages and Efficiencies in Polymer Solar Cells. *Adv. Mater.* **2008**, *20*, 2116-2121.
- (49) Liang, Y.; Feng, D.; Wu, Y.; Tsai, S.-T.; Li, G.; Ray, C.; Yu, L.: Highly Efficient Solar Cell Polymers Developed via Fine-Tuning of Structural and Electronic Properties. *J. Am. Chem. Soc.* **2009**, *131*, 7792-7799.
- (50) Chen, C.-P.; Chan, S.-H.; Chao, T.-C.; Ting, C.; Ko, B.-T.: Low-Bandgap Poly(thiophene-phenylene-thiophene) Derivatives with Broadened Absorption Spectra for Use in High-Performance Bulk-Heterojunction Polymer Solar Cells. *J. Am. Chem. Soc.* **2008**, *130*, 12828-12833.
- (51) Yamanari, T.; Taima, T.; Sakai, J.; Saito, K.: Origin of the Open-Circuit Voltage of Organic Thin-Film Solar Cells Based on Conjugated Polymers. *Solar Energy Mater. Solar Cells* **2009**, *93*, 759-761.
- (52) Zheng, L.; Zhou, Q.; Deng, X.; Yuan, M.; Yu, G.; Cao, Y.: Methanofullerenes Used as Electron Acceptors in Polymer Photovoltaic Devices. *J. Phys. Chem. B* **2004**, *108*, 11921-11926.
- (53) Al-Ibrahim, M.; Roth, H. K.; Schroedner, M.; Konkin, A.; Scharff, P.; Zhokhavets, U.; Gobsch, G.; Sensfuss, S.: The Influence of the Optoelectronic Properties of Poly(3-alkylthiophenes) on the Device Parameters in Flexible Polymer solar Cells. *Organic Electronics* **2005**, *6*, 65-77.
- (54) Al-Ibrahim, M.; Roth, H.; Zhokhavets, U.; Gobsch, G.; Sensfuss, S.: Flexible large area polymer solar cells based on poly(3-hexylthiophene)/fullerene. *Solar Energy Mater. Solar Cells* **2005**, *85*, 13-20.
- (55) Zhou, Y.; Ding, L.; Shi, K.; Dai, Y.-Z.; Ai, N.; Wang, J.; Pei, J.: A Non-Fullerene Small Molecule as Efficient Electron Acceptor in Organic Bulk Heterojunction Solar Cells. *Adv. Mater.* **2012**, *24*, 957-962.
- (56) Mikroyannidis, J. A.; Kabanakis, A. N.; Sharma, S. S.; Sharma, G. D.: A Simple and Effective Modification of PCBM for Use as an Electron Acceptor in Efficient Bulk Heterojunction Solar Cells. *Adv. Funct. Mater.* **2011**, *21*, 746-755.

- (57) Zhao, G.; He, Y.; Xu, Z.; Hou, J.; Zhang, M.; Min, J.; Chen, H.-Y.; Ye, M.; Hong, Z.; Yang, Y.; Li, Y.: Effect of Carbon Chain Length in the Substituent of PCBM-like Molecules on Their Photovoltaic Properties. *Adv. Funct. Mater.* **2010**, *20*, 1480-1487.
- (58) Mi, D.; Kim, J.-H.; Yoon, S. C.; Lee, C.; Lee, J.-K.; Hwang, D.-H.: Synthesis and Characterization of a Novel Fullerene Derivative Containing Carbazole Group for Use in Organic Solar Cells. *Synth. Metals* **2011**, *161*, 1330-1335.
- (59) Meng, X.; Zhang, W.; Tan, Z. a.; Li, Y.; Ma, Y.; Wang, T.; Jiang, L.; Shu, C.; Wang, C.: Highly Efficient and Thermally Stable Polymer Solar Cells with Dihydronaphthyl-Based [70]Fullerene Bisadduct Derivative as the Acceptor. *Adv. Funct. Mater.* **2012**, *22*, 2187-2193.
- (60) He, Y.; Chen, H.-Y.; Hou, J.; Li, Y.: Indene-C₆₀ Bisadduct: A New Acceptor for High-Performance Polymer Solar Cells. *J. Am. Chem. Soc.* **2010**, *132*, 1377-1382.
- (61) Thompson, B. C.; Frechet, J. M. J.: Organic Photovoltaics - Polymer-Fullerene Composite Solar Cells. *Angew. Chem. Int. Ed.* **2008**, *47*, 58-77.
- (62) Rondeau-Gagne, S.; Curutchet, C.; Grenier, F.; Scholes, G. D.; Morin, J.-F.: Synthesis, characterization and DFT calculations of new ethynyl-bridged C-60 derivatives. *Tetrahedron* **2010**, *66*, 4230-4242.
- (63) Yoo, S. H.; Jong Min Kum, J. M.; Cho, S. O.: Tuning the Electronic Band Structure of PCBM by Electron Irradiation. *Nanoscale Research Letters* **2011**, *6*, 545 - 551.
- (64) Matsuo, Y.; Iwashita, A.; Abe, Y.; Li, C.-Z.; Matsuo, K.; Hashiguchi, M.; Nakamura, E.: Regioselective Synthesis of 1,4-Di(organo)[60]fullerenes through DMF-assisted Monoaddition of Silylmethyl Grignard Reagents and Subsequent Alkylation Reaction. *J. Am. Chem. Soc.* **2008**, *130*, 15429-15436.
- (65) Niinomi, T.; Matsuo, Y.; Hashiguchi, M.; Sato, Y.; Nakamura, E.: Penta(organo)[60]fullerenes as Acceptors for Organic Photovoltaic Cells. *J. Mater. Chem.* **2009**, *19*, 5804-5811.
- (66) Varotto, A.; Treat, N. D.; Jo, J.; Shuttle, C. G.; Batara, N. A.; Brunetti, F. G.; Seo, J. H.; Chabynyc, M. L.; Hawker, C. J.; Heeger, A. J.; Wudl, F.: 1,4-Fullerene Derivatives: Tuning the Properties of the Electron Transporting Layer in Bulk-Heterojunction Solar Cells. *Angew. Chem. Int. Ed.* **2011**, *50*, 5166-5169.
- (67) Yamamoto, S.; Orimo, A.; Ohkita, H.; Benten, H.; Ito, S.: Molecular Understanding of the Open-Circuit Voltage of Polymer:Fullerene Solar Cells. *Adv. Energy Mater.* **2012**, *2*, 229-237.
- (68) Li, C.-Z.; Chien, S.-C.; Yip, H.-L.; Chueh, C.-C.; Chen, F.-C.; Matsuo, Y.; Nakamura, E.; Jen, A. K.-Y.: Facile Synthesis of a 56 pi-electron 1,2-dihydromethano-[60]PCBM and its application for Thermally Stable Polymer Solar Cells. *Chem. Commun.* **2011**, *47*, 10082-10084.
- (69) Kooistra, F.; Mihailetchi, V.; Popescu, L.; Kronholm, D.; Blom, P.; Hummelen, J.: New C₈₄ Derivative and its Application in a Bulk Heterojunction Solar Cell. *Chem. Mater.* **2006**, *18*, 3068-3073.
- (70) Faist, M. A.; Keivanidis, P. E.; Foster, S.; Woebkenberg, P. H.; Anthopoulos, T. D.; Bradley, D. D. C.; Durrant, J. R.; Nelson, J.: Effect of Multiple Adduct Fullerenes on Charge Generation and Transport in Photovoltaic Blends with Poly(3-hexylthiophene-2,5-diyl). *J. Polym. Sci. Polym. Phys.* **2011**, *49*, 45-51.

- (71) Kooistra, F. B.; Knol, J.; Kastenberg, F.; Popescu, L. M.; Verhees, W. J. H.; Kroon, J. M.; Hummelen, J. C.: Increasing the Open Circuit Voltage of Bulk-Heterojunction Solar Cells by Raising the LUMO Level of the Acceptor. *Org. Lett.* **2007**, *9*, 551-554.
- (72) Veldman, D.; Meskers, S. C. J.; Janssen, R. A. J.: The Energy of Charge-Transfer States in Electron Donor–Acceptor Blends: Insight into the Energy Losses in Organic Solar Cells. *Adv. Funct. Mater.* **2009**, *19*, 1939–1948.
- (73) Karakawa, M.; Nagai, T.; Irita, T.; Adachi, K.; Ie, Y.; Aso, Y.: Buckminsterfullerene Derivatives Bearing a Fluoroalkyl Group for Use in Organic Photovoltaic Cells. *J. Fluor. Chem.* **2012**, *144*.
- (74) Yang, C.; Cho, S.; Heeger, A. J.; Wudl, F.: Heteroanalogues of PCBM: N-Bridged Imino-PCBMs for Organic Field-Effect Transistors. *Angew. Chem. Int. Ed.* **2009**, *48*, 1592-1595.
- (75) Yang, C.; Kim, J. Y.; Cho, S.; Lee, J. K.; Heeger, A. J.; Wudl, F.: Functionalized Methanofullerenes Used as n-type Materials in Bulk-Heterojunction Polymer Solar Cells and in Field-Effect Transistors. *J. Am. Chem. Soc.* **2008**, *130*, 6444-6450.
- (76) Matsuo, Y.; Zhang, Y.; Soga, I.; Sato, Y.; Nakamura, E.: Synthesis of 1,4-diaryl[60]fullerenes by bis-hydroarylation of C-60 and their use in solution-processable, thin-film organic photovoltaic cells. *Tetrahedron Lett.* **2011**, *52*, 2240-2242.
- (77) Chen, C.-P.; Lin, Y.-W.; Horng, J.-C.; Chuang, S.-C.: Open-Cage Fullerenes as n-Type Materials in Organic Photovoltaics: Relevance of Frontier Energy Levels, Carrier Mobility and Morphology of Different Sizable Open-Cage Fullerenes with Power Conversion Efficiency in Devices. *Adv. Energy Mater.* **2011**, 776-780.
- (78) Veldman, D.; Meskers, S. C. J.; Janssen, R. A. J.: The Energy of Charge-Transfer States in Electron Donor-Acceptor Blends: Insight into the Energy Losses in Organic Solar Cells. *Adv. Funct. Mater.* **2009**, *19*, 1939-1948.

Chapter 5. Charge Generation and Decay Dynamics in Polymer:PFAF Organic Photovoltaic Active Layers.

5.1. General Introduction to Organic Photovoltaics.

One of the greatest and most intensely studied challenges that we face in modern scientific research is how we will meet the ever-increasing global energy demands of the future. It is widely accepted that the efficient capture and conversion of solar radiation to electricity will play a major part in meeting our energy needs. In order to accomplish this goal, it is imperative that photovoltaic (PV) technologies be able to compete with fossil fuels as well as other emerging renewable energy technologies such as wind, geothermal, and hydroelectric power generation. It was the early 1950's that saw the emergence of the first crystalline silicon PV device, which was about 6% efficient,¹ and since then, many advances in inorganic PV technologies have been realized. Now, crystalline silicon devices are in the range of 20-30% efficient,² and other inorganic PV technologies offer even higher efficiencies.³ Currently, inorganic PVs are providing practically all of the electricity we consume from PV technologies, and the future promise of inorganic PVs continues to grow.⁴ Still, these crystalline inorganic technologies are not ideal: manufacturing and ultra high-temperature purification of materials is costly, panels are thick, brittle, and cumbersome, which limits how they can be mass integrated into society and infrastructure, and in some cases they require non-earth-abundant metals. An alternative PV technology that may provide a cheaper source of energy in the future is known as organic photovoltaics (OPVs), which can avoid all of these problems: they are constructed from earth-abundant materials, processed as liquids, can be manufactured on flexible substrates using roll-to-roll processing, and can even be integrated into building materials as near-transparent thin

films or paints.⁵ The promise for such a fascinating technology relies on the principles underlying its operation, which serve as a strong motivation for this work, and will be discussed later in this chapter.

Organic photovoltaic (OPV) solar cells are a relatively new technology in the field of converting photons to electricity compared to their inorganic counterparts and have only been around for about 20 years, but much has already been learned about them. An important difference in the operation of organic and inorganic solar cells is that crystalline inorganic semiconductors photo-generate free carriers at room temperature, due to a high dielectric constant of the material(s), while in organic solar cells photon absorption produces bound, but mobile, charge pairs known as excitons. In order to get free charge from excitons, organic photovoltaics require two materials with suitably different frontier energy levels to provide the necessary energetic driving force to separate the exciton. These two materials are known as the electron donor and acceptor (or just donor and acceptor), respectively, and can be dyes, polymers, fullerenes, small molecules, carbon nanotubes, and all combinations thereof. Polymers and small molecules are currently atop the list as best choice of donor material, while fullerenes have proved champion of acceptors.⁶ One of the most beautiful advantages of OPV over crystalline silicon, at least from the perspective of a synthetic chemist, is that OPV materials can be a wide variety of compounds,⁷ but Si-based PV will always consist of Si. In OPV, as long as the materials confine to certain design rules, the only limit is the imagination.

In fact, the steady improvement in polymer:fullerene-based OPV device efficiencies over the last 12 years is attributed partly to improvements in device processing techniques, but mostly to the development of new materials. Figure 5.1 illustrates this trend, which shows a timeline of

increasing efficiency of OPV devices made from solution-processed materials as new types of donor polymers were introduced. The red trend path highlights improvements in device efficiency essentially due to optimization of device processing techniques for same type of polymers. Poly-3-hexylthiophene, P3HT, has been the most popularly studied polymer in OPV research since 2003,⁸ and devices with it as a donor have risen from 3% to about 6.5% since then (Figure 5.1). It was the emergence of new low-bandgap and other specifically-designed polymers in the last decade that marks a new trend and a steeper rise in OPV device efficiency (green trend path in the figure).

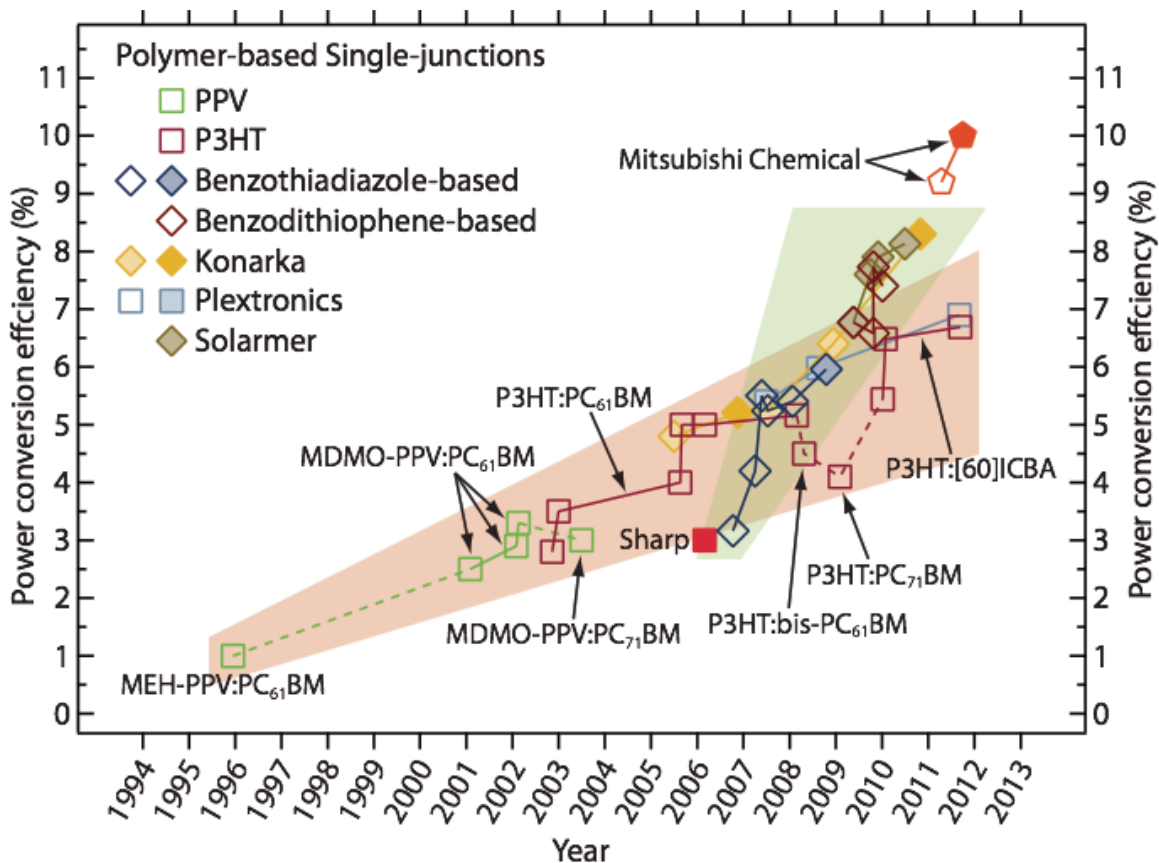


Figure 5.1. Two trends are shown for the improvement in power conversion efficiency (PCE) of certified solution-processed OPV devices. The red path corresponds to improvements in device processing techniques, and the green trend corresponds to use of new types of donor polymers. Figure courtesy of Dr. Andrew Ferguson, reproduced with permission.

The figure also demonstrates that polymer chemists have successfully designed a number of donors to be compatible with only few fullerene derivatives; OPVs by necessity are two component systems, after all. As mentioned in Chapter 4, PCBM was the fullerene used in the record efficiency device in 1995, and still remains one of the few fullerene acceptors seen in today's highest performing OPVs. It was better understanding of the role of the donor in OPV operation that drove chemists to make new polymers, which continues to produce sharp increases in PCEs. After all, the polymer is the light absorber in devices, which ultimately determines how much current is possible to get from the device. It is therefore reasonable to assume the same increases in PCE will be realized when new acceptor materials are investigated, as a result of a better understanding of the acceptor's role in charge creation in OPVs. Several examples of these types of studies, which were enabled because of the improvements in synthetic and isolation methods for large quantities of PFAFs as described in Chapters 1–3, will be discussed later in this chapter.

5.2. Charge Generation in Organic Photovoltaics.

As mentioned in the introduction, free charges are not immediately generated upon photoexcitation of OPV materials. Instead, excitons are formed, which are electron-hole pairs bound by their coulombic attraction, known as exciton binding energy. The exciton binding energy, E_{ex} , is inversely proportional to the square of the relative dielectric constant, ϵ , of the material, by:

$$E_{\text{ex}}(\text{eV}) = R_y(\text{H}) \times \frac{(m_r/m_0)}{\epsilon^2}$$

where $R_y(\text{H})$ is one Rydberg (13.6 eV), m_r is the reduced mass of the exciton, and m_0 is the free electron mass. For example, an inorganic semiconductor with a typical $\epsilon = 10$ and $(m_r/m_0) = 0.1$,

the exciton binding energy is only about 14 meV. Since kT is ca. 25 meV at room temperature, this is why the electron and hole are essentially immediately decoupled after absorption of an incident photon in inorganic materials. This is also why there is not immediately free charge in the case of organic semiconductors; the relative dielectric constant of most OPV materials is $\sim 2 - 4$, meaning the exciton binding energy is around 200 meV, which is about an order of magnitude higher than kT . Therefore, additional energy is required to split the exciton. It is also important in OPV that the free charges remain spatially separated to avoid recombination, since they will have a larger radius of coulombic attraction in the low ϵ material. The donor:acceptor motif suits these needs well, and hence the interface of the two materials is the heart of charge generation in OPVs.

Figure 5.2 shows a simplified Jablonski diagram that depicts the energetics of the photoexcited donor, D, in relation to the change in Gibbs energy (the energetic driving force for charge separation), ΔG_{FC} , associated with the uncorrelated free charge state. The energy of the free charge state, E_{FC} , can be understood by:

$$E_{FC} = |IP_D - EA_A|$$

where IP_D is the ionization potential of the donor and EA_A is the electron affinity of the acceptor. Figure 5.3 shows a band diagram of the frontier energies for hypothetical donor and acceptor materials. It is noted here that such band diagrams are not full descriptions of the energetics of all the processes taking place in the two materials since the exciton

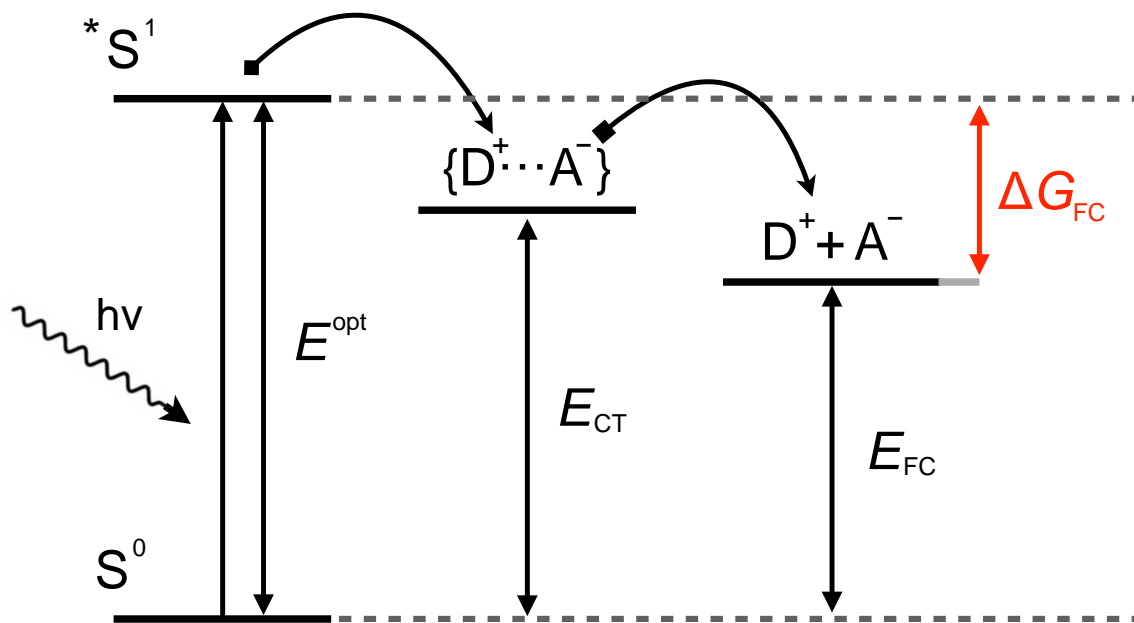


Figure 5.2. A state diagram is shown to demonstrate the loss of energy required for photogeneration of free charge in OPVs. The driving force for exciton separation to free charge, ΔG_{FC} , is the difference between the optical energy gap, E^{opt} , and the energy of the free charge state, E_{FC} . Some charge transfer state(s), $\{D^+ \cdots A^-\}$, may exist between the exciton, $*S^1$, and the uncorrelated charge state, $D^+ + A^-$, with energy E_{CT} .

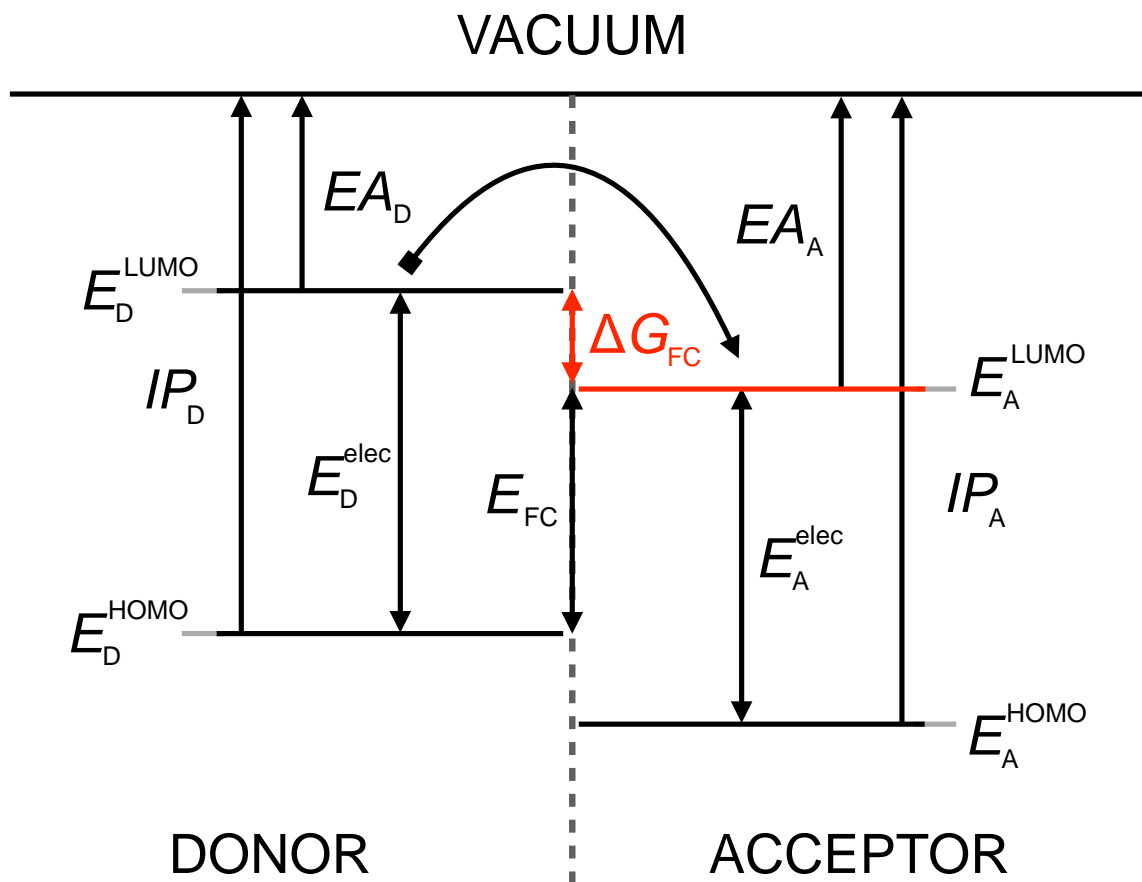


Figure 5.3. A simplified energy band diagram is shown to demonstrate the operating principles for free charge generation in OPV devices. The energy of the charge separated state, E_{CS} , is determined by the offset of the ionization potential of the donor, IP_D , and the electron affinity of the acceptor, EA_A . Note that ΔG_{FC} , as depicted here, is for free carriers only, and therefore does not include the exciton binding energy.

energy is not taken into account, but this type of figure serves use in the discussion at hand since it does correctly shown the energies of the free carriers in the binary system.

The energetic driving force for free charge carrier generation increases as the offset in the electron affinities of the donor and acceptor increases. Notice that as depicted in the Jablonski diagram, ΔG_{FC} is given by:

$$\Delta G_{\text{FC}} = E_{\text{FC}} - E^{\text{opt}}$$

which is the difference in E_{FC} and the energy of the initial excited state, quantified by the optical bandgap, E^{opt} , but in the band diagram it is the difference in the E_{FC} and the electronic gap, E^{elec} . In Figure 5.3, the free charge state corresponds to a free electron in the acceptor and a free hole in the donor. As discussed in Chapter 4, it is recognized that calculated frontier orbital energies and gas- and condensed-phase EA and IP measurements are not always correlated, but currently no reliable instrumentation exists to accurately measure such values for bulk solids of organic semiconductor materials (uncertainties are on the order of 0.3–0.4 V for IPES and UPS measurements on organic semiconductor films), and especially for their mixtures. Nonetheless, when such correlations have been shown for other data (i.e. – measurement or calculations for gas or liquid phases), it is still useful to present discussions under the assumption that these compounds show similar trends in the solid state. Indeed, it has been shown that the differences in reduction potentials for a set of acceptors in solution correlated well with the differences in open circuit voltage of devices containing those acceptors, indicating that electrochemistry can provide a good measure of the *relative changes* of EA in the solid state.⁹ Knowing the energies of the frontier electronic states *and* being able to systematically vary them can address many fundamental questions about charge generation processes in OPV active layers. One example is

the question of how large does ΔG_{FC} have to be (i.e. – how much energy will be lost) to achieve a maximum yield of free charge generation? This is an extremely important question in OPV research since the energy lost in generating free charge comes directly out of the devices V_{OC} . One currently accepted notion is that at least 0.3 eV is required to split the exciton, that is, ΔG_{FC} should be at least 0.3 eV,¹⁰⁻¹⁴ but it was a not known what ΔG_{FC} would result in a maximum of charge carrier yield and if that yield would remain constant as ΔG_{FC} further increases. The use of TMFs and other commercial fullerenes gave an answer to this question, which will be presented in the next section.

The spectroscopic tools, or measurements that can be made, to better understand the role the acceptor in OPV active layers is not one that can be achieved by fabrication and testing of devices alone. This is because optimal device performance requires the right electrode contacts, the right interfacial layers, and the right processing conditions, which introduces a number of other variables that makes it essentially impossible to truly evaluate, say, how many free-carriers are generated in in a particular polymer when one fullerene is exchanged for another in the active layer of a device. The key to answering such fundamental questions is stripping away those variables and investigating only the active layer using a number of spectroscopic techniques sensitive to photophysical processes at the donor:acceptor interface. Two such contactless techniques are described here, time-resolved photoluminescence (TRPL), which is a technique sensitive to excitons, and time-resolved microwave conductivity (TRMC), which is a technique sensitive to uncorrelated free charge carriers.

In the remainder of this chapter, discussions of PFAFs that were prepared in this work for use as new acceptor materials for OPV research will be given. In one case, the use of TMFs spanning a wide range of acceptor allowed us to experimentally determine the relationship between ΔG_{FC} and the yield of free carrier generation. In another study, pairs of TMFs with the same acceptor strength but markedly different structural properties enabled us to show for the first time experimentally that the mobility of electrons within the acceptor phase strongly correlates with the free charge yield in device-relevant mixtures of the two. In both cases, the introduction of new acceptor materials into OPV research gave us a better and clearer understanding of the photophysics of charge creation at the donor:acceptor interface and thus validates the motivations for this work.

Finally, the use of PFAFs in OPV devices will also be discussed. The enormous opportunity to conduct such studies was made possible through collaboration of our research group with Dr. Garry Rumbles, Dr. Nikos Kopidakis, and Dr. Andrew Ferguson at the National Renewable Energy Laboratory in Golden, CO, enabling access to state-of-the art OPV facilities, materials, and most importantly an array of necessary instrumentation.

5.3. Spectroscopic Techniques.

As will be shown in this work, a variety of acceptors were studied to evaluate their role in generation of free carriers in OPV active layers. This role needs to be understood from two points of reference: (i) how well excitons are quenched/relaxed, and (ii) how many uncorrelated free carriers are generated, since this is inherently a limiting factor in how much photocurrent can be produced by those materials in a device. Two techniques are described here that enabled the study of both of those perspectives. Time-resolved photoluminescence (also known as time-

correlated single photon counting) was used to determine the exciton lifetimes that can be correlated to exciton quenching efficiencies for a number of donor:acceptor blends, including the TMFs discussed below. Time-resolved microwave conductivity is a technique sensitive to free carriers, and both are described in this section.

5.3.1. Time-resolved photoluminescence, TRPL. After photoexcitation of a film of neat P3HT, initially excitons are formed, which then decay by a number of processes: radiative or non-radiative, dissociation into free carriers, and annihilation by exciton or free carriers. TRPL is a contactless technique that is sensitive to emissive excited states and provides information about the lifetime of such states. By applying an appropriate photophysical model, we can use the kinetic information obtained to determine the effect of some 'external' influence on the rate coefficients that describe the emissive excited state lifetime, such as the introduction/change of the rate coefficient for interfacial photoinduced electron transfer (i.e. – introduction of a competing exciton quenching pathway, such as dissociation at a donor:acceptor interface). By measuring the steady-state PL quenching and the change in exciton lifetime by TRPL in neat P3HT versus when an acceptor is introduced, useful information can be extracted about what (and on what time-scale) is happening at the donor:acceptor interface concerning the exciton. Concerning the measurement, a laser pulse is used to excite photoluminescence from the sample, and these emitted photons are measured as a function of time using the single-photon counting technique,^{15,16} In this technique, the excitation pulse beam is split into two beam: the first triggers a time-to-amplitude converter (TAC), which is essentially a capacitor, to begin charging, and the second beam excites the sample. PL from the sample is passed through a long-pass filter and a monochromator and collected on a photomultiplier tube. When the first photon arrives after the excitation pulse onto the photomultiplier tube, the TAC receives a stop signal, and the capacitor

is discharged. After this time-correlated photon counting process is repeated approximately 25,000 times, a histogram is generated for the TRPL decay. An example of the PL decay for neat poly-3-hexylthiophene is shown at the top of Figure 5.4. Analysis of the data is discussed in Section 5.1. Each channel corresponds to a TAC voltage.

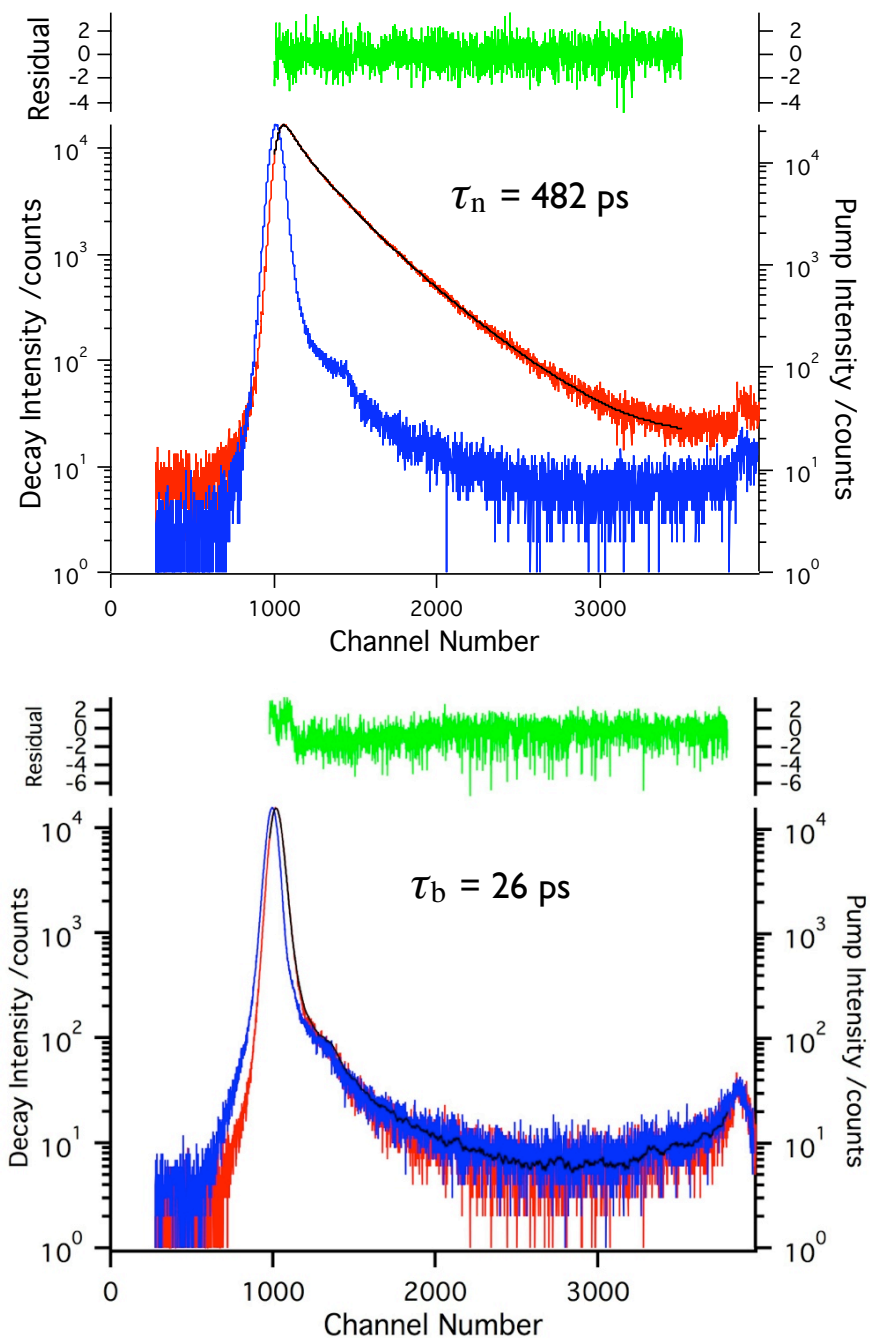


Figure 5.4. Time-resolved photoluminescence spectra are shown for a sample of neat P3HT (top) and a P3HT:60-2-1 blend (bottom). The red traces are PL decay in the sample, the blue are instrument response functions, the black are fits of the PL decay used to extract lifetimes, and the green is the residual of the fit, which represents the goodness of the fit.

Experimental Details. Fullerenes C_{60} , C_{70} , and PCBM (Nano-C, Inc.) and P3HT (Reike Materials) were used as received. PFAFs and TMFs were synthesized and purified at CSU according to experimental details in Chapter 3 (solution-phase and GTGS, respectively). Solutions of polymer and PFAF were prepared by mixing equimolar amount of fullerene to polymer according to the molar ratio in a 50:50 wt% blend of P3HT:PCBM, then stirred at 60 °C overnight in a glovebox environment. Samples were prepared on 1 cm × 2 cm quartz slides either by spin-coating neat polymer and vapor depositing a layer of fullerene on top or by spin- or drop-coating blended solutions of donor:polymer. All operations were carried out in an inert atmosphere glovebox unless otherwise noted. In cases where thermal annealing treatments of films were applied, the samples were annealed for 10–15 minutes at 150 °C in an O_2 - and H_2O -free glovebox environment. Photoluminescence measurements were performed at NREL; PL decays were recorded, after excitation through the quartz substrate at 438 nm with a train of pulses (~150 ps FWHM), for emission at 720 nm, with a cooled photon counting photomultiplier tube (Hamamatsu H6279), using the TCSPC technique. The PL decays were analyzed using an established non-linear least squares iterative reconvolution procedure, where the finite width of the instrument response function was effectively deconvoluted from the measured data to give an overall temporal response of ~20 ps.

5.3.2. Time-resolved microwave conductivity, TRMC. Time-resolved microwave conductivity (TRMC) served as the primary spectroscopic tool for characterizing charge carrier generation and decay dynamics in this work. TRMC is a powerful technique for observing fundamental processes involved in charge generation in OPV active layers since it is a contactless method, and therefore evaluation of the data is specific to processes occurring only in the active layer. This is a major benefit when new donor and acceptor materials are being evaluated for OPV applications, since the measurement avoids numerous other variables to consider if the new materials were being evaluated based on their performance in a device. Concerning the method, it is a pump-probe technique where both the initial photogeneration of mobile carriers and their eventual decay back to equilibrium are monitored through the time-resolved changes in absorbed microwave power by the sample.¹⁷⁻²⁰ A key difference between TRMC and other techniques sensitive to free carriers is that it operates on a time scale (nanoseconds to microseconds) more relevant than ultrafast spectroscopies (femtoseconds and picoseconds) to charge carrier dynamics in an OPV device. A schematic of the instrumental setup is shown in Figure 5.5. For the measurement, the sample (donor:acceptor film on a quartz substrate) is placed in an X-band microwave cavity terminated with a grating reflective to microwaves but transparent to the optical excitation that is used to generate free-carriers within the film. The reason a microwave cavity is used is two fold: (i) the sensitivity of the measurement is increased since the sample is positioned at the maximum of the microwave probe, and (ii) the data can be quantified (not just compared on a relative scale) because of the well-defined geometry and exact knowledge of the probe microwave field.

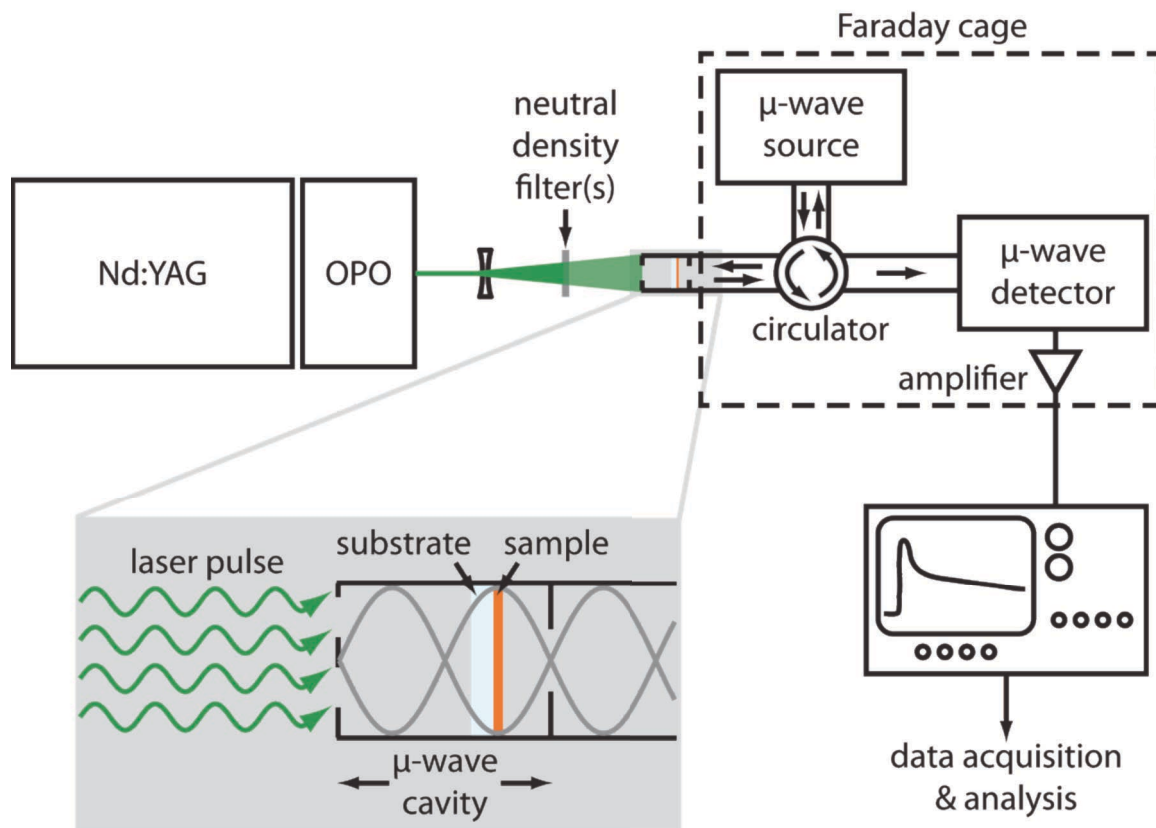


Figure 5.5. The experimental setup of the TRMC instrument is shown. A zoomed representation of the sample cavity shows the microwave-reflective but laser transparent end of the sample cavity.

The transient change in photoconductance, $\Delta G_{\text{exp}}(t)$, was measured via changes in the GHz-frequency microwave power, $\Delta P(t)$, due to absorption of microwaves by the photogenerated holes and electrons, and is given by:

$$\Delta G_{\text{exp}}(t) = -\frac{1}{K} \times \frac{\Delta P(t)}{P} \quad (1)$$

where K is a calibration factor experimentally determined from the resonance characteristics of the microwave cavity and the dielectric properties of the sample. The end-of-pulse (peak) photoconductance, ΔG_{EOP} , can be related to the product of the yield of free-carrier generation, ϕ , and the sum of the GHz-frequency electron and hole mobilities, μ_e and μ_h , respectively (called $\Sigma\mu$), by:

$$\Delta G_{\text{EOP}} = \beta q_e I_0 F_A \phi (\mu_e + \mu_h) = \beta q_e I_0 F_A \phi \Sigma\mu \quad (2)$$

where $\beta = 2.2$ and is the ratio of the interior dimensions of the waveguide, q_e is the electronic charge, I_0 is the incident photon flux of the excitation laser pulse, and F_A is the fraction of absorbed laser pump photons by the sample.

At low absorbed photon flux ΔG_{EOP} increases linearly with I_0 , however as the light intensity increases, higher order processes become important, limiting the carrier generation yield, ϕ , and the dependence becomes sublinear. The origin of the sublinearity at high excitation intensities has been ascribed to exciton-hole quenching.¹⁸ Equation 3 is used to empirically extrapolate to the linear response limit of the photoconductance at low excitation intensities, representative of terrestrial photon intensity:

$$\frac{\Delta G_{\text{EOP}}}{\beta q_e} = \frac{A I_0 F_A}{1 + \sqrt{B I_0 F_A + C I_0 F_A}} \quad (3)$$

where A , B and C are fitting parameters. Comparison of Equations 2 and 3 allows us to obtain the low-intensity, linear response limit as $A = \beta q_e [\phi \Sigma\mu]$.^{21,22} One of the primary figures of merit of

microwave conductivity data is $\phi\Sigma\mu$, which is extracted from these low-light intensity extrapolation fitting curves. This is shown in Figure 5.6.

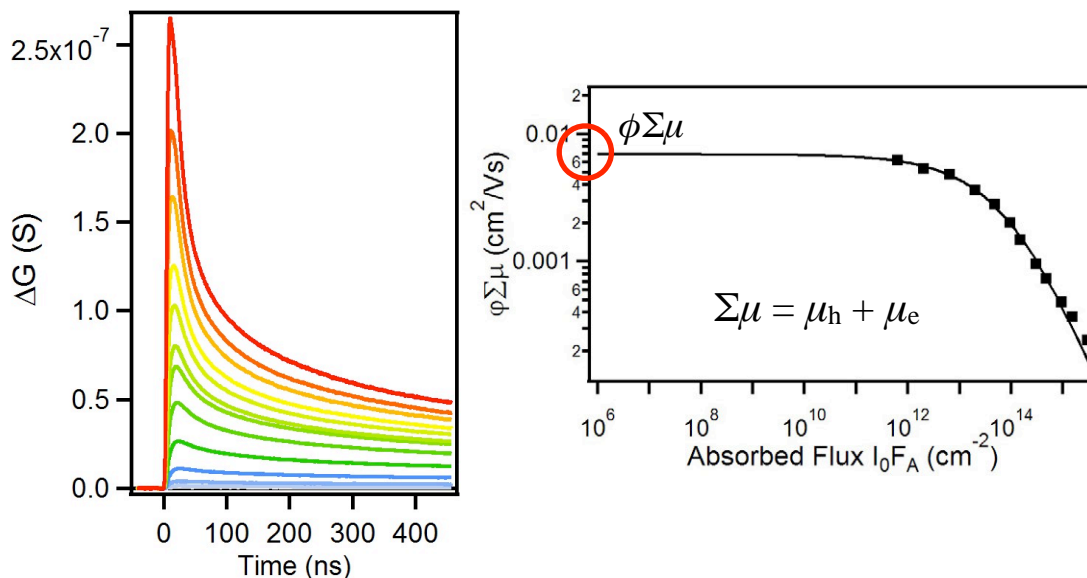


Figure 5.6. Photoconductivity transients (left) for twelve different pump excitation intensities (attenuated using neutral density filters in the laser beam path) and the corresponding $\phi\Sigma\mu$ plot (right) that shows the extrapolated linear regime of $\phi\Sigma\mu$.

Experimental Details. Samples were prepared on 1×2 cm quartz substrates and handled as described in Section 5.3.1.1. All polymer(:fullerene) films were excited through the quartz substrates with 5 ns laser pulses at a wavelength near the sample absorption maximum (generally 500 nm for P3HT, and as noted for other polymers) from an optical parametric oscillator (Continuum Panther) pumped by the 355 nm harmonic of a Q-switched Nd:YAG laser (Continuum Powerlite). Photoconductance data were recorded for up to 15 pump excitation intensities, provided sufficient signal-to-noise, which were used to extrapolate $\phi\Sigma\mu$ at low excitation intensities in the linear response regime.

5.4. Fundamental and Applied Studies of PFAFs in OPVs.

5.4.1. Exciton Quenching in P3HT:PFAF Films. Figure 5.7 shows the absorption spectra of a spin-coated film of neat P3HT, and evaporated layer of neat $C_{60}(CF_3)_2$, and a bilayer film of the two prepared by evaporating 50 nm of $C_{60}(CF_3)_2$ on top of a 150 nm thick spin-coated film of P3HT. The absorption features in the evaporated film of $C_{60}(CF_3)_2$, which contains no solvent molecules, matches those in the spectrum of $C_{60}(CF_3)_2$ in toluene. In the blend, the spectrum can be approximated as the sum of spectra of the individual constituents, which appear to more or less contribute equally to the total absorbance. The steady-state PL spectra of neat P3HT and the bilayer with $C_{60}(CF_3)_2$ are shown in Figure 5.8. Characteristic emission bands at ca. 650 and 700 nm are present in the PL spectrum of neat P3HT. $C_{60}(CF_3)_2$ is 230 mV easier to reduce than PCBM in solution, so it was hypothesized that this significant increase in acceptor strength would result in comparable or more effective exciton quenching in P3HT. Indeed, significant PL quenching is observed in the bilayer sample, measured under identical conditions as for the neat polymer. Since the exciton diffusion length (defined as the distance the exciton travels before decaying back to the ground state) is on the order of around 10 nm in P3HT,²³⁻²⁷ and the excitation penetration depth is ca. 100 nm, the amount of quenching observed is consistent with a donor:acceptor interface located 50 nm within the film with efficient exciton quenching on across a 10 nm cross-section in the sample (only 10 nm of P3HT in proximity to the bilayer interface). Nearly all of the PL intensity is quenched when $C_{60}(CF_3)_2$ is blended uniformly throughout a film of comparable thickness prepared by spin-coating from a solution containing approximately the same molar ratio of P3HT to $C_{60}(CF_3)_2$ as in the

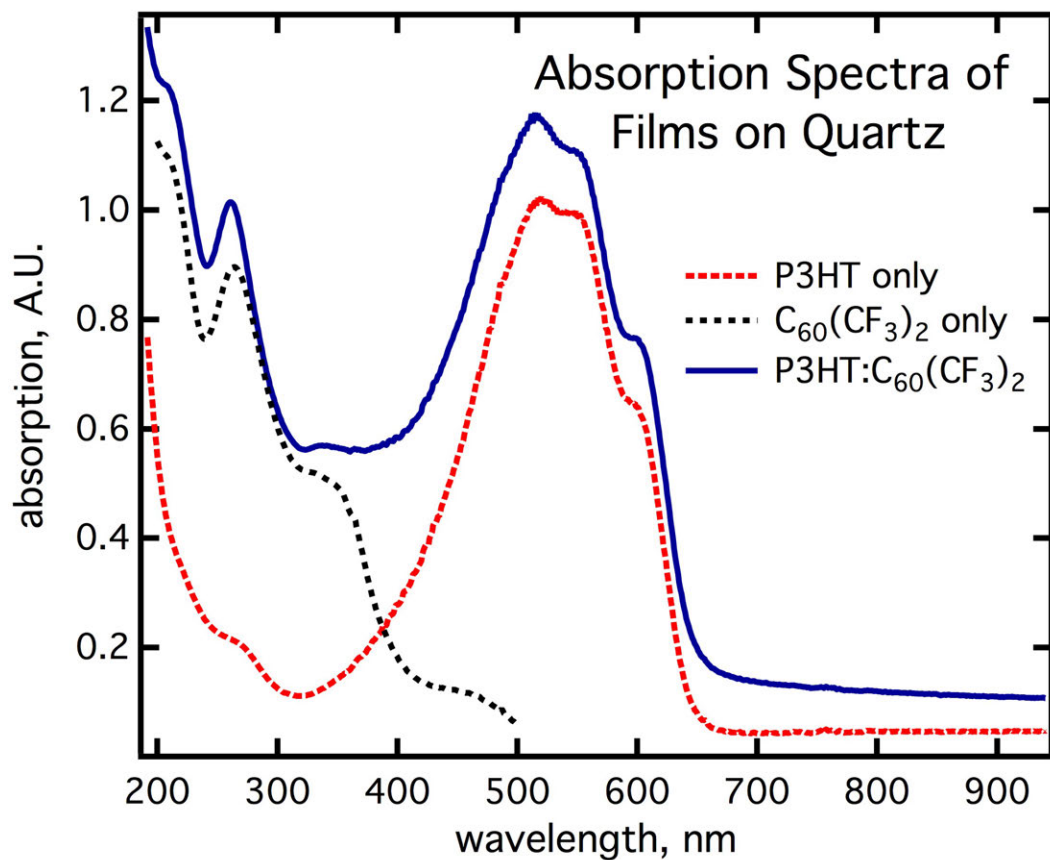


Figure 5.7. The absorption spectra are shown for solids films on quartz of neat P3HT (red dotted line), neat C₆₀(CF₃)₂ (i.e. – 60-2-1, black dotted line), and their blend (blue solid line).

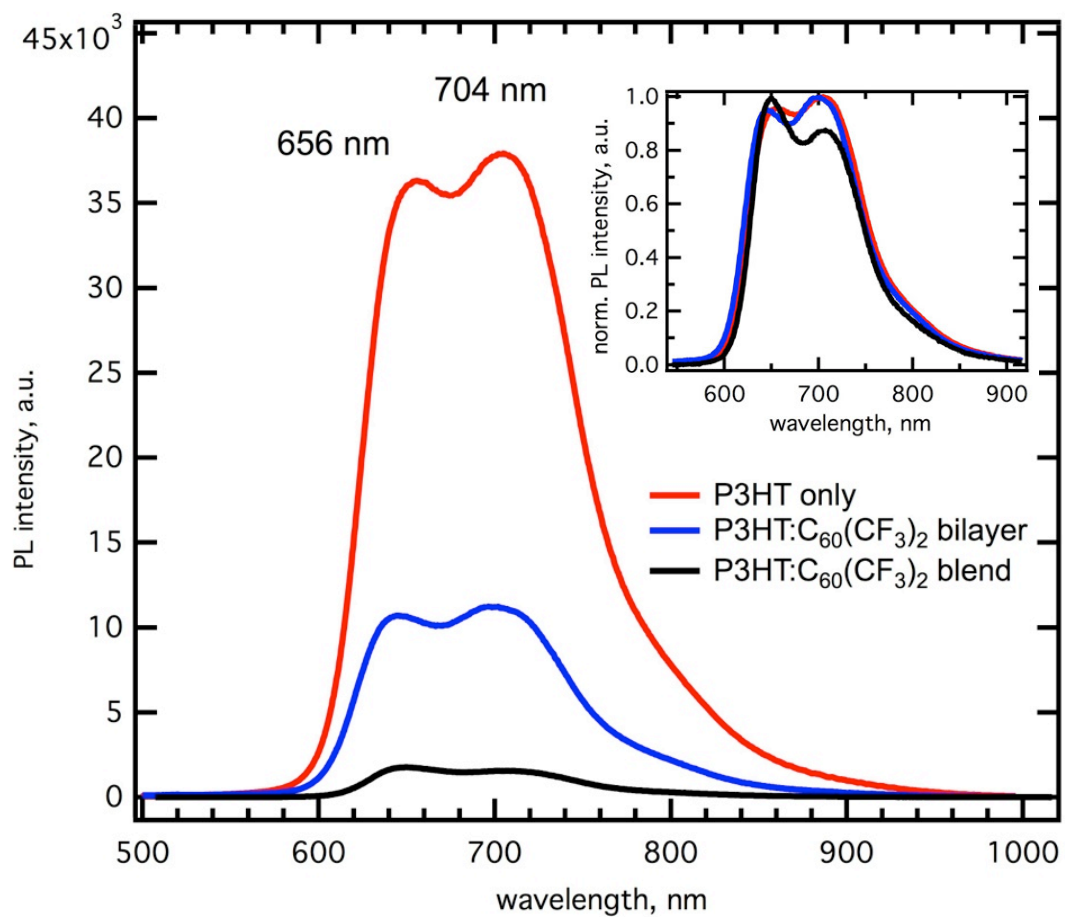


Figure 5.8. Steady-state PL spectra are shown for neat P3HT (red), a P3HT:60-2-1 bilayer (blue), and a P3HT:60-2-1 blended film (black).

bilayer, which is also shown in Figure 5.8. This indicates that the donor:acceptor interface is well distributed throughout the bulk of the film, also justifying the term “bulk heterojunction” commonly used to denote these structures. Comparable results were observed when the bilayer film was thermally annealed, indicating that a significant increase in donor:acceptor interface surface area occurs due to thermally induced intermixing of $C_{60}(CF_3)_2$ into P3HT. The same has been reported for P3HT:PCBM and other fullerene blends. The results indicate that $C_{60}(CF_3)_2$ effectively quenches excitons in P3HT.

Time-resolved photoluminescence measurements of exciton lifetimes were carried out on neat P3HT, and on blended films of P3HT:PCBM and P3HT:TMFs. For neat P3HT, it was found the average exciton lifetime was around 450 ps, which is consistent with literature reports.²⁷⁻²⁹ However, measured exciton lifetimes varied; the variation was larger between different samples than for measurements when exciting different spots of the same sample, but at most by about 25%. No significant differences were observed when exciting the films between the range of 625 and 750 nm. Therefore, this measurement was recorded each time for the neat polymer when blended D:A solutions were prepared using the same P3HT, thus giving more accurate exciton quenching efficiencies between samples when new batches of P3HT were used. When a 1:1 weight ratio solution of P3HT:PCBM was used to spin-cast a film (BHJ morphology), the exciton quenching efficiency (QE_{ex}) was ca. 78%; the QE_{ex} is calculated using the exciton lifetime in the blend and the exciton lifetime in the neat polymer used in that blend, such that $QE_{ex} = 1 - (\tau_{blend}/\tau_{P3HT})$, where τ is the exciton lifetime.

In the literature, it is common practice to prepare blends of donor polymer and fullerene acceptor based on weight ratios. However, when conducting studies involving significantly different polymers or fullerenes between samples, the differences in molar ratios are clearly

overlooked when molar masses are significantly different. Therefore, in all studies here, equal molar loadings of donor and acceptor was used when comparing data. In general, the starting point would be a 1:1 weight loading of P3HT:PCBM, and other samples would be prepared according to that molar ratio. For a P3HT:C₆₀(CF₃)₂ BHJ film, loaded in an equivalent molar ratio to the PCBM film, the QE_{ex} was on average ca. 95%; the exciton lifetimes are summarized in Table 5.1. In fact all PFAFs, regardless of electron accepting strength, had QE_{ex} values of ca. 90% or better. These data are significant since it suggests that bulk heterojunctions form from blends of PFAFs with P3HT (which is the case for P3HT:PCBM blends) and that excitons are essentially quenched quantitatively in these blends. It also implies that the changes in the structure from one PFAF to the next does not introduce a wide variety of donor:acceptor phase separation. This is very important since OPV systems principally rely on excitons as sources of free charge, so the more excitons that are quenched, the higher the potential is of collecting more of this charge in a device. However, it is important to note that exciton quenching does not necessarily equate to free charges. Exciton dissociation is but a step in a much larger and more complicated sequence of processes of converting photons to useable electricity in OPV devices. Nonetheless, having a higher exciton quenching efficiency inherently increases the maximum performance that *could* be achieved in a working device. In summary, steady-state and time-resolved PL studies of P3HT:PFAF blends revealed that PFAFs in general are highly effective at quenching PL and do so on a time-scale more efficiently than PCBM in P3HT BHJ films. In the next section, we will discuss how TRMC was used to investigate how many of these quenched excitons actually resulted long-lived free charges.

Table 5.1. Compilation of time-resolved photoluminescence quenching data for P3HT:fullerene films.

Acceptor	τ (neat P3HT), ps	τ (blend), ps	QE _{ex} , %
C ₆₀	482	239	50
C ₇₀	469	118	76
PCBM	482	105	78
C ₆₀ (CF ₃) ₂ -1	482	26	95
C ₆₀ (CF ₃) ₄ -1	482	22	95
C ₆₀ (CF ₃) ₆ -1	469	32	93
C ₆₀ (CF ₃) ₆ -2	486	27	95
C ₆₀ (CF ₃) ₈ -1	486	35	93
C ₆₀ (CF ₃) ₈ -3	469	54	89
C ₆₀ (CF ₃) ₁₀ -1	412	40	90
C ₆₀ (CF ₃) ₁₀ -2	412	43	90
C ₆₀ (CF ₃) ₁₀ -5	412	47	89
1,7-C ₆₀ (CF ₂ C ₆ F ₅) ₂	398	27	93
1,7-C ₆₀ (CF ₂ CO ₂ Et) ₂	398	23	94

5.4.2. TRMC Studies of Energetic Driving Force and Free Carrier Yield in OPV Active Layers Containing TMFs.

This section is focused on studies of quantification of intrinsic free charge generation in OPV active layers as measured by TRMC. As described in the Introduction to this chapter, it is the offset in energy of the exciton and the energy of the free carriers (that includes the EA of the acceptor material, see equation below) that provides the energetic driving force for exciton dissociation into free carriers, ΔG_{FC} . As shown in Figure 5.3, one can calculate ΔG_{FC} as long as the exciton energy (E_{ex}), IP_D , and EA_A are known (or estimated from other measurements), by the equation:

$$\Delta G_{FC} = IP_D - EA_D - E_{ex}$$

Therefore, being able to tune the frontier energy levels of the acceptor compound over a wide range can address a number of questions about the relationship of ΔG_{FC} to the yield of free carrier generation. However, the bandgap of many OPV donor polymers is around 1.5–2.0 eV (P3HT is 1.9 eV), so in theory to test the entire range of ΔG_{FC} in P3HT, for example, one would have to have a series of acceptors with EAs ranging 1.9 V. Furthermore, the acceptors should not participate in any other forms of interaction with the polymer that would affect the charge creation step. They must be interchangeable in the sense that the energetics of the system is essentially the only parameter changing. Obviously, this presents an enormous challenge. While many different types acceptors with a range of EAs exist, C_{60} derivatives are the best choice since they exhibit widely tunable properties, without having to change the substrate (i.e. – it is still C_{60}). This is important because fullerenes and their derivatives in general have low reorganization energies for electron transfer,^{30,31} and thus should offer minimal perturbation of intermediate charge transfer states (see Jablonski diagram in Figure 5.2) from acceptor to

acceptor. However, the commercially available fullerenes (as shown in Table 5.2), only offer a 0.17 V span in their EAs , which means just more than 10% of the ΔG_{FC} range (0.23 eV) that can be evaluated for most donor polymers with this acceptor set alone. Therefore, a particular series of TMFs were prepared (see Chapter 3 for synthesis and isolation of compounds) to expand the range of ΔG_{FC} . These TMFs were 60-2-1, 60-4-1, 60-6-1, 60-6-2, 60-8-1, 60-10-1, and 60-10-2; they were chosen because these TMFs have a range of $E_{1/2}$ potentials spanning 0.64 V. Combined with five commercially available acceptors, a ΔG_{FC} range of 1.24 eV was realized.

Table 5.2. The initial energy (E_{exciton}) is the exciton energy found in isolated fullerenes as measured by absorption and emission spectroscopy. The final energy (free carrier energy) is given as the difference between the fullerene EA and the polymer ionization potential (IP), which are, in turn, estimated from CV measurements (see the Methods). The change in Gibbs energy, ΔG , is tabulated according to $\Delta G = IP_D - EA_A - E_{\text{ex}}$.

Fullerene	E_{exciton} (eV)	EA_A (eV)	IP_D (F8T2, eV)	E_{FC} (eV)	ΔG (eV)
IC ₆₀ BA	1.72	4.04	5.72	1.68	-0.04
IC ₆₀ MA	1.73	4.08	5.72	1.64	-0.09
bis-PCBM	1.75	4.11	5.72	1.61	-0.14
PCBM	1.76	4.20	5.72	1.52	-0.24
PC ₇₀ BM	1.78	4.21	5.72	1.51	-0.27
60-2-1	1.77	4.43	5.72	1.29	-0.48
60-4-1	1.84	4.46	5.72	1.26	-0.58
60-6-2	2.18	4.22	5.72	1.50	-0.67
60-6-1	2.00	4.55	5.72	1.17	-0.83
60-8-1	2.07	4.62	5.72	1.10	-0.97
60-10-2	2.18	4.61	5.72	1.11	-1.06
60-10-1	2.14	4.86	5.72	0.86	-1.28

Dr. David Coffey, a collaborator for this study at NREL, came up with an elegant experimental method to actually measure the free carrier yield in donor:acceptor films containing this series of fullerene acceptors, which is fully described in the literature.³² In short, TRMC was used to measure the relative yield of free charge generation by preparing the samples in a way that there was no contribution of electron mobility in the fullerene phase, since the photoconductance signal in TRMC measurements is related to the yield of free carrier generation *and* the sum of hole and electron mobilities (refer to Section 2.2). This was accomplished by dilutely loading the fullerene into the polymer and then generating excitons in the dispersed fullerenes, and was confirmed by measurements that showed a constant free carrier yield in a dilute regime range of loadings (refer to panel d in Figure 5.9). Excitons were generated on the fullerenes by excitation of the sample at a wavelength transparent to the polymer, but not for the fullerene. The overall method is summarized as depicted in Figure 5.9.

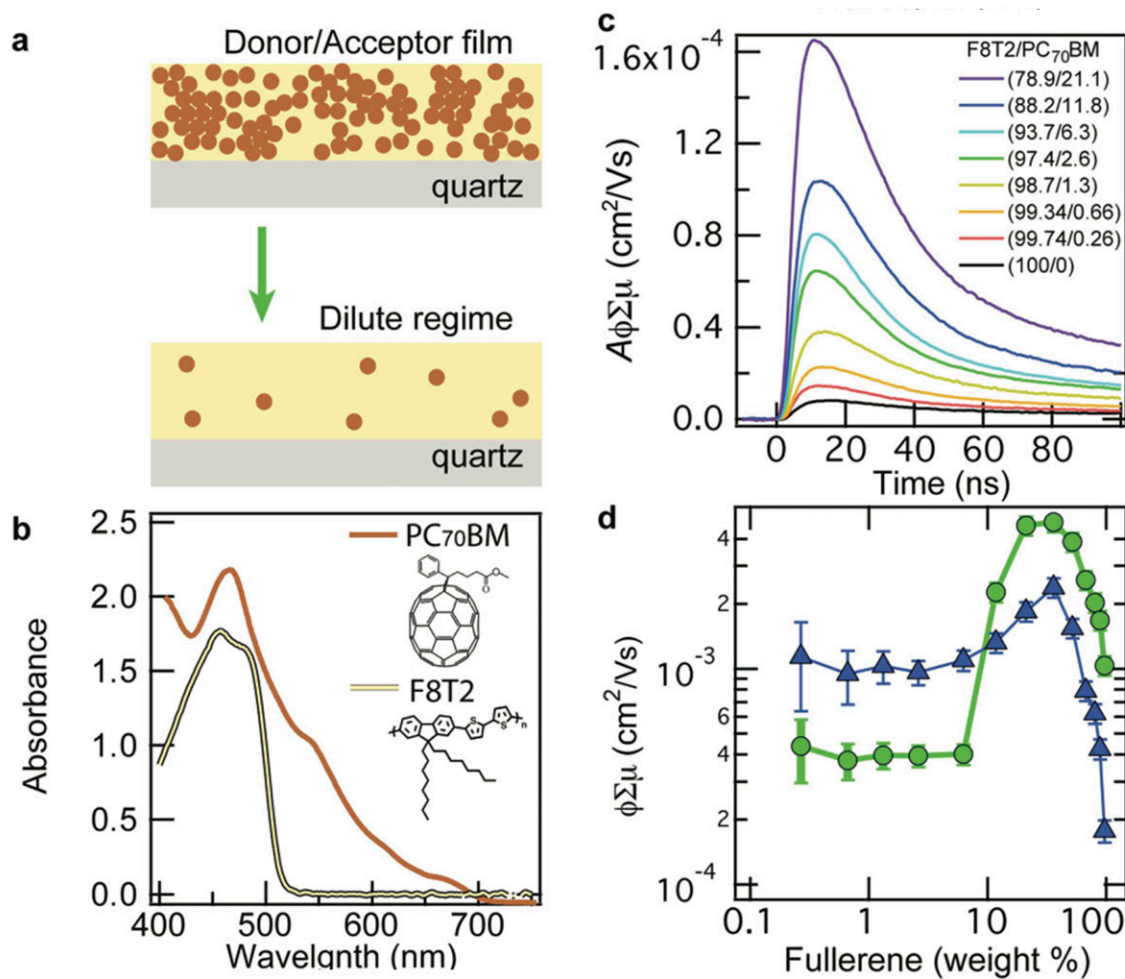


Figure 5.9. The overall method for measuring free charge generation yield: (a) fullerenes are loaded into the polymer in a dilute regime (decouples yield from mobility in $\phi\Sigma\mu$), (b) excitons were generated in the fullerene by selectively exciting them, (c) & (d) the response of $\phi\Sigma\mu$ becomes linear when no electron mobility is measured in the fullerene phase as the loading decreases. Figure adapted from ref. 32.

A set of three polymers from the polyfluorene family (F8T2, F8, and F8BT) were studied using fullerene loadings in the “dilute regime” for all of the twelve fullerene acceptors by TRMC, and the relationship between the yield of free charge generation and ΔG_{FC} was observed. Figures 5.10 – 5.12 are plots of the relative yield of free charge versus the energetic driving force. What is immediately evident in each figure is bell-curve shape of the data, which means that a maximum yield results as ΔG_{FC} increases up to a point, but then additional driving force decreases the yield of free carriers. The two vertical dashed lines in each of the three figures mark the ΔG_{FC} required to “turn on” free carrier yield and to achieve maximum free carrier yield. What is very important from a materials perspective is that this trend would not have been observed without the use of new fullerene acceptors. Consider only the data points corresponding to the commercially available fullerene acceptors, labeled in each figure. In the case of F8T2, the commercial fullerenes lie on the upslope for carrier yield before the peak is reached, and therefore taken alone the data would suggest only that free carrier yield increases with ΔG_{FC} . In the cases of the higher *IP* polymers F8 and F8BT (–5.9 and –6.1 eV, respectively),³² these commercial fullerenes show practically no part of the overall trend. By having access to TMFs, which have higher *EAs* than those commercial fullerenes, we covered the range of ΔG_{FC} needed to observe not only the optimal ΔG_{FC} for free carrier yield in each of the polymer systems, but also that additional driving force leads to an inversion of free carrier yield, which serves as the first experimental evidence for Marcus Theory description of photoinduced electron transfer in the solid-state.

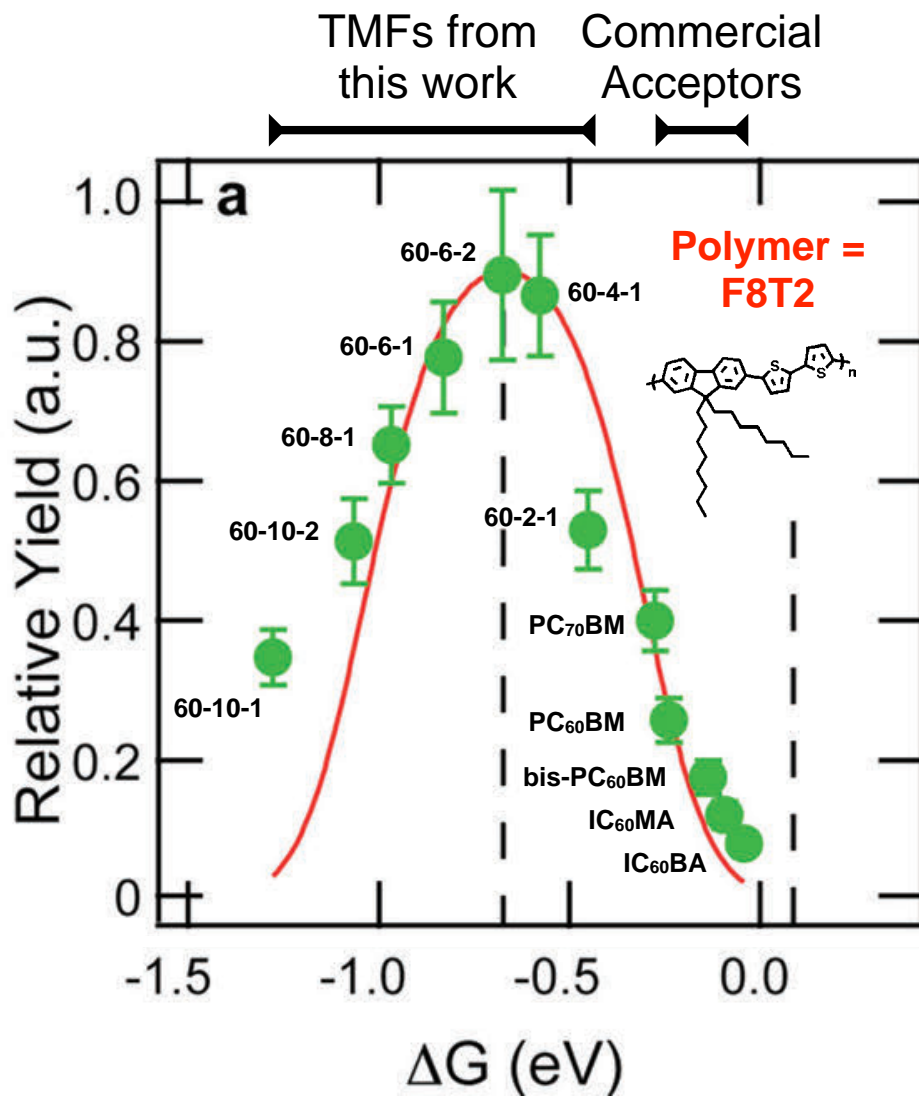


Figure 5.10. The relative yield of free charge generation as a function of energetic driving force is shown for dilute regime loadings of a range of fullerenes and F8T2.

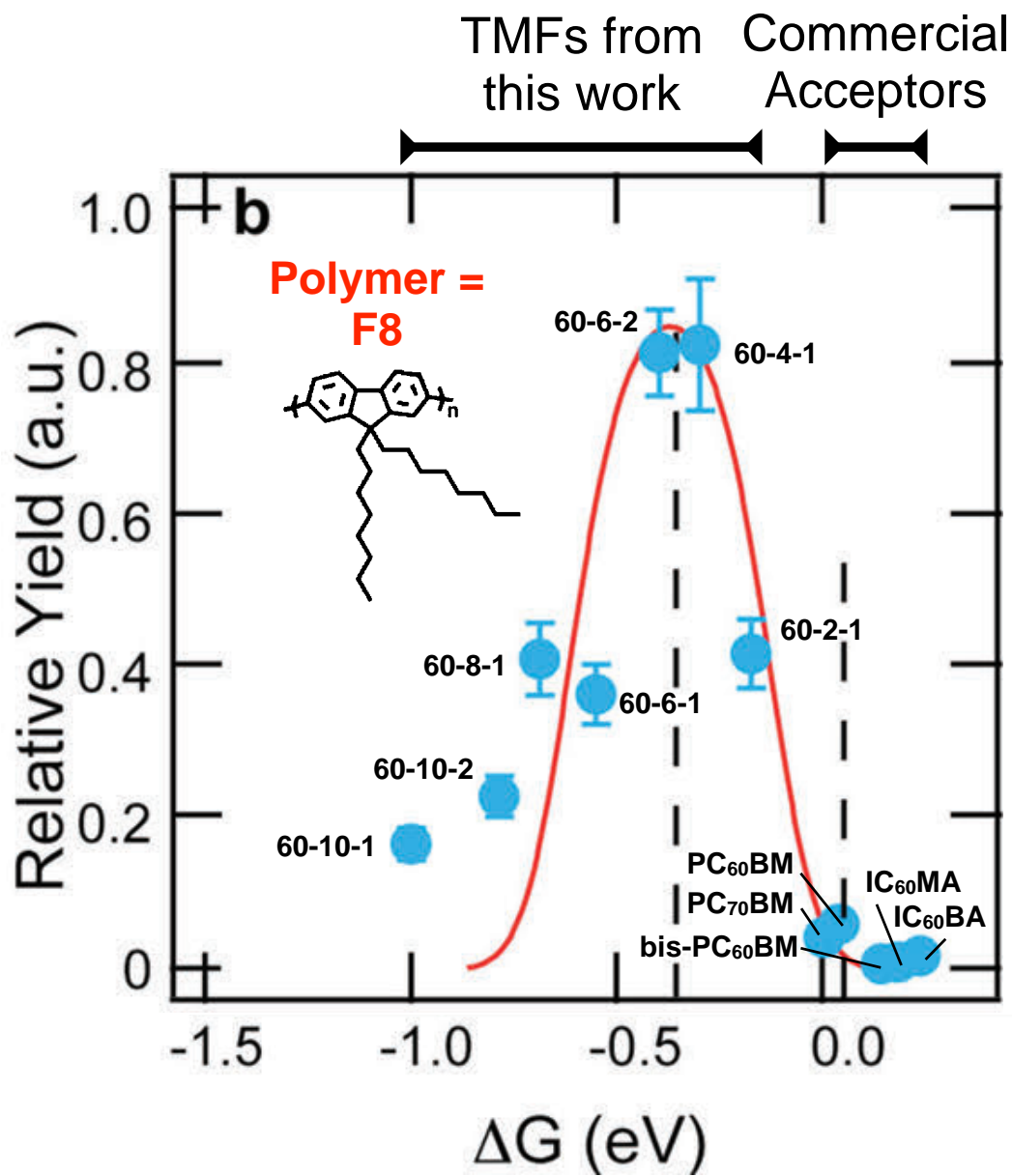


Figure 5.11. The relative yield of free charge generation as a function of energetic driving force is shown for dilute regime loadings of a range of fullerenes and F8.

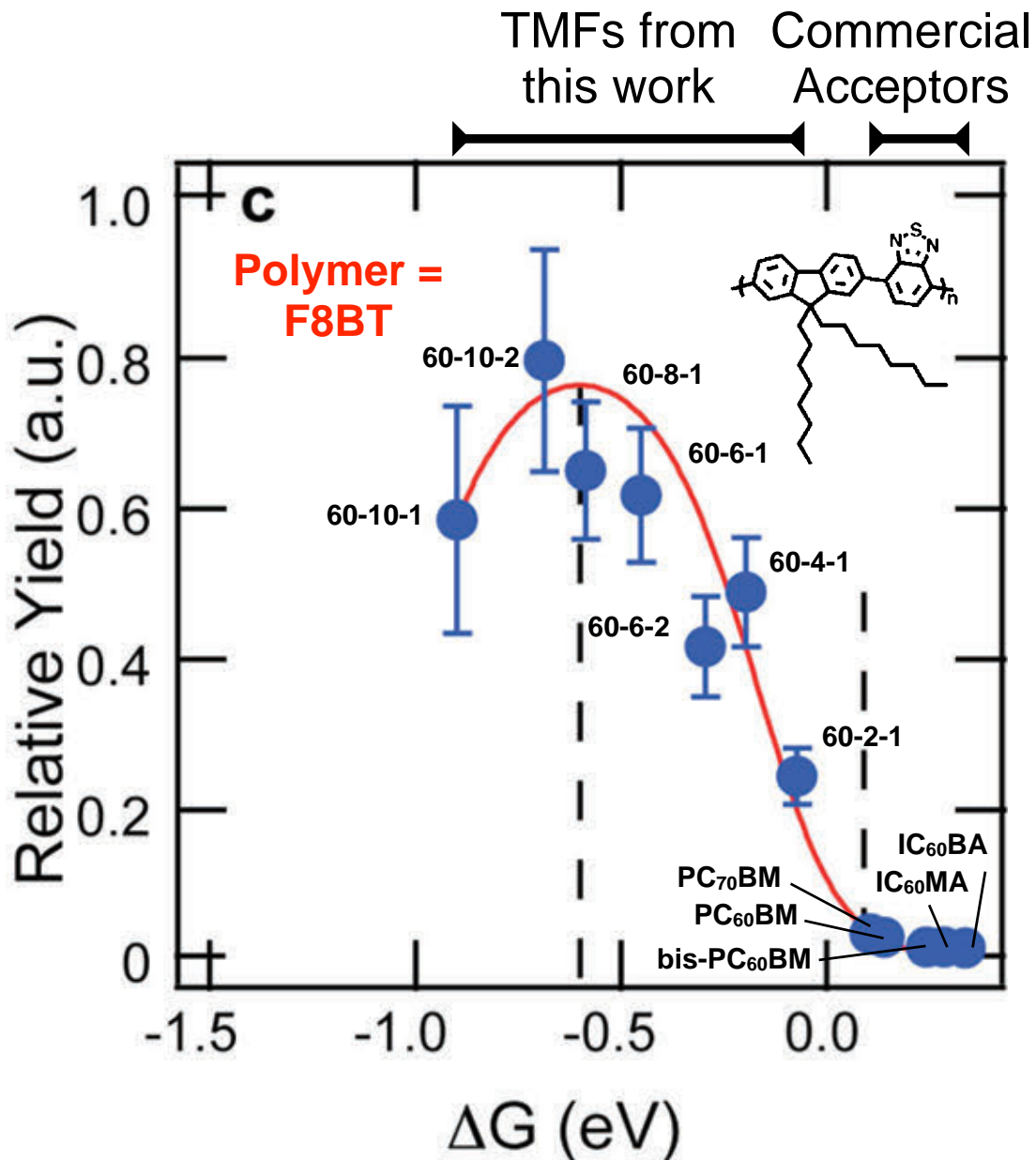


Figure 5.12. The relative yield of free charge generation as a function of energetic driving force is shown for dilute regime loadings of a range of fullerenes and F8T2.

The main conclusions from this study, which can easily be gleaned from the trends in Figures 5.10 – 5.12, gave a clear story of the charge creation step in OPV active layers: (i) charge creation yield rises gradually as the driving force, $|\Delta G_{\text{FC}}|$, is increased from zero, (ii) peak efficiency requires a significant driving force (e.g., 0.8 and 0.4 eV for F8T2:fullerenes and F8:fullerenes, respectively), (iii) greater driving forces *do not* continue to promote charge creation but rather push the system into an inverted region, and (iv) the ΔG_{FC} value that optimizes the yield is specific to the particular “donor” polymer. Taken together, these features emphasize that for efficient OPV systems, the donor and acceptor combination must be chosen properly. While such knowledge is often inferred through empirical studies, Figures 5.10-5.12 explicitly map this dependence.

Another example of a study involving energy level engineering that benefitted from the use of TMFs prepared in this work was a study of 12 new ethynylene-linked copolymers for OPV applications.³³ These types of polymers are currently very promising as OPV donor materials. However, as a result of their “design for a specific purpose”, some of these polymers have larger *EAs* that do not match well with the *EAs* of commercially available acceptors, and therefore ΔG_{FC} is low. TRMC measurements revealed that these deeper LUMO polymers indeed also have lower yields of free carrier generation. However, when $\text{C}_{60}(\text{CF}_3)_2$ was used as an acceptor, the measured $\phi\Sigma\mu$ increased by over a factor of three, shown in Figure 5.13. This serves as another example that with as much progress that has been made by polymer chemists, their efforts should not be constrained by a limited set of fullerene acceptors, and also shows that just because certain donor polymers do not perform well with commercial acceptors, this does not mean they will not perform well with other acceptors.

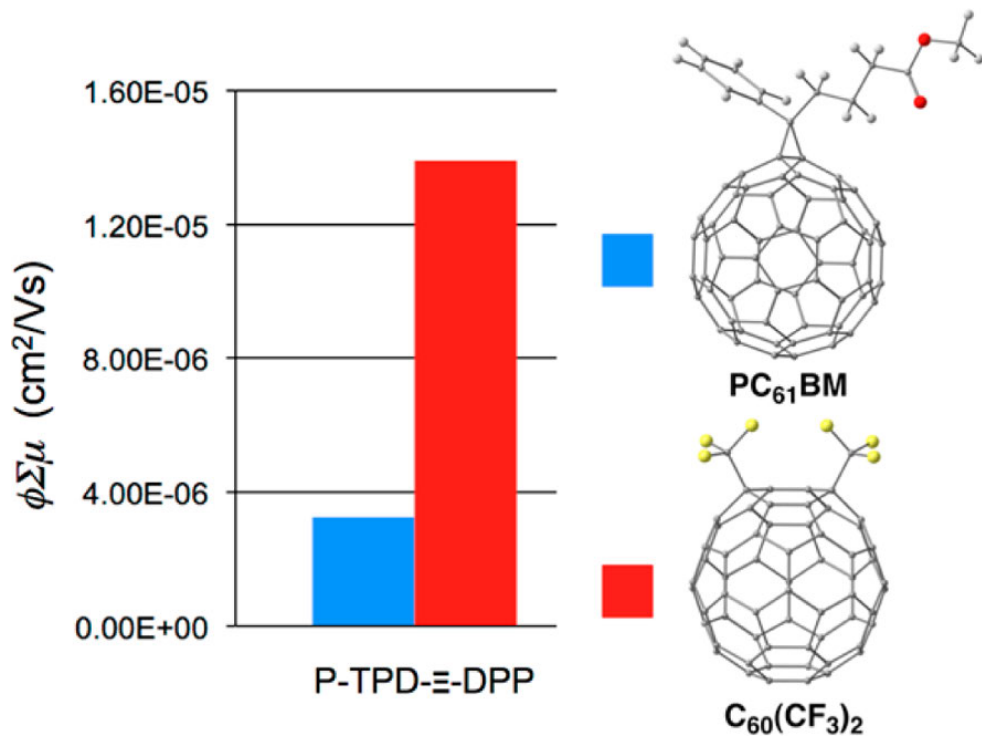


Figure 5.13. Molecular structures of fullerenes used in TRMC experiments (right) and magnitude of the $\phi \Sigma \mu$ product (left) for blends of an ethynylene-linked copolymer, P-TPD-≡-DPP with either 5 wt% PCBM (blue bar) or the molar equivalent of $\text{C}_{60}(\text{CF}_3)_2$ (red bar).³³

In fact, studies have shown that deeper LUMO donor:acceptor systems (i.e. – where the polymer and fullerene both have higher *EAs*) result in more stable OPV devices, since the energetics towards photooxidation becomes less and less competitive with polymer-to-fullerene electron transfer as frontier energies move further from vacuum.³⁴ Therefore, higher *EA* TMFs may also find use in the future when energy matched with appropriate polymers.

In summary, two examples of how the TMFs prepared in this work contributed to fundamental studies on the yield of free charge generation in OPV active layers were presented. From these studies, we learned that an optimal driving force, ΔG_{FC} , exists for maximizing the yield of free carrier generation, and that this relationship between the two is donor:acceptor pair specific. It was also shown that new types of OPV polymer materials should not be disregarded if they do not perform well with PCBM, since free carrier generation was shown to drastically increase when a more appropriately energy-matched acceptor, 60-2-1, was used.

5.4.3. TRMC Study of Electron Mobility in P3HT:TMF Active Layers.

A fundamental understanding of the relationship between molecular properties and the interfacial and bulk free charge photophysics in OPV active layers offers promise for further improvement of practical material systems by rational design. More specifically, correlating the dynamics of photo-induced free charge generation and the transport of those charges to particular molecular properties in type II polymer:fullerene heterojunctions may hold the key to realization of paradigm-shifting efficiencies in future polymer solar cells. After all, next generation high-performance OPV devices absolutely demand, among other things, two core elements: (i) highly efficient free carrier yield with minimal losses in photon energy and (ii) equally efficient collection of those charges. The former relies on appropriate choice of donor/acceptor materials

that balance minimal reorganization energy with optimally aligned energy levels, as discussed in the previous section, while the latter principally relies on high hole mobility in the donor phase and high electron mobility in the acceptor phase.³⁵ Over the past decade, a better understanding of photoinduced free charge generation has led to sharp improvements in device efficiencies, demonstrating the benefits of such fundamental studies. Surprisingly, far more efforts have been devoted to donor polymer properties than fullerene, and hence in comparison to a substantial variety of available OPV polymers,³⁶⁻³⁸ the choice of different fullerene acceptors has remained nearly constant, comprised of just a handful of different compounds, as discussed in Section 1. Additionally, in such studies the most commonly evaluated parameter when exchanging the acceptor in a series of polymer:fullerene devices is the offset in the frontier energies of the donor and acceptor, namely the HOMO and LUMO, respectively, estimated from some measurement, usually cyclic voltammetry. Fullerene-C₆₀, though, is an excellent candidate for molecule-to-material studies that go far beyond energetics. C₆₀ is an abundant, readily derivatized molecule, whose chemistry and reactions are well established by systematically varying far more than its electron accepting strength, which presents a the opportunity to explore a wide range chemical, structural, and other properties in relation to their performance in OPV active layers. As discussed in Chapters 1–3, the large-scale synthesis and improved isolation methods of TMFs offers access to a new library of diverse fullerene acceptors.

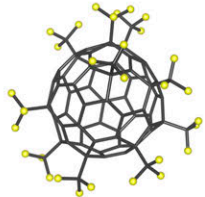
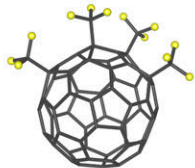
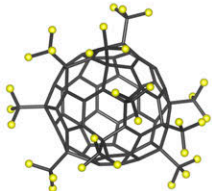
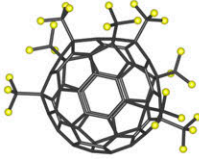
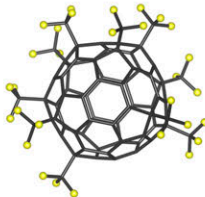
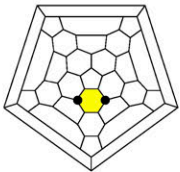
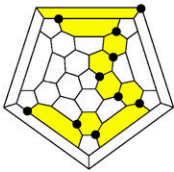
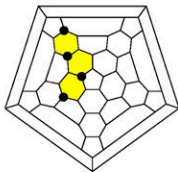
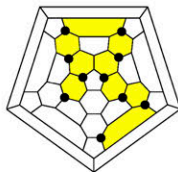
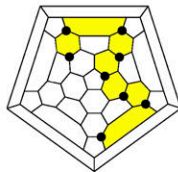
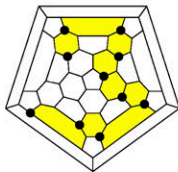
Concerning the molecular properties of a fullerene acceptor that contribute to high free carrier yield and mobilities, several factors must be considered. First, the energy of the fullerene's LUMO must be aligned to that of the polymer such that sufficient driving force ensures free-carrier generation is the predominant fate of the exciton. Previously we have shown the alignment of the donor and acceptor energy levels, or the absolute energetic driving force,

resulting in maximal free-carrier generation is specific to the donor:acceptor pairing.³² Therefore, when comparing different fullerenes in a particular polymer, they should have the same energy, which results in the same driving force for a particular polymer. Second, it is possible that fullerene derivatives having identical electron accepting strength can differ quite drastically in their exohedral modification. It is well known that the shape and position of a fullerene derivative's LUMO is determined by the pattern of the exohedral modification,³⁹⁻⁴¹ which was also shown in Chapter 3 for a series of new $C_{60}(CF_3)_{10}$ isomers. Therefore, even though the frontier energy levels of two different acceptors with a particular donor can be the same, the interaction of fullerene LUMO with the polymer may be very different, depending on its shape or location on the cage relative to the adducts. Third, once a free electron arrives in the fullerene phase, its mobility within that domain will be determined by rate of electron transfer between cages, making it very important that the electronic coupling among fullerenes in the network is amenable to rapid diffusion of electrons throughout. For fullerene derivatives, this is an especially crucial consideration, since chemically modifying the surface of the cage to achieve a desired property (i.e. – increased solubility, solid state ordering) should also be balanced with conserving the large pi-system of the cage that facilitates electron mobility. Bare cage fullerenes actually display good electron mobilities due to their extended pi-system LUMOs.⁴²⁻⁴⁴ For derivatives, though, each covalent addition to fullerene- C_{60} , or sp^2 to sp^3 hybridization of cage carbon atoms, the pi system is diminished, leaving the fullerene with a less delocalized LUMO, which in turn decreases the degree to which a network of those fullerenes can electronically couple. Fourth, regardless of LUMO location on the cage, the distance between cages should be minimized. In 2010, Nelson and coworkers demonstrated using numerical modeling methods that electron hopping rates in methanofullerene derivatives decreases as a function of increasing

aliphatic chain length of the adduct.⁴⁵ However, more recently it has been argued by Blaumberger *et al.* that the traditional rate equations for electron hopping in PCBM crystals do not apply,⁴⁶ although both findings were in agreement that increased cage-cage distance results in poorer electronic interactions in the fullerene phase.

Systematic experimental investigation of these four considerations is a major challenge, since ideally the fullerenes would have to be able to probe each consideration without affecting the others. However, such an acceptor set exists, which were synthesized and isolated in high purity for this purpose: six TMFs that were grouped into three distinct pairs based on several criteria. Schlegel diagrams, two-dimensional representations of three-dimensional objects, of the six TMFs used in this study are shown on the right in the Table 5.3, arranged in their respective pairs based on nearly identical half-wave reduction potentials measured by cyclic voltammetry.³⁹ On the left, these TMFs are highlighted as red dots on a correlation plot of DFT-predicted E_{LUMO} versus measured $E_{1/2}$ values. The black dots on the Schlegel diagrams (right) represent the location of CF_3 additions, with hexagons colored yellow where CF_3 groups are attached in a continuous fashion along a ribbon of adjacent hexagons, either in *ortho*- or *meta*- relation, highlighting their addition pattern.

Table 5.3. The TMFs used in this study are shown, with reduction potentials (ref 39), 3D representations from x-ray structures and corresponding 2D Schlegel Diagrams.

Compound	$C_{60}(CF_3)_2-1^a$	$C_{60}(CF_3)_{10}-5^b$	$C_{60}(CF_3)_4-1^c$	$C_{60}(CF_3)_{10}-3^d$	$C_{60}(CF_3)_8-1^e$	$C_{60}(CF_3)_{10}-2^f$
Abbreviation	2-1	10-5	4-1	10-3	8-1	10-2
$E_{1/2}$ vs. $C_{60}^{0/-}$	0.11 V	0.12 V	0.17 V	0.17 V	0.33 V	0.32 V
3D Structure						
2D Structure						

Careful examination of the electronic, structural, and physical properties reveal why they are excellent candidates for this study as follows. Firstly, high-quality single crystal x-ray structural information for each TMF is known, thus allowing for packing interactions to be known between fullerenes *should* these crystal structures form in the fullerene phase of the blended film. Secondly, each fullerene is known to undergo efficient and equivalent exciton quenching upon photoexcitation in P3HT films from TRPL studies (refer to Table 5.1). Thirdly, the fullerenes in each pair have the same reduction potentials, so other factors contributing to TRMC signal can be attributed to other properties/interactions. Now, in order to understand how these fullerenes compare in terms of electron mobility, it is necessary to closely examine their structure relationship to their LUMO, which is directly involved in fullerene-to-fullerene electronic coupling. In Figure 5.14, the DFT-predicted LUMO structures are shown for each of the six TMFs. Now, each CF_3 group protrudes from the cage by about 2.6 Å, so clearly in the case of C_{60} carrying two CF_3 groups, the statistical proximity that fullerene cages can be in relation to its neighbor in the solid state is lower (if they're in a completely random orientation) than when C_{60} is carrying ten CF_3 groups. According to both Nelson and Blumberger, the electron mobility in a fullerene network is lower as the distance between neighboring cages increases (although neither author agrees with the other on the mechanism for electron transport). This suggests that the mobility in the fullerene phase would be worse for $\text{C}_{60}(\text{CF}_3)_{10}$ than for $\text{C}_{60}(\text{CF}_3)_2$. What was not discussed in the either report was how the spatial relationship of the substituent on a fullerene derivative to the LUMO location on the cage will affect mobility in cases where this relationship is drastically different, (i.e. – they only investigated one type of fullerene derivative with only one addition). Now, consider the LUMO Schlegel diagrams in

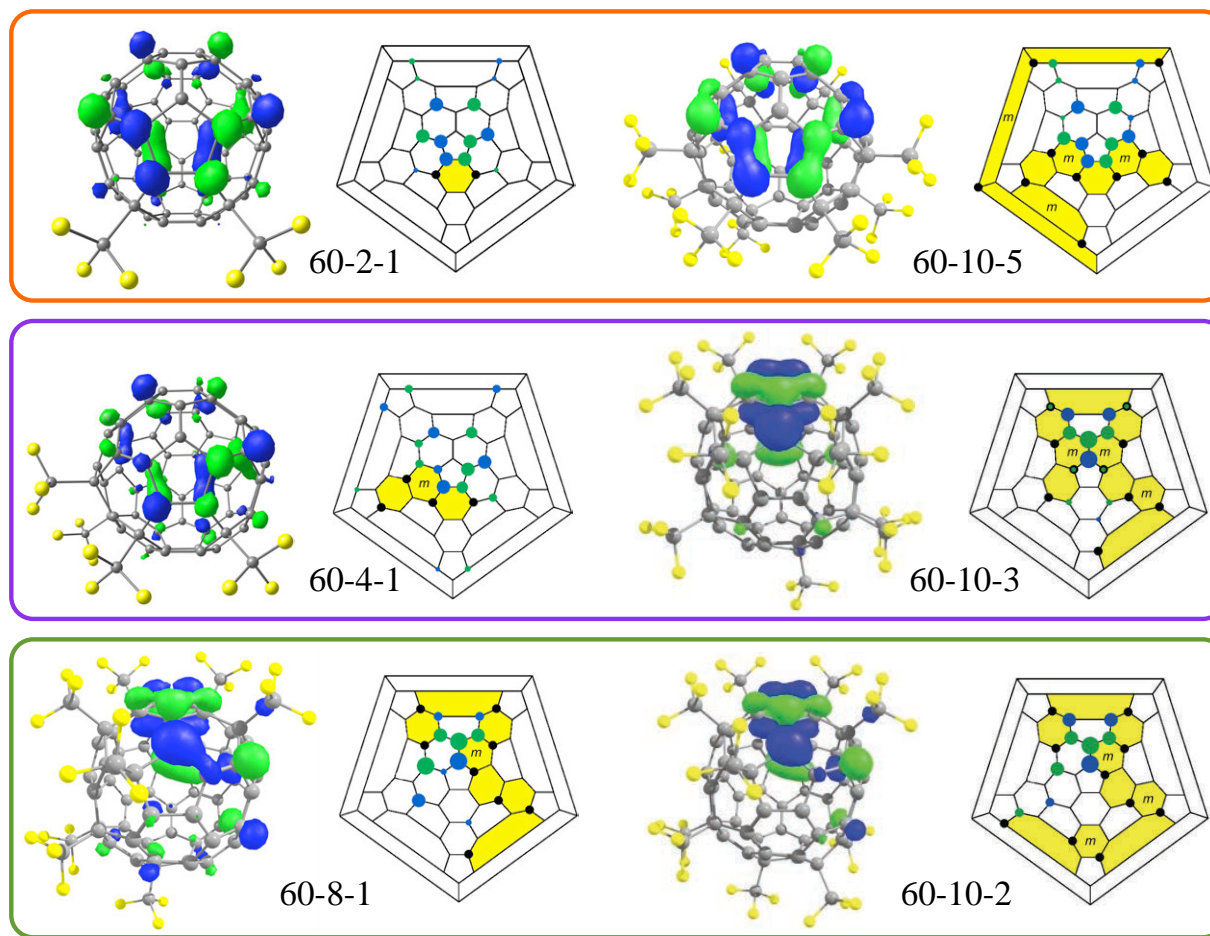


Figure 5.14. Schlegel and LUMO diagrams showing the CF_3 addition patterns (black circles on Schlegel diagrams) and the DFT-predicted cage C atom contributions to the LUMOs for the three pairs of TMFs (60-2-1 and 60-10-5, 60-4-1 and 60-10-3, 60-8-1 and 60-10-2). The blue (+) and green (–) circles represent the upper lobes of the π atomic orbitals for each cage C atom scaled approximately to its contribution to the LUMO.

Figure 5.14, which highlights how we were able to experimentally probe this relationship using these three TMFs and TRMC. It is important to realize during the following discussion that the three pairs of TMFs, circled in orange, purple, and green lines consist of TMFs with the same reduction potentials within the pair, but differ by a number of other reasons. The positive and negative lobes of the LUMO (calculated by DFT by Dr. Alexey Popov) are shown on carbon atoms as green and blue dots, respectively, with their relative sizes depicted proportionally. Shown at the top of the figure is the comparison of the first pair, 60-2-1 and 60-10-5. These two TMFs have a drastic difference in the number of CF_3 groups on the cage, two and ten, but because of their specific addition pattern, it turns out that the position of the LUMO is identical between the two (see LUMO Schlegel diagrams and LUMO structures in the figure). Therefore, between this pair of molecules it is possible to differentiate mobility based on how close these cages can approach each other in the solid due to the presence of more CF_3 groups. The second pair of TMFs, 60-4-1 and 60-10-3, also have a large difference in the number of CF_3 groups that are on the cage, however in this pair of TMFs the LUMO position is also very different. In the case of 60-4-1, the LUMO is fairly well distributed around the cage and away from the CF_3 groups. The location of the LUMO for 60-10-3 is far more localized, and in fact is primarily located on the fulvene unit of the cage that is surrounded by CF_3 groups. Between these TMFs, the difference in electron mobility is expected to be even greater than the difference observed between 60-2-1 and 60-10-5 (due to different number of CF_3 groups) since the LUMO of 60-10-3 is far less accessible. In the third pair of TMFs, 60-8-1 and 60-10-2, the cage carries essentially the same number of CF_3 groups (eight and 10, respectively), and their addition pattern is identical except for the two additional CF_3 groups in the case of 60-10-2. As such, the location of the LUMO is nearly the same for each of them. Since these are very similar molecules with

respect to their LUMO and relative cage-cage distances (estimated by number CF_3 groups are on the cage), they are expected to have similar electron mobility in their respective fullerene phases. In summary, the paired molecules have either similar number of CF_3 groups with nearly identical LUMO shape and position (60-10-8 and 60-10-2), vastly different number of CF_3 groups with nearly identical LUMO shape and position (60-2-1 and 60-10-5), or very different number of CF_3 groups and very different LUMO shape and position (60-4-1 and 60-10-3). These three unique pairs of fullerene derivatives are key to enabling this first of its kind experimental study.

Each of these TMFs were blended in equimolar loadings with P3HT, and the photoconductance of each of the six samples (as well as a neat P3HT control sample) were measured by TRMC, and their $\phi\Sigma\mu$ values were compared. For P3HT, the hole mobility is 0.014 mV/cm^2 , which has been measured in the bulk sample by pulse radiolysis¹⁹ time-resolved microwave conductivity and is assumed to remain the same in blends where loading ratios of fullerene are such that bulk crystalline phases of P3HT are conserved. Hence, if the free-carrier yield contribution to the TRMC signal is decoupled, we consider the *electron* mobility in the fullerene phase as the main contributor to “mobility” beyond what is known as the *hole* mobility in P3HT (i.e. $-\Sigma\mu = 0.014 \text{ mV/cm}^2 + \mu_e$). Therefore, since the driving force for free carrier generation is assumed to be constant (since within each pair the compounds have the same reduction potential in solution), and the hole mobility is constant in each sample (P3HT is the donor in each case), the differences in $\phi\Sigma\mu$ should be attributable to the difference between the compounds in each pair as described above. The $\phi\Sigma\mu$ for each sample is shown in Figure 5.15.

Although the reduction potentials are the same for each compound within the pairs, the TRMC data reveals some interesting differences in the measured $\phi\Sigma\mu$. For example, 60-2-1 has a measured signal over an order of magnitude that of 60-10-5, even though the only difference in these two molecules is the number of CF_3 groups on the cage, suggesting that the electron mobility contribution suffers greatly as a result of larger cage-cage distances within the domains of 60-10-5. A similar effect is seen in the case of 60-4-1 and 60-10-3, but besides the difference in the number of CF_3 groups, here the LUMO shape and position is also very different between the two. It is noteworthy that the thermally annealed sample with 60-10-3 gives rise to the lowest signal of any of the TMF:P3HT blends. This observation is consistent with the fact that this particular isomer of $\text{C}_{60}(\text{CF}_3)_{10}$ has the most localized LUMO. Also, its LUMO is located on the fulvene unit formed by the closed loop of the doubled back portion of the ribbon addition pattern, which means the LUMO is housed within a surrounding ‘forest’ of CF_3 groups that sterically hinder electronic interactions beyond the already negative impacts of having ten CF_3 groups on the cage. On the other hand, when the number of CF_3 groups on the cage is similar, the decrease in signal is less drastic. Considering the pair 60-8-1 and 60-10-2, the number of CF_3 groups is similar, the shape and position of their LUMOs are very similar, and the measured $\phi\Sigma\mu$'s are also almost the same. Therefore, the presence of just two CF_3 groups that differentiate 60-8-1 and 60-10-2 only contributes slightly to the observed decrease in electron mobility.

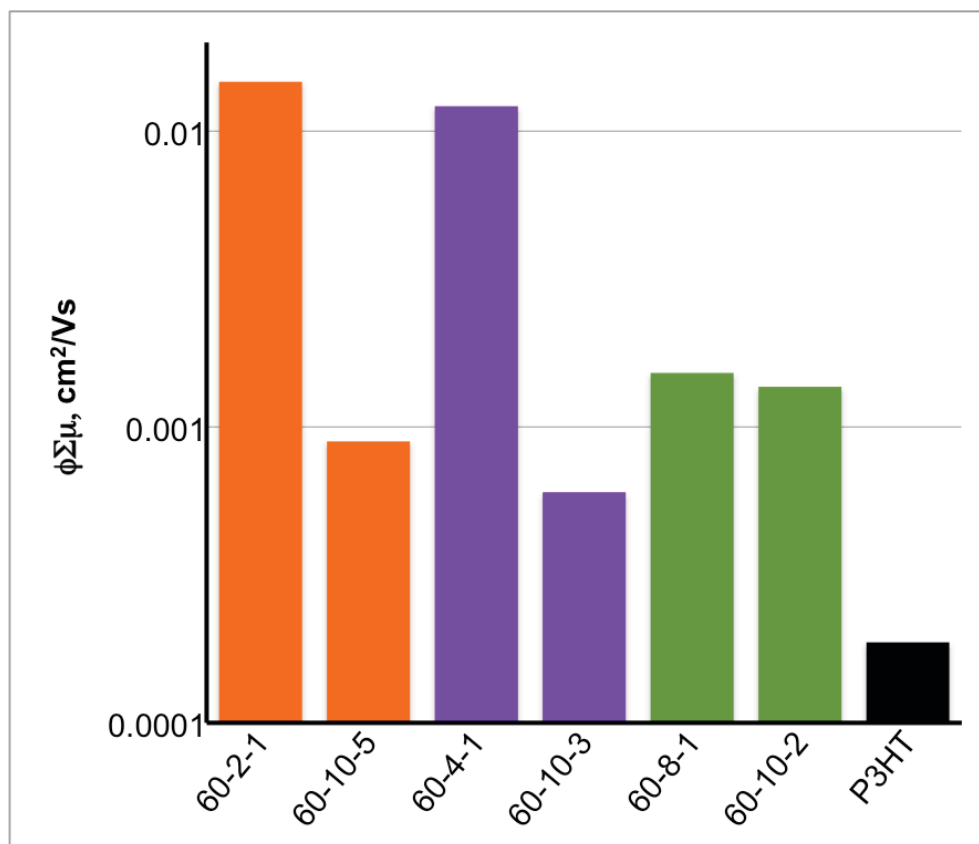


Figure 5.15. The $\phi_{\Sigma\mu}$ values are shown for each of the blends of TMFs and P3HT after thermally annealing each sample.

The effects of thermally treating the TMF:P3HT films on the measured $\phi\Sigma\mu$ are shown in Figure 5.16. For pure P3HT, the thermal anneal does not have a significant effect. The signal for all of the TMF:P3HT blends increased after the thermal treatment except for 60-10-3, which decreased by almost 40%. Therefore, one explanation for the observed trend is an increase in electron mobility in the fullerene phase as a result of lowest energy ordering of molecules in the TMF phase. In all cases besides 60-10-3, ordering of the molecules improves the LUMO-LUMO overlap between neighboring TMF molecules. Since the 60-10-3 molecules pack with the LUMO of the molecule far from each other and also shielded by CF_3 groups, then after they order during the anneal, they have an even lower probability of cage-cage electronic coupling than before which can explain why a decrease in $\phi\Sigma\mu$ was only observed in that case. This analysis of course relies on the assumption that a similar cage packing structure forms in domains of 60-10-3 in the P3HT active layer as they do in the single crystal structure. Thermally induced ordering of the TMFs in each example also may explain why the three isomers of $\text{C}_{60}(\text{CF}_3)_{10}$ have almost identical $\phi\Sigma\mu$'s before annealing (because their spatial separation is roughly the same for different isomers with the same number of CF_3 groups in random orientations), but after annealing they assume a more stable packing structure, which fine tunes the mobility either positively in the case of 60-10-2, almost not at all for 60-10-5, and negatively for 60-10-3, based on accessibility of the LUMO and particular nearest neighbor cage distances in that packing structure. The LUMO+1 was also considered in the case of 60-4-1 to explore the possibility that electron conduction could also be occurring in the LUMO+1. The relative difference in energy between the LUMO and LUMO+1 was 78 meV, which is approximately 4% population of that state at room temperature. However, there was no significant difference in the location of the LUMO and LUMO+1. The LUMO+2 position is significantly different from 60-

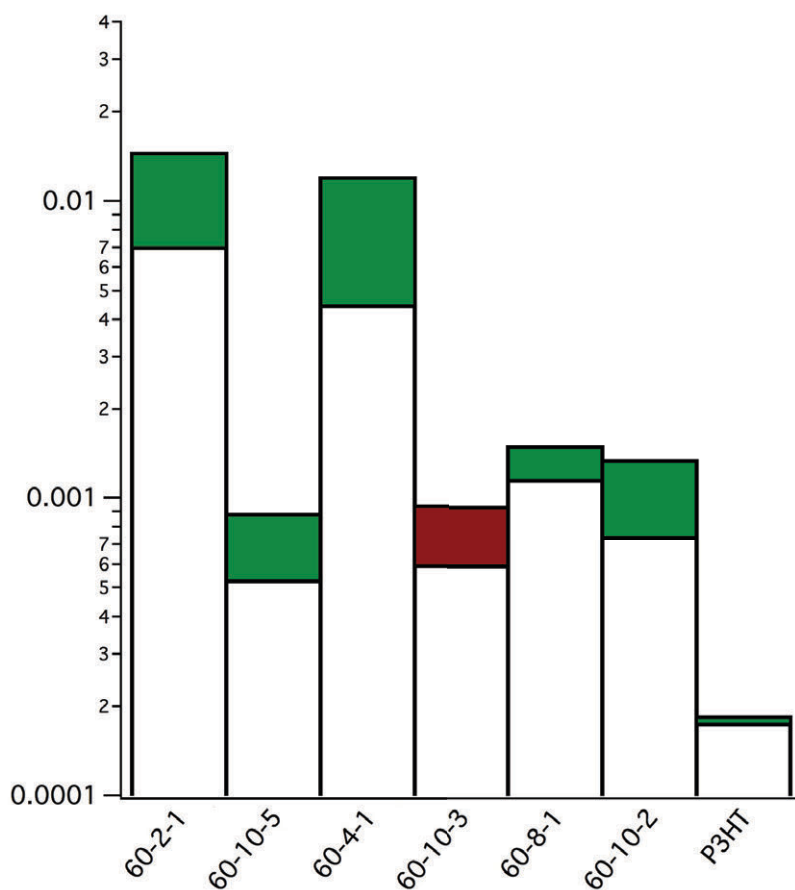


Figure 5.16. The change in $\phi\Sigma\mu$ for each P3HT:TMF sample and neat P3HT is shown after a thermal annealing treatment, with increases in $\phi\Sigma\mu$ values shown in green and decreases shown in red.

4-1's LUMO and LUMO+1, but the difference in energy is ca. 450 meV, which means it is not likely to contribute to electron diffusion in a solid of 60-4-1 molecules.

While the *qualitative* observed trends in $\phi\Sigma\mu$ values are consistent with expected electron mobilities in each TMF phase as a result of each structure and LUMO position, the quantification of these effects revealed an interesting result. For 60-2-1 and 60-10-5, the $\phi\Sigma\mu$ values after annealing are 1.5×10^{-2} and 8.9×10^{-4} , respectively. If we assume that the yield, ϕ , is the same for the pair (since they have the same driving force), and the mobility of holes in P3HT remains constant, $\mu_h = 0.014 \text{ cm}^2/\text{Vs}$, then the difference in the signal between the two samples is due to electron mobility in the fullerene phase, μ_e . For this pair, the electron mobility in 60-2-1 would be $0.23 \text{ cm}^2/\text{Vs}$. However, this value is a factor of about five times higher than what has been evaluated for PCBM by TRMC methods,¹⁸ which is suspicious. For 60-4-1 and 60-10-3, again if the ϕ is assumed to be the same between the pairs, then 60-4-1 would have a mobility of $0.29 \text{ cm}^2/\text{Vs}$. This possibility is considered by comparing the LUMOs of 60-2-1 and PCBM to each other, since they both have minimal exohedral modification (more sp^2 cage carbon atoms), as shown in Figure 5.17. Based on the assumption that better LUMO accessibility between nearest neighboring molecules contributes to better electron diffusion in the solid, then PCBM should be expected to have a higher electron mobility, which is contradictory to the electron mobility calculated for 60-2-1 from TRMC. Another possibility is that the average nearest neighbor distance in the case of PCBM is higher than for 60-2-1, but it is not likely that this difference would result in a factor of five times greater mobility in 60-2-1. This analysis is also not consistent with the 60-4-1 having an electron mobility a factor of six times higher than PCBM (0.29 versus $0.05 \text{ cm}^2/\text{Vs}$, respectively). Therefore, an alternative explanation was postulated to interpret these results.

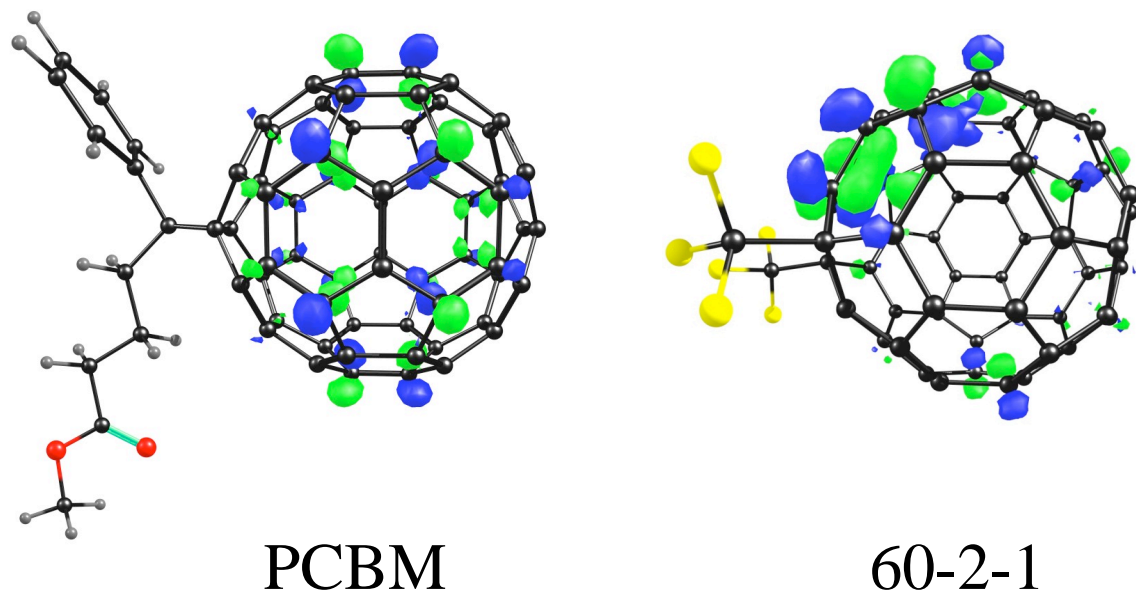


Figure 5.17. The DFT-predicted LUMO orbitals are shown for PCBM and 60-2-1. Each molecule has been positioned such that it is visualized from a “side view”. The LUMO is delocalized as a belt around C₆₀ perpendicular to the PCBM substituent (left) while it is localized close to the CF₃ groups in the case of 60-2-1 (right). The blue (+) and green (–) circles represent the upper lobes of the π atomic orbitals for each cage C atom scaled approximately to its contribution to the LUMO.

Even though the energetic driving force for free carrier generation was the same in each of the pairs of TMFs, there is indication that the yield of free uncorrelated charges measured by TRMC was not the same in each pair, at least not in the pairs where the electron mobility was expected to be drastically different (60-2-1 and 60-10-5, and 60-4-1 and 60-10-3). The normalized time-resolved photoconductivity transients at different excitation intensities for each sample are shown in Figure 5.18. The spread in photoconductivity at different light intensities, namely, the slower decay of photoconductance at the lowest light intensity, is attributed to mobility of electron in the fullerene phase. Both 60-2-1 and 60-4-1 show a significant electron mobility component. For neat P3HT, the decay of free carriers are pseudo first-order, such that holes recombine with stationary electroactive defects in the polymer, known as dark carriers in solid state physics. The same pseudo first-order decay dynamics are observed for the three isomers of $C_{60}(CF_3)_{10}$, yet the $\phi\Sigma\mu$ are increased almost an order of magnitude over neat P3HT. This suggests that the mobile holes P3HT are recombining with essentially stationary electrons at polymer:acceptor interface, meaning that the TRMC yield of free carriers in “50:50” blends of donor:acceptor is actually lower when the electron mobility in the acceptor phase is low. Since TRMC measures the gigahertz mobility of uncorrelated free carriers on timescales longer than ca. 10 ns, other processes such as recombination may be occurring on shorter timescales, and therefore not detected by TRMC.

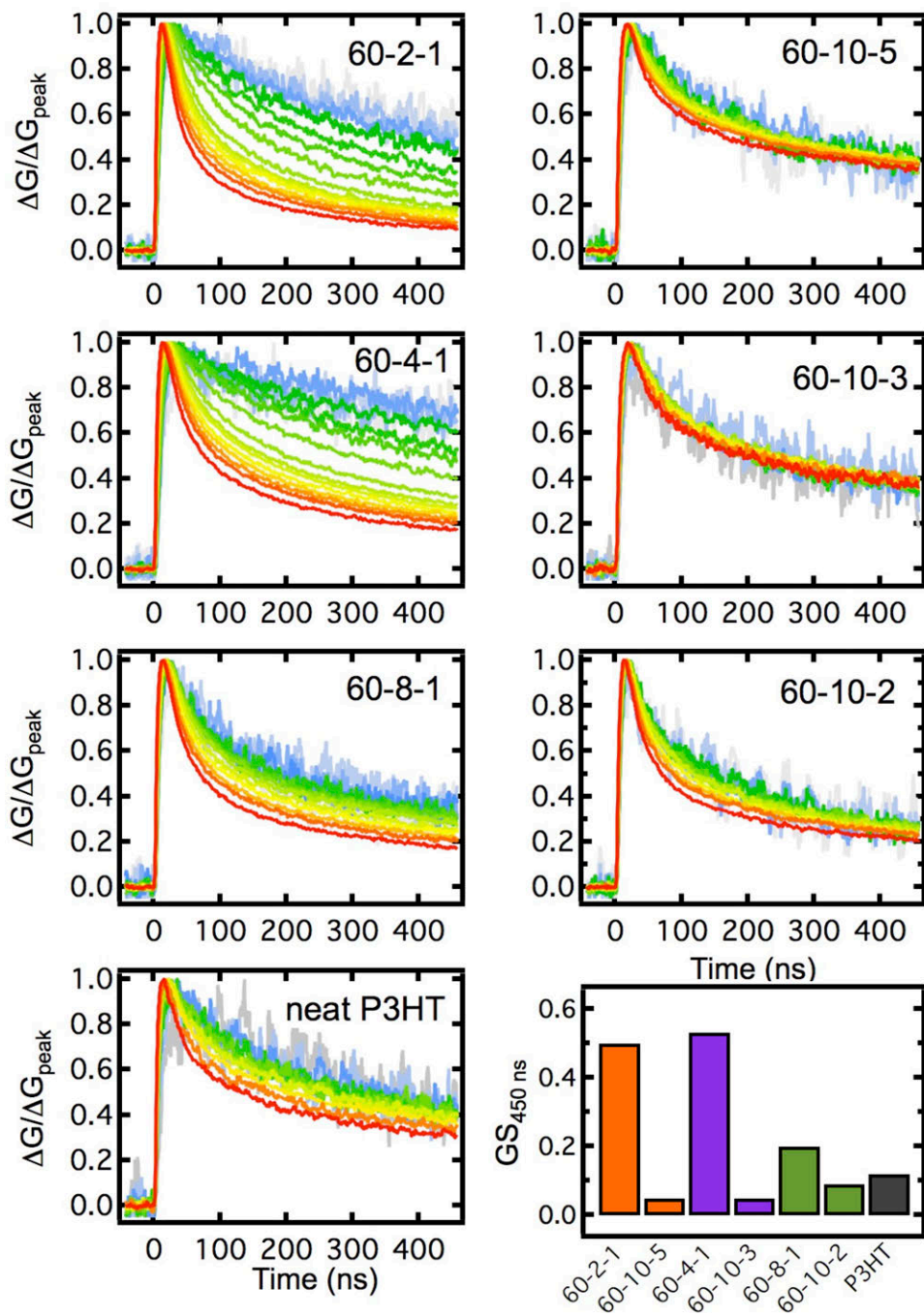


Figure 5.18. Analysis of the normalized photoconductivity transients for the three pairs of TMF:P3HT blends further supports the hypothesis that the decrease in $\phi\Sigma\mu$ is dominated by factors related to electron mobility in the fullerene phase. $GS_{450\text{ ns}}$ is the normalized difference between the photoconductance at 450 ns between the highest and lowest light intensity transients.

A possible physical representation of an example where there is low mobility in the acceptor is as follows: (i) excitons are dissociated at the donor:acceptor interface, (ii) the electrons have low mobility for diffusion away the interface, so (iii) many of these electrons undergo rapid geminate recombination with holes (which occurs on a picosecond timescale), (iv) some of the holes diffuse away from the interface ($\mu_h = 0.014 \text{ cm}^2/\text{Vs}$ for P3HT), (v) and then non-geminate/uncorrelated holes diffuse back to the polymer:TMF interface where they recombine with essentially stationary electrons. This means that the yield of free carriers is actually higher when the electron mobility in the fullerene phase is high. To date, this would serve as the first experimental evidence of this hypothesis, which is that the yield of free carriers in OPV-relevant active layers is dependent on how fast free carriers can diffuse away from the interface. The only reason this type of experiment was possible is because of the unique set of TMFs that differed in their structural and/or LUMO location. The importance of this result is that regardless of the driving force for free carrier generation in “50:50” blends of donor:acceptor, if the mobility in the acceptor phase (or presumably alternatively in the donor phase) is very low, then the yield of free carriers will be diminished, which must be considered when implementing new materials for OPV application.

5.4.4. OPV Devices Containing PFAF Acceptors.

By now, the value of fundamental studies on photoinduced electron transfer in polymer:fullerene blends has been established, as well as the importance of discovering new donor and acceptor materials for OPV applications. To this point, however, only fundamental studies of PFAFs in OPV active layers have been discussed; in the following their performance

in actual solar cells will be addressed. First, a brief description on how solar cell performance is evaluated will be given.

The performance of an OPV device is evaluated based on certain features of its current-voltage (JV) relationship, which is measured under an applied voltage range, in the dark and under illumination. Ideally, the shape of the JV curve will be that of a diode. When evaluating the JV curve characteristics of an OPV device, there are four main figures of merit: short circuit density (J_{sc}), open circuit voltage (V_{oc}), fill factor (FF), and power conversion efficiency (PCE). The PCE for a device is calculated by:

$$PCE = \frac{J_{sc} \times V_{oc} \times FF}{P_{in}}$$

where P_{in} is the power of the incident light. Consider the JV curve in Figure 5.19., the J_{sc} is defined as the current at zero voltage, the V_{oc} is defined as the voltage at zero current, and FF is defined as the ratio percentage of the maximum power achieved by the cell to the product of J_{sc} and V_{oc} . Solar cells with more perfect diode-like JV curves have higher fill factors. Currently, the best-performing OPV devices have fill factors of around 70%. Simply, J_{sc} and V_{oc} are correlated to charge generation and transport in the bulk active layer and the energy difference between the HOMO of the donor and the LUMO of the acceptor, respectively. While the factors that determine the characteristics of $J-V$ curves, J_{sc} , V_{oc} , and FF are fairly well understood, the *exact* origins and mechanisms of charge generation, recombination, transport, and energy losses in OPV devices are not yet known, and are currently under intense investigation.^{14,47-53}

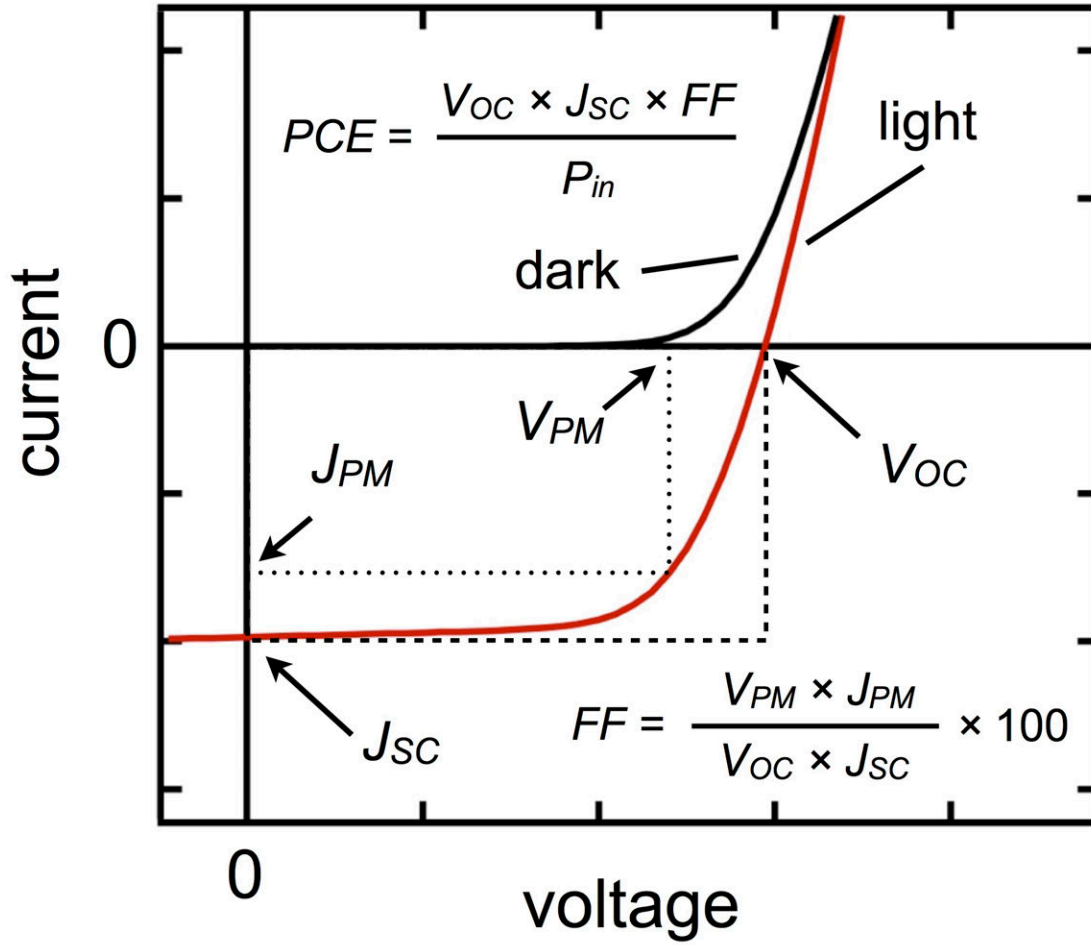


Figure 5.19. JV curve characteristics are defined for a representative OPV device.

Of all the TMFs discussed here, $C_{60}(CF_3)_2$ was the best candidate to study in OPV devices since the TRMC data revealed it has a significant electron mobility contribution in the fullerene phase to $\Sigma\mu$ based on the light intensity-dependent spread in the photoconductivity transients. Additionally, 60-2-1 can be prepared on a hundreds-of-milligrams scale, and isolated in very high purity using single stage HPLC separation, as discussed in Chapter 1. Furthermore, 60-2-1 is stable towards thermal vapor deposition, which enables a better control over active layer morphology by preparing bilayer devices. This significantly decreases the amount of time that is required to optimize device fabrication methods that in turn allows true evaluation of device performance, since the BHJ domains assemble based on a number of molecular properties and interactions between the donor and acceptor. In principle it is faster to make devices by spin coating the donor:acceptor blend, but the morphology is not as controllable when changing the donor:acceptor combinations in this method.

It is well known that the self-assembled BHJ morphology of a polymer:fullerene blend is determined by the interaction of the two in the presence of the solvent used to deposit them (namely their miscibilities with one another and their individual solubilities),⁵⁴⁻⁵⁷ and therefore two fullerenes with different chemical and structural properties are not expected to form identical bulk morphologies when deposited under identical conditions. Indeed, when a P3HT:60-2-1 device was prepared using a method that has been optimized for P3HT:PCBM devices, the 60-2-1 device had a *PCE* of essentially 0%. Device optimization studies for BHJ active layers can be extremely time consuming; it took nearly a decade for researchers to find the best techniques for P3HT and PCBM blends, and improvements beyond the active are still being made. Therefore, the active layer morphology was simplified to a bilayer, prepared by evaporating a layer of 60-2-1 on top of a spin-coated film of pure P3HT. It is important to point out again that PCBM

decomposes under these thermal deposition conditions while 60-2-1 does not (refer to Chapter 4 for full details). Several dozen devices were fabricated involving this active layer in an iterative fashion, varying the bilayer component thicknesses and choice of metal contacts in order to establish an optimized P3HT:60-2-1 device, which was then compared to a device optimized for P3HT:PCBM (see Figure 5.20), since it is the most well studied polymer:fullerene device in the literature.⁸ The optimal device architecture for P3HT:60-2-1 was found to be ITO/PEDOT:PSS/P3HT/60-2-1/Ca/Al, the details of which are described in the experimental section, with the P3HT layer being approximately 120 nm thick and the evaporated layer of 60-2-1 being ca. 80 nm.

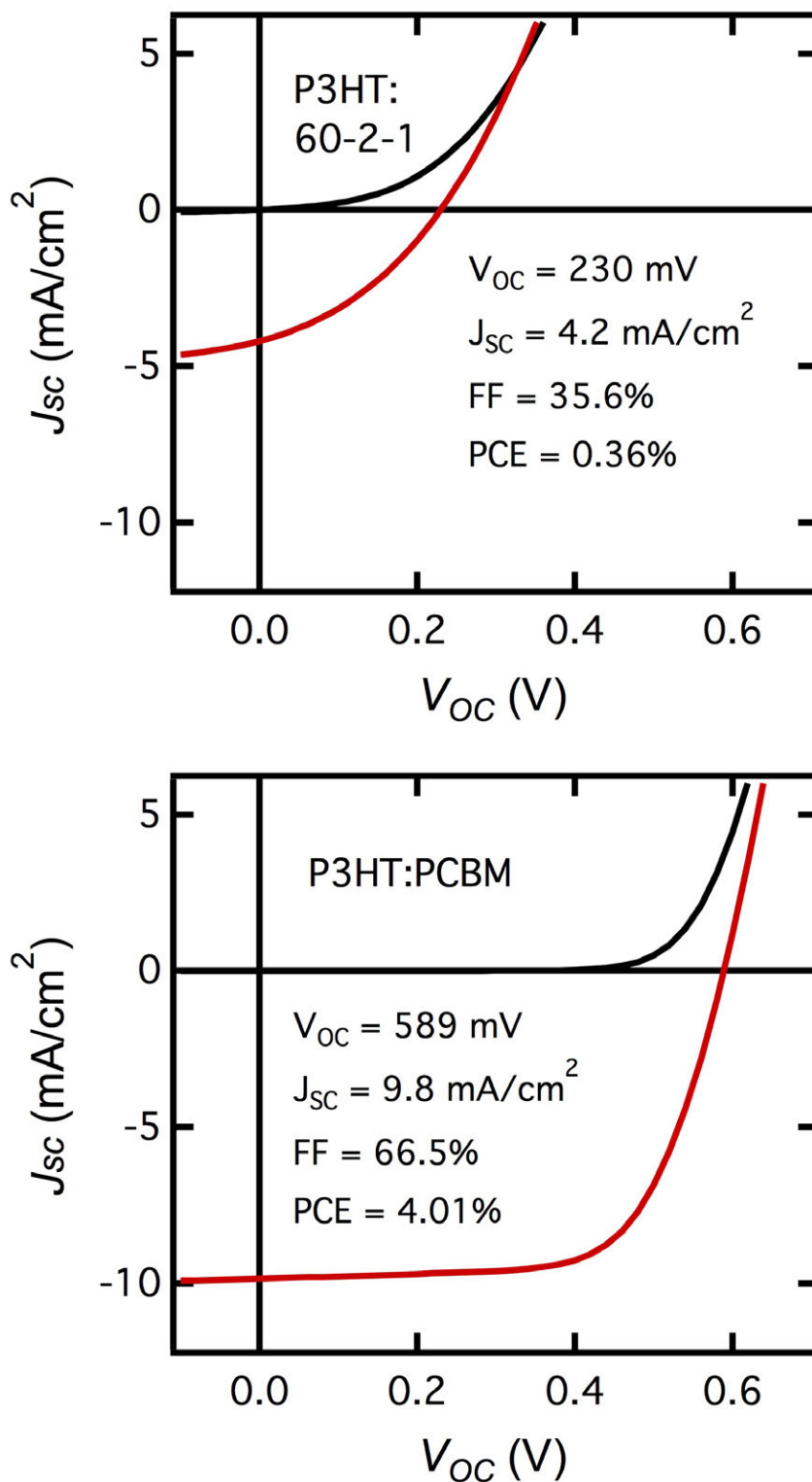


Figure 5.20. The JV curves and device characteristics of a P3HT:60-2-1 annealed bilayer device (top) and an optimized P3HT:PCBM device with a bulk heterojunction active layer (bottom).

When such devices were tested directly after fabrication, none of the devices produced photocurrent, however, after thermally annealing them in an inert atmosphere glovebox for 15 minutes at 150 °C they began to work. The temperature and duration of this annealing treatment was investigated; higher temperature anneals also optimized the device performance unless they exceeded 30 minutes at which point the device performance decreased, and lower temperature treatments resulted in improved performance, but not as significant as the 15 minute 150 °C treatment. Thermal annealing treatments on devices containing P3HT are currently common practice in OPV research, and the resulting improvements in device performance have been shown in many instances, which is attributed to increased ordering of crystalline phases of the polymer as well as more intercalation of fullerene into the amorphous polymer phases.⁵⁸⁻⁶⁰ Nonetheless, the optimized P3HT:60-2-1 device gave only a PCE of 0.36%, much lower than the PCBM device, PCE = 4.01%, measured under identical conditions. The V_{oc} (230 mV) in the 60-2-1 device was not surprising, since it is ca. 230 mV easier to reduce in solution than PCBM, which gave a V_{oc} of 589 mV. Therefore, considering contributions to voltage losses due to electron transfer in the solid state, the V_{oc} in P3HT:60-2-1 devices should be less than about 360 mV, so a lower PCE due to decreased PCE was expected. The PCBM device also had a higher fill factor, 66.5%, compared to the 60-2-1 device, 35.6%. Surprisingly, the short circuit current in the 60-2-1 device was less than half of that of the PCBM device, 4.2 and 9.8 mA/cm². Since the PCBM and 60-2-1 devices contained active layers of approximately the same thickness, thus the cross-section of photon absorption was the same, the differences in measured J_{sc} are likely due to bulk morphology of the active layer. The low fill factor and J_{sc} in the 60-2-1 devices imply that the performance of the device was limited by charge carrier recombination in the active layer, in their long-range transport to the contacts. To test whether morphology was a

limitation, thin film XRD measurements (performed by Dr. Nikos Kopidakis) on a P3HT:60-2-1 film on quartz (prepared identical to the device active layer) showed strong diffraction peaks due to large crystalline domains of $C_{60}(CF_3)_2$ in the film. In fact, clusters of 60-2-1 domains up to 4 microns in diameter could be observed by optical microscopy (Figure 5.21).

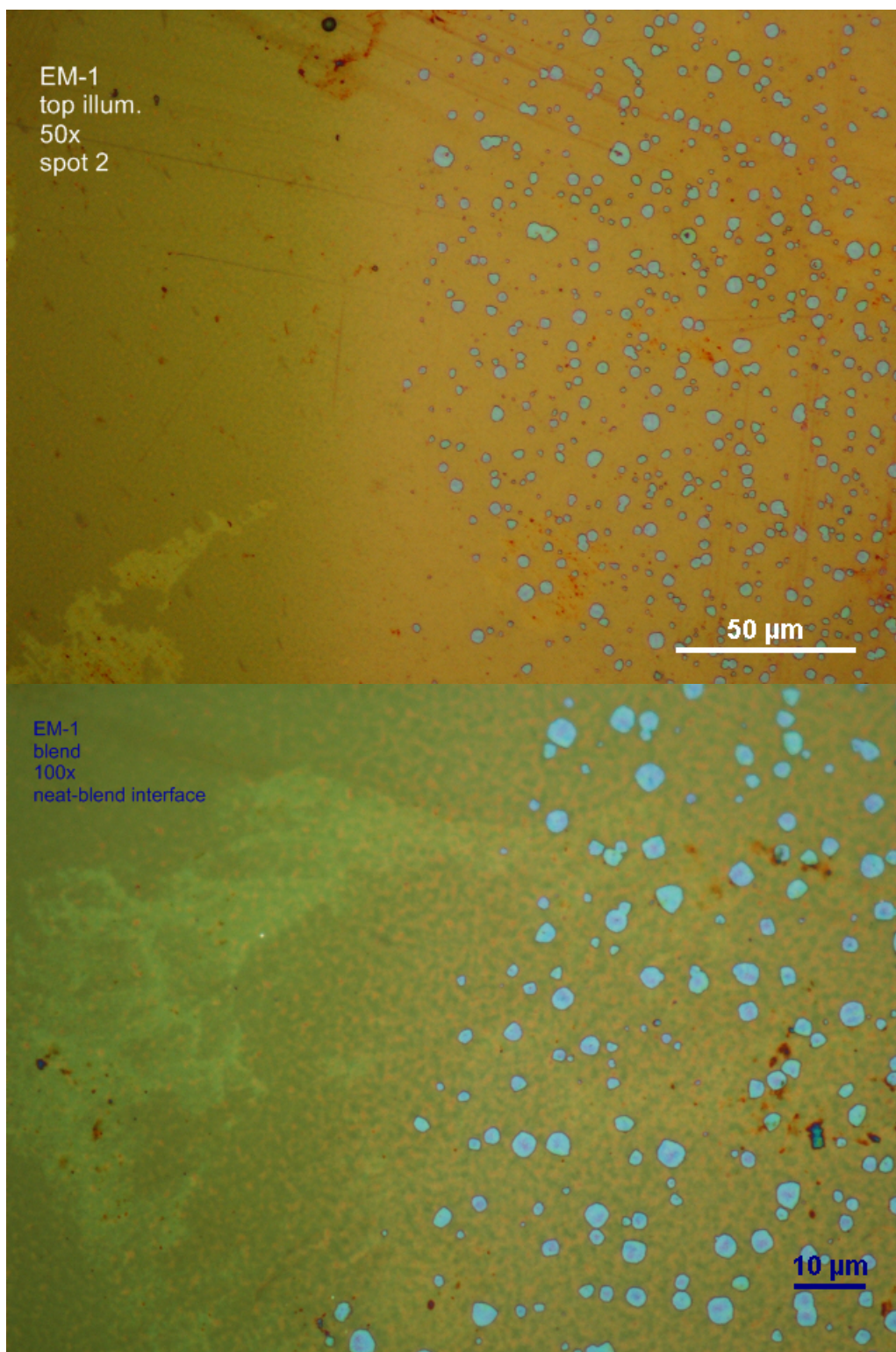


Figure 5.21. Optical micrographs of an interface between the layer of 60-2-1 and P3HT in a bilayer prepared by evaporating 60-2-1 onto spin-coated P3HT. The blue dots on the right of each micrograph are crystallites of 60-2-1.

It has been shown that a bulk morphology comprised of smaller, more dispersed, fullerene domains is optimal for charge transport and collection in devices containing P3HT⁶¹ and other donor polymers.⁶²⁻⁶⁴ These huge fullerene crystalline domains are not observed in P3HT:PCBM active layers. Clearly, the fullerene—fullerene attraction is greater than the fullerene—polymer in the case of 60-2-1 compared to PCBM. One possible explanation of why PCBM is more miscible in P3HT than 60-2-1 is that the phenyl ring and butyric acid methyl ester chain have more affinity for the hexylthiophene monomer units in P3HT and can more effectively interpenetrate the polymer chain than the shorter trifluoromethyl groups on 60-2-1. Therefore, PCBM mixing with P3HT is directed by the longer, aromatic-containing, side chain, while 60-2-1 mixing with P3HT is dominated by cage pi—pi interactions of 60-2-1 molecules, which favors formation of large fullerenes clusters. The balance is shifted towards cage—cage affinity in the case of 60-2-1, but towards side group—polymer chain interactions in the case of PCBM. The difference in dipole moment of the two molecules may also contribute to their ordering in the blend. Another difference between 60-2-1 and PCBM is the addition pattern of the substituent; PCBM is added at the junction of two hexagons on the cage while the two CF₃ groups are added in *para* positions on a hexagon. Therefore, the remaining pi-system on the cage is different since different cage carbon atoms were *sp*²—to—*sp*³ hybridized, as discussed in Chapter 1. Currently, though, it is not known whether 1,7- and 1,9-bisadducts have fundamentally different cage—cage affinities in the solid state. This study revealed that while the TRMC measurement can act as a screening tool for new donor:acceptors material combinations for OPV devices, ultimately, if the long-range mobility of free carriers is poor (as determined by the donor and acceptor domain bulk morphologies), the device will not perform well.

Very recently, a PFAF with the chemical formula $C_{60}(CF_2C_6F_4)$, prepared by Mr. Long San of the Strauss Group, with the same addition pattern as PCBM and also an aromatic portion on the substituent, was hypothesized to have good miscibility with P3HT due to its similarities to PCBM and ICMA. Figure 5.22 shows the structure of this compound, which has been termed Mohawk since the rigid fused-ring adduct protruding perpendicularly from the cage looks like a mohawk hairdo on C_{60} . Here, it will be referred to as Mohawk- $[C_{60}]$ -monoadduct, or MCMA for short.

To screen for high electron mobility in the fullerene phase (crucial for high-performance OPV active layers), P3HT:MCMA blends were studied by TRMC and compared to P3HT:PCBM blend films prepared under identical conditions. Three loading ratios of fullerene to polymer were investigated, based on 30%, 50%, and 70% weight loadings of PCBM to P3HT. Weight percent loadings were adjusted for MCMA blends so they contained identical mole loadings to the P3HT:PCBM blends. As shown in Figure 5.23, the $\phi\Sigma\mu$ values for analogous MCMA and PCBM samples were indistinguishable. The time-resolved photoconductivity transients for the MCMA samples show light intensity dependence (Figure 5.24), indicative of significant electron mobility in the fullerene phase. When compared with PCBM, the transients were almost indistinguishable.

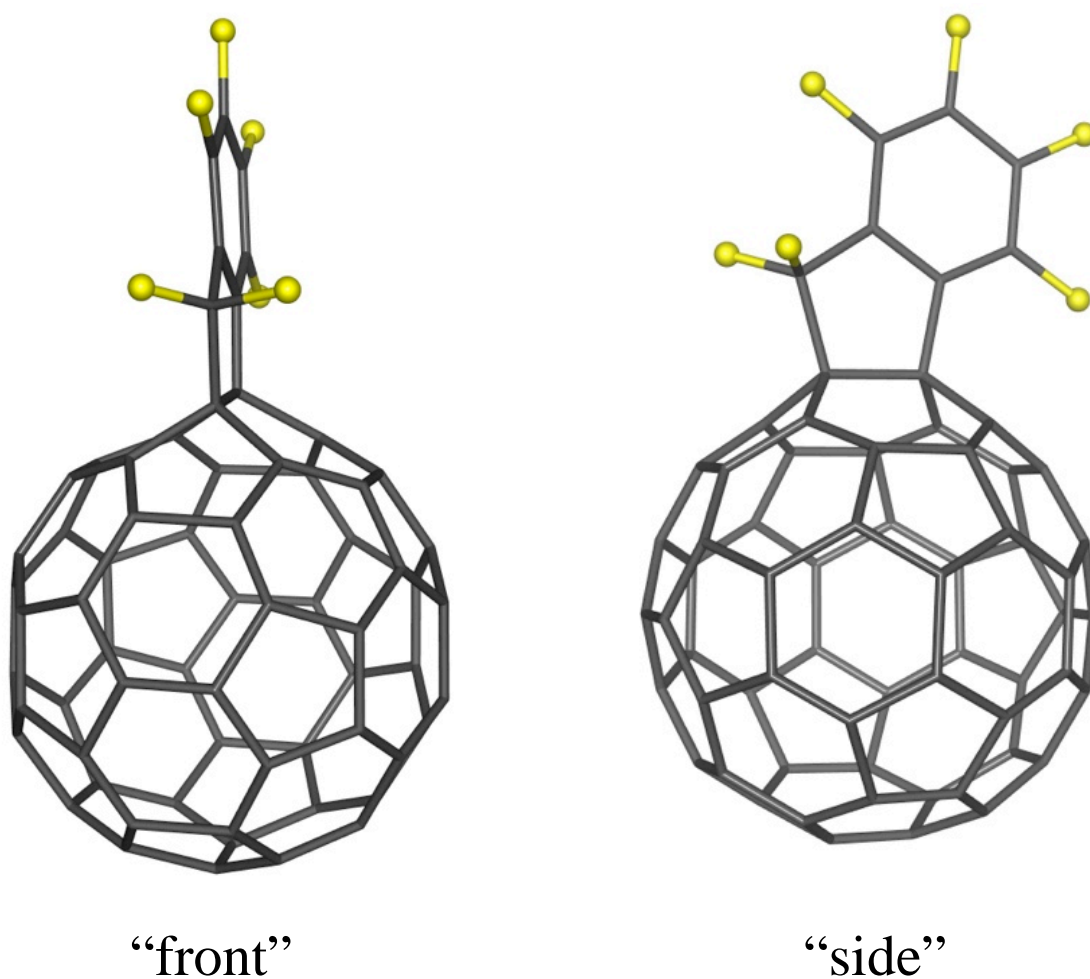


Figure 5.22. The structure of $C_{60}(CF_2C_6F_4)$, aka MCMA, from a front view and a side view of the substituent, highlighting the “mohawk hairdo” on C_{60} . Fluorine atoms are shown in yellow.

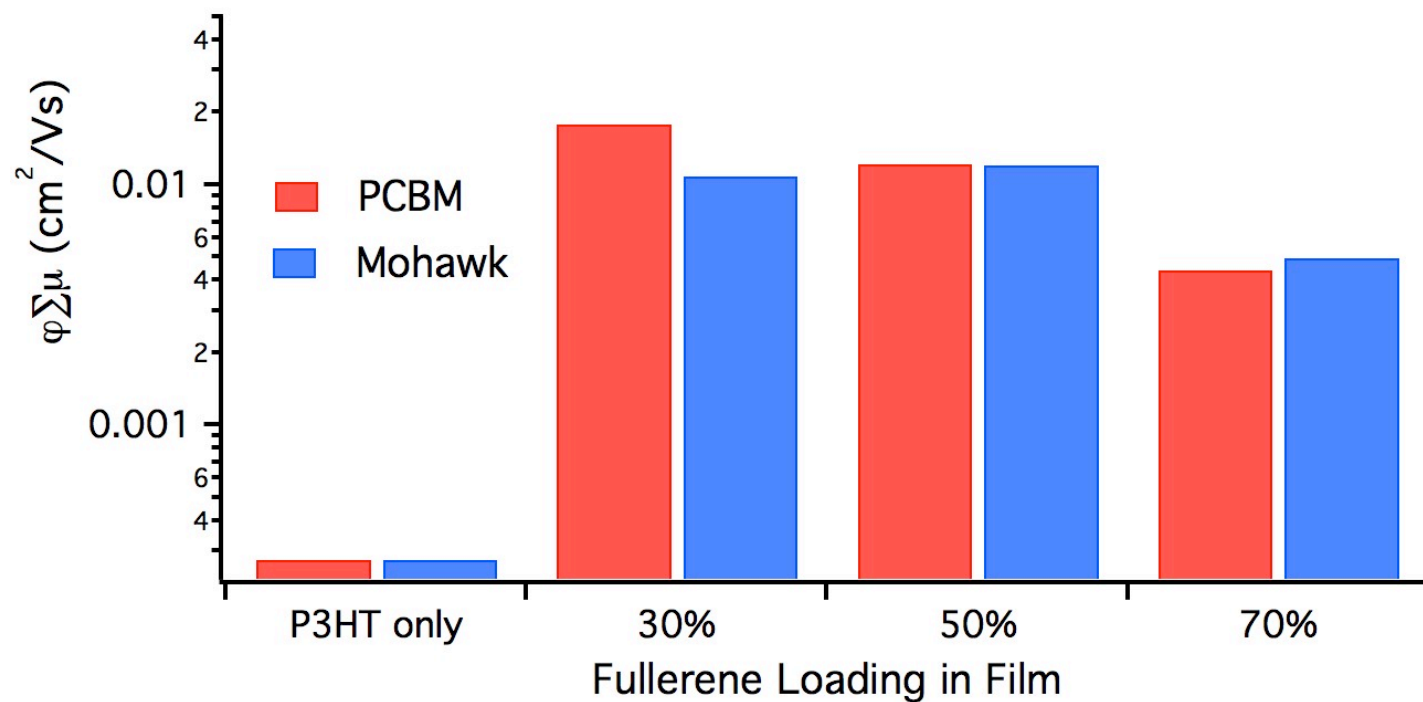


Figure 5.23. The $\phi\Sigma\mu$ values for spin-coated thin films of PCBM and Mohawk (MCMA) measured by TRMC. The percentage loadings refer to wt % loadings for PCBM:P3HT, and the corresponding molar loadings of MCMA:P3HT.

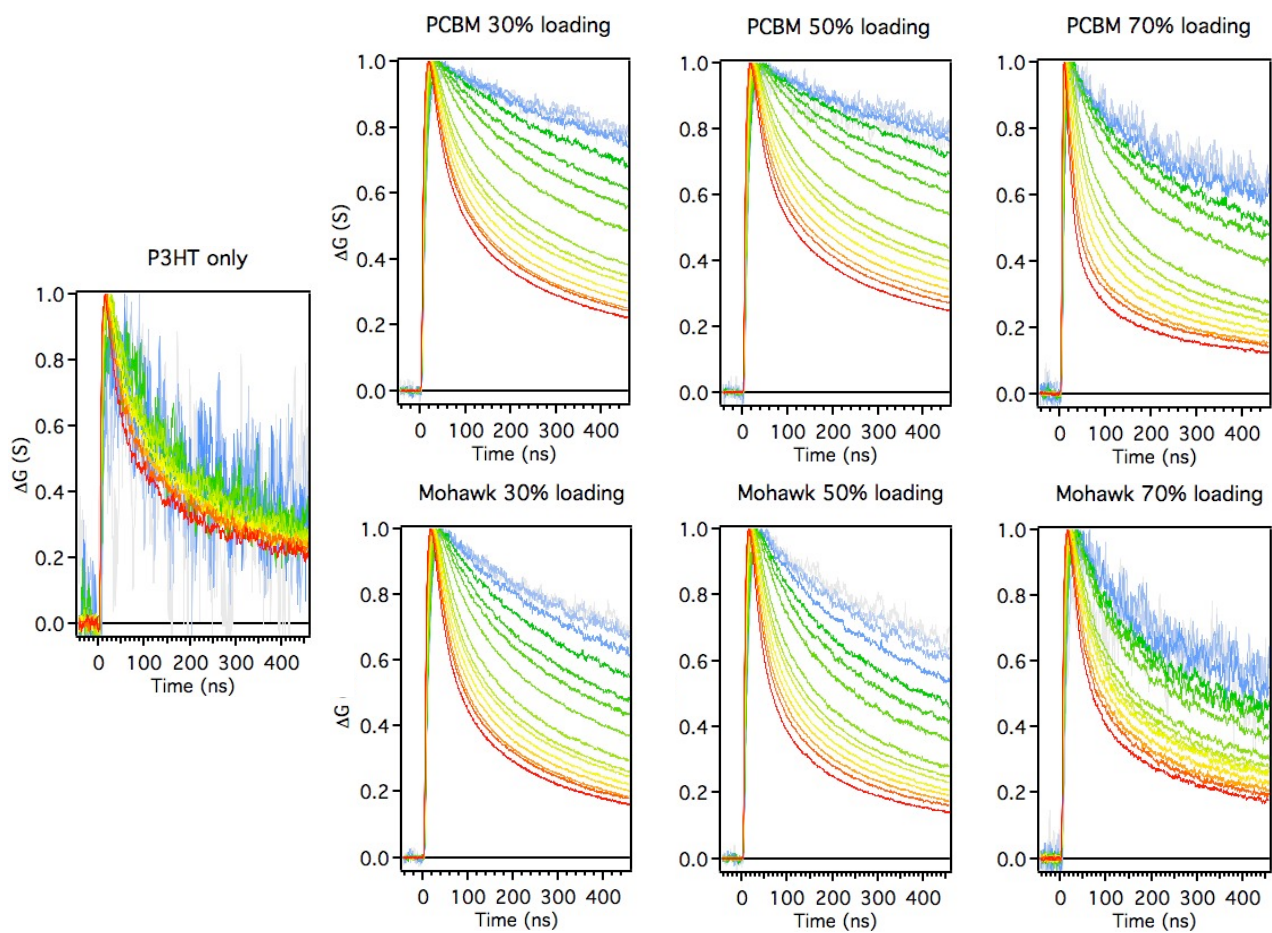


Figure 5.24. Normalized photoconductivity transients for PCBM and Mohawk (MCMA) blends with P3HT (top and bottom, respectively) and neat P3HT (far left). The percentage loadings refer to wt % loadings for PCBM:P3HT, and the corresponding molar loadings of MCMA:P3HT. The spread in photoconductance between low (blue) and high (red) light intensity indicates contribution to the signal due to electron mobility in the fullerene phase.

These promising TRMC results prompted interest in device performance, so a set of MCMA devices containing the same blend ratio active layers as the TRMC samples were fabricated with the architecture ITO/PEDOT:PSS/MCMA:P3HT/Ca/Al. Each device was prepared in duplicate for reproducibility. A set (also in duplicate) of corresponding P3HT:PCBM devices were also prepared for comparison. All 12 device active layers were deposited using the same method; therefore the active layer thicknesses are essentially constant between same-loading ratios. That is, the 30:70 PCBM and MCMA devices have the same active layer thickness as each other, the 50:50 PCBM and MCMA devices have the same active layer thickness as each other, and so on. However, since the content of P3HT dominates film thickness when spin-coating, the active layer thickness is different between samples of different loadings – i.e. the 30:70 films are thicker than the 50:50 films, which are thicker than the 70:30 films. The film thickness is important when analyzing the figures of merit for device performance (such as J_{sc}) because it: (i) determines how much light is absorbed in the film and (ii) defines the length the carriers have to travel to be collected at the electrodes (and therefore places an upper limit to allowable recombination).

Compiled in Figure 5.25 are the results of the 12 devices by each figure of merit, V_{oc} , J_{sc} , FF, and PCE, for the MCMA and PCBM devices. The data come from 2 devices for each loading (each substrate has 6 cells, or pixels), accounting for 12 measurements. All these measurement data were averaged (some pixels did not work and were truncated out) and plotted as horizontal data points. The “error bars” show the range of values that went into the average value, with the highest being the max in the data and the lowest being the min in the data.

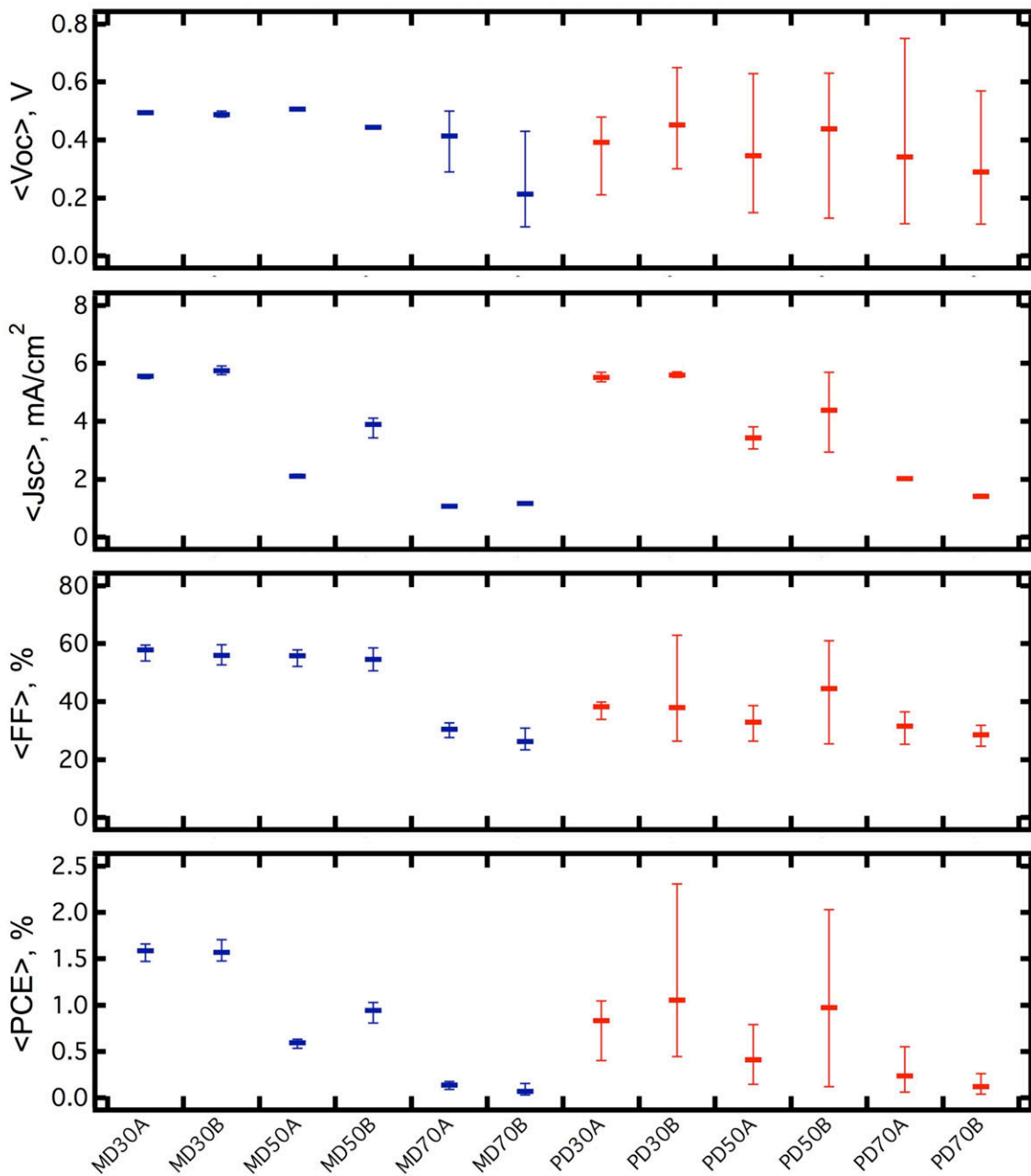


Figure 5.25. Average device performance figures of merit are given for Mohawk devices (blue) and PCBM devices (red). The bars on each horizontal data point represent the range of values for each device that constituted the average value, and serve as a depiction of the uniformity of the active layer film.

The MCMA devices produced much more consistent data than the PCBM devices, which is especially evident in the measured V_{OC} . An interesting property of MCMA is that its reduction potential is nearly the same as for C_{60} , and therefore should have a V_{OC} about 90 mV less than PCBM (since PCBM is harder to reduce than C_{60} by 90 mV in solution, i.e. – has a higher $E(LUMO)$). For PCBM:P3HT, the V_{OC} should be around 600 mV, as shown in Figure 5.25. Indeed, the V_{OC} in the MCMA 30:70 and 50:50 devices ranged from 440 to 510 mV. The 70:30 devices showed a decreased average V_{OC} , but at least one of the cell pixels in those devices had a V_{OC} in the right range. When fullerene loadings are high in these films, film uniformity and bulk morphology is poorer. Concerning the PCE, the MCMA devices were as good as or better than PCBM devices for corresponding loadings on average. However, the best individual pixel PCE was 2.3% for PCBM and 1.7% for MCMA. There are two reasons why these PCBM device PCE values are not 4% (the highest for this particular device architecture): (i) the active layers were spin-coated and rapidly dried, which is not the optimal method, and (ii) the active layers are not as thick as in the optimal devices (it requires even higher loading of material). However, since everything was prepared identically for PCBM and MCMA devices, these data can reliably serve as an initial comparison between the two.

In conclusion, TRMC can be useful technique for screening new donor:acceptor materials that may be promising for OPV devices. Molecular considerations have to be taken into account to when a high electron mobility component is observed in the photoconductance data before concluding materials will perform well in devices, since charge collection in devices depend greatly on bulk morphology. In the case of 60-2-1, large fullerene domains form in the bulk active layer, and the devices suffer from poor FF and J_{SC} . A new fullerene acceptor, MCMA, has

shown great promise for application in high-efficiency OPV devices, and therefore a full device optimization study is warranted to reveal how high the efficiency of a MCMA device can be, which is beyond the scope of this dissertation. What is important here is that TRMC was used to identify an acceptor with high electron mobility and now there is a new compound that potentially can be added to a very small group of acceptors that work well in OPV devices.

5.5. Summary and Conclusions.

A major challenge facing the fundamental and applied studies of new fullerene acceptors in OPV research, which serve to greatly benefit the OPV community, is the general inaccessibility of a wide range of fullerene acceptor compounds. The methods developed here, as discussed in Chapter 3, allowed access to a wide range of TMF acceptors, and in large quantities that enabled several OPV-relevant studies, including the first experimental determination of an optimal driving force for the relative yield of free carrier generation in a family of polyfluorene polymers by using a series of TMF acceptors with a large range of electron affinities. In another study, three pairs of TMFs showed convincing evidence that the yield for uncorrelated free charge generation in OPV device-relevant blends of donor:acceptor is a function of carrier mobility. Time-resolved microwave conductivity, which is a contactless method sensitive to free charges in OPV active layers, is an invaluable technique for probing the fundamental processes of free carrier generation, but also is a useful tool for screening potentially high-performance new donor:acceptor material combinations. Finally, a new PFAF, studied by TRMC and in OPV devices, was shown to perform comparable to PCBM, one of the best fullerene acceptors currently used in OPV research.

5.6. References.

- (1) Chapin, D. M.; Fuller, C. S.; Pearson, G. L.: A New Silicon p-n Junction Photocell for Converting Solar Radiation into Electrical Power. *Journal of Applied Physics* **1954**, *25*, 676-677.
- (2) Green, M. A.: The path to 25% silicon solar cell efficiency: History of silicon cell evolution. *Progress in Photovoltaics: Research and Applications* **2009**, *17*, 183-189.
- (3) Green, M. A.; Emery, K.; Hishikawa, Y.; Warta, W.; Dunlop, E. D.: Solar cell efficiency tables (version 39). *Progress in Photovoltaics: Research and Applications* **2012**, *20*, 12-20.
- (4) Jackson, P.; Hariskos, D.; Lotter, E.; Paetel, S.; Wuerz, R.; Menner, R.; Wischmann, W.; Powalla, M.: New world record efficiency for Cu(In,Ga)Se₂ thin-film solar cells beyond 20%. *Progress in Photovoltaics: Research and Applications* **2011**, *19*, 894-897.
- (5) Kippelen, B.; Bredas, J.-L.: Organic photovoltaics. *Energy & Environmental Science* **2009**, *2*, 251-261.
- (6) Li, C.-Z.; Yip, H.-L.; Jen, A. K. Y.: Functional fullerenes for organic photovoltaics. *Journal of Materials Chemistry* **2012**, *22*, 4161-4177.
- (7) Delgado, J. L.; Bouit, P. A.; Filippone, S.; Herranz, M. A.; Martin, N.: Organic photovoltaics: a chemical approach. *Chemical communications* **2010**, *46*, 4853-65.
- (8) Dang, M. T.; Hirsch, L.; Wantz, G.: P3HT:PCBM, Best Seller in Polymer Photovoltaic Research. *Advanced Materials* **2011**, *23*, 3597-3602.
- (9) Nardes, A. M.; Ferguson, A. J.; Whitaker, J. B.; Larson, B. W.; Larsen, R. E.; Maturová, K.; Graf, P. A.; Boltalina, O. V.; Strauss, S. H.; Kopidakis, N.: Beyond PCBM: Understanding the Photovoltaic Performance of Blends of Indene-C₆₀Multiadducts with Poly(3-hexylthiophene). *Advanced Functional Materials* **2012**, *22*, 4115-4127.
- (10) Ohkita, H.; Cook, S.; Astuti, Y.; Duffy, W.; Tierney, S.; Zhang, W.; Heeney, M.; McCulloch, I.; Nelson, J.; Bradley, D. D. C.; Durrant, J. R.: Charge Carrier Formation in Polythiophene/Fullerene Blend Films Studied by Transient Absorption Spectroscopy. *Journal of the American Chemical Society* **2008**, *130*, 3030-3042.
- (11) Clarke, T. M.; Durrant, J. R.: Charge photogeneration in organic solar cells. *Chemical reviews* **2010**, *110*, 6736-6767.
- (12) Brédas, J.-L.; Norton, J. E.; Cornil, J.; Coropceanu, V.: Molecular understanding of organic solar cells: the challenges. *Accounts of Chemical Research* **2009**, *42*, 1691-1699.
- (13) Imahori, H.; Tkachenko, N. V.; Vehmanen, V.; Tamaki, K.; Lemmetyinen, H.; Sakata, Y.; Fukuzumi, S.: An extremely small reorganization energy of electron transfer in porphyrin-fullerene dyad. *The Journal of Physical Chemistry A* **2001**, *105*, 1750-1756.
- (14) Vandewal, K.; Tvingstedt, K.; Gadisa, A.; Inganäs, O.; Manca, J. V.: On the origin of the open-circuit voltage of polymer-fullerene solar cells. *Nature materials* **2009**, *8*, 904-909.
- (15) O'Connor, D.: Time-correlated single photon counting; Elsevier Science, 1984.
- (16) Piris, J.; Dykstra, T. E.; Bakulin, A. A.; Loosdrecht, P. H. v.; Knulst, W.; Trinh, M. T.; Schins, J. M.; Siebbeles, L. D.: Photogeneration and ultrafast dynamics of excitons and charges in P3HT/PCBM blends. *The Journal of Physical Chemistry C* **2009**, *113*, 14500-14506.
- (17) Piris, J.; Kopidakis, N.; Olson, D. C.; Shaheen, S. E.; Ginley, D. S.; Rumbles, G.: The Locus of Free Charge-Carrier Generation in Solution-Cast Zn_{1-x}Mg_xO/Poly (3-

hexylthiophene) Bilayers for Photovoltaic Applications. *Advanced Functional Materials* **2007**, *17*, 3849-3857.

(18) Ferguson, A. J.; Kopidakis, N.; Shaheen, S. E.; Rumbles, G.: Quenching of Excitons by Holes in Poly(3-hexylthiophene) Films. *Journal of Physical Chemistry C* **2008**, *112*, 9865-9871.

(19) Dicker, G.; de Haas, M. P.; Siebbeles, L. D.; Warman, J. M.: Electrodeless time-resolved microwave conductivity study of charge-carrier photogeneration in regioregular poly(3-hexylthiophene) thin films. *Physical Review B* **2004**, *70*, 045203.

(20) Dicker, G.; de Haas, M. P.; Siebbeles, L. D.: Signature of exciton annihilation in the photoconductance of regioregular poly(3-hexylthiophene). *Physical Review B* **2005**, *71*, 155204.

(21) Holt, J. M.; Ferguson, A. J.; Kopidakis, N.; Larsen, B. A.; Bult, J.; Rumbles, G.; Blackburn, J. L.: Prolonging Charge Separation in P3HT–SWNT Composites Using Highly Enriched Semiconducting Nanotubes. *Nano letters* **2010**, *10*, 4627-4633.

(22) Ferguson, A. J.; Kopidakis, N.; Shaheen, S. E.; Rumbles, G.: Dark carriers, trapping, and activation control of carrier recombination in neat P3HT and P3HT: PCBM blends. *The Journal of Physical Chemistry C* **2011**, *115*, 23134-23148.

(23) Markov, D. E.; Amsterdam, E.; Blom, P. W.; Sieval, A. B.; Hummelen, J. C.: Accurate measurement of the exciton diffusion length in a conjugated polymer using a heterostructure with a side-chain cross-linked fullerene layer. *The Journal of Physical Chemistry A* **2005**, *109*, 5266-5274.

(24) Markov, D.; Tanase, C.; Blom, P.; Wildeman, J.: Simultaneous enhancement of charge transport and exciton diffusion in poly(p-phenylene vinylene) derivatives. *Physical Review B* **2005**, *72*, 045217.

(25) Choong, V.; Park, Y.; Gao, Y.; Wehrmeister, T.; Mullen, K.; Hsieh, B.; Tang, C.: Dramatic photoluminescence quenching of phenylene vinylene oligomer thin films upon submonolayer Ca deposition. *Applied physics letters* **1996**, *69*, 1492-1494.

(26) Marks, R.; Halls, J.; Bradley, D.; Friend, R.; Holmes, A.: The photovoltaic response in poly(p-phenylene vinylene) thin-film devices. *Journal of Physics: Condensed Matter* **1994**, *6*, 1379.

(27) Shaw, P. E.; Ruseckas, A.; Samuel, I. D.: Exciton diffusion measurements in poly(3-hexylthiophene). *Advanced Materials* **2008**, *20*, 3516-3520.

(28) Shaw, P.; Lewis, A.; Ruseckas, A.; Samuel, I.: Exciton annihilation and diffusion in semiconducting polymers. In *Optics & Photonics*; International Society for Optics and Photonics, 2006; pp 63340G-63340G-8.

(29) Magnani, L.; Rumbles, G.; Samuel, I.; Murray, K.; Moratti, S.; Holmes, A.; Friend, R.: Photoluminescence studies of chain interactions in electroluminescent polymers. *Synthetic metals* **1997**, *84*, 899-900.

(30) Hiroshi, I.; Kiyoshi, H.; Tsuyoshi, A.; Masanori, A.; Seiji, T.; Tadashi, O.; Masahiro, S.; Yoshiteru, S.: The small reorganization energy of C₆₀ in electron transfer. *Chemical physics letters* **1996**, *263*, 545-550.

(31) Guldi, D. M.; Martin, N.: *Fullerenes: from synthesis to optoelectronic properties*; Springer, 2002; Vol. 4.

(32) Coffey, D. C.; Larson, B. W.; Hains, A. W.; Whitaker, J. B.; Kopidakis, N.; Boltalina, O. V.; Strauss, S. H.; Rumbles, G.: An Optimal Driving Force for Converting Excitons

into Free Carriers in Excitonic Solar Cells. *The Journal of Physical Chemistry C* **2012**, *116*, 8916-8923.

(33) Braunecker, W. A.; Oosterhout, S. D.; Owczarczyk, Z. R.; Larsen, R. E.; Larson, B. W.; Ginley, D. S.; Boltalina, O. V.; Strauss, S. H.; Kopidakis, N.; Olson, D. C.: Ethynylene-Linked Donor-Acceptor Alternating Copolymers. *Macromolecules (Washington, DC, U. S.)* **2013**, *46*, 3367-3375.

(34) Hoke, E. T.; Sachs-Quintana, I. T.; Lloyd, M. T.; Kauvar, I.; Mateker, W. R.; Nardes, A. M.; Peters, C. H.; Kopidakis, N.; McGehee, M. D.: The Role of Electron Affinity in Determining Whether Fullerenes Catalyze or Inhibit Photooxidation of Polymers for Solar Cells. *Advanced Energy Materials* **2012**, *2*, 1351-1357.

(35) Dennler, G.; Scharber, M. C.; Ameri, T.; Denk, P.; Forberich, K.; Waldauf, C.; Brabec, C. J.: Design Rules for Donors in Bulk-Heterojunction Tandem Solar Cells Towards 15% Energy-Conversion Efficiency. *Advanced Materials* **2008**, *20*, 579-583.

(36) Bundgaard, E.; Krebs, F. C.: Low band gap polymers for organic photovoltaics. *Solar Energy Materials and Solar Cells* **2007**, *91*, 954-985.

(37) Nelson, J.: Polymer: fullerene bulk heterojunction solar cells. *Materials today* **2011**, *14*, 462-470.

(38) Chen, Y.-C.; Yu, C.-Y.; Fan, Y.-L.; Hung, L.-I.; Chen, C.-P.; Ting, C.: Low-bandgap conjugated polymer for high efficient photovoltaic applications. *Chemical communications* **2010**, *46*, 6503-6505.

(39) Popov, A. A.; Kareev, I. E.; Shustova, N. B.; Stukalin, E. B.; Lebedkin, S. F.; Seppelt, K.; Strauss, S. H.; Boltalina, O. V.; Dunsch, L.: Electrochemical, Spectroscopic, and DFT Study of C₆₀(CF₃)_n Frontier Orbitals (n = 2–18): The Link between Double Bonds in Pentagons and Reduction Potentials. *Journal of the American Chemical Society* **2007**, *129*, 11551-11568.

(40) Hirsch, A.: *The chemistry of the fullerenes*; Wiley Online Library, 1994.

(41) Popov, A. A.; Kareev, I. E.; Shustova, N. B.; Lebedkin, S. F.; Strauss, S. H.; Boltalina, O. V.; Dunsch, L.: Synthesis, Spectroscopic and Electrochemical Characterization, and DFT Study of Seventeen C₇₀(CF₃)_n Derivatives (n= 2, 4, 6, 8, 10, 12). *Chemistry-A European Journal* **2008**, *14*, 107-121.

(42) Singh, T. B.; Marjanović, N.; Matt, G.; Günes, S.; Sariciftci, N.; Montaigne Ramil, A.; Andreev, A.; Sitter, H.; Schwödiauer, R.; Bauer, S.: High-mobility *n*-channel organic field-effect transistors based on epitaxially grown C₆₀ films. *Organic electronics* **2005**, *6*, 105-110.

(43) Haddon, R.; Perel, A.; Morris, R.; Palstra, T.; Hebard, A.; Fleming, R.: C₆₀ thin film transistors. *Applied physics letters* **1995**, *67*, 121-123.

(44) Kobayashi, S.; Takenobu, T.; Mori, S.; Fujiwara, A.; Iwasa, Y.: Fabrication and characterization of C thin-film transistors with high field-effect mobility. *Applied physics letters* **2003**, *82*, 4581.

(45) MacKenzie, R. C.; Frost, J. M.; Nelson, J.: A numerical study of mobility in thin films of fullerene derivatives. *The Journal of chemical physics* **2010**, *132*, 064904.

(46) Gajdos, F.; Oberhofer, H.; Dupuis, M.; Blumberger, J.: On the Inapplicability of Electron-Hopping Models for the Organic Semiconductor Phenyl-C₆₁-butyric Acid Methyl Ester (PCBM). *The Journal of Physical Chemistry Letters* **2013**, *4*, 1012-1017.

(47) Bakulin, A. A.; Rao, A.; Pavelyev, V. G.; van Loosdrecht, P. H.; Pshenichnikov, M. S.; Niedzialek, D.; Cornil, J.; Beljonne, D.; Friend, R. H.: The role of driving energy and

delocalized states for charge separation in organic semiconductors. *Science* **2012**, 335, 1340-1344.

(48) Kumar, P.; Kumar, H.; Jain, S.; Venkatesu, P.; Chand, S.; Kumar, V.: Effect of active layer thickness on open circuit voltage in organic photovoltaic devices. *Japanese Journal of Applied Physics* **2009**, 48, 1501.

(49) Janssen, R. A.; Nelson, J.: Factors limiting device efficiency in organic photovoltaics. *Adv Mater* **2013**, 25, 1847-58.

(50) Hoke, E. T.; Vandewal, K.; Bartelt, J. A.; Mateker, W. R.; Douglas, J. D.; Noriega, R.; Graham, K. R.; Fréchet, J. M. J.; Salleo, A.; McGehee, M. D.: Recombination in Polymer:Fullerene Solar Cells with Open-Circuit Voltages Approaching and Exceeding 1.0 V. *Advanced Energy Materials* **2013**, 3, 220-230.

(51) Yamamoto, S.; Orimo, A.; Ohkita, H.; Benten, H.; Ito, S.: Molecular Understanding of the Open-Circuit Voltage of Polymer:Fullerene Solar Cells. *Advanced Energy Materials* **2012**, 2, 229-237.

(52) Jamieson, F. C.; Domingo, E. B.; McCarthy-Ward, T.; Heeney, M.; Stingelin, N.; Durrant, J. R.: Fullerene crystallisation as a key driver of charge separation in polymer/fullerene bulk heterojunction solar cells. *Chemical Science* **2012**, 3, 485.

(53) Guerrero, A.; Marchesi, L. F.; Boix, P. P.; Bisquert, J.; Garcia-Belmonte, G.: Recombination in Organic Bulk Heterojunction Solar Cells: Small Dependence of Interfacial Charge Transfer Kinetics on Fullerene Affinity. *The Journal of Physical Chemistry Letters* **2012**, 3, 1386-1392.

(54) Troshin, P. A.; Hoppe, H.; Renz, J.; Egginger, M.; Mayorova, J. Y.; Goryachev, A. E.; Peregodov, A. S.; Lyubovskaya, R. N.; Gobsch, G.; Sariciftci, N. S.: Material Solubility-Photovoltaic Performance Relationship in the Design of Novel Fullerene Derivatives for Bulk Heterojunction Solar Cells. *Advanced Functional Materials* **2009**, 19, 779-788.

(55) Renz, J. A.; Troshin, P. A.; Gobsch, G.; Razumov, V.; Hoppe, H.: Fullerene solubility-current density relationship in polymer solar cells. *physica status solidi (RRL)-Rapid Research Letters* **2008**, 2, 263-265.

(56) Chen, H.; Hegde, R.; Browning, J.; Dadmun, M.: The miscibility and depth profile of PCBM in P3HT: thermodynamic information to improve organic photovoltaics. *Physical Chemistry Chemical Physics* **2012**, 14, 5635-5641.

(57) Dadmun, M.; Chen, H.; Peet, J.: Correlation of Fullerene Structure to its Miscibility in P3HT and OPV Function. *Bulletin of the American Physical Society* **2013**, 58.

(58) Ray, B.; Nair, P. R.; Alam, M. A.: Annealing dependent performance of organic bulk-heterojunction solar cells: A theoretical perspective. *Solar Energy Materials and Solar Cells* **2011**, 95, 3287-3294.

(59) Zeng, L.; Tang, C. W.; Chen, S. H.: Effects of active layer thickness and thermal annealing on polythiophene: Fullerene bulk heterojunction photovoltaic devices. *Applied Physics Letters* **2010**, 97, 053305.

(60) Clarke, T. M.; Ballantyne, A. M.; Nelson, J.; Bradley, D. D.; Durrant, J. R.: Free energy control of charge photogeneration in polythiophene/fullerene solar cells: the influence of thermal annealing on P3HT/PCBM blends. *Advanced Functional Materials* **2008**, 18, 4029-4035.

(61) Hoppe, H.; Sariciftci, N. S.: Morphology of polymer/fullerene bulk heterojunction solar cells. *Journal of Materials Chemistry* **2006**, 16, 45-61.

(62) Yao, Y.; Shi, C.; Li, G.; Shrotriya, V.; Pei, Q.; Yang, Y.: Effects of C derivative in low band gap polymer photovoltaic devices: Spectral complementation and morphology optimization. *Applied physics letters* **2006**, *89*, 153507.

(63) Zhang, F.; Bijleveld, J.; Perzon, E.; Tvingstedt, K.; Barrau, S.; Inganäs, O.; Andersson, M. R.: High photovoltage achieved in low band gap polymer solar cells by adjusting energy levels of a polymer with the LUMOs of fullerene derivatives. *Journal of Materials Chemistry* **2008**, *18*, 5468-5474.

(64) Morana, M.; Azimi, H.; Dennler, G.; Egelhaaf, H. J.; Scharber, M.; Forberich, K.; Hauch, J.; Gaudiana, R.; Waller, D.; Zhu, Z.: Nanomorphology and Charge Generation in Bulk Heterojunctions Based on Low-Bandgap Dithiophene Polymers with Different Bridging Atoms. *Advanced Functional Materials* **2010**, *20*, 1180-1188.